Turbulence Structure of a Model Seagrass Meadow

by

Enrique Rafael Vivoni Gallart

S.B. Environmental Engineering Science
Massachusetts Institute of Technology, 1996

Submitted to the Department of Civil and Environmental Engineering
in Partial Fulfillment of the Requirements for the Degree of

Master of Science
in Civil and Environmental Engineering

at the

MASSACHUSETTS INSTITUTE OF TECHNOLOGY
August 14, 1998

[September 1998]

Author .....
Department of Civil and Environmental Engineering
August 14, 1998

Certified by .....
Heidi M. Nepf
Thesis Supervisor
Assistant Professor of Civil and Environmental Engineering

Accepted by .....
Joseph M. Sussman
Chairman, Departmental Committee on Graduate Studies

Eng

Turbulence Structure of a Model Seagrass Meadow

by

Enrique Rafael Vivoni Gallart

Submitted to the Department of Civil and Environmental Engineering
on August 14, 1998, in partial fulfillment of the requirements for the
degree of Master of Science in Civil and Environmental Engineering

Abstract

A laboratory study of the hydrodynamics of a seagrass meadow was conducted to investigate the effect of water depth and velocity variations during a tidal cycle on the mean and turbulent velocity fields in and above the vegetation layer. The principal goal was to characterize the turbulence structure of a depth-limited canopy, a gap that presently exists in the knowledge concerning the interaction of a unidirectional flow with an assemblage of plants. The experiments were carried out in an open channel flume with a model seagrass canopy. Proper modeling of the system for both the geometric and dynamic behavior of natural *Zostera marina* communities allows the results to be extrapolated to the conditions in a coastal, tidal meadow. The results also serve as an important comparative case to the characterization of turbulence within atmospheric plant canopies.

The laboratory study included the measurement of the mean and turbulent velocity fields with the use of an acoustic Doppler velocimeter and a laser Doppler velocimeter. Standard turbulence parameters were evaluated, including the velocity moments, the turbulence spectra, the turbulent kinetic energy budget and the quadrant distribution of the Reynolds stress. Each of these provided a means of describing the effect of submergence depth and the degree of canopy waving (*monami*) on the transport of momentum and mass between the canopy and its surrounding fluid environment. In addition, surface slope measurements were made with surface displacement gauges, the plant motion was quantified using video and camera images, and the canopy morphology was recorded from measurements taken from a random sampling of the model plants.

The investigation showed a clear link between the shear generated eddies arising at the interface of the canopy and the surface layer and the vertical exchange of momentum, the plant motion characteristics and the turbulence time and length scales. The turbulence field within the seagrass meadow was composed of a shear-generated turbulence zone near the canopy height and a wake-generated zone near the bed. In addition, a mean flow due to the pressure gradient from the water surface slope created a region of secondary maxima in the mean velocity profile near the bed. The parameter determining the seagrass turbulence structure was found to be the characteristic depth (H/h), defined such that the effective canopy height, h, reflects the plant deflection. Across the range of values considered for H/h, the flow characteristics showed a clear transition from a confined to an unbounded canopy flow. This transition was observed in all the principal turbulence parameters. From this analysis, a critical surface layer depth governing the transition between the two extreme canopy flow conditions was identified as half the effective canopy height, $H/h = 1.50$.

Thesis Supervisor: Heidi M. Nepf
Title: Assistant Professor of Civil and Environmental Engineering

Acknowledgements

First, I would like to acknowledge the support given to this research by the funding from a GEM M. S. Engineering and a National Science Foundation Fellowships during the 1996–1997 and 1997–1998 academic years, respectively. Supplementary support was also provided through an NSF grant #EAR-9629259 administered by Professor Heidi M. Nepf.

Many individuals contributed to the development and completion of this thesis. I would like to thank, first and foremost, my advisor, Heidi Nepf, for giving me the opportunity to explore this subject and for her guidance along every step of the way. After about a year and half of preliminary testing, experimental set up and literature review on my part, the topic that forms this thesis came about from her insightful suggestion as to the lack of relevant studies concerning depth-limited canopy flows.

In addition to Heidi, I would like to thank the other members of my research group, Paul Fricker, Hrund Andradottir, Laura DePaoli and Chin-Hsien Wu for their questions, comments and support throughout the two years leading up to this thesis. In particular, I am deeply indebted to Chin who has been a mentor and a close friend to me since I began my graduate studies.

Other members of the Parsons Laboratory also contributed directly to this work. Among them, I would like to mention Richard Camilli for helping me out with the surface slope measurements. I have also benefited from interactions and course work with various faculty members from our laboratory, including Prof. Ole Madsen, Prof. Harry Hemond, Prof. C.C. Mei, Prof. Eric Adams and Prof. Elfatih Eltahir, which have given me the necessary background to address the description of the turbulence structure in this hydrodynamic system. I would especially like to thank Prof. Rafael Bras for being a friend and a mentor throughout my undergraduate and graduate studies at M.I.T.

On a personal note, I have found a great group of friends in my five years at M.I.T. with whom I have created a tight support group and close friendships. My roommates during the last two years, Juan Carlos Pérez, José Oscar Mur and Carlos Hidrovo, have always lent a hand in tackling any problem that I have faced, from constructing the model plants, to writing programs for data analysis, to describing this hydrodynamic system. Many other friends have come and gone during these college years, but these have always been there for me. *Gracias, hermanos.*

And speaking about brothers, I recently have had the pleasure of living with one of my real brothers, Francisco. This has been a great time for us and his presence has helped me wrap this document up. The rest of my family, my youngest brother, Gabriel, my parents, Enrique and Mary, and my grandparents, have been the unwavering element in my life and the ones who have stood by me during each and every one of the hurdles and obstacles I have found or created along the way. *Gracias, familia.*

Table of Contents

List of Symbols

a	Vegetation density [cm^{-1}]
a_{blade}	Vegetation density blade region [cm^{-1}]
a_C	Canopy bulk canopy density [cm^{-1}]
a_H	Depth bulk canopy density [cm^{-1}]
a_{ij}	Probe geometry components
a_{mo}	Model vegetation density [cm^{-1}]
a_p	Plant vibration amplitude [cm]
a_{pt}	Prototype vegetation density [cm^{-1}]
a_{stem}	Vegetation density stem region [cm^{-1}]
A	Channel area [cm^2]
A_k	Constant in Kolmogorov coefficient
A_f	Frontal area [cm^2]
B	Canopy width [cm]
c	Speed of sound [m/s]
C_1, C_2	Conversion factors for gauges [V/cm]
$\Delta C_1, \Delta C_2$	Uncertainty factors for gauges [V/cm]
C_b	Skin friction drag coefficient
C_D	Horizontally averaged drag coefficient
C_{DC}	Canopy bulk drag coefficient
C_{DH}	Depth bulk drag coefficient
d	Displacement height [cm]
d_b	Blade width [cm]
d_{bmo}	Model blade width [cm]
d_{bpt}	Prototype blade width [cm]
d_f	Fringe spacing [μm]
d_h	Blade height [cm]
d_p	Mean plant diameter [cm]
d_s	Stem diameter [cm]
d_t	Blade thickness [cm]
D	Pipe diameter [cm]
D_T	Total nondimensional drag
D_P	Plant nondimensional drag
D_{PC}	Canopy form of D_P
D_{PH}	Depth form of D_P
D_S	Substrate nondimensional drag
D_{SC}	Canopy form of D_S
D_{SH}	Depth form of D_S
e	Natural logarithm base
E	Modulus of elasticity [N/m^2]
Eff	Efficiency ratio
Exc	Exchange ratio
Exu	Exuberance ratio
f	Darcy-Weisbach friction factor
f_1	Functional relationship in Π theory
f_b	Noise boundary frequency [Hz]
f_D	Frequency in Doppler Burst [Hz]
f_{ej}	Ejection arrival frequency [Hz]
f_{Fi}	Form drag term
f_i	Resonant frequencies [Hz]
f_η	Dissipation range frequency [Hz]
f_n	Natural frequency of vibration [Hz]
f_N	Nyquist frequency [Hz]
f_p	Plant vibration frequency [Hz]
f_{pui}	Dimensional peak frequency [Hz]
f_s	Shift frequency in Bragg cell [MHz]
f_S	Sampling frequency [Hz]
f_{sw}	Sweep arrival frequency [Hz]
f_T	ADV transmit frequency [MHz]
f_{ui}	Spectral frequency [Hz]
f_{Vi}	Viscous drag term
f_x	Total streamwise drag force
F_D	Drag force per unit mass [m/s^2]
F_{DC}	Canopy drag force [m/s^2]
F_{DH}	Depth drag force [m/s^2]
Fr	Froude number
g	Acceleration due to gravity [cm/s^2]
h	Effective canopy height [cm]
h_b	Deflected plant height [cm]
h_c	Critical surface layer depth [cm]
h_i	Interval height [cm]
h_m	Zero crossing depth [cm]
h_o	Surface layer depth [cm]
h_p	Undeflected plant height [cm]
h_{pen}	Penetration depth [cm]
h_{pmo}	Model plant height [cm]
h_{ppt}	Prototype plant height [cm]
H	Water depth [cm]
H_c	Characteristic depth
H_{mo}	Model water depth [cm]
H_o	Hole size
H_{oc}	Critical hole size
H_{pt}	Prototype water depth [cm]
i,j	Repetitive indices
I	Moment of inertia [m^4]
$I_{i,Ho}$	Indicator function
I_o	Identification function
I_u, I_v, I_w	Turbulence intensity
J	Flexural rigidity [N m^2]
k_{pui}	Peak wave number [cm^{-1}]
k_{ui}	Wave number [cm^{-1}]
K_u, K_w	Kurtoses coefficient
l_s	Plant spacing [cm]
L	Canopy length [m]
L_s	Shear length scale [cm]
L_u, L_v, L_w	Integral length scales [cm]
LAI	Leaf area index
m	Blade density

m_l	Mass per unit length of blade [g/m]
m_{mo}	Model blade density
m_{pt}	Prototype blade density
m_s	Slope of load-deflection curve
MKE	Mean kinetic energy [cm^2/s^2]
MSE	Mean square error
n	Manning coefficient
n_c	String length
n_{cr}	Critical string length
n_i	Unit normal to canopy element surface
n_{ij}	Noise moment
n_o	Sample size
n_{pui}	Nondimensional peak frequency
n_u, n_v, n_w	Nondimensional frequency
N	Plant density [plants/m^2]
N_b	Blade density [blades/m^2]
$N_{i,Ho}$	Number of events in record
N_o	Number of points in record
p, P	Pressure [N/m^2]
p_i	Spatial dimensions vector [cm]
P_i	Noise contribution factors
P_s	Shear production [cm^2/s^3]
P_v	Waving production [cm^2/s^3]
P_w	Wetted perimeter [cm]
P_W	Wake production [cm^2/s^3]
q	Turbulent kinetic energy [cm^2/s^2]
Q	Flow Discharge [L/s]
r	Relative roughness
rms	Root-mean-square velocity [cm/s]
r_{uw}	Correlation coefficient
R	Autocovariance function [cm^2/s^2]
R_e	Residual in TKE budget [cm^2/s^2]
Re_*	Roughness Reynolds number
Re_C	Canopy Reynolds number
Re_D	Drag Reynolds number
Re_H	Depth Reynolds number
R_h	Hydraulic radius [cm]
s_{pui}	Normalized peak spectral density
s_{uiui}	Normalized spectral density
S	Bed slope
S_B	Surface slope from backwater curve
S_c	Structure coefficient
S_f	Friction slope
S_{ho}	Surface slope in surface layer
S_H	Surface slope from Reynolds stress
S_i	Canopy element surface
$S_{i,Ho}$	Conditional average stress [cm^2/s^2]
S_{uiui}	One-dimensional spectra [cm^2/s]
Sk_{uiwj}	Skewness coefficient
St	Strouhal number
S_w	Water surface slope
ΔS_o	Sweep-ejection difference
SNR	Signal-to-noise ratio [dB]

t	Time [s]
t_1, t_2	Time [s]
T	Temperature [°C]
$\mathbf{T}$	Transformation matrix
T	Averaged shear stress [N/m^2]
T_d	Dispersive transport [cm^2/s^3]
T_{ej}	Ejection arrival time [s]
$T_{i,Ho}$	Fractional event time
T_p	Pressure transport [cm^2/s^3]
T_{sw}	Sweep arrival time [s]
T_s	Sampling time [s]
T_t	Turbulence transport [cm^2/s^3]
TKE	Turbulent kinetic energy [cm^2/s^2]
u_*	Friction velocity [cm/s]
u,v,w	Cartesian coordinate velocities [cm/s]
u_s	Characteristic velocity [cm/s]
$u_{rms}, \sqrt{\overline{u'^2}}, \sigma_u$	Turbulent velocity [cm/s]
uw	Reynolds stress [cm^2/s^2]
uw_{max}	Maximum Reynolds stress [cm^2/s^2]
U^*	Transformed velocity [cm/s]
U_1	Surface layer velocity [cm/s]
U_2	Vegetation layer velocity [cm/s]
U,V,W	Transformed velocities [cm/s]
U_{ave}	Average velocity flow regions [cm/s]
U_c	Canopy velocity [cm/s]
U_{ch}	Channel velocity [cm/s]
U_{eddy}	Eddy convection velocity [cm/s]
U_h	Interface velocity [cm/s]
U_m	Depth averaged velocity [cm/s]
U_{mij}	Measured moments
U_{mo}	Model canopy velocity [cm/s]
U_p, V_p, W_p	Untransformed velocities [cm/s]
U_{pt}	Prototype canopy velocity [cm/s]
ΔU	Velocity layer difference [cm/s]
$v_{rms}, \sqrt{\overline{v'^2}}, \sigma_v$	Turbulent velocity [cm/s]
v_i	Canopy element velocity [cm/s]
v_p	Particle velocity in LDV [cm/s]
v_s	Fringe velocity in LDV [cm/s]
V	Averaging volume [cm^3]
V_1, V_2, V_3	Bistatic axis velocities [cm/s]
$V_{1,0}, V_{2,0}$	Voltage reading at zero for gauges [V]
V_1, V_2	Voltage readings at run for gauges [V]
$\Delta V_{1,0}, \Delta V_{2,0}$	Uncertainty in voltage readings
$\Delta V_1, \Delta V_2$	Uncertainty in voltage readings
$w_{rms}, \sqrt{\overline{w'^2}}, \sigma_w$	Turbulent velocity [cm/s]
$\Delta x, \Delta y$	Control volume dimensions [cm]
x,y,z	Cartesian coordinates [cm]
z_b	Near bed level [cm]
z_i	Inflection point location [cm]
z_h	Height of inhomogeneity [cm]
z_o	Roughness height [cm]
α	Horizontal rotation angle [°]

$\alpha_{u,,v,w}$	Kolmogorov constants
β	Vertical rotation angle [°]
β_m	Boussinesq coefficient
δ_w	Vorticity thickness [cm]
ε	Instrument accuracy
ε_H	Material Strain
ε_T	Turbulent dissipation [cm^2/s^3]
ϕ	Phase angle [rad]
ϕ_p	Plant deflection angle [°]
γ_i	Resonant frequency coefficient
η	Kolmogorov microscale [cm]
φ	Bed angle [°]
κ	Von Karman constant
λ	Roughness density
λ_l	Laser beam wavelength [nm]
λ_m	Monami wavelength [cm]
λ_T	Taylor microscale [cm]
Λ_x	Streamwise periodicity [cm]
μ	Dynamic viscosity [Ns/m^2]
ν	Kinematic viscosity [cm^2/s]
ν_e	Extinction coefficient
θ	Bistatic angle [°]
θ_b	Angle between laser beams [rad]
θ_m	Monami phase velocity [cm/s]
ρ	Water density [g/cm^3]
ρ_s	Material density [g/cm^3]
σ	Standard deviation [cm/s]
σ_H	Material stress [N/m^2]
σ_D^2	Doppler noise error [cm^2/s^2]
σ_m^2	Electronic noise error [cm^2/s^2]
σ_t^2	Total velocity error variance [cm^2/s^2]
σ_u^2	Shear velocity error [cm^2/s^2]
Σ_i	Nondimensional event stress
τ	Lag time [s]
τ_b	Bed shear stress [N/m^2]
τ_o	Wall shear stress [N/m^2]
ω	Radial frequency [rad/s]
ξ	Scalar of vector quantity
ζ	Autocorrelation function
$\mathfrak{I}$	Integral time scale [s]

List of Figures

List of Tables

List of Photos

CHAPTER 1. Introduction

1.1 Introduction

In the past, the major motivation for studying the turbulence structure in plant canopies has been to understand the processes and mechanisms that lead to the exchange of heat, mass and momentum between the terrestrial environment and the atmosphere (*e.g.*, Raupach and Thom, 1981). Forming the lower part of an unbounded boundary layer, terrestrial vegetation canopies are subject to large scale atmospheric turbulence that determines the characteristics of the in-canopy environment. Thirty years of research into plant canopy turbulence has led to the quantification of the characteristic scales and processes responsible for the turbulent structure observed in many types of vegetation, from Amazonian forests to croplands. Recently, Raupach *et al.* (1996) published an excellent work that provided a clear understanding of the interaction of coherent eddies with the canopy environment based on the analogy of a mixing layer between two coflowing fluids. The similarities among the two hydrodynamic systems in terms of profiles of the velocity statistics and the turbulent kinetic energy budget suggested that the previous conceptualization of canopy flow as perturbation of boundary layer flow was incorrect. Viewing canopy turbulence as an expression of the shear generated instabilities formed at the inflection point of the velocity profile located at the canopy height shed a new light upon the phenomenon and allowed for a reinterpretation of previous data.

While a great deal is known about the unconfined canopy flow case, much less is known about the turbulence structure of a confined canopy flow, such as that occurring in aquatic systems bounded by a free surface. Only a handful of papers have addressed the flow through emergent and submerged vegetation, the most notable of which are laboratory studies of open channel flow through flexible and rigid artificial plants (*e.g.*, Murota *et al.* 1984; Tsujimoto *et al.*, 1996; Lopéz and García, 1996), numerical studies of the flow through a confined and unconfined canopy (Burke and Stolzenbach, 1983; Shimizu and Tsujimoto, 1994), and the recent work in describing the turbulence, drag and diffusion through emergent plant canopies (Nepf *et al.*, 1997b; Nepf and Vivoni, 1998). Otherwise, evidence of the effect of aquatic plant canopies on a unidirectional flow comes from a disparate group of research fields interested in the subject for a variety of different reasons, *e.g.* the conveyance of water through vegetated canals (*e.g.*, Kouwen, 1992), the cycling of particulate and dissolved matter in coastal systems (*e.g.*, Leonard and Luther, 1995), and the transport of sediment in regions of varied bottom roughness

(*e.g.*, Tsujimoto, 1997), among other topics. Despite considerable research within these fields, the changes in the turbulence structure induced by variations in the degree of confinement have not yet been addressed.

In particular, a topic that deserves immediate attention is the transition between the two extreme boundary conditions in plant canopy flows, one with no upper limit and the other bounded at the height of the plants. The gap between the unbounded (*i.e.*, atmospheric vegetation) and constrained (*i.e.*, emergent aquatic vegetation) conditions is a crucial missing piece in our present knowledge concerning the turbulence structure in a plant canopy flow. To fill this gap, this work uses a laboratory experiment to examine the effect of changing the water depth on the various measures of canopy turbulence. The results of this study provide the first description of the transition in the turbulence structure from unconfined to confined flow, defining how the paradigms established for the unbounded flow through atmospheric vegetation change as the depth of the overlying boundary layer is diminished.

The interaction of a unidirectional flow with a vegetation canopy is a dynamic process that not only involves the conversion of mean flow energy into turbulence but also the response of the roughness elements to the aerodynamic or hydrodynamic forcing. In vegetation with substantial flexibility, plant bending and movement are important dynamic responses that are indicative of the dominant turbulence structure within the flow. The coherent waving of flexible cereal crops such as rice, barley, and wheat over windy days, called a *honami*, is a striking example of the interaction of the wind with a vegetation layer and has been studied in both field (Finnigan, 1979a, 1979b; Maitani, 1979) and laboratory atmospheric conditions (Finnigan and Mulhearn, 1978; Brunet *et al.*, 1994; Shaw *et al.*, 1995). A similar phenomenon has been observed in aquatic systems (*monami*), *e.g.* in seagrass meadows in field studies (Fonseca and Kentworthy, 1987; Ackerman and Okubo, 1993, Grizzle *et al.*, 1996) and in laboratory studies with submerged model plants (Kouwen *et al.*, 1969, 1973), although very little quantitative measurement of the waving motion or its relation to the turbulence structure have been made. Except for the important contribution made by Murota *et al.* (1984), the coherent waving of aquatic plants has received little attention from a hydrodynamic points of view in the past. Recently, however, more interest has been placed on determining the turbulence structure through waving aquatic plants (*e.g.*, Ikeda and Kanazawa, 1996) with the results from the atmospheric canopies serving as a strong background.

There is a need to investigate how the variation of water velocity affects the turbulence structure in a depth limited canopy flows as a means of providing a useful comparison and quantifying the effect of coherent canopy waving. Addressing both issues simultaneously allows the description of the relative importance of the depth and velocity variation on the mean and turbulence fields within and above the meadow. In addition, the possibility of incorporating the variation of the velocity into a more generalized conceptual model based solely on the variation of the depth (H) normalized by an effective canopy height, h, is potentially a significant result. It would imply that the turbulence structure can be parameterized exclusively on a single parameter, the depth of the surface layer, that takes into account the velocity

variation simply through a change in the canopy height. Reducing both effects to a single parameter, H/h, that varies between emergent conditions ($H/h \leq 1.00$) and unconstrained conditions ($H/h \rightarrow \infty$) would advance our understanding of the transition between the two types of canopy flows and the turbulence structures associated with each, *i.e.* wake generated turbulence and shear generated turbulence.

This experimental study set out to recreate in a laboratory setting the field conditions of a seagrass meadow. The seagrass meadow was chosen as a representative type of submerged vegetation due to a particular interest expressed in the marine biology literature for understanding the relationship between the flow environment and the biological, chemical and ecological functioning of the plant community. A seagrass meadow is not a canopy *per se*, as the strict definition of a canopy implies a separated crown region of increased density, but the term is loosely used in many studies to imply an assemblage of plants. In this study, the terms *meadow* and *canopy* will be used interchangeably to describe the seagrass system and compare it to other plant canopies.

The results from this study are applicable to other types of flexible, submerged plant canopy, including river and channel vegetation, submerged plants in the littoral zones of freshwater lakes, wetland vegetation in periodically inundated regions and macroalgae. In fact, these results could potentially be extrapolated to other hydrodynamic systems that have as a lower boundary condition an assemblage of flexible elements that constitute a significant portion of the flow, such as cilia that line internal body cavities, groups of benthic animals and worms attached to the lower portions of a lake or stream, and even to man-made flexible linings used for a variety of industrial purposes.

Seagrass meadows are an important part of the world biosphere, comprising one of the most productive ecosystems on Earth (Thayer *et al.*, 1975), but do not receive the attention commensurate with the role they play in the marine environment or on a global scale in general. The absence of a hydrodynamic focus to the past investigations on the interaction of flow with the meadow has lead to erroneous interpretations concerning the velocity measurements taken within field and laboratory conditions (Fonseca *et al.*, 1982). Thus, describing the flow through these submerged meadows from a quantitative hydrodynamics perspective provides a prime opportunity to transfer knowledge across interdisciplinary boundaries. A brief background of the hydrodynamics of seagrass meadow, in particular, and submerged vegetation, in general, and the implications of the interaction between a flow and the meadow will be a useful introduction to this experimental study.

1.2 Background and Motivation

Plant canopies that undergo periodic or permanent inundation are commonly found in the littoral zones of freshwater, brackish and saline lakes, along river banks and channels, in floodplains and in large expanses of low-lying coastal shore. Seagrass meadows, in particular, occupy extensive regions of the near-coast continental shelf throughout the world, with meadow sizes ranging on the order of a few meters to several kilometers. The term *seagrass* refers to an assemblage of twelve different genera (about sixty species) of aquatic angiosperms that are completely adapted to life underwater and is derived from the resemblance that many of these species have with their terrestrial counterparts (den Hartog, 1970). Seagrass communities form an essential part of the marine environment by creating sources of food and habitat for fish and other fauna, modifying their surroundings through sediment stabilization and changes in the current and wave regime, and mediating the exchanges of material between the terrestrial and open ocean ecosystems. Understanding how seagrasses affect the hydrodynamics of shallow coastal waters and the transport of dissolved and particulate species is essential in determining the role of these ecosystems as material sources and sinks.

The depth to which seagrass ecosystems are found depend upon the light attenuation properties of the water column. In clear waters, seagrasses can reach depths of approximately 20 to 30 meters. In contrast the high turbidity characteristic of regions with sediment input or elevated degrees of wave-resuspension can limit seagrass growth to depths on the order of one meter (Thayer *et al.*, 1975). Because of their shallow sublittoral existence, seagrass communities are subject to the diurnal or semidiurnal fluctuations in water depth and current velocity that result from the action of tides. Typically within coastal regions and embayments, the current resulting from the propagation of the tidal wave reverses direction during the tidal cycle, the flood tide directed onshore as the tide is rising and the ebb tide directed offshore for the falling tide (Pond and Pickard, 1978, p. 206). Along with the variation of the current direction and speed during the tidal cycle, the level of submergence of the seagrass meadow changes from mean low water (MLW) to mean high water (MHW) levels, which depending upon the geometry of the coastline imply changes in water depth over the tidal cycle from a few up to about ten meters (Komar, 1998, p. 90). As a result of the action of tides, seagrass meadows are subject to flow depths and current speeds. The impact of these factors on the plant-flow interaction will be explored in this study.

The modifications made by the seagrass meadow on the flow environment are numerous, ranging from the small scale, as in creating a low energy environment well suited as a fish habitat, to the large scale, as in the alteration of coastal accretion or subsidence and effects on embayment circulation patterns. Previous laboratory and field studies in coastal seagrass meadows have described the general effects that these systems have on a unidirectional current of uniform velocity. Marked contrasts in the mean and turbulent velocity fields have been observed in vegetated regions as compared to unvegetated zones.

Reduced velocities within the seagrass meadow (*e.g.*, Fonseca *et al.*, 1982, Gambi *et al.*, 1990; Ackerman and Okubo, 1993) are a result of the drag exerted by the plants on the current and the redirection of flow over the top of the canopy. Higher turbulence levels relative to the unvegetated zones are due to the production of turbulence at the canopy-water interface as pointed out by Gambi *et al.* (1990) and the turbulence production in the plant wakes (Nepf *et al.*, 1997b). In addition, the plant canopies induce changes in the turbulence scale that ultimately lead to variations in the diffusion and mixing within the plant stand. Despite qualitative and quantitative measures that have been obtained of the flow conditions through a seagrass meadow, a generalized conceptual understanding of the hydrodynamics of an aquatic plant canopy has not been developed to its fullest extent.

The baffling effect of the submerged macrophytes promotes sediment settling (Fonseca and Fisher, 1986; Fonseca, 1989; Almasi *et. al.*, 1987), while the extensive plant rhizome system stabilizes the underlying sediment surface (Thayer, 1975). By stabilizing sediment and minimizing erosion, seagrass systems should play an important role in the geomorphological development of coastal zones, as observed for coastal marshes (French and Stoddart, 1992). Moreover, it is well known that aquatic plants attenuate wave energy responsible for sediment resuspension (Ward *et al.*, 1984; Fonseca and Calahan, 1992), leading to further enhancement of particulate retention. Along with inorganic sediments, particulate organic matter and plant detritus also accumulate within vegetated regions due to the low energy flow conditions relative to open water. This in turn leads to a significant effect on the transport of contaminants, trace metals and nutrients associated with the organic particles (*e.g.*, Schlacher-Hoenlinger and Schlacher, 1998; Barko *et al.*, 1991).

Several other processes that are essential to seagrass ecology are linked to the flow environment. Seagrasses are capable of withstanding strong flow conditions due to their ability to respond to external forcing via plant bending. Under prone conditions, the seagrass meadow is capable of redirecting flow over the canopy, thus protecting the underlying root-rhizome complex from wave or current scour (Fonseca *et al.*, 1982). The survival and reproductive success of the ecosystem is also influenced by the changes in advection and diffusion induced through the interaction of the tidal currents with the meadow. The dispersal of seeds (Orth *et al.*, 1994), and the adsorption of essential nutrients and gases directly through the leaves (Fonseca and Kenworthy, 1987) is influenced by the flow conditions mediated by the plants themselves. Even the photosynthetic rate is influenced by the reduction of the diffusive boundary layers on the seagrass blades as the current velocity increases (Koch, 1994) and by effect of self shading as the plants bend or move in response to the flow (Fonseca *et al.*, 1982). The flow modification by the seagrass plants also affect the geochemical cycling of dissolved and particulate material between the sediments and the water column since the interaction of the flow and the plants create differential pressure gradients on the sediment surface that drive advective circulation patterns within the porous bed (*e.g.*, Koch, 1993). In summary, the microflow environment generated within the seagrass meadow directly

affects the properties of the fluid motion and indirectly affects a host of biological, geochemical and ecological processes within the seagrass community.

This laboratory study focused on a particular seagrass species commonly found along the East Coast of the United States, and even common in localized areas of Boston Harbor (Chandler *et al.*, 1996). *Zostera marina* L., or eelgrass, has formed the cornerstone of much of the current knowledge about the hydrodynamics of seagrass systems and seemed an appropriate choice to represent other seagrass and submerged macrophytes. As other seagrasses, *Zostera marina* meadows grows on the soft sediment substrate in shallow bays, saline pools and brackish streams and are directly subject to tidal and/or river currents. A field investigation performed as a companion to this laboratory study provided some first hand knowledge of an eelgrass ecosystem and the variety of flow conditions which these meadows encounter (Vivoni *et al.*, 1997, unpublished data). During the course of the field program, the variations in tidal current and in wind induced waves were noticeable during the course of a single day. In addition, the localization of the eelgrass meadows varied from the shallow waters of a coastal shoal with a water depth on the order of a meter, to more interior regions where the eelgrass meadow extended to depths on the order of five meters. Typical characteristics of the eelgrass meadows encountered during the field experiment and the modeling of the laboratory study based upon the field conditions are discussed in Section 2.2 and cited in **Table. 2.1**.

The large, natural variability in the flow conditions to which a typical eelgrass meadow is subjected is difficult to reproduce in a laboratory model. Wind waves and currents change in direction and in magnitude frequently during the course of a single day. Eelgrass blades can be stagnant in the water column during part of the tidal cycle and then deflect in response to the flood or ebb tide during another period of time. In addition, the water depth varies in response to the tidal fluctuations, so that the plants constitute a larger or smaller portion of the total flow. To avoid these complexities, this experimental study focused exclusively on investigating the effect of a unidirectional current on a model eelgrass meadow, reproduced to faithfully capture the dynamic conditions in the field situation. Wind waves and the unsteady effects from the tidal variation have been ignored. In essence, this laboratory study attempts to take a snap shot of the eelgrass meadow behavior at particular instances where the depth of the overlying surface layer and the velocity through the canopy has changed. From these snapshots, the variation of the turbulence structure over the tidal cycle can be pieced together.

1.3 Goals

As described previously, this thesis intends to address two main issues, the effect of (1) the depth of submergence and of (2) the velocity on the turbulence structure of a seagrass meadow. Through different types of turbulence analyses, the study shows that the depth-limited flow through a plant canopy demonstrates a clear asymptotic behavior that controls the transition between a shear and a wake-dominated turbulence structure, *i.e.* between an unconstrained and a constrained boundary condition. It will also be shown that the velocity and waving motion of the flexible plant canopy does not appreciably alter the turbulence structure, although intensity changes are observed. The characteristic depth (H/h) will be shown to govern the turbulence structure variation due to changes in the depth and velocity of the flow. Finally, the potential application to the tidal flow through seagrass meadows and river flow at various stages through channel vegetation will be presented in an attempt to lay the groundwork for future numerical and theoretical models.

The thesis is divided into four chapters. The introduction presented as Chapter 1 was intended to motivate the need for the laboratory study and the potential usefulness of the results. Chapter 2 addresses describes the experimental methods used for this laboratory study, including the dimensional analysis used to choose realistic, appropriately scaled flow conditions, a description of the instrument technology, and an error analysis. Chapter 3 presents the results from the measurements of velocity profiles, surface slope and plant motion, and an extensive discussion of the analyses performed on these data. Chapter 4 is dedicated to summarizing the main features presented in the thesis and rendering the final conclusions on the turbulence structure in the model seagrass meadow.

CHAPTER 2. Experimental Methods

2.1 Introduction

A laboratory study was designed to explore the turbulence structure of a flexible plant canopy in an aquatic environment, addressing a lack of detailed studies performed for this hydrodynamic system and pursuing the description of the dominant transport processes in seagrass meadows. A laboratory model scaled to field conditions that includes a high degree of morphological complexity can simulate a seagrass meadow more faithfully than traditional vegetative models. A branched architecture and segmented plant body can create the vertical inhomogeneity characteristic of natural meadows. A canopy morphology with vertical gradients, in turn, can recreate the features observed in field measurements, such as the secondary maxima in the mean streamwise velocity near the bottom substrate (Ackerman and Okubo, 1993). Devoid of the morphological complexity, a laboratory canopy, such as those represented by rigid cylinders, can not be expected to exhibit the dynamic conditions found in coastal seagrass beds.

A laboratory study also provides the opportunity to control various parameters that influence the meadow behavior and isolate the specific effects of a single parameter on the turbulence structure. As mentioned in Chapter 1, an aquatic system is well suited to describing the effects that depth limitations, and thus boundary layer development, have on canopy turbulence. During the thirty years of atmospheric canopy flow research, this aspect has only been explored by Seginer *et al.* (1976), who compared the turbulence within a confined and an unconfined canopy in a wind tunnel study. With the ability to confine the seagrass canopy by changing the water depth, this laboratory study can reveal the transition between the two extreme pictures of canopy turbulence, wake-generated versus shear-generated.

In addition, the laboratory model was designed to recreate the unidirectional flow conditions that prompt canopy waving, as observed in the field by Grizzle *et al.* (1996) in the Jordan River in Maine, and Ackerman and Okubo (1993) in Woods Hole, Massachusetts, among others. The recreation of the monami motion in a laboratory setting is an important step in understanding the implications of the phenomenon to the turbulence structure of aquatic canopies. Laboratory experiments that consider the effect of depth variation and velocity variation separately can together be used to give a picture of how tidal variations in coastal areas affect the transport of momentum between the regions outside the canopy and the in-canopy region.

2.2 Dimensional Analysis and Scaling

An important aspect of any laboratory study is the proper modeling of the system to be reproduced under controlled conditions. Similarity between the prototype and the model can be achieved by scaling the geometry of the two systems and matching the dynamic nondimensional parameters. On most occasions, the geometric scaling can be easily achieved, while the dynamic scaling is somewhat more troublesome or even impossible. This experimental study attempts to describe the turbulence characteristics of seagrass meadows by performing a series of experiments in a laboratory setting. To properly extrapolate the results obtained from the flume experiments to field conditions, the two systems must be dynamically similar. To this end, a dimensional analysis was undertaken to derive the relevant parameters and match these to field observations from various eelgrass (*Zostera marina*) meadows.

Dimensional analysis is a tool used to determine the important parameters in any dynamic system, establish the nondimensional parameters that govern the system and simplify the functional relationships among these parameters. For unidirectional flow through a seagrass meadow in regions of no coastal slope, as shown in **Figure 2.1**, the system parameters are:

$$U, H, h_p, \phi_p, a, \rho, \mu, g, C_D, J, p_i, \tag{2.1}$$

where U is the mean velocity in the longitudinal direction (cm/s), H is the water depth (cm), h_p is the undeflected plant height (cm), ϕ_p is the deflection angle (°), a is the vegetation density (cm^{-1}), ρ is the water density (g/cm^3), μ is the dynamic viscosity (Ns/m^2), g is the acceleration due to gravity (cm/s^2), C_D is the drag coefficient, J is the flexural rigidity (Nm^2) and p_i is a vector containing the relevant spatial dimensions for the plant elements, including the blade dimensions (width, d_b, and thickness, d_t) and the plant spacing (l_s) (cm). These variables are a consequence of either the flow conditions (U, H), the plant canopy (h_p, C_D, J, p_i , a, ϕ_p) or the environment (g). We have ignored the effects of a bed slope and bottom shear stress due to the negligible slope in both coastal seagrass meadows and in the laboratory flume and the small bottom shear stress in canopy flows.

Applying the Buckingham Π theory to this set of parameters, we can form the following functional relationship:

$$f_1\left(\frac{U}{\sqrt{gH}}, \frac{HU}{\nu}, \frac{H}{h_b}, Ha, \frac{\rho U^2 H^4}{J}, C_D, \frac{p_i}{H}\right) = 0, \tag{2.2}$$

where we have used the variables g, H and U as the fundamental dimensions and introduced the deflected plant height, $h_b = h_p \cos\phi_p$ and the kinematic viscosity $\nu = \mu/\rho$. The terms in **Eq. 2.2** are the Froude number Fr, the depth Reynolds number Re_H, the characteristic depth H_c, the vegetation density Ha, the plant stiffness, the drag coefficient and the length scales. Considering the complexity of canopy flows, reducing this set of nondimensional variables to a more direct functional relationship is difficult. The goal is thus to model each of these parameter as faithfully as possible in the laboratory setting.

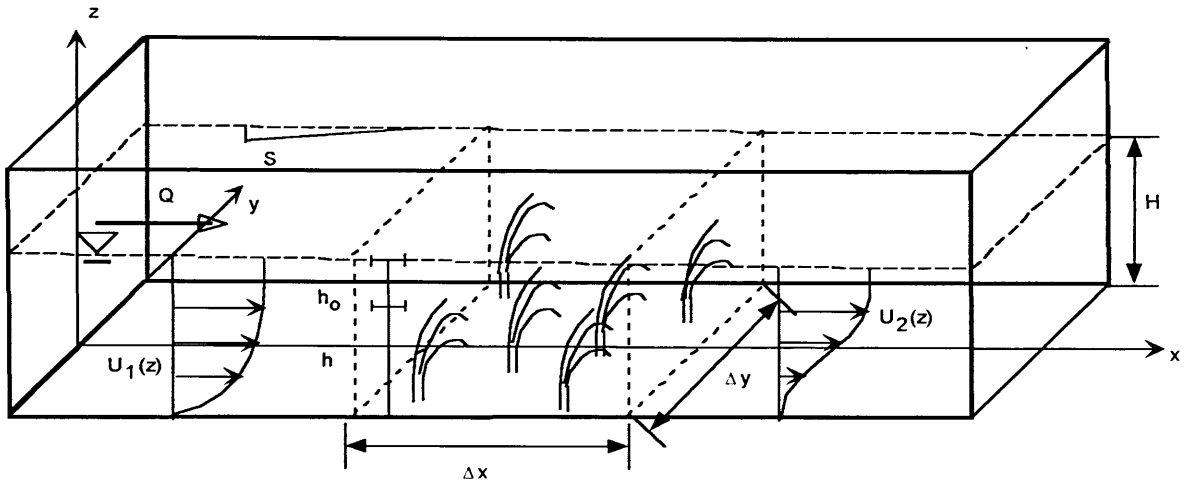

Figure 2.1. Sketch of the control volume for the laboratory study of flow through a flexible plant canopy (dimensions Δx, Δy, H). Also shown are the flow discharge (Q), the plant height (h_p), surface layer depth (h_o) and the surface slope (S). The incident open channel flow velocity profile and the shear layer profile caused by the canopy are shown before and after the control volume.

Characteristics of natural eelgrass beds were taken from field measurements in Massachusetts Bay (Chandler *et al.*, 1996), from a field study performed in Chincoteague Bay, Maryland (Vivoni *et al.*, 1997, unpublished data), and from other studies along the Atlantic and Pacific coast of the United States (Worcester, 1995; Ackerman and Okubo, 1993; Gambi *et al.*, 1990), as shown in **Table 2.1**. The parameter ranges from the field conditions were used in the scaling analysis to obtain the necessary laboratory values to ensure dynamic and geometric similarity.

To create similarity conditions between the laboratory model and the field conditions (prototype), the nondimensional terms in **Eq. 2.2** should be equal. For the depth Reynolds number (Re_H), the ratio of the inertial to the viscous forces, similarity implies that:

$$\left(\frac{UH}{\nu}\right)_{mo} = \left(\frac{UH}{\nu}\right)_{pt}, \tag{2.3}$$

where the subscripts *mo* and *pt* refer to the model and the prototype. Using the range of values from the field condition (U_{pt} = 0–100 cm/s; H_{pt} = 100–500 cm) and the laboratory results from Chapter 3 (U_{mo} = 2–27 cm/s; H_{mo} = 16–44 cm), we can show that the two systems have similar Re_H. The laboratory Reynolds number range ($4300–4.36\times10^4$) is well within the range of the field Reynolds number ($0–5\times10^6$). Re_H similarity ensures that the dynamic characteristics in the flume represent the field conditions well. A second type of dynamic similarity is achieved by matching the Froude number:

$$\left(\frac{U}{\sqrt{gH}}\right)_{mo} = \left(\frac{U}{\sqrt{gH}}\right)_{pt}, \tag{2.4}$$

Table 2.1. Field conditions for *Zostera marina.*			
Parameter	**Massachusetts Bay**	**Chincoteague Bay**	**Ranges**
Water depth	100 cm	95 cm	100–500 cm
Blade height	30 cm	28 cm	20–100 cm
Blade width	0.4 cm	0.26 cm	0.3–0.5 cm
Blade density	1800 blades/m^2	3800 blades/m^2	400–6000 blades/m^2
Mean velocity	10 cm/s	5 cm/s	0–100 cm/s

the ratio of inertial to gravity forces. Since gravitational acceleration is constant in both systems, **Eq. 2.4** becomes another relationship between the flow velocity and the water depth. Using the values for U and H, the laboratory Froude number (0.02–0.09) is found to be in the low end of the field Froude number range (0–0.32). The two dynamic conditions, Re_H and Fr similarity, cannot be satisfied simultaneously, as is the case with most laboratory experiments involving free surface flows. Under most circumstances, obtaining Reynolds number similarity is preferred due to the overriding importance of viscous effects, as compared to gravity. In this experimental study, the Froude number is much smaller than unity, implying subcritical conditions where this parameter plays a minor role. Other researchers have pointed to the negligible role of the Froude number in open channels flows involving flexible plants (Dunn *et al.*, 1996; Kouwen and Unny, 1973).

Geometric similarity between the model and prototype ensures that the proper scaling is made to the physical objects in the model, while the dynamic similarity described above leads to similar behavior. On most occasions, obtaining geometric similarity is quite straightforward. For this study, it implied matching the characteristic depth, the plant density and the nondimensional plant dimensions. Assuming that similar deflection angles (ϕ_p) are obtained by matching the dynamic characteristics, the required undeflected plant height (h_p) can be calculated from:

$$\left(\frac{H}{h_p}\right)_{mo} = \left(\frac{H}{h_p}\right)_{pt} . \tag{2.5}$$

Using the range of water depths and undeflected plant heights from the field (h_{ppt} = 20–100 cm) and laboratory conditions (h_{pmo} = 16 cm), the characteristic depth (H_c) is found to be reasonably similar in the two systems. The laboratory setting places limits upon H_c (1–2.75) that are not present in the field conditions (H_c = 1–25). Regardless, the range of values for the characteristic depth in the flume is sufficiently large to explore the effects of depth variation on turbulence structure in the seagrass meadow.

Matching the plant dimensions was performed by assuring that the blade width to height ratio

$$\left(\frac{d_b}{h_p}\right)_{mo} = \left(\frac{d_b}{h_p}\right)_{pt} \tag{2.6}$$

was similar in the two systems. Using the laboratory and field plant heights and the blade widths (d_{bpt} = 0.26–0.5 cm; d_{bmo} = 0.28 cm), the nondimensional plant size in the laboratory model (0.018) is within the range of field conditions (0.003–0.025).

Scaling the plant density consisted of matching the parameter Ha for the model and prototype. The plant density parameter a is defined here as the frontal area per unit volume occupied by the plant. It can be expressed as the number of blades per unit area (m) times the blade width, d_b:

$$a = md_b . \tag{2.7}$$

The model plant density, a_{mo}, is a function of the field blade density, chosen to represent a low density canopy (m_{pt} = 600 blades/m^2), the field and laboratory blade widths and the water depths in the two systems. The choice of a low density canopy as the modeled system corresponds to a need for laboratory experiments of low velocity and low density meadows as expressed by Worcester (1995). With these values, the model blade density required to simulate the conditions of a low density seagrass meadow is m_{mo}= 1950 blades/m^2, which was achieved by creating a canopy with 330 plants/m^2, each with 6 blades/plant. These results show that the model seagrass meadow must be denser than the prototype (a_{pt} = 240 cm^{-1}; a_{mo} = 550 cm^{-1}) for proper geometric scaling between the two systems.

Finally, the scaling of the plant stiffness was performed by matching the nondimensional flexural rigidity between the two systems:

$$\left(\frac{\rho U^2 H^4}{J}\right)_{mo} = \left(\frac{\rho U^2 H^4}{J}\right)_{pt} . \tag{2.8}$$

Although the similitude in stiffness is purely a geometric condition, the strong interaction between fluid flow and plant motion makes this parameter dynamically important. The degree of stiffness of the model plays a crucial role reproducing the behavior of natural eelgrass beds. The large range of values for H and U prevent that the flexural rigidity be precisely matched across all cases. Nevertheless, what can been done is to show that for a particular set of values, the flexural rigidity is reasonably scaled. Using representative values for the model and prototype velocity and water depth (H_{pt} = 100 cm; H_{mo} = 44 cm; U_{pt} = 5 cm/s; U_{mo} = 11 cm/s) which satisfy Reynolds number similarity, the model flexural rigidity must be J_{mo} = 0.2 J_{pt}. Unfortunately, field measurements of the stiffness of seagrasses, J_{pt}, are nonexistent in the literature and the only available values for submerged vegetation lack the necessary geometric information in $J = EI$ to carry out a full dimensional analysis. In its place, it can be shown that the model flexural rigidity is within the range of the stiffness of Bermuda grass of similar length as *Zostera marina*, as reported by Kouwen and Li (1980). With the choice of these parameters, the behavior, size and flexibility of the natural vegetation is reproduced well in the laboratory model and the results from the flume experiments can be extrapolated to field conditions.

2.3 Experimental Setup

The experimental study was conducted in the Ralph M. Parsons Laboratory for Hydrodynamics and Water Resources in the Department of Civil and Environmental Engineering at the Massachusetts Institute of Technology over a period of time extending from September 1996 to May 1998. The following sections are dedicated to describing the experimental facilities and instrumentation used in this characterization of seagrass meadow turbulence. Detailed descriptions of the two velocity measurement devices, an acoustic Doppler velocimeter and a laser Doppler velocimeter, are given, including an estimation of the experimental errors associated with each instrument and the preliminary tests performed to ensure the proper operation of the instruments. Methods used to estimate the water surface slope and the characteristics of the canopy motion are described as well.

2.3.1 Experimental Facilities

The experimental runs were conducted in a glass-walled, recirculating flume of dimensions 24 m long, 38 cm wide and 60 cm deep and zero bed slope, as pictured in the schematic of **Figure 2.2**. The open channel can be used to simulate a unidirectional current or two dimensional waves through the use of either a Weinman model 3G-181 pump or a wave-generator. For the present study, only the effects of a flexible vegetation canopy on a unidirectional current were investigated.

The flow discharge supplied by the pump was varied by adjusting an Asahi diaphragm valve in the return piping. The flume is equipped with a paddle wheel flow gauge manufactured by Signet Scientific Company (El Monte, CA), installed two meters from the valve in order to monitor the flow rate (Zavistoski, 1994). Preliminary studies demonstrated that the flow rate could be adjusted within the range from 20 to 240 gallons per minute (1.26 to 15.14 L/s) at all the experimental water depths. The resolution of the valve was adequate, allowing flow rate adjustments within 5 gpm (0.32 L/s). The operation of the current was straightforward with an electrical control panel allowing manual activation of the pump.

Upon entering the upstream end of the flume through an inlet pipe, the flow was dampened by placing a piece of rubberized coconut fiber (F.P. Woll & Company; Philadelphia, P.A.) encased in a small Plexiglas tray. The inclusion of the fiber was an important step in ensuring that the turbulence generated at the inlet was dissipated quickly. A meter downstream of the inlet, a second piece of rubberized fiber, six centimeters in width, was placed over the entire depth and followed by a short array of randomly placed circular cylinders also extending over the water depth. The purpose of both structures was to ensure lateral and vertical uniformity in the conditions upstream of the test section and to erase any possible turbulence signature imparted by the inlet condition. The last modification made to the flow before entering the stilling region consisted of passing through a 0.45 m long flow straightener located a meter downstream of the cylinder array, the purpose of which was to eliminate possible secondary currents initiated upstream of the test section. Further details can be seen in **Figure 2.2**.

The test section consisted of randomly placed model plants each constructed individually to meet the specifications determined through the scaling analysis (Section 2.2). Placing the model plants within the glass-walled flume entailed constructing a series of Plexiglas sheets, each having dimensions of 1.22 m in length, 37 cm in width and 1.5 cm in thickness. Six sheets were placed along the flume bottom and fastened by wedging the sides with long wooden strips and with all-purpose waterproof tape. The Plexiglas sheets were secured well to the flume bottom to ensure that flow in the gap between the two surfaces was negligible. A toe (1:10 slope) was placed at the transition between the condition upstream of the test section which was a hydraulically smooth glass bottom and the Plexiglas sheets, which were roughened by using an adhesive mesh tape (mesh size 0.2 cm and thickness 0.025 cm). Increasing the roughness in the test section bottom boundary was intended to more realistically mimic the interplant substrate roughness in seagrass meadows, as compared to a smooth Plexiglas bottom. Preliminary tests, however, showed that both the smooth and roughened boundary without the plant canopy were hydraulically similar and the effect of the mesh tape was negligible.

Each Plexiglas sheet served to hold a maximum of 2000 plants within the horizontal area of 0.45 m^2 through 0.64 cm holes drilled into the sheets. The plant arrangement was generated from a computer program that created a 1m length template of randomized positions with the restriction that individual plant stems must be placed at least one diameter apart (Nepf *et al.*, 1997; Mugnier, 1995). A random plant arrangement was expected to model the natural conditions more faithfully than the typical staggered patterns used in other vegetative flow studies (Kouwen and Unny, 1973; Dunn *et al.*, 1996), with the caveat that defining the interplant spacing is more difficult for the random case. In addition, the random pattern eliminated the potential for preferential flow pathways introduced by a periodic arrangement. A summary of the details about the test section can be found in **Table 2.2**.

The model plants consisted of two parts, each differing substantially in morphology and stiffness. The lower stem region was constructed from short wooden dowels of mean height 2.23 ± 0.43 cm and 0.635 cm in diameter. Use of the short wooden dowel corresponds well to the characteristics of the natural eelgrass plants that have a bundled stem region near the bottom substrate. The blade region consisted of 6 blades constructed from sheets of a green-colored vinyl plastic (PVCA Copolymer) of mean dimensions 13.74 ± 0.04 cm in length, 0.28 ± 0.01 cm in width and 0.025 cm in thickness. Again, these dimensions reproduce field conditions as shown in the dimensional analysis of Section 2.2. The total undeflected plant height, h_p was measured to be 15.97 ± 0.04 cm from a group of ten randomly selected plants. For the experimental runs designed to compare between different flow rates, the plant flexibility led to substantial decreases in the plant height. Visual observations from video taping the waving canopy led to estimates of the deflected plant height, h_b.

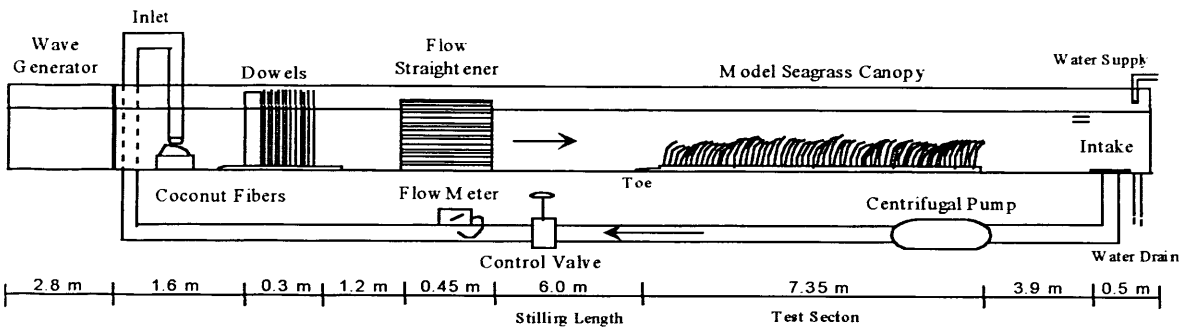

Figure 2.2 Schematic representation of experimental set up in the 24-m long flume. The water depth and the flow discharge were varied during the experimental runs. Schematic not to scale.

In addition to giving the plant a more complicated morphology, the practical purpose of the stem was to secure the entire plant firmly within the hole drilled into the Plexiglas bottom, upon which the blades could be fastened. Cloth tape was used to fastened the blades around each stem in such a way as to maximize the independent movement of each blade. A total of 2000 plants were constructed prior to the experimental studies, in order to cover a broad range of possible vegetation densities from 100 to 1000 plants per square meter. An intermediate density, 330 plants per m^2, was chosen as an appropriate value in this study based on scaling arguments and instrument considerations. A summary of the details about the model plants, including the dimensions and the material properties, can be found in **Table 2.2**.

2.3.2 Acoustic Doppler Velocimetry

The acoustic Doppler velocimeter (ADV) is a new tool in laboratory and field measurement of mean and turbulent flows developed by the U.S. Army Corps of Engineers Waterways Experimental Station (WES) in association with SonTek, San Diego, CA (Kraus *et al.*, 1994). It has been well received by the research community as evidenced by the number of recent publications that report the use of the instrument for turbulence measurements (Brunk *et al.*, 1996; López and García, 1996; Dunn *et al.*, 1996; Sukhodolov *et al.*, 1998; Biron *et al.*, 1998). As any new instrument, researchers have begun to evaluate ADV performance and suggest methods to quantify the errors associated with the instrument electronics and turbulence and shear within the sampling volume (Nikora and Goring, 1998; Voulgaris and Trowbridge, 1998). In light of these recent developments, an error analysis for the velocity data gathered with the ADV probe is possible. The next sections will briefly describe the ADV technology used in this experimental study, including the sensor specifications and the principles of the Doppler shift effect. In addition, the results from a series of preliminary tests conducted to determine the proper operating conditions for the ADV probe will be presented along with an error analysis of the ADV performance under the experimental conditions.

Table 2.2. Summary of canopy and plant characteristics.		
Canopy Parameters		
Undeflected plant height	h_p	15.97 cm
Mean plant diameter	d_p	1.50 cm
Canopy width	B	38 cm
Canopy length	L	7.32 m
Plant spacing	l_s	5.50 cm
Plant density	N	330 plants/m^2
Roughness density	λ	0.79
Leaf Area Index	LAI	0.76
Blade Parameters		
Blade length	d_h	13.74 cm
Blade width	d_b	0.28 cm
Blade thickness	d_t	0.025 cm
Blade density	N_b	6 blades/plant
Material Parameters		
Modulus of Elasticity	E	2.76 x 10^9 N/m^2
Moment of Inertia	I	3.65 x 10^{-15} m^4
Flexural rigidity	J	1.01 x 10^{-5} N m^2
Mass per unit length	m_l	9.46 x 10^{-4} kg/m
Material density	ρ_s	1.38 g/cm^3
Vibration Frequency	f_n	3.06 Hz

2.3.2.1 Technology Description

The ADV is a versatile instrument capable of operating under both laboratory and field conditions. The instrument used in this experimental study was an ADVField probe (Serial number 1073) purchased in 1994 from SonTek and recalibrated in June 1997 before the present study was undertaken. The ADVField probe is capable of remotely-sensing the three dimensional velocity of particles traveling through a small sampling volume located 5 cm from the apparatus. The sampling volume is approximately cylindrical in shape with a vertical scale of 9mm and a lateral dimension of 6 mm, making the sampling volume approximately 0.25 cm^3. The measurement volume can be placed a few millimeters away from a solid boundary, making it suitable for use in boundary layer laboratory studies (Cabrera and Lohrmann, 1993). An instrument traverse was used to place the ADV probe and the sampling volume at any *x, y, z* location of interest, as pictured in **Photo 2.1**.

The ADVField probe consists of three modules: a measuring probe, a signal conditioning module and a signal processing module. The measuring probe and the conditioning module are encased in a portable unit that is relatively easy to use and comes with a 10 meter cable that allows the deployment of the instrument in a remote location. The processing module, on the other hand, is within a separate, waterproof aluminum housing and contains the electronic components necessary to process the acoustic signal received by the probe. The measurement probe consists of a thin stem that is approximately 25 cm long upon which the downward-facing transmitter and receiver arms are placed, as shown in **Figure 2.3**.

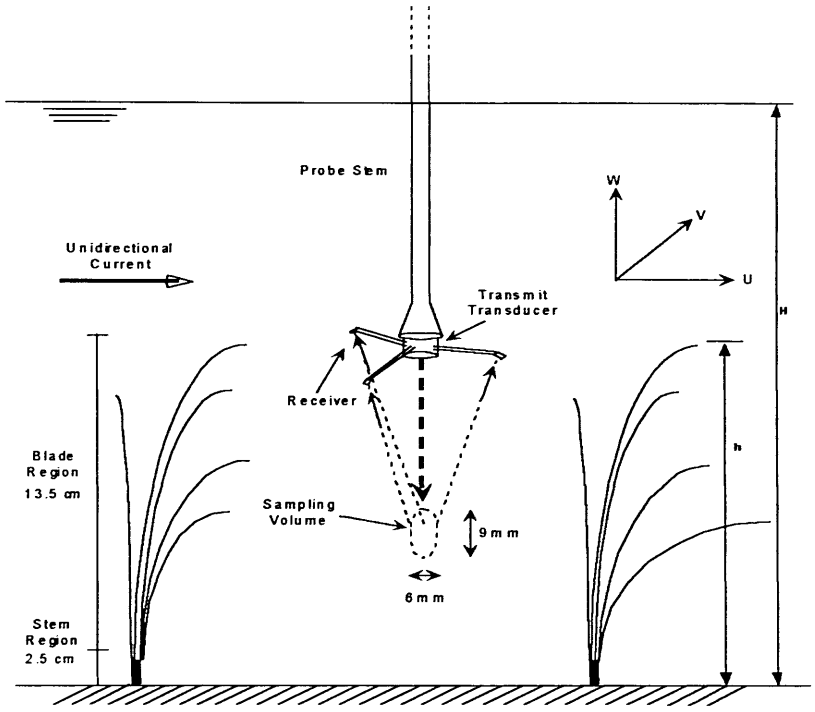

Figure 2.3 Acoustic Doppler Velocimeter (ADV) measurements within the model seagrass meadow. Probe geometry and canopy characteristics also shown. The ability to obtain the point measurement without disrupting the sampling volume is a primary advantage of the ADV.

The ADV functions based on the Doppler shift of periodic short acoustic pulses transmitted at 10 MHz from a transmit transducer located in the central portion of the probe (Kraus *et al*, 1994). As the pulse travels along the transmit beam, a fraction of the acoustic energy is scattered back by small particles, bubbles or sediment suspended in the water. Three 10 MHz receive transducers, spaced at 120° azimuth angle intervals and slanted 30° from the axis of the transmit transducer, receive the frequency-shifted echo pulses originating at the intersection of the transmitter and receiver beams. The velocity along the beam or bistatic axis is calculated by the ADV processing module from the phase data of successive coherent pulses using the Doppler relation:

$$V = \frac{c(d\phi/dt)}{4\pi f_T} \tag{2.9}$$

where V is the velocity along the beam axis; c is the speed of sound in water, a function of water temperature (T in °C); f_T is the transmit frequency; and the phase data is given by

$$\frac{d\phi}{dt} = \frac{1}{\tau}\tan^{-1}\left[\frac{\sin(t)\cos(t+\tau) - \sin(t+\tau)\cos(t)}{\cos(t)\cos(t+\tau) + \sin(t)\sin(t+\tau)}\right] \tag{2.10}$$

where ϕ is the signal phase in radians, t is time and τ is the time between pulses.

Photo 2.1. Acoustic Doppler velocimeter set up at the sampling region within the plant canopy. The location of the probe can be adjusted in each direction by the longitudinal, lateral and vertical traverses.

Doppler shifts measured at the three receivers thus provide estimates of flow velocity along three different directions, which are then converted to the Cartesian coordinate system velocity components, based on a factory-calibrated transformation matrix, **T**, that depends on the probe geometry, unique for each instrument (Lohrmann *et al.*, 1994). The probe coordinate system is defined such that the positive x direction is towards a specific receiver arm that is red-colored, the positive z direction is towards the probe and the positive y direction is the defined by the right hand rule, as is pictured in **Figure 2.3**. In the present study, the x direction was along the longitudinal flume axis ($x = 0$ at the canopy edge), the y axis corresponded to the cross stream direction ($y = 0$ at the centerline of the flume) and the z direction was normal to the bed ($z = 0$ at the bottom boundary). The velocity components (u,v,w) along the orthogonal axes are computed from the velocities along each acoustic axes (V_1,V_2,V_3) as:

$$\begin{bmatrix} u \\ v \\ w \end{bmatrix} = \mathbf{T} \cdot \begin{bmatrix} V_1 \\ V_2 \\ V_3 \end{bmatrix} \tag{2.11}$$

where the factory calibrated transformation matrix, **T**, for Probe 1073, provided by SonTek is:

$$\mathbf{T} = \begin{bmatrix} a_{11} & a_{12} & a_{13} \\ a_{21} & a_{22} & a_{23} \\ a_{31} & a_{32} & a_{33} \end{bmatrix} = \begin{bmatrix} 2.706 & -1.363 & -1.344 \\ -.012 & 2.338 & -2.328 \\ 0.346 & 0.346 & 0.341 \end{bmatrix}. \tag{2.12}$$

The information provided from the factory calibration matrix will be crucial in estimating the errors associated with the probe electronic noise and those introduced by averaging over the sample volume.

SonTek quotes the following performance characteristics for the ADVField probe: a velocity resolution of 0.1 mm/s and a velocity bias ± 0.5%; no measurable zero-offset in the horizontal direction and no need for routine recalibration of the probe; and a random noise approximately 1% of the velocity range setting at the 25 Hz sampling frequency (f_S). The lack of any appreciable zero-offset in the horizontal velocity is due to the inherent characteristics of all Doppler based systems. It makes the instrument well-suited for monitoring low-flow conditions, a particularly attractive feature for the present experimental study where we expected to have low velocities in the canopy region near the bed.

The primary disadvantages of using the ADV in our experimental conditions were the loss of a substantial amount of measurable water depth due to the distance between the probe and the sampling volume and the potential for a slight positive bias in the Reynolds stress measurement for flows less than 10 cm/s (Lohrmann *et al.*, 1995), although this was not corroborated in our study as evidenced in Section 3.3.2.2 concerning noise estimation. Near a free surface, the ADV is not able to capture a total of seven centimeters. Interest in obtaining flow measurements in the surface region led to the use of a second velocity measurement device, a laser Doppler velocimeter, in the experimental study. The information provided with the auxiliary instrument give us a complete picture of seagrass canopy turbulence.

2.3.2.2 Preliminary Tests

A series of preliminary tests were conducted in order to choose the appropriate operating conditions for the experimental runs. Among the input variables necessary to operate the ADV were the desired sampling rate, the velocity setting and the sampling time. The ADV can be operated over a range of sampling rates from 0.1 to 25 Hz. Because of our interest in obtaining high frequency resolution for turbulence measurements, the highest sampling rate provided by the instrument was chosen for all the velocity time series, despite the fact that 25 Hz sampling rate is prone to higher noise levels. The choice of velocity setting and sampling time were based upon several preliminary velocity records taken upstream and within the test section. Each parameter was crucial for obtaining accurate velocity statistics.

Table 2.3. Velocity range settings for ADV (SonTek, 1996).		
Velocity Range Setting	Max. Horizontal Velocity	Max. Vertical Velocity
± 3 cm/s	± 30 cm/s	± 8 cm/s
± 10 cm/s	± 60 cm/s	± 15 cm/s
± 30 cm/s	± 120 cm/s	± 30 cm/s
± 100 cm/s	± 300 cm/s	± 75 cm/s
± 250 cm/s	± 360 cm/s	± 90 cm/s

An important input parameter in the use of the ADV is the velocity range setting, which controls the time lag between the pair of coherent acoustic pulses sent by the transmitter. Standard systems provide the user with five possible velocity settings, ±3, ±10, ±30, ±100, ±250 cm/s. It is recommended that the velocity range of the ADV be set to the minimum value covering the range of velocities expected in a given flow since the lower settings have inherently less noise. The cited velocity ranges, however, correspond to the bistatic axis velocities (V_1, V_2, V_3) and do not match precisely the measurable range of velocities in an orthogonal coordinate system. For this reason, SonTek provides a table to guide the user in the selection of an appropriate velocity setting, reproduced here as **Table 2.3**.

The appropriate velocity range for the experimental conditions was chosen based upon a series of 10-minute velocity records taken at a mid-depth point upstream of the test section for the three lowest velocity settings ($x = -1$m, $y = 0$, $z = 13$ cm). Each velocity record was analyzed to determine the percent deviation of a running average from the mean of the 10-minute record, shown to be long enough to be considered a steady state value. This analysis was performed for three statistics: the mean streamwise velocity (U), the streamwise turbulence velocity (u_{rms}) and the Reynolds stress (uw).

As expected, the performance of the probe improved with decreasing velocity range for identical flow conditions. The lowest setting had the smallest velocity standard deviation, which presumably is attributed to having a lower noise component since any contribution by turbulence was identical among the tests. The ±3 cm/s velocity settings also showed the shortest time interval over which the running average deviated from the 10-minute mean by more than a few percent. The optimum velocity range, however, was determined to be ± 10 cm/s based on the results of two additional 10-minute records taken within and above the canopy ($x = 1.8$ m, $y = 0$, $z = 11$ cm and 21 cm). The presence of the canopy increased the above canopy mean velocity to approximately 21 cm/s, approximately twice the mean flow at the upstream points. Measurements at the ±3 cm/s velocity setting led to spurious results because the instantaneous velocities above the canopy exceeded the maximum horizontal velocities quoted by SonTek. The ± 10 cm/s velocity setting did not suffer from these spurious velocity measurements due to the high horizontal and vertical maximum velocities (±60 and ±15 cm/s), values that are unattainable under the

present experimental conditions, and is robust enough to capture possible low velocity flows (~ 2 cm/s) measured within the canopy.

Upon choosing the ±10 cm/s velocity setting for our experimental conditions, the results from the same set of tests were used to determine the sampling time for the ADV time series. Due to the larger variability in the statistics for samples within the canopy, the proper choice for determining the sampling time was the in-canopy sample. The running average of the mean and turbulent velocities was well within 5% of the long term mean for sampling times greater than one minute. The Reynolds stress, however, did not approach these uncertainty limits until the running average was about seven minutes. In a similar application of an ADV probe, Dunn *et al.*(1996) chose three minutes as an appropriate averaging time for their probe and accepted a 15% error in the estimation of the Reynolds stress as a limitation of their study. The tradeoff between sampling time and accuracy was justified by the fact that their interest was in calculating the vertical gradient of the Reynolds stress, such that the precise magnitude of the statistic was inconsequential. This study, on the other hand, requires a small error in the estimation of the Reynolds stress, a quantity which will be essential in describing the momentum exchange between the overlying surface layer and the canopy region. For this reason, the sampling time chosen for all the ADV time series was ten minutes, corresponding to a record length of 15000 points at the f_S = 25 Hz , recognizing that this record length may not in fact be required at vertical points that do not demonstrate a large degree of intermittency in the Reynolds stress. The results obtained from the experiments will shed more light upon the reasons behind the need for long sampling times to obtain appropriate turbulence statistics as will be discussed in Chapter 3.

Figure 2.4 shows the results from the two experiments taken within the test section. The differences between the in canopy and surface layer records are most apparent in the asymptotic decrease in Reynolds stress error for each record. For a sampling time of ten minutes, the measurement error introduced into the Reynolds stress by having a limited averaging length are at most 5% of the true long term value, an acceptable uncertainty. The percentage deviation in the mean and turbulent velocities are at most on the order of 1% as the running average approaches the long term mean value.

Alternatively, an estimate of the mean square error for the mean velocity introduced by an averaging period of length T_s can be obtained from (Tennekes and Lumley, 1972):

$$MSE = \overline{\left(U_T - U\right)^2} \cong \frac{2\overline{u^2}\Im}{T_s} \qquad \textbf{(2.13)}$$

where U_T is the average velocity in the period T_s = 10 minutes, U is the true mean value, u is the turbulent velocity and $\Im$ is the integral time scale, estimated from the autocovariance function of the velocity signal. Although each velocity record will have its particular integral time scale and variance, typical values from the experimental results delineated in Chapter 3 can be used to estimate the mean square error for the estimation of velocity based upon our averaging period. Using $\Im \sim 0.75$ s and $u^2 \sim 2.25$ cm^2/s^2, an

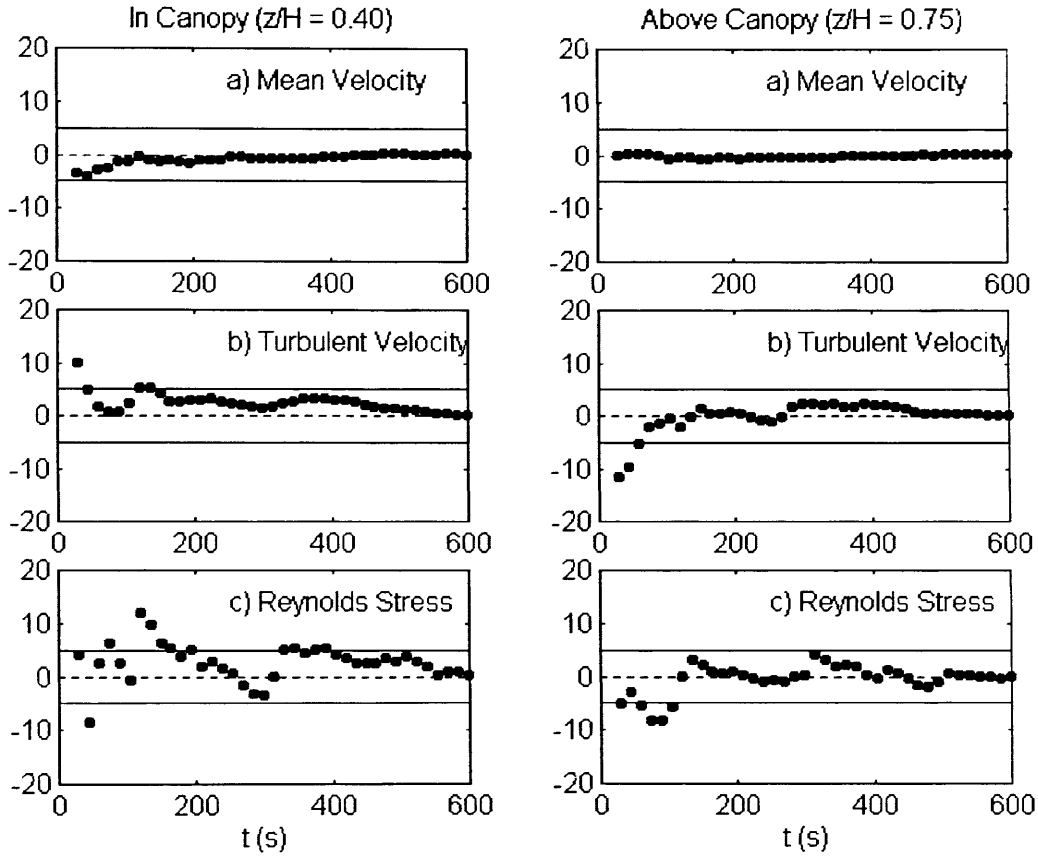

Figure 2.4. Percentage deviation of the running average statistic referenced to the 10-minute average statistic. (a) Mean velocity $(1\text{-}U/U_{10})\times 100\%$ (b) Turbulent velocity $(1\text{-}u_{rms}/u_{rms10})\times 100\%$ (c) Reynolds Stress $(1\text{-}uw/uw_{10})\times 100\%$. The right hand column represents values for a velocity record taken within the canopy at a nondimensional depth $z/H = 0.4$, where H is the water depth. The left hand column corresponds to a velocity record above the canopy at $z/H = 0.75$. The dotted line represents identical values between the running average and the long time average, while the solid lines are the ± 5% deviation intervals. Both 10-minute records taken with a ±10 cm/s velocity setting at (x = 1.8m, y = 0).

estimated mean square error is small, approximately 0.6%, consistent with part (a) of **Figure 2.4**. Thus, the sampling time chosen for the velocity records is sufficiently large such that we may consider the mean statistics obtained from the ten minute sample approximately as long time averages.

Equivalent statements about the higher moments, such as the covariance (*i.e.* Reynolds stress), skewness and kurtoses coefficients, can be obtained as well, although the mean square error should be expected to be larger considering that higher moments are more sensitive to the sample size. From Lumley and Panofsky (1964), we can obtain an estimate of the mean square error for the covariance of a Gaussian process with zero mean as:

$$MSE = \frac{4\overline{u^2}\Im}{T_s} \tag{2.14}$$

or two times the value for the first order statistics, MSE = 1.2%. The accuracy associated with this mean square error is $\varepsilon = \sqrt{MSE/\overline{u^2}}$ = 7%, which is comparable to the percentage deviation estimated from the running average and the 10-minute mean Reynolds stress statistics. Similarly, the kurtoses coefficient is approximately five times the mean square error for the second moment (MSE = 6%). Taking into consideration the limitations in sample length, the restrictions imposed by obtaining the samples within a reasonable amount of time and the small mean square errors for the turbulence statistics of interest, the sample time of ten minutes is considered very reasonable.

A second important parameter in the proper operation of the ADV is the signal to noise ratio (SNR), measured in dB, which expresses the magnitude of the echo received at the receive transmitter relative to the electronic noise level of the instrument (Kraus *et al.*, 1994). The quoted minimum value for the signal-to-noise ratio for reliable turbulence statistics at 25 Hz sampling frequency is 15 dB. Preliminary tests demonstrated that this minimum value for the SNR was unattainable for the water used in the experimental setup. Appropriate measures were required to increase the value of this parameter. To this end, the water was seeded with spherical hollow spheres manufactured by Potter Industries Inc. of Carlstadt, NJ. The mean particle size, 11.4 microns, and density, 1.062 g/cm^3, allow these spheres to be two orders of magnitude smaller than the lateral dimension of the sampling volume (0.6 cm), as well as neutrally buoyant in the flow. These properties are essential for the proper operation of the acoustic probe whose velocity measurement is based upon the assumption that the particles traversing the sampling volume represent the velocity of the fluid that carries them.

In order to achieve high SNR values for the duration of the experiment, the flume water had to be heavily seeded. A set of preliminary tests were undergone to determine the concentration of seeding material required for appropriate signal-to-noise ratios. Varying amounts of a 55 g/L concentrated solution of the seeding material were sequentially added to the flume, whose volume of water was approximately 2.1 m^3 at a water depth of 28 cm. After each seeding, the flume water was mixed well to ensure a homogeneous distribution of the particles and a velocity record was obtained. The mean and standard deviation of the signal-to-noise ratio time series at each seeding are presented in **Figure 2.5**. A minimum volume of one liter of the solution was required to obtain reliable results for each velocity component. This corresponds to a flume water concentration of 25 mg/L, well within the range quoted by SonTek (10-50 mg/L).

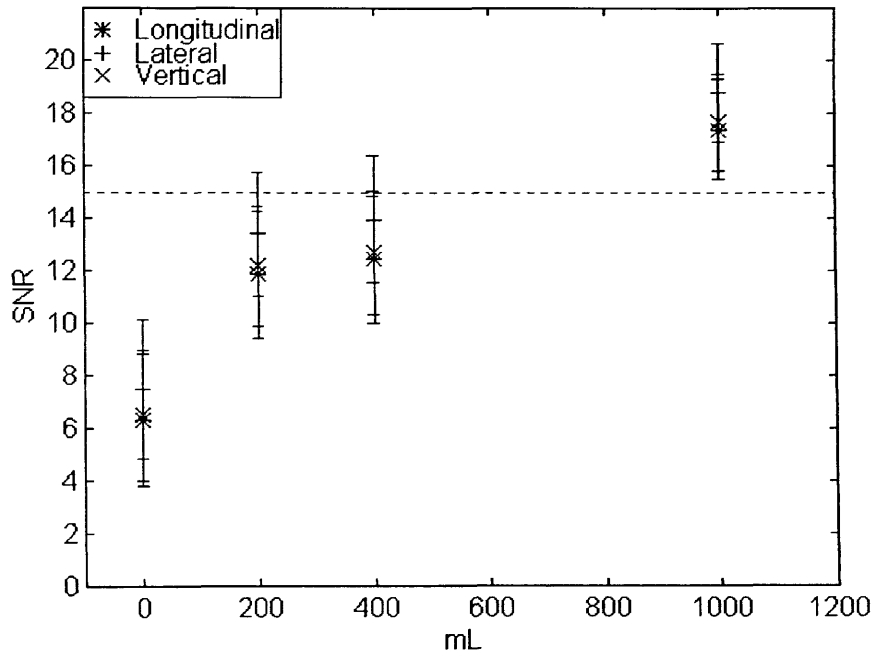

Figure 2.5 Signal-to-noise ratio response to a 55 g/L solution of seeding material for each velocity component. The markers represent the mean values over the 10-minute *SNR* record and the error bars denote one standard deviation of *SNR*. The horizontal dashed line is the minimum required SNR for proper operation at 25 Hz (15 dB).

During the measurement of a velocity profile, containing anywhere from 17 to 41 vertical samples each lasting ten minutes, the *SNR* was observed to decrease due to particle settling, removal in the upstream turbulence dampening structures and accumulation of particles at the water surface. In order to obtain appropriate *SNR* values for each experiment, the flume water was homogenized before each velocity record, making sure that any settled and floating particles were well mixed throughout the water column. Inevitably, however, seeding had to be added periodically to ensure the proper *SNR* for each experiment. With the precautions taken to maintain high mean *SNR* values and the monitoring of the velocity record to ensure that instantaneous *SNR* were also above the acceptable minimum, we have a good deal of confidence that the quality of the data with respect to electronic noise is high.

2.3.2.3 Error Analysis

The performance of the acoustic Doppler velocimeter has been evaluated in a series of laboratory and field conditions by the system designers at SonTek (Lohrmann *et al.*, 1994; Kraus *et al.*, 1994; Lohrmann *et al.*, 1995) who compared the probe measurements with results from an LDV system. Based on these tests, the ADV accuracy has been estimated as being approximately 1% of the velocity setting, which would imply an error of ± 0.1 cm/s for our experimental conditions. A recent study by Voulgaris and Trowbridge (1998) avoided a direct comparison between these two instruments that are each

potentially subject to errors by developing a ground-truthing technique. The mean velocity and Reynolds stress measured by the ADV were within 1% of the estimated true value, a considerable improvement upon the SonTek specifications.

Voulgaris and Trowbridge (1998) estimated the potential sources of noise to the velocity signal for an open channel flow. The total velocity error variance, σ_t^2, is the sum of the noise contributions from the ability of the electronic circuitry to resolve the phase shift, σ_m^2, the Doppler phase error, σ_D^2 , and the shear within the sampling volume, σ_u^2. The Doppler phase error variance, in turn, consists of a contribution from turbulence within the sample volume, from the effect of a finite residence time of particles and a term due to the divergence of the acoustic beam. Empirical expressions for each of the noise contribution terms were presented and applied to a case of turbulent open channel flow in a laboratory flume. The largest contribution to the total variance was the turbulence component of the Doppler phase error, while the shear term became increasingly important as the sampling volume approached solid boundaries ($z/H < 0.1$). In absolute terms, however, it was concluded that the noise terms were not significant and could be ignored in highly turbulent flow fields, such as boundary layers.

Appendix A is dedicated to describing the estimation of the noise error based upon the empirical expressions obtained for a specific ADV electronic design and under open channel flow conditions. Applying the empirical relationships for the present case should be done with caution for several reasons. On one hand, the ADV electronic circuitry has changed during the course of system development and the expression for the noise due to the electronic circuitry may not apply to all the probes manufactured by SonTek. Secondly, the empirical constants in expression **Eq. A2** and the relationships in equations **Eq. A5** through **Eq. A8** were derived from turbulence measurements in an open channel flow and with different acoustic systems, including a Doppler sonar and a Doppler current profiler (Zedel *et al.*, 1996; Lhermitte and Lemmin, 1994) but which were all based on a pulse-to-pulse coherent method. The applicability of these empirical relationships to the shear velocity structure of an aquatic plant canopy flow and to the ADVField probe used in this study may not be appropriate.

To corroborate this point, an estimate of σ_t^2 was made using the expressions in Appendix A and disregarding the potentially discrepancies mentioned above. A still water sample was taken to estimate the uncertainty component due to the electronic noise, σ_m^2, although it has been widely recognized that this is by no means the optimum measure of this value (Nikora and Goring, 1998; Voulgaris and Trowbridge, 1998). The optimum condition to measure the electronic noise is a uniform, laminar flow, where the contributions from the shear and Doppler terms are negligible. These conditions, however, were difficult to produce in this laboratory experiment. In its place, a no-flow sample with a well seeded water to ensure the proper signal-to-noise ratio and with identical settings to the experimental runs was obtained, the results of which are shown in **Table 2.4**.

Table 2.4. Statistics for the still water sample using the ADV.			
	x	y	z
Mean Velocity [U; V; W] (cm/s)	–0.0197	–0.0067	–0.0832
Turbulent Velocity [u_{rms}; v_{rms}; w_{rms}] (cm/s)	0.3616	0.4005	0.0697
Reynolds Stress $[uw; uv; vw]$ (cm^2/s^2)	–0.0045	–0.0074	0.0017
Skewness Coefficient [Sk_{uuu}; Sk_{www}]	0.1479	–	–0.2621
Kurtoses Coefficient [K_u; K_w]	5.2138	–	7.4786

It is evident from the statistics that the mean velocities and the Reynolds stress are negligible, leading to the conclusion that the velocity and stress profiles obtained during this experimental study are not contaminated by the electronic noise. The turbulent velocity for the horizontal components, on the other hand, are significant, on the same order as the measured values in the lower canopy region ($z/h_p \leq 0.25$). This behavior, however, is an artifact of having no motion through the sampling volume and under normal operating conditions it improves since the electronic noise reduces with increasing turbulence (SonTek, 1995). At this point it should also be noted that the horizontal components have inherently more noise due to the probe geometry, a feature which is borne out in the transformation matrix and incorporated in the subsequent calculations. For this reason, the appropriate estimate for the uncertainty due to the sensor's electronic ability to resolve the Doppler shift is the variance obtained from the vertical component, $\sigma_m^2 = 4.86\times10^{-3}$ cm^2/s^2. This estimate is comparable to that obtained by Voulgaris and Trowbridge (1998).

Also to note from **Table 2.4** is that the method for correcting the ADV data suggested by Nikora and Goring (1998) should not be employed. The corrected velocity moments in this simple technique are obtained as the difference between the measured moment ($U_{mi,j}$) and the moment of the noise from the still water sample ($n_{i,j}$). The first four moments are obtained as:

$$\begin{aligned}
\overline{U}_i &= \overline{U}_{mi} - \overline{n}_i \\
\overline{U_i' U_j'} &= \overline{U_{mi}' U_{mj}'} - \overline{n_i' n_j'} \\
\overline{U_i'^3} \Big/ \left(\overline{U_i'^2}\right)^{3/2} &= \left(\overline{U_{mi}'^3} - \overline{n_i'^3}\right) \Big/ \left(\overline{U_{mi}'^2} - \overline{n_i'^2}\right)^{3/2} \\
\overline{U_i'^4} \Big/ \left(\overline{U_i'^2}\right)^{2} &= \left(\overline{U_{mi}'^4} - \overline{n_i'^4}\right) \Big/ \left(\overline{U_{mi}'^2} - \overline{n_i'^2}\right)^{2}
\end{aligned} \qquad \textbf{(2.15)}$$

The proposed method does not seem reasonable for the present study due to the large moments calculated for the still water sample. Performing this operation would alter significantly the profiles for the turbulence velocity, skewness and kurtoses measured within the plant canopy. Again, the failure of the procedure lies in assuming that the electronic noise component in the ADV is equivalent at all measured velocities and can be estimated from still water samples.

The flow-related contributions to the total error variance can be estimated by referring to the equations presented in Appendix A. To this end, a worst case scenario was constructed to identify the largest possible error variance. Taking the most extreme experimental conditions, experimental run 6 (H = 28 cm, Q = 15.14 L/s), at a position of maximum turbulence dissipation and large shear (z/h_p = 0.75), the mean velocity ($U \sim$ 10 cm/s), velocity difference ($\Delta U \sim$ 1.3 cm/s) and the dissipation ($\varepsilon \sim 14$ cm^2/s^3) were used to obtain σ_D^2 and σ_u^2. This resulted in values of $\sigma_D^2 = 8\times10^{-2}$ cm^2/s^2 and $\sigma_u^2 = 5.6\times10^{-1}$ cm^2/s^2 for the Doppler noise and the shear noise terms, respectively. The total velocity variance based on these estimates is $\sigma_t^2 = 0.64$ cm^2/s^2, due to the high shear contribution to the total error.

At this point, we conclude this discussion by stating that the value obtained for the total error variance can be used in conjunction with T, the transformation matrix, to determine by how much the measured velocity moments deviate from the true values. The measured statistics are a combination of the true statistics (denoted by a tilde) and a quantity depending on the error variance and the probe geometry.

$$\begin{aligned}
\langle u'w' \rangle &= \langle \tilde{u}'\tilde{w}' \rangle + (a_{11}a_{31} + a_{12}a_{32} + a_{13}a_{33})\sigma_t^2, \\
\langle u'^2 \rangle &= \langle \tilde{u}'^2 \rangle + (a_{11}^2 + a_{12}^2 + a_{13}^2)\sigma_t^2, \\
\langle v'^2 \rangle &= \langle \tilde{v}'^2 \rangle + (a_{21}^2 + a_{22}^2 + a_{23}^2)\sigma_t^2, \\
\langle w'^2 \rangle &= \langle \tilde{w}'^2 \rangle + (a_{31}^2 + a_{32}^2 + a_{33}^2)\sigma_t^2.
\end{aligned} \tag{2.16}$$

For an ideal, perfectly constructed probe, the factor $P_1 = a_{11}a_{31} + a_{12}a_{32} + a_{13}a_{33}$ in the covariance expression is equal to zero. The value obtained from T for P_1 for the ADVField probe used in this study is 0.0064. This low value makes the estimation of the Reynolds stress extremely accurate, even for the extreme condition described above where $<u'w'>$ = 4.24 cm^2/s^2 (within 0.1 % of the true value), despite the large value calculated for the error variance. Similarly, the error for the turbulent energy $<w'^2>$ = 4.77 cm^2/s^2 in the vertical direction is small (within 3% of the true value) due to the small value of the factor $P_4 = a_{31}^2 + a_{32}^2 + a_{33}^2 = 0.3557$. For the horizontal components, however, the same can not be said. It is well recognized that the ADV performance is much better for the vertical velocity than the two horizontal components, as is apparent from the factors P_2 and P_3 obtained from the probe geometry:

$$\begin{aligned}
P_2 &= a_{11}^2 + a_{12}^2 + a_{13}^2 = 10.9865 \\
P_3 &= a_{21}^2 + a_{22}^2 + a_{23}^2 = 10.8860
\end{aligned} \tag{2.17}$$

and the ratio of the noise factors between the streamwise and vertical components is P_2/P_4 = 30.89. Using the value obtained for σ_t^2 results in noise contributions of the same order as the measured horizontal turbulent velocities (52.8% of the true statistic for $<u'^2>$ = 13.32 cm^2/s^2; and 102% of the true statistic for $<v'^2>$ = 6.86 cm^2/s^2). These results suggest an unreasonably high estimate for σ_t^2 due to the excessive contribution from the mean shear term. Since the turbulent velocities obtained with the ADV are comparable to those obtained with the laser Doppler velocimeter, whose small sampling volume is not

subject to shear. We suspect this is an overestimation and a better estimate of the total noise error in the ADV is $\sigma_m^2 = 4.86\times10^{-3}$ cm^2/s^2, obtained from the vertical velocity component, as recommended by Voulgaris and Trowbridge (1998).

2.3.3 Laser Doppler Velocimetry

The laser Doppler velocimeter (LDV) has been used as a research tool in the turbulence community for many years. LDV theory has received considerable attention and the technology has become a standard, especially for detailed laboratory studies where the LDV presents considerable advantages over previously used technologies such as hot film anemometers. The following sections will briefly describe the laser Doppler technology and its implementation for this laboratory study. In addition to this, a description of a series of preliminary tests made to choose the operational parameters and an error analysis for the velocity measurements obtained from the laser Doppler velocimeter will be presented. By no means does this section attempt to describe the full details of the LDV theory developed over the last twenty years. This instrument was employed by Zavistosky (1994) in a similar flume study with rigid vegetation and the results from that study can be easily extrapolated to this case. For more details of the laser Doppler method for flow measurement, the reader is referred to Buchhave *et al.* (1979).

2.3.3.1 Technology Description

The laser Doppler velocimeter employed for this experimental study was a Dantec Measurement Technology (Skovlunde, Denmark) instrument capable of measuring the two dimensional velocity components at a single point. This particular velocity measurement device is based on the Doppler burst principle and uses a burst correlation processor within the Dantec 58N40 Flow Velocity Analyzer (FVA) unit. The 300mW blue-green argon-ion laser manufactured by Ion Laser Technology of Salt Lake City, UT, produces a laser beam which is subsequently split into two beams, blue and green, of wavelengths, 488 nm and 514.5 nm, respectively. The laser light produced by the argon-ion laser is directed at the Dantec optics system, whose function is to direct and focus the incident beams to a small volume within the flow field and collect the backscattered light from this volume while simultaneously filtering out other light sources or light scattering from outside the sampling volume (Buchhave *et al.*, 1979).

A simplified description of how the laser system works should help in the discussion of the principles used in this technique. The laser Doppler system consists of several modules: the laser generation system, a beam separator and Bragg cell, the photomultipliers, the processor and the probe unit. The argon ion laser and the optics system are placed precisely on a mounting bench to ensure proper alignment between the laser beam and the focusing system. Once the laser beam has been directed at the optics system and split into two blue-green beams, the frequency of one of the beams is shifted by 40 MHz in the Bragg cell. The frequency shift is particularly important for the implementation of laser technology

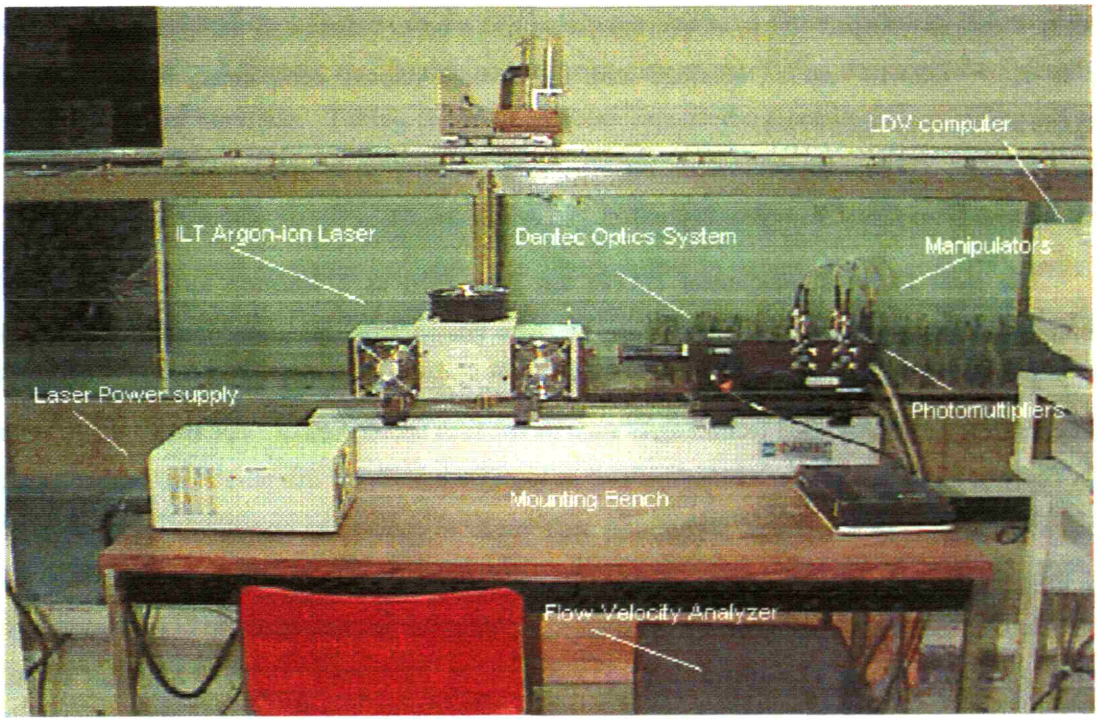

Photo 2.2. LDV system components used for the experimental study.

to velocity measurements, since it allows the directional ambiguity of the Doppler system to be resolved (Dantec, 1990). The shifted and unshifted beams are then split into the two wavelength components mentioned previously and passed through a fiber optic cable to the probe unit. Alignment of each beam with the fiber optic cable is achieved via the use of a manipulator, thus ensuring that each beam is sufficiently strong and well focused. Within the portable probe unit, a lens directs the four beams, two for each orthogonal velocity component, to a single point, located at a distance of 20 cm from the probe lens. The same probe unit receives the light backscatter from the sampling volume and directs it to the photomultiplier units via a receiver fiber optic cable, and subsequently to the FVA unit that carries out the signal processing. Details concerning the configuration of the LDV system are shown in **Photo 2.2**.

Laser Doppler velocimetry is based on measurement of the Doppler shift of scattered light created as particles pass through a fringe pattern formed at the intersection of two coherent laser beams. In the 2D systems used in the experimental study, this meant that at the sampling volume, both pairs of green and blue beams, formed fringe patterns that were orthogonal to each other and perpendicular to their respective axes. The sampling volume is ellipsoidal in shape due to the laser beam's Gaussian light intensity distribution and measures 76 μm in diameter and 0.64 mm in length (Dantec, 1990a). A schematic of the fringe pattern is shown in **Figure 2.6**.

As small particles within the fluid randomly pass through the parallel fringes of alternating light intensity they absorb the laser light in an alternating pattern, more when the lighter bands are passed and less when the darker bands are passed. This intensity fluctuation is known as a Doppler burst. The result is a randomly spaced collection of bursts that are identified as particles if they have the proper signal

strength. If the fringe spacing is known *a priori*, then the information obtained from the Doppler burst is equivalent to the particle's velocity. The fringe spacing (d_f) can be calculated easily from knowledge of the laser light wavelength (λ_l) and the angle between the incident light beams (θ_b):

$$d_f = \frac{\lambda_l}{2\sin(\theta_b/2)}. \tag{2.18}$$

For the specifications of the probe used in this experimental study (θ_b = 0.236 rad; λ_l = 488 nm, 514.5 nm), the spacing between the fringes for the longitudinal component (green beams) was 2.185 μm and for the vertical component (blue beams) was 2.073 μm. This implies that the sampling volume contained a total of 34 and 36 fringes, respectively. The velocity of the particle (v_p) traveling through the fringes is calculated from the fringe spacing and the Doppler frequency of the burst (f_D) (Zavistosky, 1994).:

$$v_p = f_D d_f \tag{2.19}$$

To account for the ambiguity in direction, the frequency shift induced in the Bragg cell creates a non-stationary fringe pattern, moving at a velocity much greater than the expected particle velocity:

$$v_s = f_s d_f \tag{2.20}$$

where v_s is the fringe pattern velocity and f_s is the frequency shift induced in the Bragg cell. Particles traveling in the direction opposite to the movement of the fringes will encounter the fringes more often than particles moving in the direction of the fringe movement, and the direction of the particle movement can be obtained from this frequency shift.

Implicit in the laser Doppler method described herein is the assumption that the particle size is much smaller than the sampling volume, such that it creates the Doppler burst as it passes each fringe individually, and that the particle velocity is representative of the fluid velocity. Neutrally buoyant particles with diameters of the order of 50 μm or less are consistent with these assumptions (Buchhave *et al.*, 1979). Although our experimental study did not require seeding for use of the LDV, the typical particle used for the ADV setup that could have remained within the flume met these two requirements.

One of the principal advantages of using the LDV is the measurement of the velocity without interfering with the flow. The probe can be submerged within the flow or placed outside the flume and the laser beams directed into the flow. In this experimental study, the laser probe was mounted on a tripod directly adjacent to one of the flume side walls and the laser beams passed through the flume glass and directly into the flow region, as shown in **Photo 2.3**. The convergence of the four laser beams upon the sampling volume required the removal of a group of plants between the flume wall and the centerline position in the region where the vertical velocity profiles were taken. A maximum of five plants were removed to prevent plant interference on the laser beams. The effect of this removal on the velocity statistics, however, is expected to be negligible, as discussed more thoroughly in Section 2.4.1.

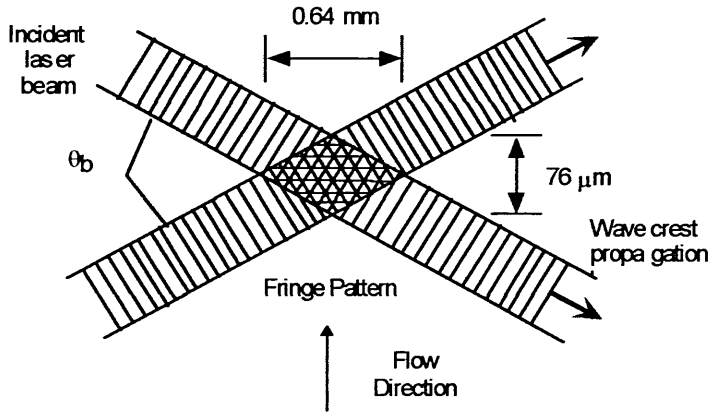

Figure 2.6. Fringe pattern created by the intersection of two incident laser beams. The sampling volume created by two pairs of beams is ellipsoidal in shape with the stated dimensions. The measured velocity is perpendicular to the fringe pattern for each direction.

Another advantage of the LDV is that the sampling volume created at the intersection of the laser beams is quite small, such that the inaccuracies associated with having turbulence and shear within the sampling volume can be neglected. The sampling volume for the LDV was also relatively easy to locate. The vertical location of the sampling volume was adjusted by using a point gauge placed at the centerline position and at the longitudinal location of the sampling region (x = 660 cm, y = 0), as seen in **Photo 2.3**. The intersection of the four laser beams was placed at the tip of the point gauge by adjusting the vertical position of the mounting tripod and the vertical location was recorded to the nearest millimeter. For the experimental setup, the vertical range of the traversing mechanism allowed the placement of the sampling volume to within 2 cm from the bottom and the free surface for the measurement of the two velocity components, and within 0.7 cm from the bottom and 0.2 cm from the free surface for the longitudinal component.

2.3.3.2 Preliminary Tests

As with the acoustic Doppler velocimeter, a series of preliminary tests were performed to determine the optimum operating conditions for the laser Doppler velocimeter. Due to the supplementary role of the LDV and the applicability of the tests conducted with the ADV, exhaustive preliminary testing was not necessary. It must be noted that the purpose of using the LDV was two-fold. Firstly, the LDV allowed for the velocity in the near surface region to be measured since the instrument does not have the depth limitations of the ADV. Secondly, the LDV can obtain much higher sampling frequencies, ranging from 100 to 500 Hz, depending on the flow conditions and the operational settings, thus allowing for the resolution of higher frequency turbulence than that obtainable with the ADV.

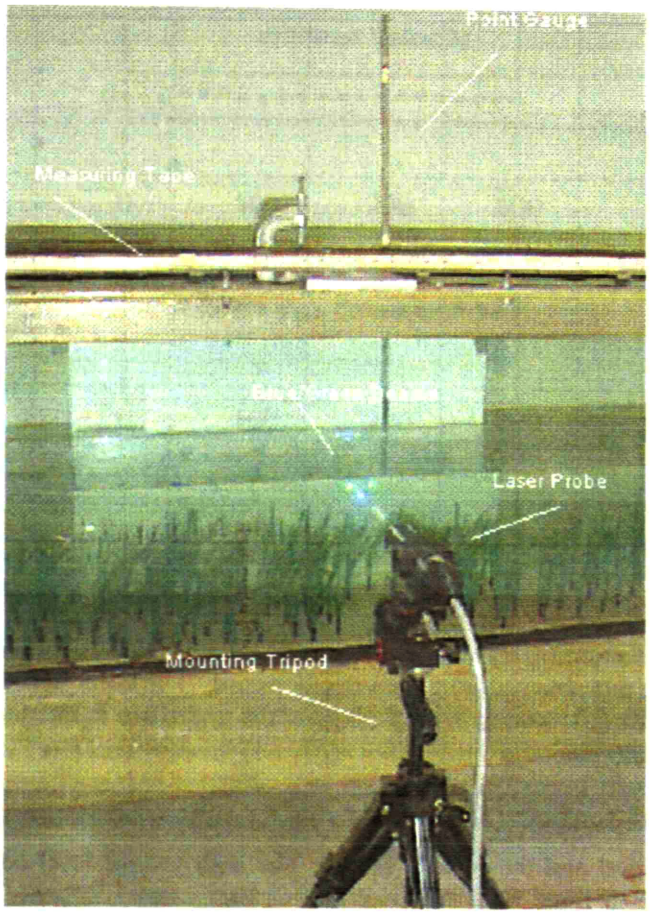

Photo 2.3. Laser Doppler velocimeter probe set up at the sampling region within the plant canopy. The LDV sampling volume at the intersection of the four beams was located at the centerline position and positioned vertically with the use of the point gauge. The vertical (blue) and longitudinal directions (green) were measured at the intersection of the two beams.

Previous experience with the use of the LDV by Zavistosky (1994) facilitated the process of testing the instrument. Among the parameters that were determined before using the LDV were the seeding amount, the operational settings, the sampling time and the vertical sampling region. The seeding amount, operational settings and the probe alignment were manipulated to obtain high sampling frequencies in the range of 50 to 150 Hz, with a goal frequency of 80 Hz. Preliminary observations led to the conclusion that the best LDV performance, in terms of having high sampling frequencies, was obtained when the flume was not seeded. For this reason, the LDV measurements were made only after the seeded flume water used for the ADV measurements had been replaced with clean water. In addition, the flume side wall closest to the laser beams was thoroughly cleaned to avoid the possible diminished light intensity caused by dirt or other particles on the glass surface. A noticeable improvement in the sampling rate was witnessed with clearer water and a cleaner glass surface.

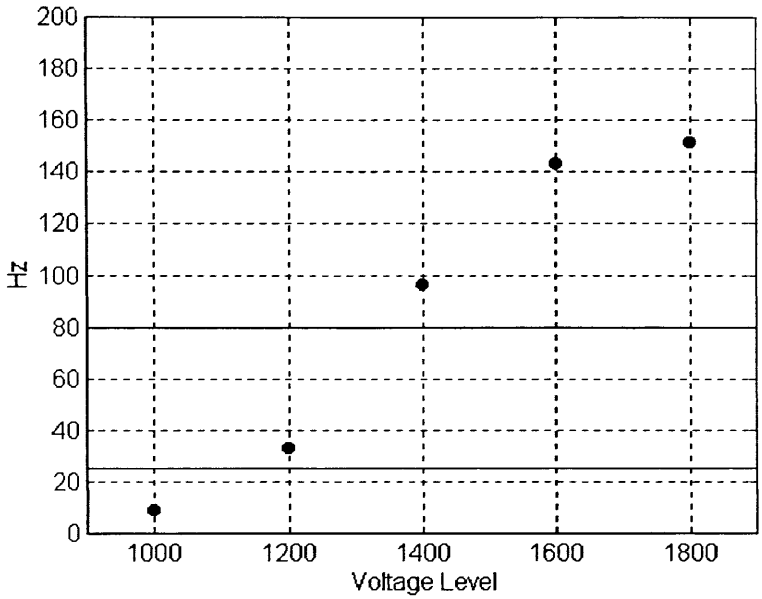

Figure 2.7. Relationship between the high voltage setting for the LDV photomultipliers and the mean sampling rate obtained from the velocity record. The lower horizontal solid line represents the ADV sampling frequency (f_S = 25 Hz) and the upper line is the goal frequency for the LDV measurements (80 Hz).

The operational parameters of concern during the velocity measurements were the high voltage setting, the validation level and the velocity range. The high voltage level controls the power in each photomultiplier, and thus how much amplification is made to the signal received from the laser light beams. Higher voltage in the photomultiplier leads to the identification of weaker bursts as particles crossing the fringe pattern and to a higher sampling frequency. At the same time, however, the amount of background noise in between the arrival of particles is increased. For this reason, a compromise must be made between having high sampling rates and minimizing the signal noise. A series of velocity records were taken in the sampling region at different voltage settings, as shown in **Figure 2.7**. From this preliminary test, it was concluded that a voltage settings greater than 1200 volts was required and that the goal frequency of 80 Hz could be achieved with the setting of 1400 volts.

The selection of the other two operational parameters was more straightforward. The validation level for the signal determines the threshold value for a Doppler burst to be considered a particle traversing the sampling volume. Signals having a signal-to-noise ratio below the selected validation level are rejected during the signal processing (Dantec, 1990b). As the high voltage level, this parameter is crucial to obtaining high sampling rates. Throughout the present study, the validation was kept at the minimum acceptable value −3 dB for the number of fringes in the sampling volume, to ensure that the greatest number of bursts would be identified as particles.

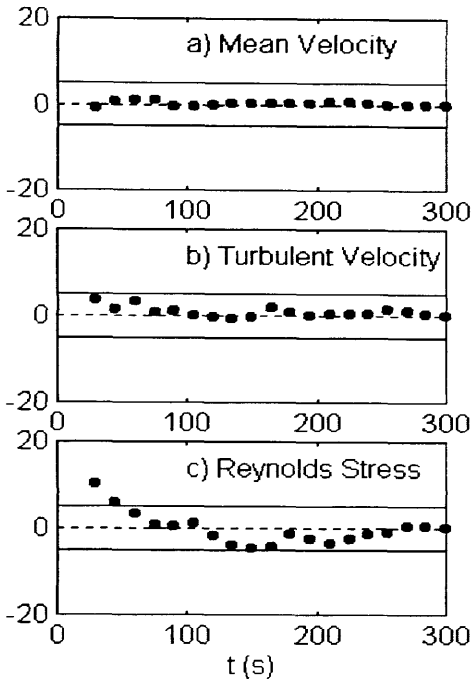

Figure 2.8. Percentage deviation of the running average statistic referenced to the 5-minute average statistic. (a) Mean velocity $(1\text{-}U/U_5)\times 100\%$ (b) Turbulent velocity $(1\text{-}u_{rms}/u_{rms5})\times 100\%$ (c) Reynolds Stress $(1\text{-}uw/uw_5)\times 100\%$. The dotted line represents identical values between the running average and the long time average, while the solid lines are the ± 5% deviation intervals.

The velocity setting was controlled by the bandwidth for each velocity component. With knowledge of the expected maximum velocities for the particular record, a decision could be made as to which bandwidth to choose. Usually, the bandwidth was set to the smallest value, 0.12 MHz, corresponding to a velocity range of −13 to 13 cm/s. Occasionally, a higher setting of 0.4 MHz was required for the near surface region. Inspection of the velocity histogram presented in the user interface would show quite clearly when a velocity range was exceeded by aliasing the signal to lower velocities. The proper adjustments to the bandwidth setting were then made accordingly.

The sampling time was determined using a similar procedure to that undertaken for the ADV and presented in Section 2.3.2.2. A five minute velocity record, taken at a vertical position of $z/h_p = 0.4$ within the canopy, was analyzed to determine at which time a running average was within a certain percentage of the 5 minute average, as shown in **Figure 2.8**. The record length was limited to a five minutes due to limitations placed by the high sampling rates. It is apparent from the results of this preliminary test that the mean and turbulent velocities as well as the Reynolds stress are quite well behaved, having deviations within 5% of the long term average for the majority of the record. To ensure that the record was long enough in a statistical sense, however, we chose a sampling time for the velocity records of five minutes. With this choice, the record length was both manageable and sufficient to describe the long term statistical quantities.

Finally, a series of preliminary tests were carried out to determine the sampling locations for the LDV during the experimental runs described in Section 2.4.2. As mentioned previously, the role of the laser Doppler velocimeter was supplementary, being used exclusively in the near surface region for most of the runs. For all of the cases, a single LDV profile was taken at the centerline position, instead of the multiple profiles taken with the acoustic Doppler velocimeter. This was justified based on the lateral homogeneity observed in the region above the canopy. The LDV profile consisted of at most 8 points for the large flow depths (H/h_p = 1.50, 1.75, 2.75) and of entire vertical profiles for the low flow depths (H/h_p = 1.00, 1.25). The results from the LDV measurements were incorporated into the ADV data set.

2.3.3.3 Error Analysis

Due to the previous experience with the laser Doppler velocimeter in a similar laboratory setup by Zavistosky (1994), the estimation of the errors involved in making the velocity measurements is based on a discussion presented by that author. The inaccuracies in the velocity measurements are largely due to the misalignment of the probe. The probe alignment was performed by making sure that the tripod base upon which the laser probe was mounted was properly leveled before each velocity record was taken. This ensured that the probe was properly aligned in the vertical and lateral direction at the longitudinal position of interest. The longitudinal alignment was performed with the use of an L-shaped ruler used between the probe and the flume glass wall. The longitudinal position was adjusted until the sampling frequency of the preliminary velocity record was maximized.

The errors introduced in the longitudinal position and the squareness to the side were introduced as the tripod was raised or lowered during a traverse. Realigning the beams to negate the rotation caused by the tripod shaft was attempted, but this almost certainly resulted in some variability. The rotation error was estimated as $\pm 0.18°$, which introduces a velocity measurement error of ± 0.15 mm/s. Also, the probe could tip forwards or backwards, introducing a second type of angular error, approximately $\pm 0.15°$, which corresponds to a velocity error of ± 0.15 mm/s. Along with the errors associated with the signal processing in the Flow Velocity Analyzer (± 0.15 mm/s) and the other positioning errors, Zavistosky (1994) computed through the constant odds method of Kline and McClintock (1953), that the total error in the velocity measurement was 1.4 mm/s, a value which will be used for this experimental study.

2.3.4 Surface Slope Measurement

Estimating the water surface slope is a difficult task in laboratory flume experiments due to the small differences in water depth along the longitudinal direction, usually on the order of tenths to hundredths of centimeters. Obtaining an independent measure of the water surface slope, however, is an important part of any hydraulics study. For the purpose of the present study, the surface slope is used to obtain estimates of the canopy drag and important hydraulic and turbulence parameters such as the friction velocity for each experimental condition. Others have recognized the difficulty in obtaining accurate measurements of the water surface slope (Nezu and Rodi, 1986; Tsujimoto *et al.*, 1992), the latter of these proposing a method to correct for the surface slope inaccuracy in an open channel flow with rigid vegetation. An application of this procedure to flexible vegetation was complicated due to the numerous assumptions made to derive the governing stress equation and the vertical inhomogeneity in the canopy density and drag coefficient. The measured surface slopes, however, will be compared to the calculations based on a backwater model for open channel flow with vegetation presented by Dunn *et al.* (1996).

The water surface slope measurement is particularly important in this experimental study because the flume is not of the more commonly encountered titling variety, where the bed slope is adjusted carefully and the surface slope matches it under uniform conditions. Two independent estimates of the flume bed slope using a point gauge and a ruler led to the conclusion that the flume has no appreciable slope. Not having a mechanism to adjust the bed slope, the driving fluid force in the flume is the pressure head provided by the centrifugal pump. The pressure differential in turn creates the water surface slope that causes fluid to flow along the longitudinal axis. Using open channel flow terminology, the laboratory flume can be described as a gradually varying flow condition.

The water surface slope was measured with a pair of resistance-type surface displacement gauges with a resolution of 0.2 mm placed at the two extremes of the canopy using vertical traverses ($x_1 = -10$ cm and $x_2 = 750$ cm), as shown in **Figure 2.9**. Each 40 cm long gauge was placed at a centerline position ($y_1 = y_2 = 0$) and such that each experimental depth could be measured without altering the vertical placement. Voltage output from the surface displacement gauges was directed to a Protecno signal amplifier and subsequently to an electrometer (Keithley 199 System DMM/Scanner) for voltage readings and data storage. The electrometer had the ability to resolve voltages to the nearest 0.01 mV, more than sufficient for the differences in voltages between the two gauges. It produced a digital record at a frequency of 60 Hz that was subsequently filtered using an instrument function and recorded manually at discrete sampling times.

Conceptually, the estimation of the surface slope using surface displacement gauges is straightforward. The slope is obtained by measuring the difference in voltage readings from the two gauges during each experimental run relative to a still water condition. The voltage reading is converted to a vertical displacement by calibrating each instrument voltage reading against a known distance. The

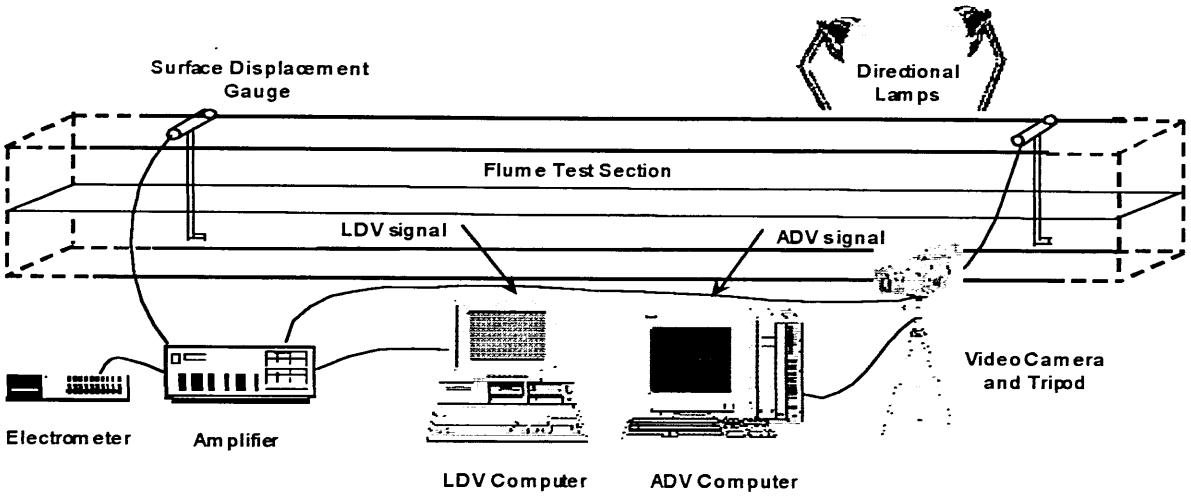

Figure 2.9. Schematic of the equipment used for the surface displacement and plant motion measurements. For clarity, the velocity measurement instruments have been excluded, although the two computers are shown.

vertical displacement is then divided by the longitudinal distance between the two gauges, measured to an accuracy of 0.1 cm by using a tape measure, to obtain the surface slope in the flume. Using this procedure, the surface slope is calculated as:

$$S_w = \frac{dH}{dx} = \frac{1}{\Delta x}\left[\frac{1}{C_2}\left(V_2 - V_{2,0}\right) - \frac{1}{C_1}\left(V_1 - V_{1,0}\right)\right]. \tag{2.21}$$

Each term in this equation consisted of a mean value and a standard deviation obtained from the multiple readings. The mean value of each calibration factor and voltage reading were used to determine the surface slope. Each surface displacement gauge was calibrated to determine the conversion factor between the voltage reading and the vertical distance (C_1 and C_2). The calibration recording consisted of sampling the voltage reading every fifteen seconds for a period of 2.5 minutes at two positions, each one centimeter from a pre-determined "zero" location. The voltage readings from still water ($V_{1,0}$ and $V_{2,0}$) and from the experimental conditions (V_1 and V_2) were recorded at ten second intervals for a period of 3 minutes at the zero location. The measurement of the distance between the two gauges resulted in the value for Δx. The uncertainty in the slope reading, expressed as a 95% confidence value, was determined by using the constant odds method of Kline and McClintock (1953) as follows:

$$\Delta S_w = \left(\frac{1}{\Delta x}\right)\sqrt{\frac{\left(V_2 - V_{2,0}\right)^2}{C_2^4}\Delta C_2^2 + \frac{\left(V_1 - V_{1,0}\right)^2}{C_1^4}\Delta C_1^2 + \left(\frac{1}{C_2^2}\right)\left(\Delta V_2^2 + \Delta V_{2,0}^2\right) + \left(\frac{1}{C_1^2}\right)\left(\Delta V_1^2 + \Delta V_{1,0}^2\right)} \tag{2.22}$$

where ΔC_1, ΔC_2, ΔV_1, $\Delta V_{1,0}$, ΔV_2, $\Delta V_{2,0}$ are the 95% confidence values for the respective parameters, calculate by assuming a Gaussian distribution of the sample and equal to $1.96\sigma/\sqrt{n_o}$, where n_o is the sample size and σ the standard deviation of the reading.

Despite the small uncertainties obtained from the slope measurements, several factors may lead to errors in the estimation of this quantity. If the free surface velocity in the flume was large, the introduction of the gauges into the flow caused significant disturbances around the two gauge cylinders. These disturbances may lead to errors in the estimation of the surface slope by raising the water around the gauge slightly, especially at the downstream gauges exposed to higher surface velocities for the high discharge cases. Another possible source of error for the slope estimate is the instrument drift inherent in the signal amplifier. The effects of instrument drift, however, were dealt with by ensuring stable voltage readings for each record and by minimizing the time taken between voltage readings. Regardless, the use of the surface displacement gauges provided a simple technique for measuring the surface slope independently from the velocity records. Chapter 3 will compare the results from this set of experiments with alternative slope estimates made using the data from the velocity profiles.

2.3.5 Plant Motion Measurements

The quantification of the plant motion at the different water depth and flow discharge settings was performed with the use of a Hitachi video camera and a Kodak DC50 digital camera. The recording instruments were set up at a lateral position within the canopy. The video camera was mounted at the level of the flume bottom approximately a meter away from the flume glass wall, so as to capture a large region of plant motion. The video recordings captured an area of the x-z plane that was 50 cm in width (x direction) and 37 cm in height (z direction). A schematic of the set up is shown in **Figure 2.9**.

Two types of imaging techniques were employed to characterize the plant motion during each experimental run. The first type consisted simply of recording the plant motion under well lit conditions. Directional lamps were used to illuminate the recording region from above and a white poster board was placed on the opposite flume side wall to eliminate interference from other light sources and objects behind the flume wall. The second imaging technique was a shadow graph. For this technique, a strong light source from an overhead projector was used to shine light from the opposite flume wall, through the canopy and onto a semitransparent Mylar sheet placed on the flume wall closest to the recording instruments. The video and digital cameras were used to record the shadows casts by the plants onto the Mylar sheet, thus effectively reducing the canopy space to two dimensions (x, z). Distances in the vertical and longitudinal direction were scaled by a one centimeter interval grid printed onto a transparent sheet.

Two types of information about the plant motion were recorded. From the direct images, the individual plant blades were observed and the oscillation frequency (f_p) was recorded for a group of ten plants. The frequency was measured as the number of oscillations during the entire record for the group of plants. From the shadow graph, the plant bent height (h_b) and the amplitude of motion (a_p) were recorded from a group of ten plants during specific time frames. In addition, the monami wavelengths was estimated from a selected number of time frames that clearly showed the phenomenon. Both types of

data were recorded from either replaying the video recording using a video cassette recorder or by using imaging software tools for the images obtained from the digital camera.

2.3.6 Ancillary Equipment

The computer equipment used during the course of this experimental study were a MICRON 200 MHz Pentium computer with Windows 95 operating system and a Compaq Prolinea 386 with Windows 3.1 operating system, for the ADV and LDV data, respectively. The velocity data was stored in Iomega Zip disks as a backup to the files on the computer hard drives. The ancillary equipment is also shown in **Figure 2.9**.

2.4 Experimental Design

The experimental design consisted of performing preliminary tests necessary to assure the quality of the velocity data, choosing the set of operating conditions that fulfilled the two-pronged goal of the experimental study and preparing the data analysis tools required to process the raw data and compute the turbulence statistics. Firstly, a sample velocity record was analyzed to assure proper statistical behavior and corroborate the conclusions about the instrument operating conditions. Secondly, an equilibrium region within the canopy was defined by taking longitudinal and lateral profiles and a sampling location was chosen for the vertical profiles. Spatial heterogeneity within the sampling region necessitated the use of lateral averages in order to account for differences imparted by a complicated interior canopy geometry. Thirdly, five experimental runs were designed to demonstrate the effect of depth variation on the turbulence characteristics and three experiments to show the effect of canopy waving by choosing the appropriate flow rate and water depth combinations. Lastly, the experimental design included the processing of the raw velocity signals and the extraction of the turbulence statistics through the use of MATLAB and WinADV programs.

2.4.1 Preliminary Tests

Statistical tests based on a subsample of a velocity record were performed to corroborate that the time series for the three velocity components were stationary in the mean and variance. A one minute sample randomly taken from a ten minute time series at a point at the level of the canopy top was analyzed (x = 695.5 cm, y = 0, z = 16 cm). The reason for choosing a subsample instead of the entire record was that the statistical analyses were simplified with a smaller sample size. Results from the subsample can easily be extrapolated to the full velocity record to show that the velocity time series do in fact meet the standard assumptions made in turbulence analysis.

The statistical tests showed that the time series could be described by a Gaussian distribution characterized by the sample mean (m) and sample standard deviation (S) as distribution parameters for

each velocity component $\sim N(m,S^2)$. In addition, the velocity time series were shown to be stationary in both the mean and the variance through use of the Kendall-Ranking test and the F-distribution test (Jenkins and Watts, 1968). Using the stated accuracy for the velocity instruments, the sample sizes were shown to be of sufficient length to account for the associated errors. Finally, the subsample record was used to show that confidence intervals on the velocity statistics can be constructed at the 95% level, a procedure repeated during the data analysis. In summary, the statistical tests on the subsample showed that the full record was stationary in the first two moments, long enough to account for instrument accuracy and described by a Gaussian distribution. Having confidence in the velocity signal, the next step was to determine the sampling location.

In accordance with the purpose of studying the turbulence characteristics of a waving seagrass meadow in a one-dimensional framework, a region within the canopy that exhibited uniform conditions was chosen for conducting the vertical profiles. It was important to choose a sampling region with fully developed flow, unaffected by either wall or edge effects. To this end, a longitudinal traverse through the canopy at a specific depth of $z/H = 0.4$ was taken under the most extreme waving conditions. The results from an extreme case should be applicable to all the flow conditions explored in this study. Reproducing the conditions in experimental run 6, with a water depth of 28 cm and the maximum flow rate of 15 L/s, was deemed appropriate. The sampling region determined in this manner should be a conservative estimate for the other water depths and flow rates since fully developed conditions should be obtained over a shorter distance into the canopy for less severe canopy waving. The mean and turbulent velocity at each point along the longitudinal traverse are shown in **Figure 2.10**.

The longitudinal profile of the mean velocity within the canopy shows how the approaching flow is quickly reduced, as expected due to the increased drag exerted by the plants upon the flow. The plants extract energy from the mean flow which is converted to either the kinetic energy of plant motion or to turbulence that scales on the plant dimensions. The increased drag within the meadow forces a vertical redistribution of the flow, as the water will flow through the region of less resistance, the surface layer, leading to decreased velocities through the canopy. The velocity profile reaches a minimum at a distance of two meters from the canopy edge, after which it recuperates and levels off after three meters, fluctuating about a mean velocity of $U = 7.7$ cm/s. Based upon the mean velocity profile, the choice of the sampling region anywhere beyond 3 meters seems reasonable.

Observations of the plant motion, however, led to the choice of a sampling region at $x = 660$ cm, where the canopy waving was in full effect. It was evident from visual observations that the plant motion changed substantially over the length of the canopy. In the first two meters, the plants were prone and exhibited little vertical or lateral vibration. As the shear layer developed between the vegetation and surface layer, instabilities generated at the interface between the two regions led to vortices that traveled downstream and imparted momentum to the flexible plants and subsequent plant vibrational response.

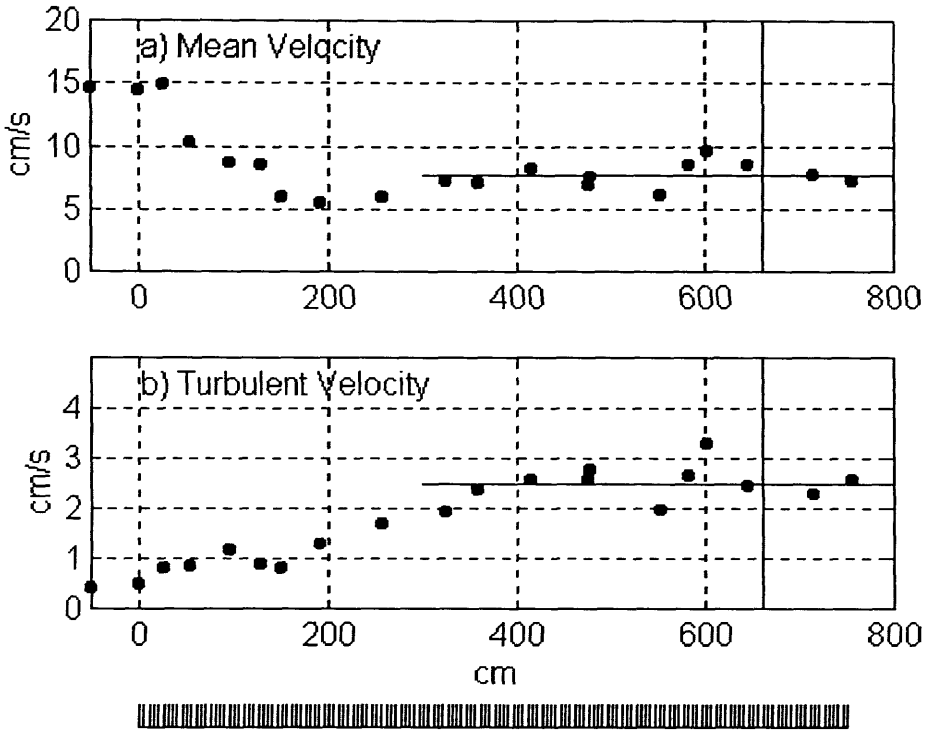

Figure 2.10. Longitudinal traverse through the plant canopy. (a) Mean velocity profile U (b) Turbulent velocity profile u_{rms}. The bottom sketch represents the longitudinal extent of the canopy, approximately 7.32 meters long. The horizontal lines denote the longitudinal average velocities in the fully developed region (U = 7.7 cm/s; u_{rms} = 2.5 cm/s). The vertical lines denote the position of the sampling region.

After the initial two meters, the degree of plant motion increased gradually over the canopy length until a fully developed region could be observed after five meters. Interestingly enough, the initial experimental set up was limited to a five meter long canopy. After witnessing the development of the monami effect, the canopy length was extended to 7.5 meters to obtain a sampling region where the plant motion experience no further downstream development. The alteration to the experimental set up proved to be crucial for recreating monami conditions.

Having determined the longitudinal location of the sampling region, a lateral profile at the location x = 660 cm, z/H = 0.4 was obtained to determine the effects that proximity to the flume walls imparted on the mean and turbulence velocity. Width limitation is a drawback of many laboratory experiments that attempt to describe either two or three dimensional phenomenon. Flow through vegetation has been shown to be three-dimensional, especially in the canopy space. In this study, however, the heterogeneity in the vertical direction is by far the most interesting aspect. By choosing a sampling region with a uniform canopy behavior and averaging laterally, the flow can be considered spatially homogeneous in two dimensions and interest can be focused on the vertical coordinate.

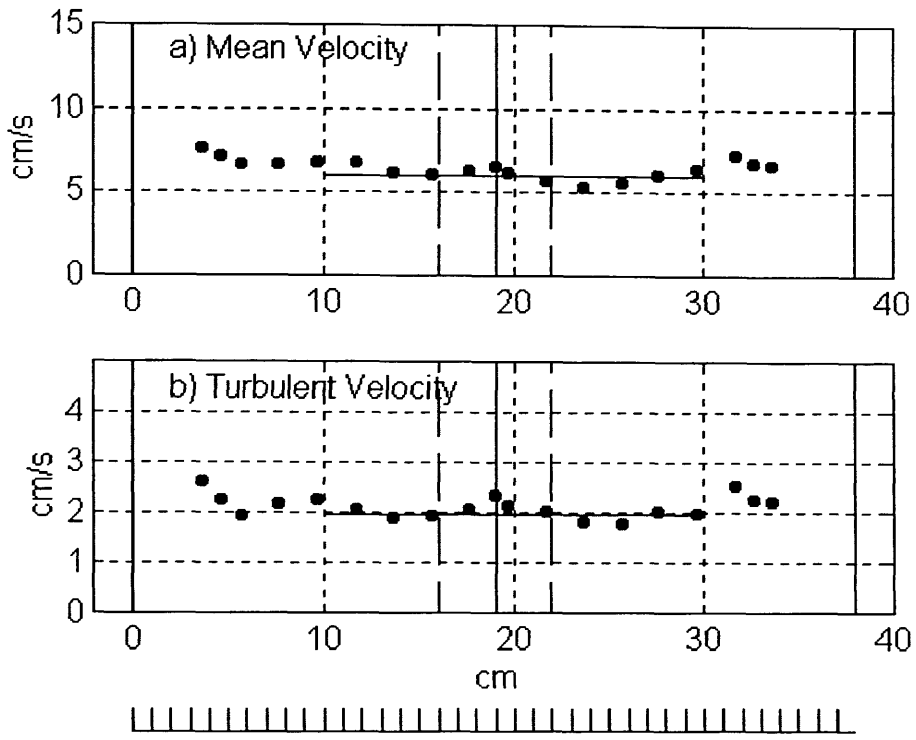

Figure 2.11. Lateral traverse through the plant canopy. (a) Mean velocity profile U (b) Turbulent velocity profile u_{rms}. The bottom sketch represents the lateral extent of the canopy, spanning the flume width 38 cm. The horizontal lines denote the longitudinal average velocities in the region unaffected by wall effects (U = 6.05 cm/s; u_{rms} = 1.98 cm/s). The solid and dashed vertical lines denote the position of the three vertical profiles, one along the flume centerline and the other two spaced 3 cm from the centerline.

The lateral profile of the mean and turbulent velocities in **Figure 2.11** show that the interior 20 cm of the flume are devoid of wall effects. Limitations in ADV probe placement made the estimation of velocities at distances less than 4 centimeters from the walls difficult. Regardless, an interior region of near constant velocities was well defined with lateral means of U = 6.05 cm/s and u_{rms} = 1.98 cm/s. Integrating the information from the longitudinal and lateral profiles, we defined the equilibrium region as the canopy space exhibiting fully developed conditions (7 m $\leq x \leq$ 5 m; 10 cm $\leq y \leq$ 30 cm). Sampling within the equilibrium region was expected to produced velocity profiles with no longitudinal development and uninfluenced by the glass walled flume. Vertical profiles within the equilibrium region were expected to display somewhat similar characteristics. Whether a single profile along the centerline was representative of the lateral average was tested by taking two preliminary profiles at the lateral positions y = 0 and +3 cm. The mean and turbulent velocities for the three velocity components are shown in **Figure 2.12.**

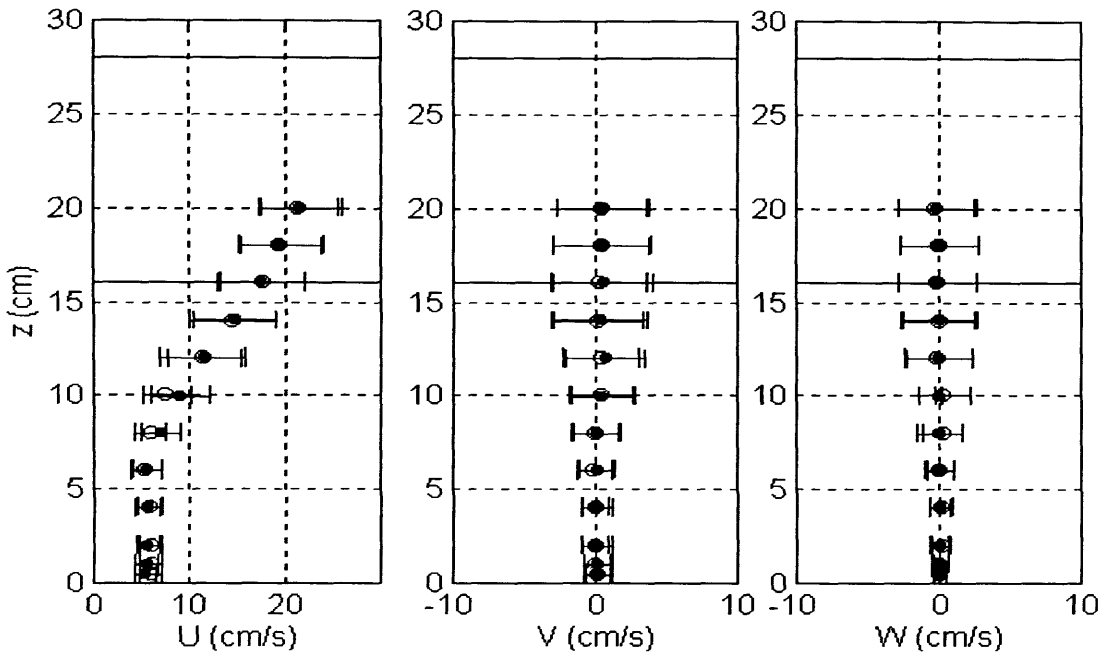

Figure 2.12. Spatial heterogeneity tests showing the three velocity components from two profiles taken within the sampling region (x = 660cm) at two lateral positions: (•), centerline position y = 0; (o), offset position y= + 3cm. The symbols represent the time average velocity (U, V, W), while the bars are the standard deviations of the velocity components (u_{rms},v_{rms},w_{rms}). The horizontal lines are the free water surface at $z = H$ = 28 cm and the canopy top at $z = h_p$ = 16 cm.

The need for multiple profiles within the sampling region is apparent from a comparison of points within the canopy, $z \leq$ 16 cm, while above the canopy, the variations among the two profiles are somewhat smaller. To obtain these velocity profiles a number of plants were removed from the sampling region in order to prevent any interference by plant blades. Both the ADV sampling volume and the LDV beams can be disrupted by the plant motion, leading to erroneous velocity statistics. Because the flow conditions are fully developed at the sampling region, the removal of a few plants (at maximum five plants) did not affect the profiles of the velocity statistics. Based on these results, choosing to perform multiple lateral profiles for each experimental run seemed reasonable and the removal of a few plants acceptable.

The last set of preliminary tests were designed to determine the flow discharge and water depth combinations to fulfill the intentions of the laboratory experiments, compare the turbulence characteristics at various water depths and flow velocities. Five water depths were chosen (H = 16, 20, 24, 28 and 44 cm), covering a range from nearly emergent vegetation to fully submerged conditions. Limitations in discharge placed by the flume pump meant that the highest water depth had a maximum channel flow velocity, $U_{ch} = Q/A$, of 9 cm/s. A velocity record taken at the midpoint of the canopy (z = 8 cm) under these conditions had a mean velocity of approximately 2 cm/s. This in-canopy velocity was chosen as the basis for comparison among the depth cases (*Case A*). By taking velocity records at the same location for

the other water depths, the flow rates were adjusted until the mean velocity was close to the prescribed 2 cm/s. In this manner, the effects of flow depth on the turbulence within the seagrass meadow could be isolated from the effects of flow rate. In addition, the depth variation cases were chosen such that relatively little plant swaying occurred and the coherent plant waving was not present (monami). Justification for this procedure are two fold. By matching the in canopy velocity for each water depth, the flexible plants are subject to the same Reynolds number regime. Reynolds number similarity ensures that the plant motion is reasonably similar among the depth cases, despite the differences in surface layer velocities. Secondly, matching the velocity in a region of the canopy where the Reynolds stress is negligible implies that the water depth cases have similar surface slopes based on the balance of forces on a control volume containing the plants, as in the definition sketch shown in **Figure 2.1**.

The effect of velocity on the turbulence characteristics of the flexible plant canopy was investigated by choosing three flow regimes at a water depth of H = 28 cm. Here again, the effects of velocity were isolated from the effects of water depth by choosing a specific water depth and varying the discharge. Visual observations led to the choice of three flume discharges Q = 6.31, 10.72 and 15.14 L/s (Q = 100, 170, 240 gpm), corresponding to a low, intermediate and high flow regime. In a similar approach, Murota *et al.* (1984) chose two flow velocities and defined the regimes as slowly swaying and rapidly swaying. In the context of this study, the low flow regime has no swaying, the intermediate flow regime has slowly swaying flow and the high flow regime has rapidly swaying conditions. The high flow regime exhibited coherent waving motions and large vertical and lateral plant vibrations, clearly the condition described in field conditions as a monami.

2.4.2 Experimental Runs

A total of seven experimental runs were carried out during this study. The controllable variables in the flume study were the flow discharge and the water depth. The investigation made no attempt at exploring other potential effects such as varying the canopy density or plant morphology. Experimental runs 1-4 and 7 (*Case A*) were designed to explore the variation in flow depth at constant in canopy velocity on the profiles of the mean velocity statistics, momentum exchange, turbulence scales and spectra, canopy drag and other turbulence characteristics. The nondimensional depth, H/h_p, was used to distinguish between the depth variation cases. Experimental runs 4-6 (*Case B*) were designed to elucidate how increased flow discharge at a constant water depth affected the beforementioned profiles. The discharge Q was used to distinguish between the three cases. As mentioned in Section 2.4.1, preliminary testing determined the flow discharges at each water depth that led to constant in canopy velocities for *Case A*, and the discharges leading to different plant motion flow regimes for *Case B*. **Table 2.5** lists the relevant parameter space for each experimental run.

Table 2.5. Experimental conditions.				
Experimental Run	Water Depth H (cm)	Discharge Q (L/s)	Channel Velocity U_{ch} (cm/s)	Number of points
1A	16	1.26	2.07	19
2A	20	2.52	3.32	23
3A	24	4.73	5.19	27
4A,B	28	6.31	5.93	31
5B	28	10.72	10.08	30
6B	28	15.14	14.23	30
7A	44	15.14	9.06	47

Each experimental run consisted of three velocity profiles at the three predetermined lateral positions (y = −3cm; y = 0; y = +3cm). The lateral positions were each at different locations relative to upstream plants, so that the lateral averaging took into account the variations of flow conditions caused by positioning within or outside an element wake. Taking precautions in positioning the profile relative to the plant wakes, however, was not thought to be crucial to this experimental study. The characterization of the flow field behind of a single plant showed that the wake extended for a substantial distance away from the element, approximately 75 plant diameters in the downstream direction and 20 diameters in the lateral direction. Considering that the plant spacing was on average about 5.5 cm, these results imply that wake overlap within the plant canopy is substantial. Therefore, any profile location will be influenced by many plant wakes and it would be difficult to isolate locations that can be considered within or outside of a plant wake. Similar results were obtained in a study performed by Dunn *et al.* (1996) who showed that the difference between profiles taken inside or outside of a cylinder wake were not significant.

The number of sampling locations within a vertical profile depended on the water depth and the limitations of the two instruments. The ADV was used to measure as much of the water column as possible, while the LDV served to supplement this data with measurements in the near surface region. Measurements from the ADV included the three dimensional velocity components, while the LDV data consisted only of the streamwise and vertical velocities. The number of vertical points within each profile are shown in **Table 2.5**. The vertical resolution of the sampling points was 1 cm over most of the water depth except close to the bed where the resolution was increased to better capture the velocity gradients. The vertical position of the sampling volume was identical for every lateral profile and for all the experimental runs. Errors associated with vertical positioning were minimal, the maximum measured discrepancy had a 95% confidence interval of 0.05 cm from the lateral mean. The lowest most measurement made during a vertical profile was at a distance of 0.05 cm, the limiting distance from a boundary for the ADV without having interference from bottom reflection (SonTek, 1996). No limitations existed in the measurement of near surface streamwise velocities with the LDV, although the vertical component was not measurable at distances less than two centimeters from the bottom and free surface.

2.4.3 Experimental Procedure

The experimental procedure for each velocity record was straightforward. Before starting each velocity measurement, the flume water was prepared for the corresponding velocity instrument. If operation of the ADV was called for, the seeding material was added and allowed to mix throughout the flume volume to make certain that consistent signal-to-noise ratios were obtained during the ten minute velocity record. On the other hand, if the LDV was to be used, the flume was cleaned thoroughly and the water replaced so that the appropriate sampling rates and data validations were recorded. Once this was completed, the flume was turned on for at least half an hour to ensure that any lateral or longitudinal oscillations induced from the onset of flow were dissipated. During this time, each instrument was aligned with the flume coordinate system to ensure minimal alignment errors and the experimental settings were recorded. Among the recorded settings were the location of the sample volume (x, y, z), the flow rate (Q), the water depth (H) and the water temperature (T). The flow discharge was measured from the flow meter installed in the flume return piping (in $10 \times$ gpm), the water temperature recorded from a submerged thermometer placed near the inlet region (in °C) and the water depth measured from a ruler placed along the flume side wall at the sampling location within the canopy (in cm). This procedure was repeated at every vertical position in the velocity profile as the instrument traverses were moved from the bottom boundary to the free surface.

Two additional sets of experiments were conducted for each run, the measurement of the surface slope (S_w) using the surface displacement gauge system described in Section 2.3.4 and the quantification of the plant motion and deflected plant height (h_b) using a video camera as described in Section 2.3.5. Although these were not performed simultaneous to the velocity measurements, the repeatability of the experiments enable us to assume that the same conditions could be met by adjusting the water depth and the flow discharge. The estimate of the plant height from the video recordings was confirmed with measurements of the undeflected and deflected plant height of a group of ten randomly selected plants. Other canopy characteristics were also measured with a similar random selection of a group of plants.

2.4.4 Data Processing and Storage

The velocity data from both instruments was obtained from the files created by the ADV and LDV software interfaces (*.*adv* and *.*prn*). Functions created by SonTek allowed for the extraction of the velocity (*.*vel*), signal-to-noise ratio (*.*snr*), correlation (*.*cor*) and amplitude (*.*amp*) time series from the main ADV program. Similarly, the LDV software program enabled the user to export the velocity data as well as other statistics to other data analysis programs. Under most circumstances, the velocity records were exported to MATLAB and the majority of the data analysis was performed without the help of the instrument software interfaces.

An important tool used in this experimental study was a software package developed by Tony L. Wahl at the Water Resources Research Laboratory of the U.S. Bureau of Reclamation for the analysis of acoustic Doppler velocimeter data. The Windows-based program calculates the mean and turbulence statistics for the ADV files easily, without the hassle involved in extracting the velocity files from the raw data files. The results from WinADV were useful for inspecting the velocity records quickly and assessing potential problems with the data. In addition, the output from the program served to corroborate the results obtained from the analysis performed using MATLAB based programs. It also provided easy access to the distance between the sampling volume and the bottom boundary calculated during the calibration of the ADV before each record.

A suite of computer programs and functions were designed in MATLAB version 4.2 to obtain the results presented later in Chapter 3. Among these were programs intended to extract the velocity data from the raw files outputted by each instrument, correct for probe misalignments (ADV) and unequal sampling intervals (LDV), compute mean and turbulent velocity statistics, carry out the conditional sampling techniques, perform spectral analysis, estimate drag characteristics and determine the important hydraulic parameters and turbulence scales. The output data from these programs were stored in **.mat* files and also in Microsoft Excel format, which allowed for easy access to the data and the computation of laterally averaged statistics. Appendix B shows an example of the MATLAB functions and programs.

The two important corrections made to the velocity data before the computation of the turbulence statistics are worth mentioning at this point. On the one hand, it has already been commented that the alignment of the ADV with the flume coordinates was an important first step in preparing each experimental run. This procedure was difficult to do precisely and a correction of small tilt angles was necessary before the computation of the velocity statistics. Under open channel flow conditions, the correction for misalignment can be achieved in a straightforward fashion by making the *a priori* assumption that the long term mean vertical and lateral velocity components must be zero due to the water depth and width constraints of the flume. The same need not be true for flow in the plant canopy, where substantial vertical or lateral velocities may be introduced as a result of secondary currents within the flume or vertical motion induced by the canopy elements. For this reason, a velocity record was obtained at a point 0.5 meters upstream of the canopy before each velocity profile was taken as a means of transforming the coordinate system for the velocity records taken within the canopy. Implicit in this procedure was the assumption that the probe alignment remained identical throughout the traversing depth and that the relative position of the probe with respect to the flume remained unchanged as the traverse was moved from the upstream location into the equilibrium region. Results from the coordinate transformation seem to point to the corroboration of these two assumptions.

The coordinate transformation used the raw velocity data, denoted in this context as U_p, V_p, W_p, to calculate the horizontal and vertical rotation angles, α and β, as:

$$\alpha = \tan^{-1}\left(\frac{V_p}{U_p}\right); \beta = \tan^{-1}\left(\frac{W_p}{U_p}\right) \tag{2.23}$$

The transformed velocities (U, V, W) can be computed from simple trigonometric relationships between the two coordinate systems:

$$\begin{aligned} V &= V_p \cos(\alpha) - U_p \sin(\alpha) \\ W &= W_p \cos(\beta) - U_p \sin(\beta) \\ U^* &= U_p \cos(\alpha) + V_p \sin(\alpha) \\ U &= U^* \cos(\beta) + W_p \sin(\beta) \end{aligned} \tag{2.24}$$

The procedure is first applied to the horizontal rotation angle and subsequently to the vertical angle, as demonstrated by the intermediate streamwise velocity U^*. In our experimental study, the rotation angles were computed at the upstream point and then used to transform the velocities for each velocity profile point. The values of the rotation angles were quite small, ranging from α = 1.05° to 3.16° for the horizontal rotation and β = 0.11° to 0.83° for the vertical rotation. The misalignment in the horizontal direction was larger than in the vertical direction, as expected due to the difficulty in aligning the red-colored receiver arm with the flume longitudinal axis. The corrections made to the raw velocity components based on the coordinate transformation were negligible for the streamwise component but substantial for the vertical and lateral velocities.

As mentioned previously, the laser Doppler velocimetry records data at unequal intervals since the particles that scatter the laser beam pass through the fringe pattern randomly. Although unequally spaced samples present no significant problems to calculating the mean and turbulent velocity statistics, spectral analysis techniques are much simplified if the record has a single sampling frequency. For this reason, the velocity record was resampled at its mean frequency. The velocity at each sampling point was interpolated from the two closest points. The resampling and interpolation scheme resulted in velocity time series that were not statistically different from the raw record.

2.5 Conclusions

The experimental methods described in this chapter made it possible to characterize the effect of water depth and velocity on the turbulence structure of a boundary layer limited plant canopy flow. Coastal seagrass meadows of *Zostera marina* species have been properly modeled in a laboratory flume by taking into account the dynamic and geometric characteristics of the two systems. With the proper modeling, the velocity measurements made with the use of two technologies, acoustic and laser Doppler velocimetry, in the laboratory flume can be extrapolated to the coastal eelgrass canopies. Complemented with surface slope and plant motion measurements, the velocity measurements will provide a clear picture of seagrass canopy turbulence and momentum exchange.

CHAPTER 3. Experimental Results and Discussion

3.1 Introduction

This laboratory study designed to investigate the turbulence structure within a model seagrass meadow provided a wealth of information that allows a clear and coherent picture of the interaction of the submerged canopy with a unidirectional flow to emerge. Through the combination of the data provided by the three types of experiments thoroughly described in Chapter 2, the plant motion visualization, the surface slope measurements and the velocity records from the two instruments, this chapter is dedicated to describing the characterization of the turbulent flow in and above the seagrass meadow. Frequently, the results obtained from the open channel flow experiments will be compared to typical results from the characterization of flow over atmospheric plant canopies, at times finding similarities in the two systems and at times pointing out the specific features that make the aquatic system unique. The discussion of each topic covered within this chapter will include the comparison among the depth and velocity variation cases. It is the intent of this experimental study to obtain a detailed understanding of how the depth of the overlying water layer affects the characterization of the flow through the plant canopy in terms of mean velocity statistics, turbulence, drag and hydraulic features, spectral properties and the structure of the momentum transport, among others. In addition, describing the effect of canopy waving on the turbulence structure is also sought.

This chapter is rather extensive in size and diverse in content. Each section treats a specific topic of its own, although an attempt has been made to interrelate the various results in the discussion. For example, the plant motion characterization, specifically the plant vibration frequency, is cited frequently in other sections that attempt to relate forcing in the system via the arrival of turbulent structures and the turbulence time scale to the response by the flexible canopy elements. The overall intent is to provide a complete and clear understanding of the behavior of a plant canopy in an aquatic system forced by a water surface slope. This can only been done successfully by presenting evidence from various types of analysis and arguing how the disjunctive pieces relate to our conceptual model. The conceptual model arises slowly as the different pieces are placed together. Hopefully, by the end of this chapter, the reader is able to appreciate how the various lines of evidence render support for the conceptual model of the turbulence structure synthesized in the conclusion. The framework for the rest of the chapter is initially set by considering the theoretical analysis of this hydrodynamic system.

3.1.1 Theoretical Analysis

The governing equations for the flow of water in and above a seagrass meadow are the conservation of mass and momentum represented by the three dimensional continuity and Navier-Stokes equations. Neglecting the Coriolis force in this system due to the limited areal expanse of typical seagrass meadows $\mathcal{O}$(100m), the governing equations for an incompressible fluid can be expressed as:

$$\frac{\partial u_i}{\partial x_i} = 0 \tag{3.1}$$

$$\frac{\partial u_i}{\partial t} + u_j \frac{\partial u_i}{\partial x_j} = -\frac{1}{\rho}\frac{\partial p}{\partial x_i} + g_i + \nu \frac{\partial^2 u_i}{\partial x_j^2}. \tag{3.2}$$

Tensor notation has been employed in **Eq. 3.1** and **3.2** with the position and velocity vectors represented by x_i and u_i; the pressure by p; the body force vector by g_i; the density of water by ρ; and the kinematic viscosity of water by ν. The body force vector g_i is defined as:

$$g_i = \left(g\sin\varphi,\quad 0,\quad g\cos\varphi\right), \tag{3.3}$$

where φ is the bed angle. For most wetlands and open channel flows with vegetation, the angle φ is very small and the gravitational force g_i is reduced to an expression involving the bed slope, $g_i = (gS,\ 0,\ -g)$, where $S = \sin\varphi$ (García, 1996). As previously described in Section 2.2, this laboratory experiment models a seagrass meadow in a region of no bed slope ($\varphi = 0$) and the x-component of g_i can be ignored.

In a turbulent flow environment, the instantaneous governing equations are time-averaged via the use of Reynold's decomposition to obtain equations for the mean flow (Kundu, 1990). In our particular experiment, the flow is a rough turbulent condition based on the Reynolds number criteria, $u_* h_p/\nu \approx 2400 >> 55$, where h_p is the plant height (16 cm) and u_* is the friction velocity (~ 1.5 cm/s) (Bandyopadhyay, 1987). Reynolds decomposition is simply the separation of the variables in **Eq. 3.1** and **3.2** into their mean part and deviation from the mean:

$$u_i = \overline{u_i} + u_i', \tag{3.4}$$

$$p = \overline{p} + p', \tag{3.5}$$

where the overbar and the prime represent the temporal mean and deviation from temporal mean which are denoted as turbulence quantities, respectively. For any scalar or vector quantity of interest, represented here by the variable ξ, the time-averaged quantity can be obtained as:

$$\overline{\xi}(x,t) = \frac{1}{T}\int_T \xi(x, t+t_o)dt_o, \tag{3.6}$$

where T is a time period long enough to ensure stationary behavior of ξ. By introducing **Eq. 3.4** and **3.5** into the governing equations and time averaging via the procedure in **Eq. 3.6**, the governing equations for a turbulent flow can be derived:

$$\frac{\partial \overline{u_i}}{\partial x_i} = 0 \tag{3.7}$$

$$\frac{\partial \overline{u_i}}{\partial t} + \overline{u_j}\frac{\partial \overline{u_i}}{\partial x_j} + \frac{\partial \overline{u_i' u_j'}}{\partial x_j} = -\frac{1}{\rho}\frac{\partial \overline{p}}{\partial x_i} + g_t + \nu \frac{\partial^2 \overline{u_i}}{\partial x_j^2}. \tag{3.8}$$

The time-averaged equations are almost identical to the instantaneous governing equations since the time-average of the turbulent velocities in **Eq. 3.5** and **3.6** are zero. The additional term in **Eq. 3.8** represents the spatial gradient of the time-averaged correlation between the velocity components and is usually non-zero for anisotropic turbulence (Kundu, 1990).

The complex geometry of canopy flows requires appropriate spatial averaging in addition to the traditional temporal averaging performed for turbulence studies. Wilson and Shaw (1977) and Raupach and Shaw (1982) developed the operation of the horizontal average for canopy environments, which was later expanded to a volume average for rigid and flexible canopies by Raupach *et al.* (1986) and Finnigan (1985). The volume-average and the departure from the average constitute a spatial decomposition similar to what Reynold's decomposition accomplishes for temporal averaging. The time-averaged quantities in **Eq. 3.7** and **3.8** can be decomposed into the spatial mean part and the deviation:

$$\overline{u_i} = \langle \overline{u_i} \rangle + \overline{u_i}'', \tag{3.9}$$

$$\overline{p_i} = \langle \overline{p_i} \rangle + \overline{p_i}'' \tag{3.10}$$

where the angle brackets denote the volume-averaged quantity and the double primes the deviation. The volume average of vector represented by ξ over the three dimensional canopy space can be obtained as:

$$\langle \xi \rangle (x,t) = \frac{1}{V} \iiint_{V^f} \xi(x+r,t)dr, \tag{3.11}$$

where the averaging volume V^f is a multi-connected space that excludes the canopy elements. In practice, the angle brackets represent a horizontal average over a thin slice of V^f. Substituting the spatial decomposition of the time-averaged quantities into **Eq. 3.7** and **3.8** results in the appropriate governing equations for canopy flow (Raupach *et al.*, 1986):

$$\frac{\partial \langle \overline{u_i} \rangle}{\partial x_i} = 0 \tag{3.12}$$

$$\frac{\partial \langle \overline{u_i} \rangle}{\partial t} + \langle \overline{u_j} \rangle \frac{\partial \langle \overline{u_i} \rangle}{\partial x_j} = -\frac{\partial \langle \overline{p} \rangle}{\partial x_i} + \frac{\partial \tau_{ij}}{\partial x_j} + f_{Fi} + f_{Vi}, \tag{3.13}$$

where the last three terms in the momentum equation are the volume-averaged momentum flux, the form drag and the viscous drag. The momentum flux, in turn, is composed of the volume-averaged turbulent stress term, a spatial covariance term known as the dispersive stress, and the molecular stress term:

$$\tau_{ij} = -\left\langle \overline{u_i' u_j'} \right\rangle - \left\langle \overline{\tilde{u}_i \tilde{u}_j} \right\rangle + \nu \frac{\partial \left\langle \overline{u_i} \right\rangle}{\partial x_j}. \tag{3.14}$$

The form and viscous drag terms in **Eq. 3.13** arise naturally from the volume averaging operation and can be expressed in integral form as (Raupach *et al.*, 1986):

$$f_{Fi} = \frac{1}{V} \int_{S_i} \int \overline{p} n_i dS \tag{3.15}$$

$$f_{Vi} = -\frac{\nu}{V} \int_{S_i} \int \frac{\partial \overline{u_i}}{\partial n} n_i dS \tag{3.16}$$

where S_i is the surface of the plant elements and n_i is the unit normal vector to the surface S_i. Fortunately, the governing equations for the canopy environment do not depend explicitly on the velocity of the canopy elements, v_i, and thus are valid for both rigid and waving canopies. If the rough surface is in motion relative to a fixed coordinate system ($v_i \neq 0$), the volume average operator of **Eq. 3.11** does not commute with spatial differentiation or with temporal averaging (Raupach *et al.*, 1986). The form and viscous drag terms in **Eq. 3.15** and **3.16** are commonly lumped into a total streamwise drag force (f_x) within the averaging volume, *i.e.* $f_x = f_{Fi} + f_{Vi}$, that is parameterized by the last term shown in **Eq. 3.18**, where C_D is the drag coefficient and a is the vegetation density (Raupach *et al.*, 1991).

Applying the governing equations to the steady, two dimensional (x, z) flow through a seagrass meadow of negligible slope, we can express **Eq. 3.12** and the x-component of **Eq. 3.13** as:

$$\frac{\partial \left\langle \overline{U} \right\rangle}{\partial x} + \frac{\partial \left\langle \overline{W} \right\rangle}{\partial z} = 0 \tag{3.17}$$

$$\left\langle \overline{U} \right\rangle \frac{\partial \left\langle \overline{U} \right\rangle}{\partial x} + \left\langle \overline{W} \right\rangle \frac{\partial \left\langle \overline{U} \right\rangle}{\partial z} = -\frac{1}{\rho} \frac{\partial \left\langle \overline{P} \right\rangle}{\partial x} + \frac{1}{\rho} \frac{\partial \left\langle \overline{\mathrm{T}} \right\rangle}{\partial z} - 1/2 C_D a \left\langle \overline{U} \right\rangle^2, \tag{3.18}$$

where the horizontal and temporal mean velocity is denoted as $\left\langle \overline{U} \right\rangle$.

The spatial and temporal-averaged shear stress term, τ_{ij}, can be simplified from **Eq. 3.14** to:

$$\left\langle \overline{T} \right\rangle = -\rho \left\langle \overline{uw} \right\rangle \tag{3.19}$$

by neglecting the molecular stress and the dispersive stress as compared to the Reynolds stress. The former is a usual assumption in turbulent flows, while the latter is justified on the grounds that the lateral dimensions of the canopy elements are much smaller than the canopy height so that the correlation between the spatial deviations of the u and w on the horizontal plane are small (Brunet *et al.*, 1994).

Using the z-momentum equation that reduces to a balance between gravity and the vertical pressure gradient, the spatial and temporal-averaged pressure can be obtained by applying the zero pressure boundary condition at the free surface ($z = H$):

$$\langle \overline{P} \rangle = \rho g (H - z). \tag{3.20}$$

Taking the partial derivative of **Eq. 3.20** with respect to x and introducing this result and **Eq. 3.19** into **Eq. 3.18** leads to the final form of the spatial and temporal-averaged streamwise momentum equation:

$$\langle \overline{U} \rangle \frac{\partial \langle \overline{U} \rangle}{\partial x} + \langle \overline{W} \rangle \frac{\partial \langle \overline{U} \rangle}{\partial z} = -g \frac{\partial H}{\partial x} - \frac{\partial \langle \overline{uw} \rangle}{\partial z} - 1/2 C_D a \langle \overline{U} \rangle^2. \tag{3.21}$$

Most laboratory studies of rough turbulent boundary layers simplify **Eq 3.21** for practical use by assuming steady, uniform flow, such that the inertial terms on the left hand side of **Eq. 3.21** can be neglected, resulting in a simple balance between the surface slope in the seagrass meadow and the Reynolds stress and drag created by the meadow:

$$g \frac{\partial H}{\partial x} = -\frac{\partial \langle \overline{uw} \rangle}{\partial z} - 1/2 C_D a \langle \overline{U} \rangle^2. \tag{3.22}$$

This result is very useful since it provides a method of estimating the drag coefficient from measurements of the surface slope and the Reynolds stress profile (Dunn *et al.*, 1996):

$$C_D(z) = \frac{g S_w - d\left(\langle \overline{uw} \rangle\right)/dz}{1/2 a \langle \overline{U} \rangle^2}, \tag{3.23}$$

where the water surface slope, S_w, has been introduced:

$$S_w = -\frac{\partial H}{\partial x}. \tag{3.24}$$

Section 3.5 presents the results from applying **Eq. 3.23** to the data obtained from the surface displacement gauges and the velocity measurements. In addition, **Eq. 3.22** indicates that in the near-bed region ($z = z_b$) a characteristics velocity u_s can be defined for the system:

$$u_s = \sqrt{\frac{2 g S_w}{a(z_b) C_D(z_b)}}. \tag{3.25}$$

Tsujimoto *et al.* (1992) presented a similar definition for u_s in an open channel flow with rigid vegetation, but neglected the variation of the drag coefficient and vegetation density with height. For emergent vegetation ($H \leq h_p$), u_s characterizes the entire flow region since the Reynolds stress profile is uniform. For submerged vegetation ($H \geq h_p$), u_s is approached far from the vegetation layer interface, near the bottom (Tsujimoto *et al.*, 1992). As mentioned in Section 2.4, the effect of varying H/h_p was investigated by matching the in-canopy velocity among the depth cases. Formally, the in-canopy velocity refers to the characteristic velocity, since the measurements were taken at a point of negligible Reynolds stress gradient ($z_b/h_p = 0.25$). By matching u_s in the runs of *Case A* and knowing that $a(z_b)$ and $C_D(z_b)$ remain constant in this region, the forcing, represented by the water surface slope, is being matched across experimental cases as well.

3.2 Canopy Morphology

Characterizing the canopy morphology is an important step in describing the model seagrass meadow and comparing the results to other plant canopies. This section is dedicated to presenting the results obtained from estimating the canopy density parameters, the results from the plant motion visualization experiments that give a better insight into the canopy waving parameters and the plant deflection angle and the results from the estimation of the plant flexibility and the natural plant vibration frequency. Each of these parameters will be useful when discussing the results from the velocity measurements and attempting to extract information on the canopy drag and the momentum transfers responsible for the plant motion.

3.2.1 Canopy Density Parameterization

The model plants consist of three distinct plant regions: (1) an underlying stem area connected to the (2) blade region by a (3) sheath zone that serves as a transition between the morphologies. As the blades branch out from the stem, the frontal area increases steadily from the cylinder-like cross sectional area to the value in the flexible blade region. Over the short distance in between these two zones, the frontal area is estimated by considering the degree of blade overlap and ensuring a smooth transition between the two frontal areas. In the blade region, the heterogeneity in leaf orientation complicates the estimation of the frontal area. Most of the plants orient themselves with the largest horizontal length scale, the blade width d_b, facing the flow and frontal area can be estimated from the blade width and the number of blades per plant. The effect of plant deflection can be incorporated either by calculating the projection onto a vertical plane or by using the deflection height as a normalization parameter.

Among the various parameters available from the literature to describe the canopy density, the frontal area per unit volume occupied by the plant was chosen as the most appropriate. The depth-variable canopy density $a(z)$ was calculated by segmenting a group of ten plants, each with six blades, into one centimeter intervals and obtaining an estimate of the area occupied by the stem and the blades for each vertical interval. A grid was constructed for each plant upon which the blade and stems were laid flat and the plant silhouette traced onto the paper. The frontal area (A_f) was estimated from measuring the stem diameter or the blade widths for each interval. Averaging over the plants, the canopy density can be calculated as:

$$a(z) = \frac{NA_f(z)}{\Delta x \Delta y h_i(z)} \tag{3.26}$$

where N is the number of plants in the horizontal bed area ($\Delta x \Delta y$) (330 plants/m^2) and h_i is the height for segment i (1 cm) This estimate of the canopy density is a vertically-varying counterpart to the canopy density defined in **Eq. 2.6**, where the density was estimate as md_b, m being the number of blades per unit

bed area, $N/\Delta x\Delta y$. A common procedure is to integrate the vertically inhomogeneous density over the canopy height and define a single parameter, either a roughness density as:

$$\lambda = \frac{N}{\Delta x \Delta y} \sum_i A_f(z_i) \tag{3.27}$$

or the leaf area index (*LAI*) (Kaimal and Finnigan, 1993):

$$LAI = \int_0^h a(z)dz \tag{3.28}$$

in order to facilitate the easy comparison between canopies of different morphology. **Eq. 3.27** and **3.28** are the discrete and continuous representation of the integrated canopy density. The roughness density, λ, has been used widely for a variety of surface roughness, including two dimensional bars, cylinders, spheres and cubes (Raupach *et al.*, 1991), whereas *LAI* is more commonly used for vegetation canopies.

The results from the estimation of the canopy density are presented in **Figure 3.1**. The canopy density (cm^{-1}) has been normalized by the deflected plant height, h_b, in order to point to the effect of streamlining on the canopy morphology. Several notable features should be pointed to in the canopy density profiles. The three different curves represent the variation of the canopy morphology for the experimental conditions in this laboratory study. The open circle (o) profile is the canopy density for *Case A*, where the in-canopy velocity was matched and the water depth was varied. As expected, changing the water depth has no appreciable effect on the canopy morphology. The other two profiles correspond to the increased discharge cases in experimental runs 5 and 6.

As the velocity is increased, the plants become more prone so that the canopy height is effectively reduced. This is apparent by normalizing the vertical distance by the undeflected canopy height, h_p, in **Figure 3.1**. The increase in velocity also reduces the plant frontal area by exposing less of the plant to the flow. A qualitative description of the decrease in plant frontal area with increased velocity is obtained by nondimensionalizing the canopy density with the deflected canopy height h_b. This normalization introduces the product $h_b = h_p\cos\phi_p$ into **Eq. 3.26**. The cosine of the deflection angle can be used with A_f to form the projection of the plant frontal area onto the vertical plane, $A_f\cos\phi_p$, which will decrease as the deflection angle increases. Using h_b as a normalization parameter for the canopy density in **Figure 3.1** is equivalent to plotting the projection of the canopy density and indicative of the streamlining of the plant canopy with increased velocity, as shown in the progression from the lower velocity and higher canopy density case (o) to higher velocity and lower canopy density case (•).

Figure 3.1 also quantifies the vertical inhomogeneity of the canopy morphology. The lower stem region has a smaller canopy density (a_{stem} = 0.016 cm^{-1}) than the blade region (a_{blade} = 0.055 cm^{-1}), joined by a transition zone where the measured density is assumed to vary linearly. This complicated morphology should lead to differences in flow resistance between the two regions and affect the velocity profile accordingly. The vertical inhomogeneity adds a degree of complexity to the laboratory model that

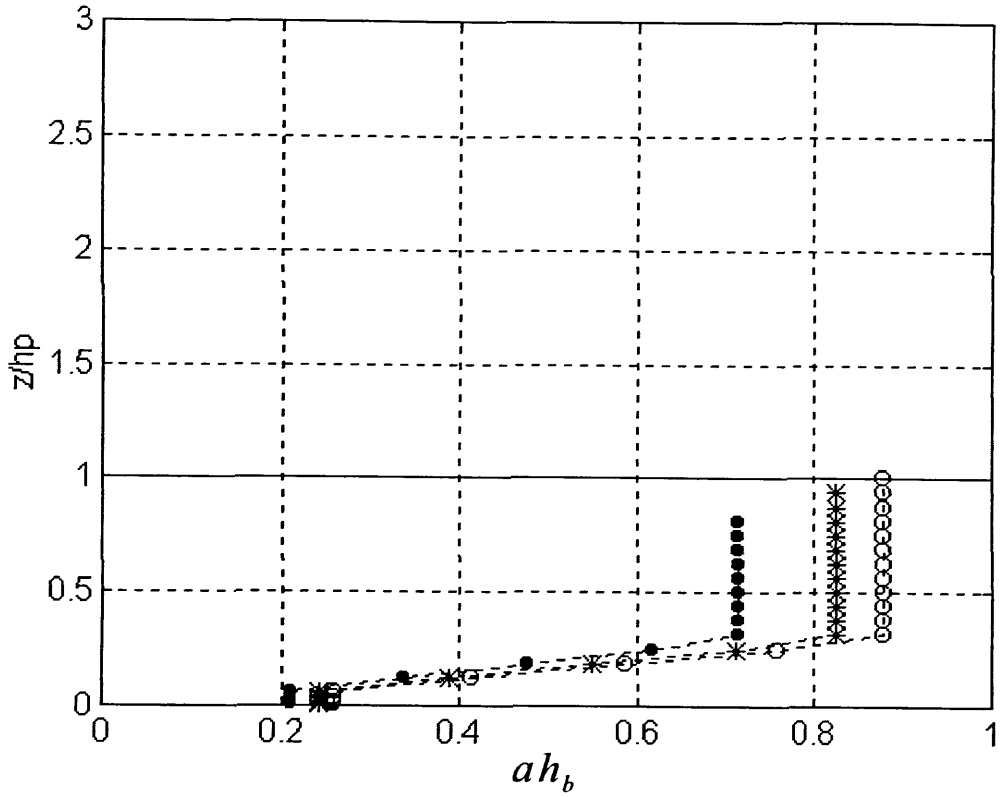

Figure 3.1. Canopy morphology represented by the nondimensional canopy density parameter, ah_b, where the h_b is the deflected canopy height, as a function of the nondimensional depth z/h_p. The open circles (o) represent experimental conditions for *Case A*, while stars (*) and solid circles (•) are for *Case B*, run 5 and 6, respectively. The horizontal solid line represents the top of the canopy. The decrease in height and density are indicative of the streamlining effect.

has been lacking in other vegetative flow studies through rigid or flexible cylinders (Dunn *et al.*, 1996). A study by El-Hakim and Salama (1992) with regards to the velocity profile through a submerged, branched and flexible model roughness approached the degree of complexity attempted in this laboratory study. Other laboratory studies that use the real plants inside open channel flow have also taken into account the complex plant morphology (Fonseca *et al.*, 1982; Gambi *et al.*, 1990)

The roughness density λ and the leaf area index *LAI* were calculated from the canopy density profiles. Because each parameter is the vertical integration of the canopy density, they can be used interchangeably ($\lambda \approx LAI$). The results for the canopy profile representing the experimental runs in *Case A* (o) are shown in **Table 2.2**, $\lambda = 0.79$ and $LAI = 0.76$. For the higher velocity cases at $H = 28$ cm, both the roughness density and the leaf area index decrease to $\lambda = 0.73$ and $LAI = 0.71$ for experimental run 5 (*) and $\lambda = 0.62$ and $LAI = 0.60$ for experimental run 6 (•). The small discrepancies in the values of the two parameters correspond to the different integration methods and are not significant. **Table 3.1** shows a comparison between the canopy density parameters from the model seagrass meadow to other plant canopies. It is apparent that laboratory models tend to have lower values for the leaf area index than the

Table 3.1. Comparison of physical characteristics from different plant canopies.				
Canopy	**Reference**	h_p	*LAI*	l_s
Model Meadow (LF)[a]	This study	15.97 cm	0.76	5.50 cm
Model Wheat (WT)[b]	Brunet *et al.* (1994)	4.7 cm	0.47	0.50 cm
Model Cylinders (WT)	Seginer *et al.* (1976)	19 cm	1.00	2.12 cm
Model Cylinders (LF)	Dunn *et al.* (1996)[(1)]	11.75 cm	0.92	7.62 cm
Model Cylinders (LF)	Tsujimoto *et al.* (1992)[(2)]	4.1 cm	0.30	1.0 cm
Corn Field	Shaw *et al.* (1976)	2.25 m	1.50	N/A[(3)]
Aspen Forest	Amiro (1990)	10 m	1.95	N/A
Zostera marina Meadow	Gambi *et al.* (1990)	11.44 cm	0.90	3.77 cm

(a) LF = Laboratory Flume study; (b) WT = Wind Tunnel study; (1) Experimental run 1; (2) Series R; (3) Not Available

natural canopies and that the present study is well within the values obtained by other researchers in wind tunnel and flume studies. Larger values for $LAI \approx 3$–5 have also been reported in the literature (Kaimal and Finnigan, 1993). For *Zostera marina* meadows, Gambi *et al.* (1990) reports a range of *LAI* from 0.36 to 1.10 over a range of plant densities from 400 to 1200 blades per square meter.

From knowledge of the roughness density, estimates of the mean plant spacing and the effective plant diameter can be obtained from two alternative expressions for the roughness density. For a vertically homogeneous canopy, the roughness density can be expressed as (Raupach, 1992):

$$\lambda = \frac{d_p h_p}{l_s^2} = \frac{N d_p h_p}{\Delta x \Delta y} \tag{3.29}$$

where d_p is plant diameter or width, l_s is the plant spacing, h_p is the plant height and $N/\Delta x \Delta y = m = 330$ plants/m^2. Using the roughness density for the undeflected cases, $\lambda = 0.79$, the effective plant diameter is estimated as $d_p = 1.50$ cm and the mean plant spacing $l_s = 5.50$ cm, as shown in **Table 2.2**. These two parameters indicate the spacing and the width of the plants as if they were cylinders. The effective plant width, d_p, is much larger than the actual blade width, $d_b = 0.28$ cm. As expected, the value for the effective plant width corresponds well to the actual blade width times the number of blades per plant ($N_b d_b = 1.68$ cm). The mean spacing obtained in this fashion ($l_s = 5.50$ cm) also corresponds well to the actual plant spacing within the canopy, which was estimated by choosing ten plants and measuring the distance to the adjacent plants. Averaging over the random sample resulted in a measured plant spacing of 5.60 ± 0.5 cm, rendering further support to the simple relationship presented in **Eq. 3.29**. **Table 3.1** summarizes the mean plant spacing for a number of laboratory and field experiments of plant canopy turbulence.

3.2.2. Plant Motion Characterization

The plant motion measurements described in Section 2.3.5 allowed the estimation of the deflected plant height h_b, the plant deflection angle ϕ_p, and the plant vibration frequency f_p, for each experimental run. The deflection height and the vibration frequency were measured directly, while the deflection angle was obtained from measurements of the mean longitudinal excursion, a_p. A simple trigonometric relationship leads to the deflection angle from the measurement of h_b and a_p:

$$\phi_p = 90 - \tan^{-1}\left(\frac{h_b}{a_p}\right) \tag{3.30}$$

The deflected plant height and angle were obtained from averaging the measurements of ten plants at five different time periods, leading to a total of fifty measurements per estimate. The large sample size was deemed necessary considering the plant-to-plant variability and the temporal variation of these parameters. The vibration or oscillation frequency was measured by counting the number of excursions made by a random sample of ten plants for the duration of the video recording. The mean and the 95% confidence interval values from the plant motion visualization are shown in **Table 3.2**. The confidence intervals for the deflection angle were obtained by using the constant odds methods of Kline and McClintock (1953) to **Eq. 3.30**. **Figure 3.2** shows a simple schematic defining the parameters measured from the plant motion images.

Table 3.2. Plant motion characteristics.

Experimental Run	Plant Deflected Height h_b (cm)	Plant Deflection Angle ϕ_p (degrees)	Plant Deflection Amplitude a_p (cm)	Plant Vibration Frequency f_p (Hz)
1A	15.8 ± 0.5	5.4 ± 0.04	1.5 ± 0.6	–
2A	15.8 ± 0.2	7.6 ± 0.03	2.1 ± 0.5	0.09 ± 0.03
3A	16.0 ± 0.2	7.9 ± 0.02	2.2 ± 0.4	0.16 ± 0.02
4A,B	15.7 ± 0.3	8.2 ± 0.02	2.3 ± 0.4	0.16 ± 0.02
5B	15.2 ± 0.2	10.5 ± 0.03	2.8 ± 0.4	0.22 ± 0.02
6B	13.7 ± 0.4	18.2 ± 0.04	4.5 ± 0.6	0.42 ± 0.04
7A	15.7 ± 0.4	8.3 ± 0.03	2.3 ± 0.5	0.15 ± 0.01

Despite the variability witnessed during the estimation of the deflection height and angle, the results shown in **Table 3.2** are encouraging for several reasons. On one hand, the plant height for *Case A* experiments (runs 1–4, 7) are within 2% of the undeflected plant height (h_p = 15.97 ± 0.04 cm) estimated from a group of ten plants. This implies that for the depth variation cases, the undeflected plant height is the appropriate canopy length scale. The larger variability in the deflected height estimate from the cases with the monami (runs 5 and 6) is due to taking the measurements during plant motion, thus the interval represents the variability due to the oscillations. The emergent case (H/h_p = 1.00) has a large variability due to the stationary deflection of some plants. The small deflection angles for *Case A* experiments (less than 10°) also lends support to the use of h_p as the effective canopy height.

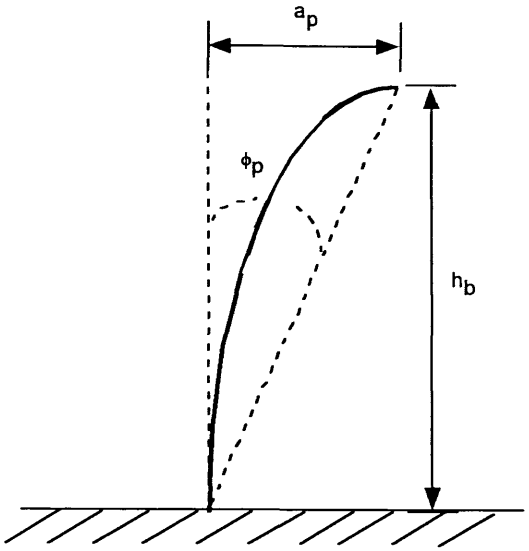

Figure 3.2. Definition sketch for the plant motion characterization. The deflected plant height, h_b, the deflection angle, ϕ_p, and the plant motion amplitude, a_p, are shown.

The results from the plant motion characterization also demonstrate quite clearly that the velocity variation cases (runs 4–6) exhibit quite different degrees of bending. The mean deflection angle for *Case B* progressively increases from 8 to 18 degrees as the flow discharge is increased and the mean deflected height decreases approximately 2 centimeters over the same range. For these experimental runs, the use of the deflected height h_b as the effective canopy top is more appropriate than using the undeflected canopy height, as was indicated by the normalization used for the canopy morphology in **Figure 3.1**. The deflected height measurements, h_b = 15.21 and 13.74 cm, compare well to the estimates of the effective canopy top from the Reynolds stress profiles, as discussed in Section 3.3.3.

The effect of velocity on the streamlining of canopy morphology can be further explored by comparing the degree of bending and the effective canopy height (h) with an appropriate velocity scale, the mean streamwise velocity at the interface of the vegetation and surface layers, U_h. **Figure 3.3** shows the variation of the mean deflection height and angle with the interface velocity U_h. It can be seen that for *Case A* (o), the mean canopy height, the mean amplitude and the deflection angle remain constant, despite the increase in the interface velocity. The deflection angle exhibits a small increase in value, from 5 to 8 degrees, as the characteristic depth increases, but this difference is within the estimation errors from this parameter and no physical interpretation is warranted. Considering that *Case A* runs were designed to match the in-canopy velocity, obtaining a constant mean canopy height is a reassuring sign that the dynamic behavior is similar. Increased deflection and waving become more notable in *Case B* (*), where a slight decrease in the mean canopy height and a marked increase in the deflection angle occur as the interface velocity is increased. It can be seen from **Figure 3.3** that a threshold interface velocity, U_h, near 10 cm/s leads to significant changes in the flow regime.

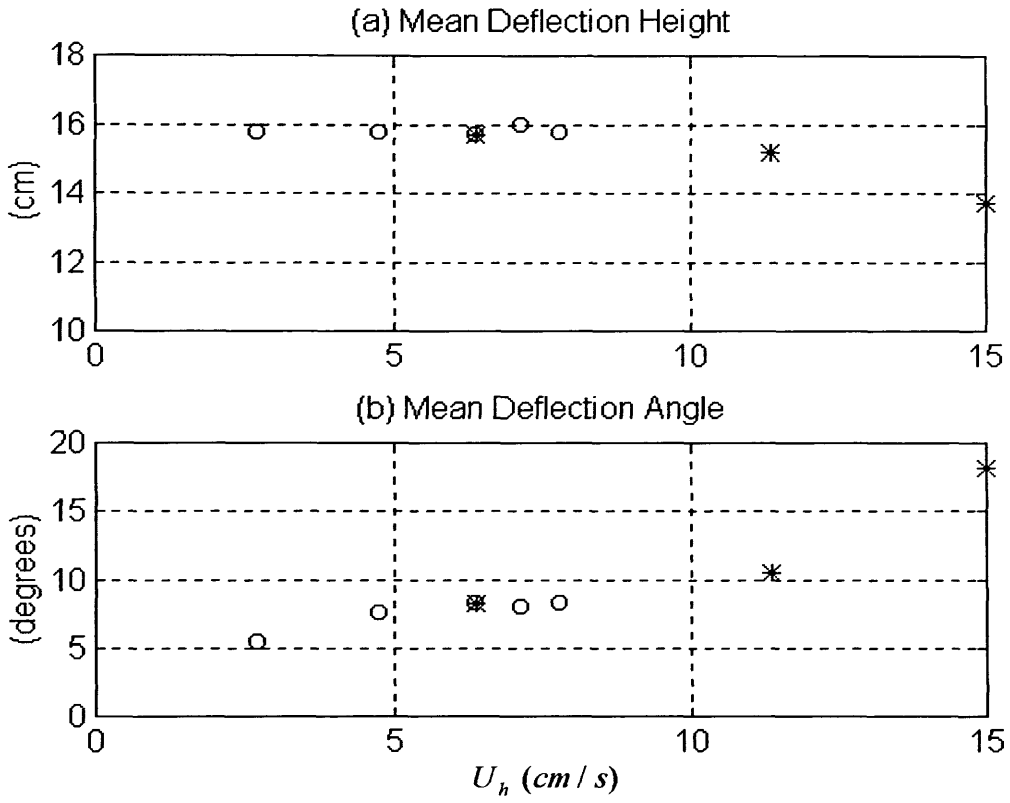

Figure 3.3. Effect of velocity on canopy streamlining and waving. Both the mean deflection angle ϕ_p and the deflected height h_b vary significantly with the velocity at the canopy top for values of U_h greater than 10 cm/s for *Case A* (o) and *Case B* (*) experiments.

Previous researchers have classified flow through flexible roughness and grass-lined channels into categories based on the plant motion. Kouwen and Unny (1973) observed three flow regimes, an erect regime, where the plants were stationary; a waving regime, where the plants undergo coherent oscillations; and a prone regime, where the plants are completely bent over. The authors showed that only two distinct hydraulic regimes existed for these three categories, the erect behavior including the waving motion and the prone behavior, where the canopy behaves as a smooth boundary. The erect behavior was hydraulically indistinguishable from the waving behavior. The results from the plant motion characterization for these experimental runs indicate that this may not be the case. The small deflection angle and the low plant vibration frequency for *Case A* (o) in **Figure 3.3** are consistent with the erect category, while the higher velocity runs in *Case B* (*) distinctly exhibit the waving regime. The differences between the two cases in terms of the deflection angle and the deflected height are substantial and may indeed lead to different hydraulic behaviors. This point will be explored further in Section 3.4 where the hydraulic characteristics of the experimental runs will be presented.

The plant vibration frequency estimated from the number of excursions made by ten plants during the recording period increased for both the depth variation and velocity variation cases as shown in

Table 3.2. Although increasing the depth for *Case A* did not affect the level of the mean plant height, the increased velocity at the canopy top led to higher plant oscillations. For the emergent case, no plant vibrations were observed, the blades were erect and stationary. The plant vibration frequency rose sharply as the plants were initially submerged and then reached an asymptotic value of 0.15 Hz for characteristic depths (H/h_p) greater than 1.50. This asymptotic behavior will be seen for other parameters derived from the velocity measurements when comparing across the depth variation cases. The plant motion for the depth variation cases progressively increased in coherency, *i.e.* the swaying became more organized and the motion seemed to propagate downstream from plant to plant. The increased coherency, however, did not appear to impact the frequency of motion. In summary, the motion within the meadow in terms of the oscillation frequency for *Case A* can be considered to be within the bounds of the erect regime despite the small degree of swaying observed.

As for *Case B*, the sharp increase in the plant vibration frequency with increasing velocity corresponds to the higher deflection angles and the lower canopy height. The experimental runs with the higher velocity exhibited large amplitude swaying motion and organized canopy waves propagating downstream, a condition described as a monami for aquatic plants ('mo' = aquatic plant; 'nami' = wave from Japanese). The plant waving was characterized by small and frequent motions that are periodically interrupted by larger amplitude motions. The highest velocity case also demonstrated higher frequency plant motions unassociated with the monami motion with lateral vibrations of the plant elements. These experimental runs displayed that the passage of the canopy wave seemed to be in groups of two or three, an effect that had been observed to a smaller degree in other runs. Finnigan (1979a,b) first described a similar effect in a wheat meadow with the arrival of packets of wind gusts composed of two to three waves. The plant responds to the arrival of the first gust motion by bending and before it has had time to relax to its erect, vertical position, a second gust arrives and forces it to bend again. The effect is visually observed as a staggered bending motion of the plant blade. These visual observations can be explained quite well by analyzing the structure of the momentum transfer between the canopy and the surface layer, as will be presented in Section 3.6. In summary, the motion within the meadow for *Case B* can be described as a waving regime ranging from little or no swaying to rapidly swaying.

Figure 3.4 relates the plant vibration frequency to the interface velocity and shows that there is a linear increase in the plant oscillations with the slip velocity at the canopy top, as expected from the previous discussion and from **Figure 3.3**. One way to quantify this linear relationship is by finding the regression line for the data obtained from the different velocity and depth cases. The regression analysis resulted in an empirical relationship between the vibration frequency and the velocity at the canopy top:

$$f_p = 0.031U_h - 0.071, \qquad \textbf{(3.31)}$$

which has an R^2 value of 0.94 for the data points. The limited experimental conditions explored in this study do not allow us to make any general conclusions about this relationship or even to imply that it is

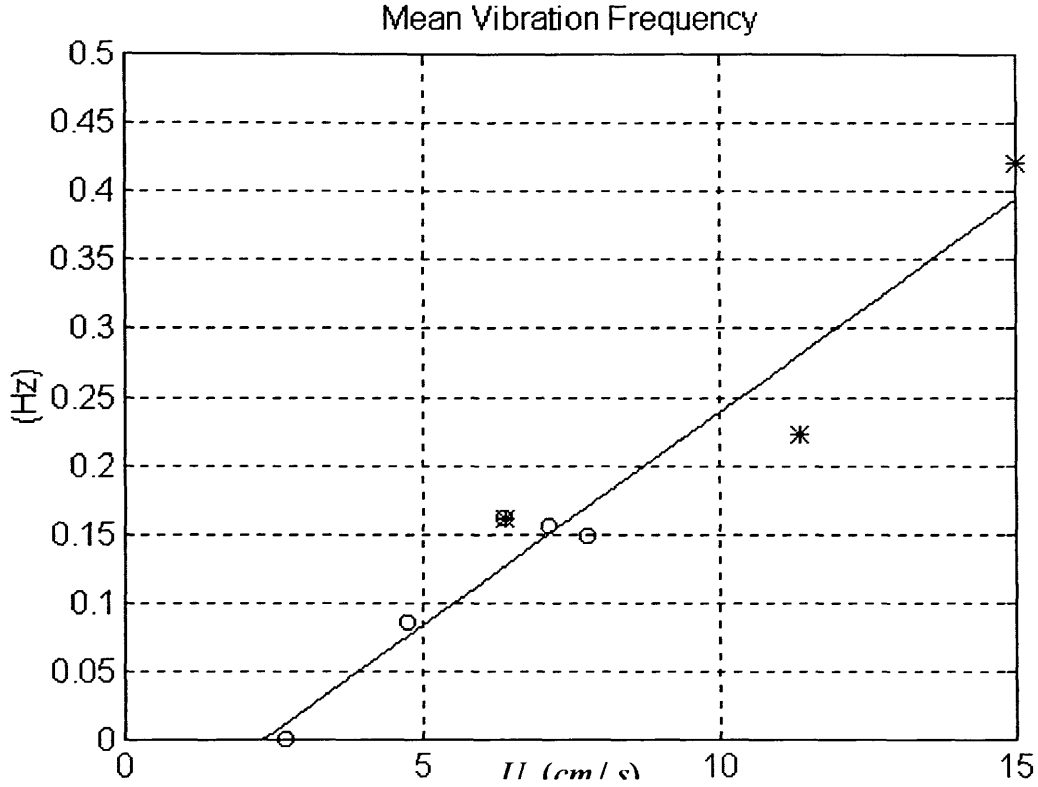

Figure 3.4. Effect of the interface velocity on the plant oscillation frequency. *Case A* (o) and *Case B* (*) oscillating frequency f_p increase linearly with the slip velocity U_h. The solid line represents the least-squares regression fit to the data points ($R^2 = 0.94$).

valid for other flow conditions, plant height and plant stiffness. Instead, we can suggest that the plant oscillation frequency can be parameterized by the slip velocity, U_h, a parameter that can be obtained easily from the velocity profile and an estimate of the canopy height. With additional data points over other flow conditions, a relationship like **Eq. 3.31** would be a useful tool for field researchers interested in quantifying the plant motion without taking video recordings, a challenging task during a field study.

The last piece of information that can be estimated from the plant visualization experiments is the wavelength of the canopy wave or monami. The estimation of the wavelength was only possible for the experimental condition with the most extreme waving, experimental run 6. Even then, the visual estimation of the wavelength was not an easy task due to the poor structural definition of the monami as it passed the recording area. As the wave passed, the half wavelength was estimated as the distance between a wave trough observed as the plants bent and the previous crest where the plants were returning to the undeflected position. The monami wavelength (λ_m) was estimated from the passage of twenty different waves through the recording region. The measured value was $\lambda_m = 40.00 \pm 2.15$ cm in length, which is approximately equal to $2.5h_p$. As compared to the wavelength reported by Finnigan (1979a), $\lambda_m = 5$ to $8h_p$, in a wheat meadow, the phenomenon in this laboratory flume is of reduced length, potential due to the limited depth of the overlying layer. In addition, the monami waves had a lateral scale smaller than

the flume width, B, due to the side-wall effects. Two distinct wave trains could be observed from the video recordings, so that the lateral scale of a monami in the flume is estimate to be 0.75 to $1.00h_p$, also smaller than the several canopy heights in width estimated by Finnigan (1979a).

With the estimate of the monami wavelength λ_m and the plant vibration frequency f_p for experimental run 6, the monami phase velocity can be calculated simply from $\theta_m = \lambda_m f_p$, which results in $\theta_m = 16.84 \pm 1.75$ cm/s. This estimate is reasonably close to the observed monami velocity, estimated from timing the passage of a travelling canopy wave in the video recordings. The phase velocity is an indication of the convection velocity of the coherent eddies that are formed at the interface between the vegetation and surface layer regions. Other studies have shown that the convection velocity is twice the interface velocity, $2U_h$, for a laboratory study of a waving wheat canopy (Shaw *et al.*, 1995) and 1 to $1.4U_h$ for a laboratory study of submerged flexible vegetation (Ikeda and Kanazawa, 1996). The estimate of the phase velocity in this laboratory study is approximately 0.95 to $1.16U_h$, for experimental run 6, which is in the range of observed values by Ikeda and Kanazawa (1996). Thus, the plant motion response to the eddies at the canopy height propagates downstream at a velocity that is comparable to the velocity at the canopy height. This result seems reasonable since the eddies at the canopy height are expected to travel at or slightly above the local velocity for that elevation. In Section 3.6, an analysis will be made to show that the plant motion and the monami activity are directly related to the arrival of downward motions or sweeps by matching the frequency of arrival of the sweeps with the plant motion frequency.

3.2.3. Plant Flexibility

As described in Section 2.2, the characterization of the plant flexibility is an important step in modeling a seagrass meadow in a laboratory experiment with artificial roughness. It was mentioned that the scaling between the model and the prototype depended a great deal on the range of values for the velocity U and the water depth H in the two systems, and that representative values were chosen to show that the artificial roughness was within the range of stiffness required to properly model submerged vegetation. The prototype chosen to scale the stiffness was a particular type of submerged aquatic plant (Bermuda grass) chosen to have similar dimensions to *Zostera marina*, for lack of information on eelgrass itself. This section briefly outlines how the flexural rigidity, $J = EI$, for the plastic material used in the experiment was obtained and how it can lead to estimates of other plant motion parameters, specifically the fundamental vibration frequency.

The flexural rigidity for the model plants was calculated from the dimensions of the roughness elements and the properties of the plastic material. From a material data sheet provided by the manufacturers of the plastic, a vinyl PVCA copolymer (Comcographics, Devens, MA), the modulus of elasticity in bending E was obtained, as shown in **Table 2.2**. The modulus of elasticity of a material is a coefficient relating the stress placed on a material to the strain experienced by the material before the

material yield has been reached (Beer and Johnston, 1981). In the initial portion of a stress-strain diagram, the stress is linearly related to the strain, a relationship known as Hooke' Law:

$$\sigma_H = E\varepsilon_H , \tag{3.32}$$

where σ_H is the stress and ε_H is the strain. The modulus of elasticity for the plastic material is usually calculated by performing a load-deflection test based on the procedures of the American Society of Testing Materials (ASTM Test D790). In the procedures for the test, the modulus of elasticity is defined as (ASTM, 1997):

$$E = \frac{d_h^3 m_s}{4 d_b d_t^3} , \tag{3.33}$$

where the variables pertinent to the blade geometry have been used, the blade length, d_h, for the beam span, the blade width, d_b, for the beam width, and the blade thickness, d_t, for the beam depth. The slope of the tangent to the straight line portion of the load deflection curve is represented by m_s. Using the values for the parameters in **Eq. 3.33** shown in **Table 2.2**, we can calculate the slope of the load-deflection curve, $m_s = 0.19$ N/m. The moment of inertia, I, necessary to calculate the flexural rigidity can be obtained from knowing the blade geometry and the axis about which the plant blade will bend. The standard formula for the calculation of I for a rectangular region rotating about the y-axis of a blade oriented with the width and height perpendicular to the flow is (Beer and Johnston, 1981):

$$I = \frac{1}{12} d_t^3 d_b . \tag{3.34}$$

With knowledge of the flexural rigidity EI, an estimate can be made of the natural frequency of vibration for the plant blades. If a blade is considered as a single-span beam or cantilever, the resonance frequencies can be calculated from the equation (Blevins, 1984, p. 104):

$$f_i = \frac{\gamma_i^2}{2\pi}\left(\frac{EI}{m_l d_h^4}\right)^{1/2} ; \qquad i = 1, 2, 3... \tag{3.35}$$

where the subscript i refers to the different harmonics, γ_i is a dimensionless parameter which is a function of the boundary conditions applied to the beam, m_l is the mass per unit length and d_h is the beam length represented by the blade height. The measurement of the mass per unit length was performed by weighing the blades of ten randomly sampled plants and dividing by the total blade length, a procedure that resulted in $m_l = 9.46 \times 10^{-4} \pm 7.27 \times 10^{-5}$ kg/m. Standard tables give the value for the γ_i coefficients for different types of beams. The most appropriate beam type representing the plant blades is a clamped-free beam, having one clamped extreme and one free extreme. The clamped-free beam has the following values of γ_i for the first three oscillation modes (Blevins, 1984, p. 108):

$$\gamma = \begin{cases} 1.875 \text{ Hz for } i = 1 \\ 4.694 \text{ Hz for } i = 2 \\ 7.854 \text{ Hz for } i = 3 \end{cases}. \quad \textbf{(3.36)}$$

The natural frequency $f_n = f(i = 1)$ of the plant blades can be estimated from **Eq. 3.35** by using the parameters in **Table 2.2** and the value for $\gamma_1 = 1.875$. The blades have a natural frequency of vibration equal to 3.06 Hz or 19.24 rad s^{-1}. Compared to the plant oscillation frequencies estimated for the experimental runs (0.085 – 0.421 Hz) from the video recordings, it is apparent that the plants are not being forced at their fundamental frequency but rather at a frequency that is an order of magnitude smaller. The higher resonant frequencies for the model plant blades are 19.19 Hz and 53.73 Hz. The value for the modulus of elasticity, the moment of inertia and the natural frequency are also presented in **Table 2.2** along with the other parameters that characterize the model plants and the canopy.

3.3 Velocity Statistics

This section presents the single-point mean and turbulence statistics for the three velocity profiles of each experimental run obtained using the acoustic Doppler velocimeter and the supplementary measurements made with the laser Doppler velocimeter. Statistics up to fourth order were computed from each velocity time series. These include the streamwise mean velocity, the turbulence intensities, the skewness and the kurtoses coefficient profiles. In addition, the turbulent kinetic energy and the correlation coefficient profiles are presented to address the issue of momentum transfer between the vegetation and the surface layers. The appropriate horizontal and temporal averaging, as discussed in Sections 2.4 and 3.1.1, were performed to obtain the set of statistics for each parameter.

The results from the velocity profiles for the two experimental cases (*Cases A* and *B*) will be presented simultaneously and discussed with appropriate references made to the characteristic results in other plant canopy flows. In addition, the effect of the depth and velocity variations across the experimental cases will be explored by comparing specific quantities derived from the velocity statistic profiles. In this way, the changes in the depth of the surface layer and the interface velocity can be shown to cause variations in the turbulence structure within the seagrass meadow.

In each of the following figures, the data point in the profile represents the temporal and horizontal averaged quantity, while the horizontal bars are the 95% confidence intervals on the horizontal average, *i.e.* reflect horizontal variability within the canopy. For each parameter, the horizontal mean is denoted by the use of angle brackets, while the temporal mean is denoted with an overbar. Each velocity statistic profile is presented in the appropriate nondimensional form and plotted against the nondimensional distance z/h_p, where h_p is the undeflected mean plant height.

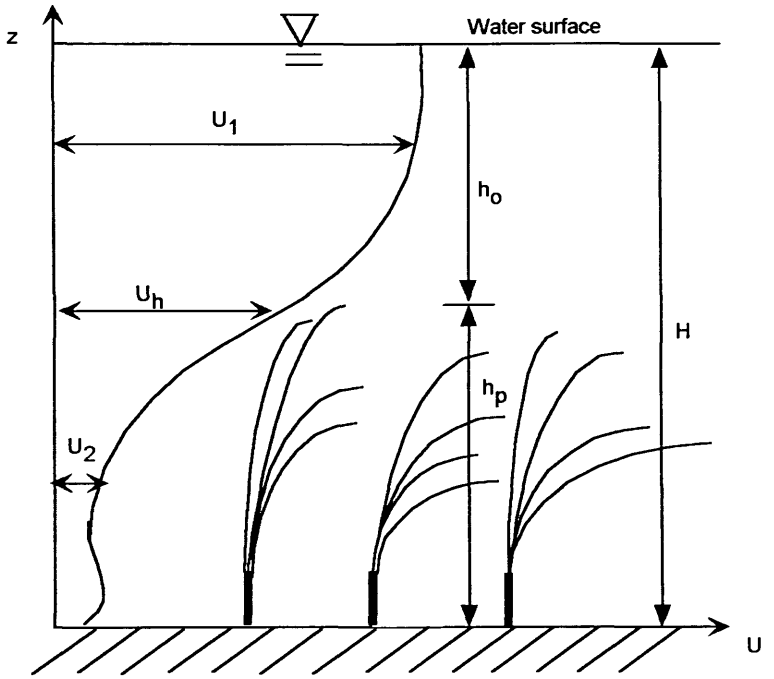

Figure 3.5. Schematic of the relationship between the mean streamwise velocity profile and the canopy morphology. Three relevant velocity scales and three length scales have been included: the interface or slip velocity, U_h, the surface layer velocity, U_1, the vegetation layer velocity, U_2, the water depth, H, the vegetation layer depth, h_p, and the surface layer depth, h_o.

It is worthwhile to present a schematic of the measured velocity profile within the seagrass meadow and discuss its relevant velocity and length scales. **Figure 3.5** shows that the shape of the velocity profile can be related to the different canopy morphology regions. Three different flow regions can be identified from the velocity profile, the near-bed secondary maximum at the level of the plant stem, a constant in-canopy region associated with the canopy density transition zone, and a highly sheared flow region within the plant blades extending from a mid-canopy height to the surface layer. The model plants extract momentum from the flow and create the shear layer between the vegetation and surface layers. The transformation between the open channel flow velocity profile upstream of the canopy and the in-canopy shear velocity profile is pictured in **Figure 2.1**.

The shear profile represented in the schematic is characteristic of other types of flow, particularly a mixing layer, where two coflowing streams of different velocities (U_1 and U_2) mix across a plane. Raupach *et al.* (1996) showed that the analogy with the mixing layer is a better representation of flow through plant canopies than the traditional boundary layer concept. Based on this analogy, the schematic of **Figure 3.5** shows the two relevant velocity scales for the mixing layer, U_1 for the surface layer and U_2 for the vegetation layer. The surface and vegetation layer depth scales also prove to be important parameters for the description of the system. Reference will be made in the following discussion to the mixing layer analogy and the velocity difference between the two layers will be used to estimate parameters related to the instability mechanisms created at the interface.

3.3.1 Mean Streamwise Velocity Profiles

The mean streamwise velocity profiles for the depth and velocity variation cases, *Cases A* and *B*, respectively, are shown in **Figures 3.6** and **3.7** in dimensional and nondimensional form. The temporal and horizontal averaged velocity has been normalized by total forcing in the system, represented by a velocity scale known as the friction or shear velocity, u_*. There are several potential estimates of the friction velocity based either on the longitudinal pressure gradient, the Reynolds stress profile or the logarithmic velocity layer, as will be discussed in greater detail in Section 3.4.3. The most appropriate choice for nondimensionalizing the mean velocity profile is the total forcing in the system, obtained as the shear velocity estimate based on the total water depth (H) and the surface slope:

$$u_* = \sqrt{gHS_w} \,, \tag{3.37}$$

where S_w is the water surface slope as defined in **Eq. 3.24**. The results of the surface slope experiments are discussed in detail in Section 3.4.2 and the values used in **Eq. 3.37** are shown in **Table 3.5**. The values for the friction velocity and the water depth for the experimental runs are shown in **Table 3.3**.

The purpose of presenting the dimensional and nondimensional version of the mean velocity profile is to be able to discuss the depth and velocity variations in absolute and relative terms. For the depth-varied cases, the dimensional profiles in **Figure 3.6a** show that the absolute velocity inside the canopy region is constant across the depth-variation, a condition which was assured by matching the characteristic velocity u_s. In this way, the transition from the shear turbulence regime to the wake turbulence regime can be quantified for similar in-canopy conditions. For the velocity-varied cases, the velocity within the vegetation layer and the degree of shear in the surface layer increase with the flow discharge for identical flow depths, as shown in **Figure 3.7a**.

By using the friction velocity defined by **Eq. 3.37** as a nondimensional parameter, the differences between the velocity profiles in relationship to the total forcing in the system can be distinguished. For the *Case A* experimental runs, the nondimensional velocity within the meadow decreases as the characteristic depth (H/h_p) increases, as shown in **Figure 3.6b**. This implies that the velocity in the vegetation region becomes a smaller portion of the total velocity as the surface layer increases. This corroborates the expected trend for the transition between a shear dominated to a wake dominated flow, where less of the total friction is carried by the lower canopy regions as the interfacial shear increases. Contrary to the depth-varied cases in **Figure 3.6b**, the friction velocity normalization, as shown in **Figure 3.7b**, is reasonably successful in collapsing the profiles for the *Case B* experimental runs. This demonstrates that the increase in flow discharge does not change the relative degree of friction carried by the lower canopy region. Thus, for the velocity-varied cases, the mean velocity inside the meadow is the same proportion of the total forcing in the system.

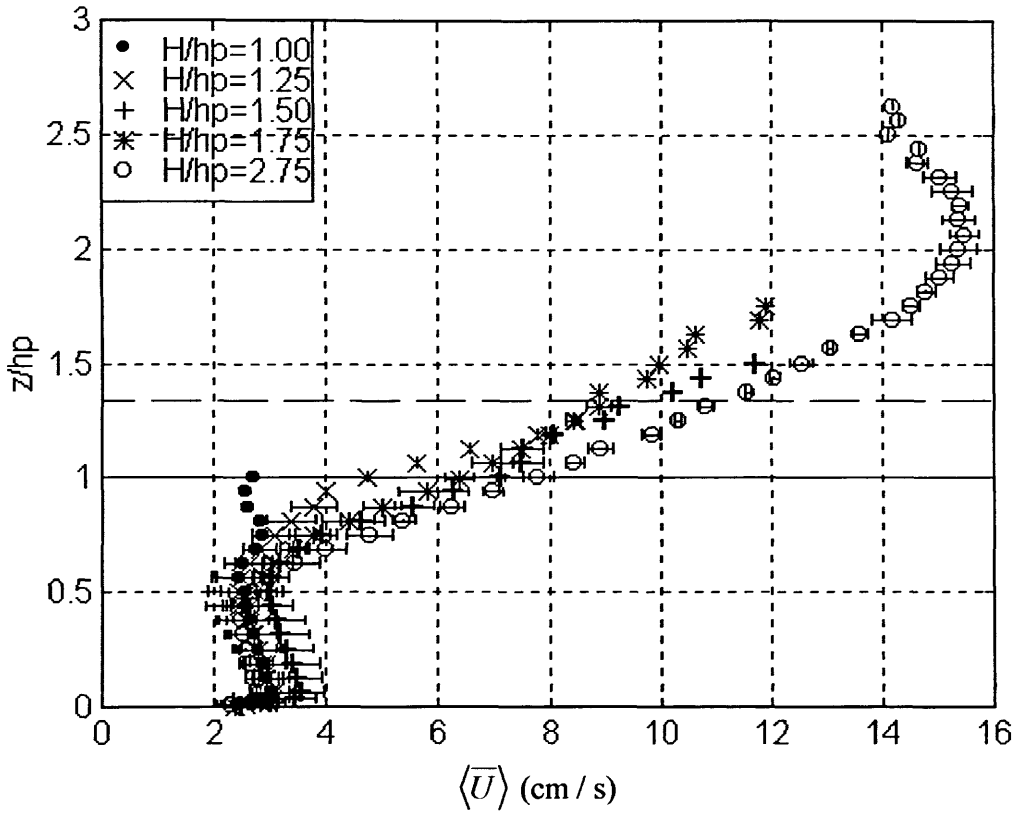

Figure 3.6a. Dimensional mean streamwise velocity profile for the *Case A* experimental runs. The horizontal solid line at z/h_p = 1.00 represents the undeflected canopy height, while the horizontal long dashed line (—) is the height of inhomogeneity z_h/h_p for an unbounded flow. The horizontal bars are the 95% confidence level on the horizontal average for the three ADV profiles, while the symbols without the bars are the LDV measurement points.

Figure 3.6a shows that the variation in the characteristic depth (H/h_p = 1.00, 1.25, 1.50, 1.75, 2.75), or inversely the relative roughness ($r = h_p/H$ = 1.00, 0.87, 0.67, 0.57, 0.36), imparts a different overall shape to the mean velocity profile. The profile for H/h_p = 2.75 is a shear profile with a distinctive region of near uniform velocity close to the free surface that is indicative of the outer layer, while the profile for H/h_p = 1.00 is approximately uniform over the entire flow depth, varying only in response to the inhomogeneity in canopy morphology. The two extreme cases are bridged by the profiles for H/h_p = 1.25, 1.50 and 1.75 that demonstrate how the shear profile develops as the surface layer depth, h_o, increases. All the profiles share the same general shape and velocity magnitude in the in-canopy region where an important velocity bulge was measured for all the velocity profiles. This secondary maximum, also measured in other field and laboratory plant canopy flows, has been an issue of discussion within the canopy turbulence research community for many years due to the implications it has for modeling the transport in the system with a flux-gradient relationship.

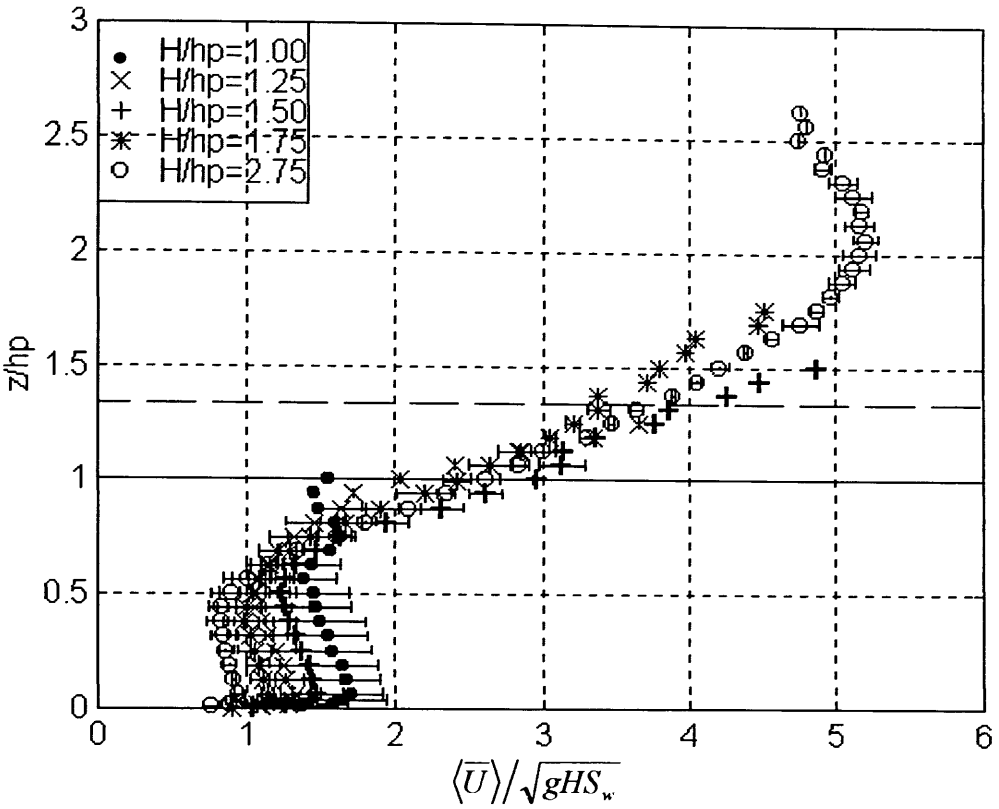

Figure 3.6b. Mean streamwise velocity profile for the *Case A* experimental runs nondimensionalized by the friction velocity based on the water depth and the surface slope. The horizontal solid line at $z/h_p = 1.00$ represents the undeflected canopy height, while the horizontal long dashed line (—) is the height of inhomogeneity z_h/h_p for an unbounded flow. The horizontal bars are the 95% confidence level on the horizontal average for the three ADV profiles, while the symbols without the bars are the LDV measurement points.

The velocity profiles in **Figures 3.6** and **3.7** also show quite clearly that the vegetation layer is subject to more horizontal inhomogeneity than the surface layer. The deviation from the horizontal average, represented by the horizontal bars, is on average 1.8 times larger within the canopy than in the surface layer. The horizontal deviation observed in the mean velocity profile corroborates the need for lateral averaging within the canopy and suggests that in the above canopy region horizontal averaging is not as crucial. For flow over a rough surface, Raupach *et al.* (1980) found that the horizontal inhomogeneity extended up to a vertical distance $z_h = h_p + l_s$, where l_s is the element spacing, 5.5 cm in these experiments. For the seagrass meadow, this estimate would imply that the horizontal inhomogeneity extends to an elevation $z_h/h_p = 1.34$, as shown in **Figures 3.6** and **3.7** by the horizontal long dashed line. Inspection of the horizontal variations shows that the height of inhomogeneity for the *Case A* experiments with substantial vertical extent increases from $z_h = h_p$ to $1.25h_p$ for the characteristic depths $H/h_p = 1.50$ to 2.75, as shown in **Table 3.3**. The height of inhomogeneity was estimated crudely from the profiles of the horizontal variation of the mean streamwise velocity by setting a threshold

Table 3.3. Physical parameters for the *Case A* and *B* experimental runs.							
Parameter / Run	**1A**	**2A**	**3A**	**4A,B**	**5B**	**6B**	**7A**
Characteristic depth H/h	1.00	1.25	1.50	1.75	1.87	2.15	2.75
Surface layer depth h_o/h	0.00	0.25	0.50	0.75	0.87	1.15	1.75
Shear Length Scale L_s (cm)	–	7.64	11.27	10.73	9.34	8.70	10.50
Inflection point z_i (cm)	–	13.00	13.90	14.40	14.30	12.00	14.40
Inhomogeneity height z_h (cm)	–	–	16.00	19.00	16.00	15.00	20.00
Vorticity thickness δ_w (cm)	–	3.57	7.23	9.10	9.07	9.26	13.28
Friction velocity u_* (cm/s)	1.72	2.32	2.40	2.63	3.69	4.76	2.97
Slip velocity U_h (cm/s)	2.70	4.73	7.12	6.38	11.36	14.99	7.81
Surface velocity U_1 (cm/s)	–	6.64	9.03	9.21	15.78	21.99	13.35
Vegetation velocity U_2 (cm/s)	2.69	2.75	3.17	2.75	4.81	6.06	2.59
Extinction coefficient ν_e	–	1.70	2.20	2.00	1.95	1.75	2.20

minimum value of 0.1 cm/s for the 95% confidence interval. As the surface layer depth is increased, the region of inhomogeneity becomes larger, a trend which supports the level of inhomogeneity in an unbounded flow over a rough surface (Raupach *et al.* 1980). **Table 3.3** also shows that the height of the inhomogeneity decreases with increasing flow discharge. If z_h is nondimensionalized by the deflected canopy height, h_b, however, the elevation for the experimental runs in *Case B* is comparable with a mean and 95% confidence interval values of 1.14 ± 0.07 cm/s, suggesting that the effect of the flow discharge is not as important as the depth variation in determining the region where horizontal inhomogeneity is important.

Figure 3.7a shows the variation of the dimensional mean streamwise velocity profile with the flow discharge (Q = 6.31, 10.72, 15.14 L/s) for the experimental runs in *Case B* at the specific depth H = 28 cm. The decrease in plant height associated with the higher interface velocities can be quantified by using the deflected height (h_b) as a substitute for the undeflected canopy height in the characteristic depth (H/h) and the nondimensional surface layer depth (h_o/h), as shown in **Table 3.3** for runs 4, 5 and 6. There is a slight increase in these two parameters with the flow discharge which indicates that the surface layer becomes larger with the reduced canopy height. The general profile shape for the experimental runs in *Case B* also exhibit the velocity bulge near the model plant stems and the sheared region in velocity profile near the bottom, as was observed for *Case A*. This secondary shear region near the bed has a similar shape and magnitude across the experimental runs in *Cases A* and *B*, reaching minimum values on the order of 2.3 cm/s for the bottom most point.

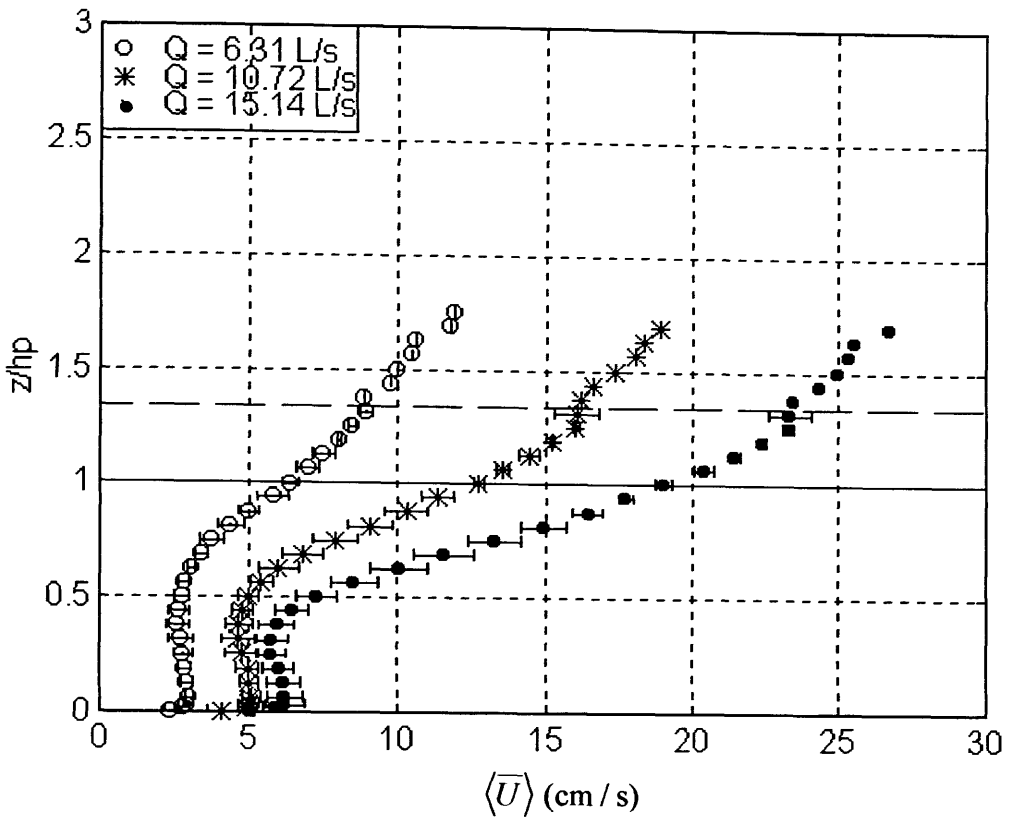

Figure 3.7a. Dimensional mean streamwise velocity profile for the *Case B* experimental runs The flow discharge Q is used to distinguish among the different velocity cases. The horizontal bars at each height and lines at z/h_p = 1.00 and 1.34 are as described in **Figure 3.6**.

Inflection in Shear Profile and Mixing Layer Analogy

The streamwise velocity profile is characterized by an inflection point at the top of the canopy (z/h_p = 1.00). The location of the inflection point, z_i, can be obtained from two mathematical definitions of an inflection point, either the location of the maximum of the mean velocity gradient profile or from the elevation at which the second derivative of the mean velocity profile is equal to zero:

$$z_i = \begin{cases} d\langle\overline{U}\rangle/dz\big|_{\max} \\ \left(d^2\langle\overline{U}\rangle/dz^2\right) = 0 \end{cases} \quad \textbf{(3.38)}$$

The velocity gradient for each profile was calculated by central differencing at the interior points and by backwards and forwards differencing at the bottom and top points, respectively. The second criteria was applied to determine the level of the inflection point by using a linear interpolation between the points near zero in the second derivative of the velocity profile. Results from applying this criteria for the *Case A* and *B* experimental runs led to the values shown in **Table 3.3**, which suggest that the inflection point in the velocity profile is slightly less than the undeflected canopy height (h_p = 16 cm). The mean location of

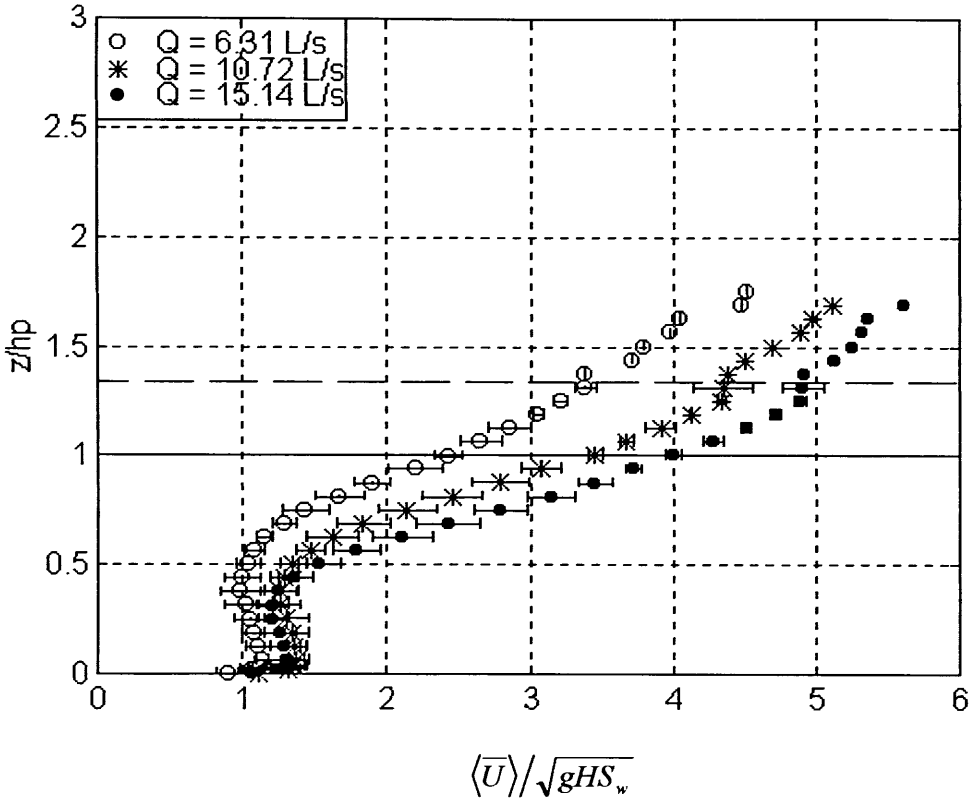

Figure 3.7b. Mean streamwise velocity profile for the *Case B* experimental runs nondimensionalized by the friction velocity, u_*. The flow discharge Q is used to distinguish among the different velocity cases. The horizontal bars at each height and lines at z/h_p = 1.00 and 1.34 are as described in **Figure 3.6**.

the inflection point for the *Case A* experimental runs is comparable for the different depths, averaging 0.87 ± 0.04 h_p. There is a marked decrease in the location of the inflection point for *Case B* due to the higher plant deflection which reduces the effective canopy height.

Quantification of the degree of shear in the velocity profile can be obtained by defining a shear length scale, L_s (Raupach *et al.*, 1996):

$$L_s = \frac{\langle \overline{U} \rangle (h)}{\left(d\langle \overline{U} \rangle / dz \right)(h)}, \tag{3.39}$$

where the mean velocity and the velocity gradient are evaluated at the effective canopy height, h_p for the undeflected and h_b for the deflected cases, respectively. The shear length scale is an indication of the strength of the shear in the velocity profile. It decrease for increasing levels of shear, since the velocity gradient in the denominator of **Eq. 3.39** becomes larger. Values for L_s in atmospheric canopies vary depending on the leaf area index and range between 0.12 to 0.85h_p. An accepted typical value, as quoted by Raupach *et al.* (1996), is that the shear length scale is one-half the canopy height, $L_s = 0.5h_p$. For the experimental runs in *Case A*, the shear length scale varies from 0.47 to 0.72h_p, well within the range of

values for other plant canopies. The shear length scale among the *Case B* experimental runs averages $0.63h_b$ and remains constant, indicative that the strength of the shear among the profiles is comparable. We expect that for the low characteristic depth cases, the value of L_s becomes large and as H/h increases an asymptotically decreasing behavior is observed for L_s. The shear length scale decreases significantly as the surface layer depth (h_o) is initially increased beyond emergent conditions and it asymptotes to a constant level after h_o exceeds one half of the canopy height (H/h_p = 1.50). This asymptotic behavior is also characteristic of other flow parameters and will be discussed in Chapter 4.

The significance of the shear length scale in the eddy structure within a plant canopy was described by Raupach *et al.* (1996) for atmospheric conditions. Eddies in the atmospheric boundary layer that are larger than the shear length scale act as inactive turbulence essentially because they are felt exclusively as horizontal motions at the level of the canopy and do not induce vertical exchange with the canopy. The eddies that have a length scale comparable to L_s, on the order of half the canopy height, constitute the active turbulent components, conducive to vertical transfer. These eddies are the result of the instabilities generated at the inflection point in the sheared velocity profile. The larger scale eddies act to make the active turbulence created at the canopy height intermittent. The turbulence created by eddies of length scales smaller than the shear length scale, is considered to be fine-scaled. It contributes little to vertical exchange and only plays a role in dissipating turbulent kinetic energy within the canopy.

In the context of a submerged plant canopy, the free surface constrains the boundary layer and the development of large eddies. The depth of the surface layer should play a key role in the determining the largest size of the eddies that can interact with the canopy and cause vertical exchange. In this sense, the shear length scale can not play such a pivotal role in determining the size of the active eddies as compared to the surface layer depth, h_o. A clear example of how the size of the active eddies should not be governed by the L_s, is seen in experimental run 2, where the surface layer depth is one half the shear length scale. There is no plausible explanation of why an eddy traveling in the surface layer would be twice the size of the layer.

A better understanding of the situation can be obtained by calculating the vorticity thickness which is the vertical length scale of the mixing region between two coflowing streams of different velocities. It is defined in an analogous way to the shear length scale as the ratio of a velocity scale to the gradient of the velocity at a specified location:

$$\delta_w = \frac{\Delta U}{\left(d\langle\overline{U}\rangle/dz\right)_{\max}}, \tag{3.40}$$

where $\Delta U = U_1 - U_2$ is the difference between the velocities in the surface and vegetation layers, respectively. The velocity in the vegetation region was calculated by averaging the mean streamwise velocity for the points less than $z/h_p = 0.5$, while the surface layer velocity was obtained by averaging the velocity for vertical points greater than z/h_p = 1.00. These definitions seem reasonable considering that

the flow is not precisely a mixing layer with two well developed regions of known approach velocities. **Eq. 3.40** has an analogous form to the shear length scale, L_s, since the location of the maximum velocity gradient coincides with the effective canopy height and the velocity difference is reasonably well approximated by U_h. The ratio of the vorticity thickness to the shear scale for atmospheric canopies was shown to be $\delta_w/L_s = 2$ by Raupach *et al.* (1996), based on two assumptions: (1) the inflection point of the mean velocity profile was located at $z = h$, and (2) $U_2 << U_h$, the velocity in the vegetation region much smaller than the interface velocity. The ratio of δ_w/L_s should be interpreted as a nondimensional number that indicates the relative size of a mixing layer as compared to the strength of the shear in the mixing layer. Large values of δ_w/L_s indicate that the mixing layer is broad and weak, while the values of the ratio smaller than unity imply that the mixing region is thin and strong. This experimental study provides a unique opportunity to describe the variation of this ratio with the surface layer depth above the canopy, h_o.

Using the values of the shear scale, the vorticity thickness and the surface layer depth from **Table 3.3** for all the experimental runs except the emergent case, the parameter δ_w/L_s was found to increase linearly with h_o/h, where h is the effective canopy height, as shown in **Figure 3.8**. The regression line to the data was found to be the following ($R^2 = 0.94$):

$$\frac{\delta_w}{L_s} = 0.532\left(\frac{h_o}{h}\right) + 0.409. \qquad \textbf{(3.41)}$$

The linear increase of the ratio δ_w/L_s with the normalized surface layer depth suggests that in the aquatic system the mixing region becomes progressively broader and weaker as the depth of the overlying water increases. The value for unbounded atmospheric canopies $\delta_w/L_s = 2$ agrees with the trend suggested in **Eq. 3.41** and is reached when the depth of the surface layer is 3 times the effective canopy height or at a characteristic depth $H/h \approx 4.00$.

Returning to the earlier discussion about the relationship between the shear scale and the turbulent eddy structure, the ratio δ_w/L_s shows that the use of L_s as the length scale that characterizes eddies as inactive, active or fine-scaled is only appropriate for unbounded flows that have large values of δ_w/L_s. For confined flows, the surface layer constrains the eddy size to a maximum vertical scale h_o, so that the shear scale is no longer the relevant scale. As the depth of the surface layer increases, the importance of L_s as a defining scale increases. The size of the active eddies that are critical to vertical transfer is determined by two different length scales, the surface layer depth and the shear length scale, the importance of which depends primarily on the size of h_o. In confined flows with low values of h_o, the maximum eddy size (h_o) is small enough so that the turbulence actively affects the vertical transfer of momentum. A transition to higher values of h_o implies that inactive turbulent motions arise and the active component is scaled by the degree of shear in the mixing layer formed at the interface between the canopy and the overlying water.

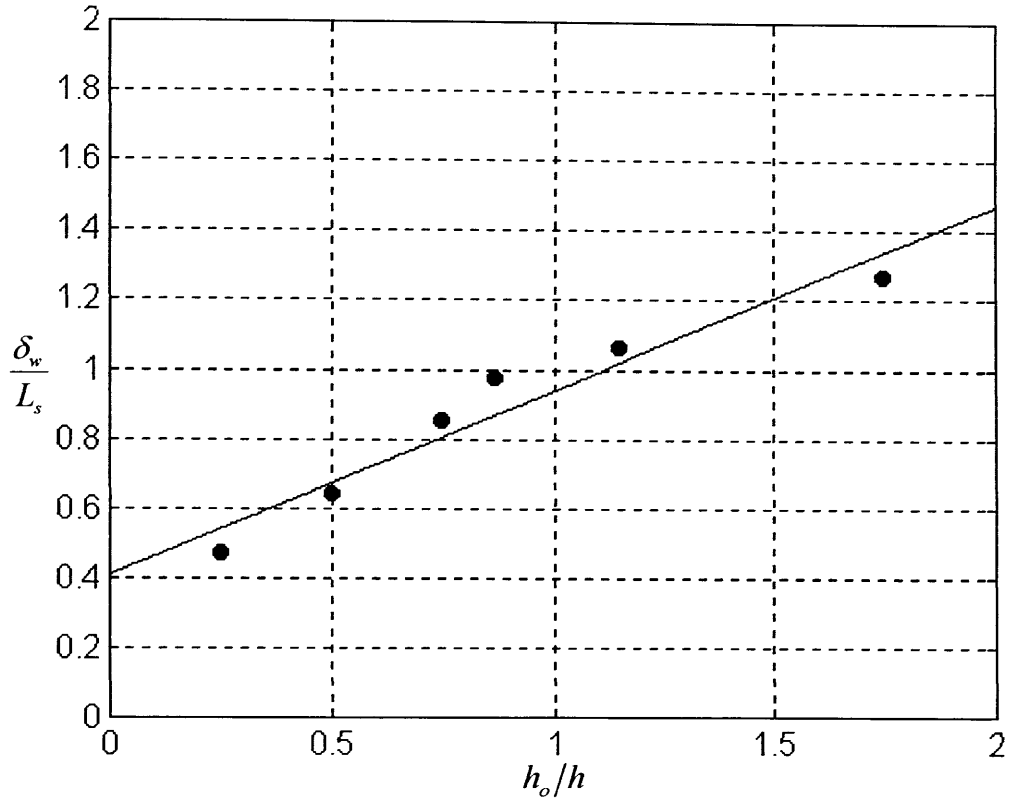

Figure 3.8. The variation of the ratio δ_w/L_s with the normalized surface layer depth for the experimental runs in *Cases A* and *B*. The value of δ_w/L_s in unbounded flows is reached at a surface layer depth of $h_o/h = 3.00$.

Exponential Profile

Three decades of work in atmospheric plant canopies have led to numerous attempts to model the velocity profile within and above the vegetation. Among the oldest and most widely used expressions is the exponential wind profile (Cionco, 1965). The mean velocity profile in the upper canopy region ($0.6 \leq z/h_p \leq 1$) can be described well by an exponential curve of the form:

$$\frac{\langle \overline{U} \rangle(z)}{U_h} = \exp\left(-\nu_e\left(1-\frac{z}{h}\right)\right), \qquad \textbf{(3.42)}$$

where ν_e is an extinction coefficient. Raupach and Thom (1981) summarize how the exponential velocity profile is derived from the assumptions of local transport within the canopy and a constant mixing length parameterization for the momentum diffusivity. Additional assumptions must be made to derive **Eq. 3.42**, including a constant canopy density and drag coefficient. The numerous assumptions imbedded in the exponential profile of **Eq. 3.42** render it nothing more than a simple single-parameter empirical fit. Applying **Eq. 3.42** to the mean streamwise velocity profiles of **Figures 3.6** and **3.7** showed quite clearly

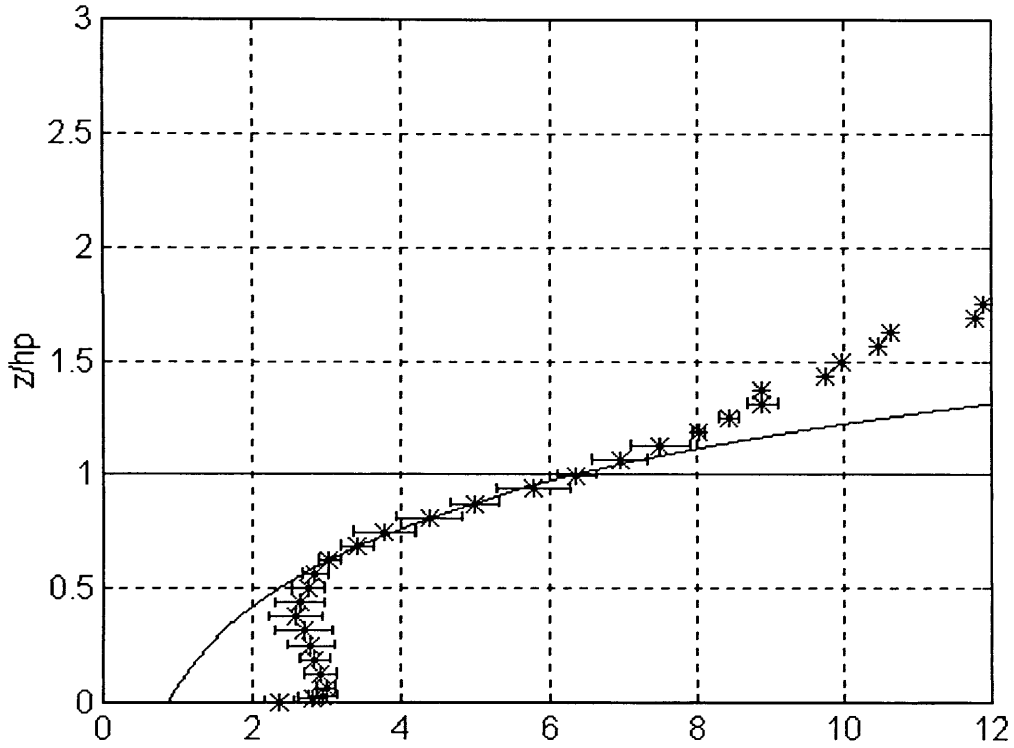

Figure 3.9. Exponential profile fit to the mean streamwise velocity profile of experimental run 4 (H/h_p = 1.75, Q = 6.31 L/s), represented by the solid line. The best-fit profile was obtained from the extinction coefficient $\nu_e = 2$. The region of validity of the exponential profile is limited to the upper canopy ($0.6 \leq z/h_p \leq 1$). Close to the bed and in the surface layer, the assumptions upon which the exponential profile are based are not valid.

that the exponential profile is only valid over a restricted vertical distance. An example of the exponential fit to the velocity profile of experimental run 4 is shown in **Figure 3.9**. The exponential profile cannot cope with the constant velocity region within the lower canopy nor the surface layer velocity profile. Nevertheless, the value of the extinction coefficient can give some insight into how much the velocity is attenuated within the upper canopy, a region where the plants are rapidly absorbing flow momentum. The extinction coefficient was obtained by finding the best fit exponential profile to the mean streamwise velocity profiles in the upper canopy region. **Table 3.3** shows the extinction coefficient for the all experimental cases. For the experimental runs in *Cases A* and *B*, the extinction coefficient averages $\nu_e = 1.97$. This value is well within the range for numerous canopies $\nu_e \approx 1$–4, as summarized by Kaimal and Finnigan (1993). *Case A* experimental runs appear to have an asymptotically increasing behavior, while the experimental runs in *Case B* have a decreasing value of the extinction coefficient with increasing velocity.

Secondary Maximum

The mean velocity profiles contain a region of near constant non-zero flow within the canopy that exhibit a local maximum. Below the level of $z/h_p = 0.5$, the mean streamwise velocity increases slightly with depth into the canopy and a small bulge is observed at a depth of $z/h_p \approx 0.1$ for the experimental runs in *Cases A* and *B*. This near-bed bulge has been observed in other field and laboratory plant canopy flow measurements (Shi *et al.*, 1995, 1996; Ackerman and Okubo, 1993; Shaw, 1977, among others). Several explanations have been laid forth to account for the unexpected velocity bulge, including instrumentation error, terrain slope effects, the influence of gaps in the canopy overstorey, vertical inhomogeneity in the canopy density profile and blow-through from the leading edge of the canopy (Raupach and Thom, 1981; Shaw, 1977). To date, a consensus has not been reached regarding the formation of the velocity bulge for atmospheric canopies. For aquatic canopies, however, it will be shown that secondary maximum effect is due to the vertical inhomogeneity in the canopy density and the effect of blow-through.

For these experiments, experimental errors and the bed slope effect can safely be ruled out as possible culprits. The relatively large spacing between plants, $l_s = 5.50$ cm, could potentially lead to the existence of gaps in the canopy that allow surface layer eddies to transport momentum efficiently to the lower canopy region. Once in this region of low density, the higher momentum fluid would speed up and the velocity bulge would be observed. Although plausible, this does not seem to be the reason for the secondary maxima in this system. Estimates of the momentum penetration depth suggest that the surface layer momentum does not reach the lower canopy region at the level of the velocity bulge. The vertical inhomogeneity in the canopy density profile, as presented in **Figure 3.1**, should, however, play a role in the formation of the secondary maxima since the stems are substantially less dense than the transition or blade regions.

The most plausible explanation for the velocity bulge in the near bed region has been alluded to in Section 3.1.1, where the balance of forces within the lower canopy region led to the definition of the characteristic velocity u_s in **Eq. 3.2.7**. The three components of the longitudinal force balance are the vertical gradient of the Reynolds stress, the longitudinal gradient of the pressure force and the total streamwise drag force exerted by the plant canopy. At the level of the velocity bulge in the near bed region (z_b), the gradient of the Reynolds stress is negligible compared to the other two terms, so that the drag force exerted by the canopy is balanced exactly by the water surface slope. Because the characteristic velocity at z_b is non-zero, then the water surface slope must be forcing flow through the canopy in the lower region. If the characteristic velocity is matched, then the surface slope estimates should be comparable, as demonstrated later in Section 3.4. Therefore, the flow in the lower region is a result of blow-through, *i.e.* a layer of fluid that enters the canopy at the leading edge and is advected in the longitudinal direction as a result of the pressure gradient in the flume. The interaction of the blow-through layer with a low density stem region bounded by a flat surface at the bottom and a region of

higher density at the top makes the velocity profile within the layer appear with a secondary maximum, a flow situation very similar to plane Poiseuille flow.

The implications of the blow-through observed in the model seagrass meadow can be significant for understanding and modeling the transport between a meadow and the surrounding fluid masses. It suggests that the meadow environment has two potential sources for material and scalar exchange, the overlying surface layer and the underlying blow-through layer. The momentum exchange between the vegetation layer and the surface layer will be shown to affect the upper canopy region ($z/h_p > 0.25$), but have relatively little impact on the lower canopy. The blow-through effect may be responsible for transport within the lowest portion of the meadow, a region of active nutrient uptake and plant growth, by exchanging material across the meadow edges. In meadows of reduced size, the percentage of the area affected by horizontal material exchange could potentially be significant.

The laboratory experiments suggest that blow-through is possible if the appropriate forcing is present in the system, yet it does not guarantee that the flow exists under the more complicated field conditions. Field studies would need to be conducted to determine if flow from the meadow edges is advected at a location near the bottom substrate and whether or not it is a significant source of water renewal as compared to the exchange occurring across at the canopy height. In general, however, an aquatic system with a surface slope will be pressure driven and the blow-through should be a feature of the velocity profile.

3.3.2 Turbulent Velocity Profiles

From a statistical point of view, the second moment of a random variable describes the deviation of a distribution from its mean, usually expressed as either the variance or the standard deviation. In turbulence measurements, the temporal deviation from the mean is known as the turbulent velocity, often represented as the root-mean-square (*rms*) amplitude or standard deviation (σ). Following the notation established in Section 3.1.1, the mean velocity will be represented by $\langle \overline{U_i} \rangle$ and the *rms* velocities by $\langle \overline{u_i} \rangle$. For convenience, the turbulent velocity can also be represented by any of the following:

$$u_{rms} = \sqrt{\overline{u^2}} = \sigma_u = u' . \tag{3.43}$$

The velocity records obtained from the acoustic Doppler and laser Doppler velocimeters were analyzed to determine the turbulent velocities by calculating the sample standard deviation of each velocity time series. For example, the sample standard deviation for the longitudinal component is:

$$\sigma_u = \sqrt{\frac{\sum \overline{U}^2 - (\sum \overline{U})^2 / N_o}{N_o - 1}} , \tag{3.44}$$

where N_o is the number of samples in the velocity record. The turbulent velocities are frequently nondimensionalized by the mean streamwise velocity to form the turbulence intensity. This parameter is

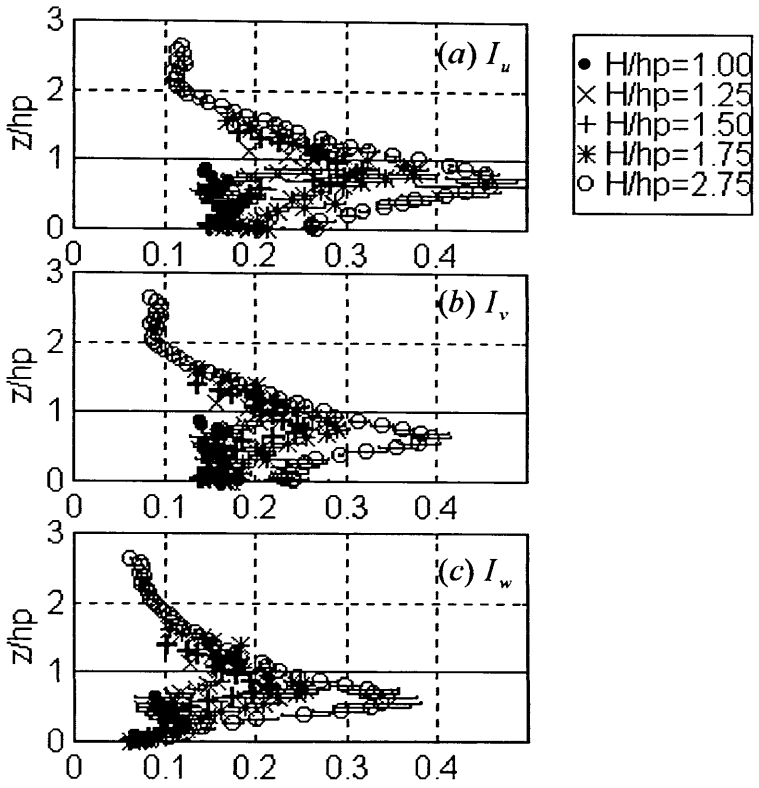

Figure 3.10. Turbulence intensity profiles for the *Case A* experimental runs: (a) the longitudinal, (b) the lateral and (c) the vertical turbulence intensities. The peak location and the turbulence strength varies significantly with the characteristic depth (H/h_p). Comparing the three profiles shows that the intensity decreases in the order I_u, I_v and I_w.

the simplest indicator of the turbulence strength and allows an easy comparison of the turbulent velocity to the magnitude of the mean flow. The turbulence intensity for the three velocity components are:

$$I_u = \frac{\left\langle \sqrt{\overline{u^2}} \right\rangle}{\langle \overline{U} \rangle};\ I_v = \frac{\left\langle \sqrt{\overline{v^2}} \right\rangle}{\langle \overline{U} \rangle} \text{ and } I_w = \frac{\left\langle \sqrt{\overline{w^2}} \right\rangle}{\langle \overline{U} \rangle}. \qquad \textbf{(3.45)}$$

The turbulence intensity profiles from the *Cases A* and *B* experimental runs are shown in **Figures 3.10** and **3.11**, where it is apparent that the turbulence intensity within the canopy is greater than in the surface layer. In general, the turbulence intensities for the vertical and lateral components are smaller than the streamwise intensity and the progression suggested by Shaw *et al.* (1974), $I_u > I_v > I_w$, from observations in a corn canopy, is observed for both cases. The turbulence anisotropy was further explored by calculating the ratios of the v_{rms} and w_{rms} to the u_{rms} velocities, as shown in **Figure 3.12** for the experimental runs in *Case A*. In the surface layer, the velocity ratios have constant values $v_{rms}/u_{rms} = 0.75$ and $w_{rms}/u_{rms} = 0.6$ for all the experimental cases, implying that in the surface layer the turbulence is anisotropic. As the depth into the canopy increases, the degree of isotropy increases linearly up to $0.5h_p$ to values in the range of 0.8–1.0. Closer to the bed, the v_{rms}/u_{rms} velocity ratio remains constant, while the

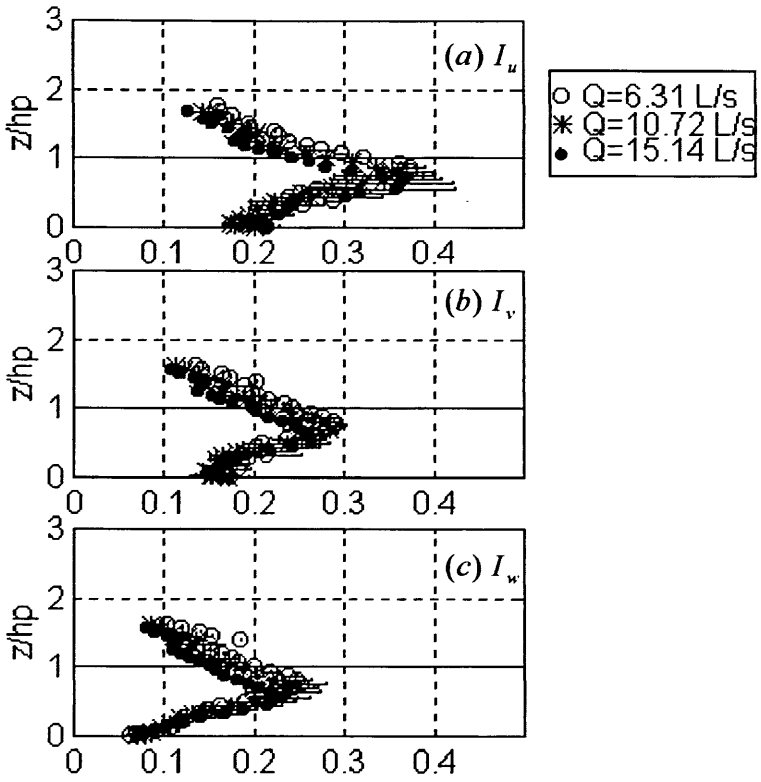

Figure 3.11. Turbulence intensity profiles for the *Case B* experimental runs: (a) the longitudinal, (b) the lateral, (c) the vertical turbulence intensity. The peak location and value decreases slightly with increasing flow discharge. Using the deflected canopy height, h_b, to nondimensionalize the vertical axis collapses the location of the turbulence intensity peaks.

w_{rms}/u_{rms} decreases because vertical fluctuations are more constrained by the bottom. An interesting trend is observed for v_{rms}/u_{rms}, it becomes closer to unity near the bed as H/h_p decreases, an indication of the transition from shear to wake turbulence that is typically horizontally homogenous.

The turbulence intensity profiles for *Cases A* and *B* demonstrate that a region within the canopy near $0.75h_p$ has a high degree of turbulence, with average peak values equal to $I_u = 0.30$, $I_v = 0.24$, $I_w = 0.21$ for all the experimental runs. These turbulence intensity levels are common in other plant canopy measurements as summarized by Cionco (1972) from observations of different types of vegetation. The streamwise intensity was found to be $I_u \approx 0.4$ for crop meadows, $I_u \approx 0.6$ for temperate forests and $I_u \approx 0.7$–1.2 for tropical forests. In addition, the turbulence intensity profiles of uniform canopies have been found to be uniform in height if waving is not present (Cionco, 1972). Finnigan and Mulhearn (1978) and Finnigan (1979a), however, showed that plant waving in laboratory and field canopies can lead to profiles that have a similar shape to the profiles from *Cases A* and *B*, an increasing intensity as the canopy height is approached and peak near the canopy top, attributed to an increase in waving motion.

The location and the value of the peak turbulence intensities varies between the experimental cases due to the effect of the changing the water depth and the velocity. For *Case A*, it can be seen that

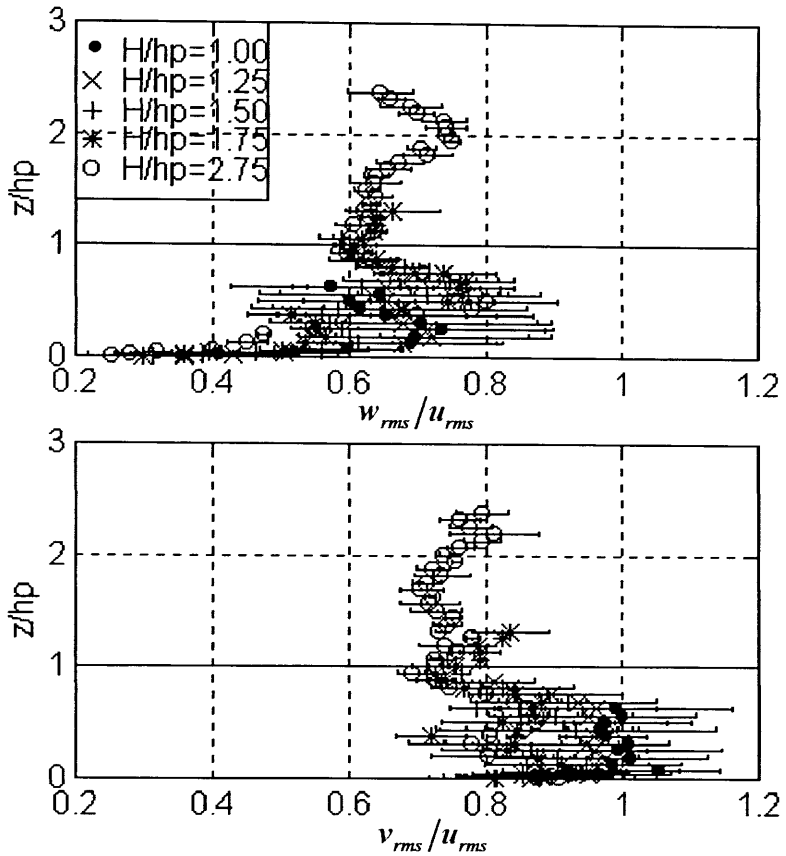

Figure 3.12. Turbulence anisotropy for the *Case A* experimental runs. The top figures shows the ratio of the vertical to the streamwise *rms* velocity, while the bottom figure is the ratio of the lateral to the streamwise *rms* velocity. Inside the canopy, the turbulence becomes more isotropic in the horizontal and less isotropic in the vertical direction. The effect of H/h_p on the isotropy is significant, with increasing isotropy with decreasing characteristic depth.

the peak location decreases as the characteristic depth increases, from z/h_p = 1.00 for H/h_p = 1.25, to z/h_p = 0.67 for H/h_p = 2.75. The decrease in the peak location with the depth indicates that the turbulence strength penetrates the canopy to a greater extent for larger surface layer depths. In addition, it reflects the slight increase in the plant motion observed as the depth of the overlying layer was increased. Plant waving is a response to higher interfacial velocities, as shown in **Figure 3.4**. The peak value variation with the characteristic depth exhibits an asymptotic behavior, increasing sharply for the lower depths and reaching a constant value of 0.45 for the larger values of H/h_p. Similarly for *Case B*, the location of the peak in the turbulence intensity decreases slightly with increasing flow discharge, from $0.79h_p$ to $0.69h_p$ for I_u due to plant bending. The value of the turbulence intensity at the peak location decreases with flow discharge. In dimensional terms, however, the *rms* velocities are larger for the higher flow discharge case throughout the profile. In summary, the turbulence intensity profiles from *Cases A* and *B* indicate that a level at approximately $0.75h_p$ is the most intense turbulent region in the flow domain. This result will be corroborated by the other velocity statistics, the skewness and the kurtoses, in this region.

The decrease in the peak location is an artifact of the normalization by the mean streamwise velocity. The profiles of the *rms* velocities peak precisely at the canopy top, z/h_p = 1.00. and remain constant in the above canopy region to about 1.25–1.50h_p. This region of constant turbulent velocity is commonly found in the profiles for atmospheric plant canopies, with typical velocities values equal to u_{rms}/u_* = 1.5–2.0 and w_{rms}/u_* = 1.1. This friction velocity, u_*, is based on the Reynolds stress in the constant stress layer above the canopy, a feature that is not present in this system, as discussed later on in Section 3.3.3. For comparisons sake, the value of the Reynolds stress at the canopy top can be used as an estimate of the friction velocity,

$$u_* = \sqrt{\left|\overline{uw}(z = h_p)\right|}. \tag{3.46}$$

Using this estimate for the friction velocity produces average values of u_{rms}/u_* = 1.77 and w_{rms}/u_* = 1.09 at and above the canopy height which are within the same range as those obtained in atmospheric plant canopies. This estimate for u_* will be discussed along with other possibilities in Section 3.4.3.

A final note concerning the high turbulence intensities in the flow through plant canopies should be addressed. The high intensities have spurred a great deal of controversy concerning the applicability of Taylor's frozen turbulence hypothesis for these flows. This hypothesis assumes that turbulent eddies remain intact as they pass a fixed point in space and allows the conversion of velocity data from temporal to spatial domain. For turbulence intensities on the order of unity, however, the frozen turbulence hypothesis is generally not valid (*e.g.* Kaimal and Finnigan, p. 102). However, these authors point out that the application of Taylor's hypothesis can still be used because the eddy convection velocity at the level of the canopy height is higher than the local mean velocity. Two-point correlation analysis have shown that the eddies typically travel at approximately twice the interface velocity, $U_{eddy} \approx 2U_h$ (Shaw *et al.*, 1995). This would imply that in the region of maximum turbulence intensity, the non-local velocity U_{eddy} would lead to smaller turbulence intensity levels. For example, the peak turbulence intensity for H/h_p = 2.75 would be reduced from 0.45 to 0.19 under this assumption. Similarly, in Section 3.2.3, it was pointed out that the convection velocity estimate from the monami wavelength and the vibration frequency was ~U_h so that the normalizing velocity scale for the turbulence intensity in the region where Taylor's hypothesis might be invalid (0.75h_p) is much larger than the local mean velocity, thus leading to smaller values for the intensities.

The inability to measure the eddy convection velocity from single point velocity measurements has resulted in the use of Taylor's hypothesis with the local velocity by many researchers (Brunet *et al.*, 1994; Raupach *et al.*, 1991, among others), with the recognition that the turbulence intensities might exceed the validity of the hypothesis. With appropriate caution, Taylor's hypothesis will be used to estimate the turbulence length scales and the wave number in Sections 3.7 and 3.8.

3.3.3 Reynolds Stress Profiles

The temporal averaging performed on the governing equations results in the formation of terms that are products of the turbulent velocity components, as discussed in Section 3.1.1, whose relative contribution to the total stress is more important than the molecular or dispersive stresses. These turbulent covariance terms form the Reynolds stress tensor. The diagonal terms in the tensor are turbulent velocities described in the Section 3.3.2, while the off diagonal terms are the covariances between the three velocity components. In this flow situation, the covariance of u and w is the most significant term since it represents the vertical transport of streamwise momentum. The Reynolds stress $\overline{uw}$ was obtained from the velocity records by computing the sample covariance as:

$$\overline{uw} = \frac{\sum \overline{UW}}{N_o - 1} - \frac{\sum \overline{U} \sum \overline{W}}{N_o (N_o - 1)}, \tag{3.47}$$

and subsequently averaging over the lateral profiles to obtain the stress profiles shown in **Figures 3.13** and **3.14** for *Cases A* and *B*. The Reynolds stress profiles are nondimensionalized by the square of the friction velocity defined in **Eq. 3.37**:

$$\frac{\langle \overline{uw} \rangle}{u_*^2} = \frac{\langle \overline{uw} \rangle}{gHS_w}. \tag{3.48}$$

Eq. 3.48 and the associated figures show the ratio of the turbulent stress to the stress needed to balance the forcing in the system provided by the surface slope. In this way, the Reynolds stress profiles quantify how the total stress in the system is partitioned at the different vertical locations. If the measured Reynolds stress accounted for all the forcing, the stress profile in the surface layer would follow the theoretical distribution:

$$\tau(z) = \rho g H S \left(1 - \frac{z}{H}\right). \tag{3.49}$$

Extrapolating the Reynolds stress profile linearly to the bottom boundary would give a value of unity, since the bed shear stress should balance the forcing in the system, gHS_w. **Figures 3.13** and **3.14** show that an extrapolation to $z/h_p = 0$ of the stress profile in the surface layer produces values that are less than unity for all the experimental cases. The extrapolation to the bottom would result in estimates of the friction velocity that are slightly smaller than the value obtained from **Eq 3.49**, as will be discussed in Section 3.4.3. Small deviations from the theoretical distribution are seen for every experimental case, as exemplified in **Figure 3.15** for experimental run number 7. The discrepancy between the theoretical model and the measured profile are due to the effects of the other terms in the Reynolds stress tensor ($\overline{uv}$ and $\overline{vw}$) that have been neglected in the Reynolds stress profile of $\overline{uw}$ and the action of the secondary currents within the flume (Nagakawa and Nezu, 1993; Dunn *et al.*, 1996). Profiles of the other Reynolds

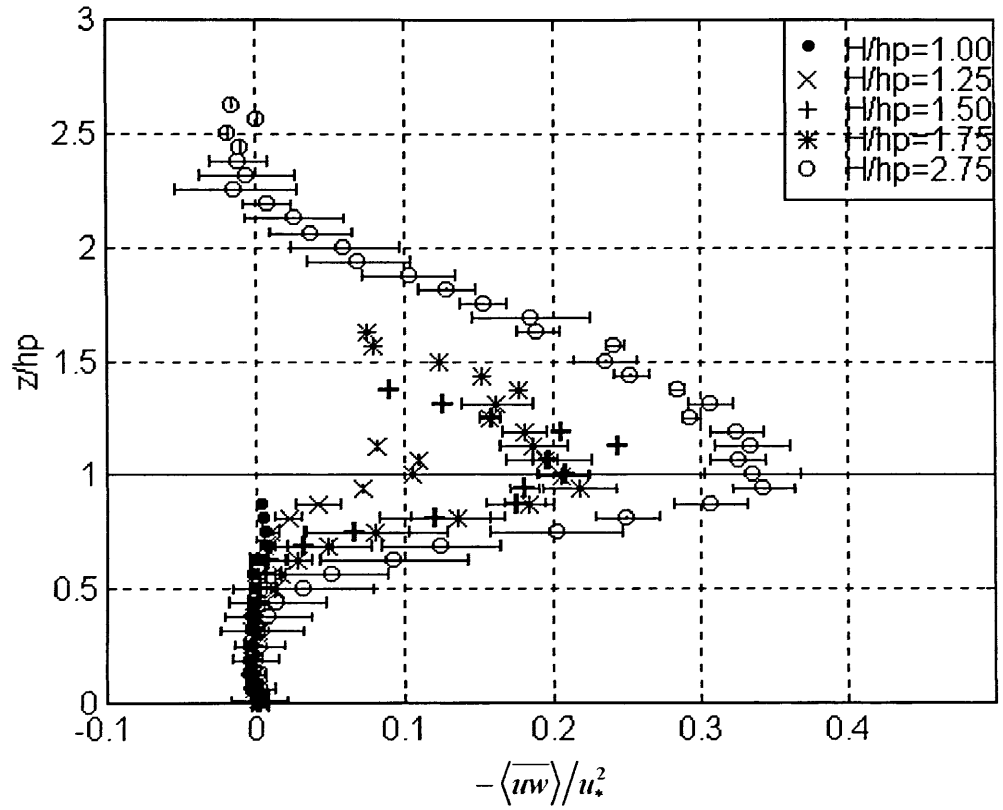

Figure 3.13. Reynolds stress profiles for the *Case A* experimental runs. Nondimensionalization by the square of the friction velocity shows that the measured stress is a larger portion of the total forcing as the characteristic depth is increased. Also, notice the rapid attenuation of the Reynolds stress in the canopy and the region of negligible stress near the bottom.

stress components showed that these were negligible as compared to the profile of uw and support the use of the latter as a good estimator of the Reynolds stress tensor.

An alternative to using the total forcing gHS_w to nondimensionalize the Reynolds stress profile is to divide the stress profile by the maximum value (uw_{max}) occurring at the effective canopy height, h. This nondimensionalization is successful at collapsing the profiles due to the simple geometric shape of the profile, characterized by a peak at the canopy height and a decrease away from the interface of the surface and the vegetation regions. This procedure, however, was not applicable to the lowest characteristic depth, $H/h_p = 1.00$, since the vertical velocity at the canopy height was unavailable from the laser Doppler velocimeter. In addition, the physical insight provided by the use of the friction velocity of **Eq. 3.37** made this nondimensionalization more appropriate.

As is customary, the negative of the Reynolds stress is plotted in **Figures 3.13** and **3.14** versus the nondimensional distance from the bottom (z/h_p). The peak in the Reynolds stress profiles coincides quite well with the undeflected canopy height for *Case A*, while the peak value occurs slightly below $z/h_p = 1.00$ for the experimental runs of *Case B*, as seen in the highest flow discharge case. If the vertical

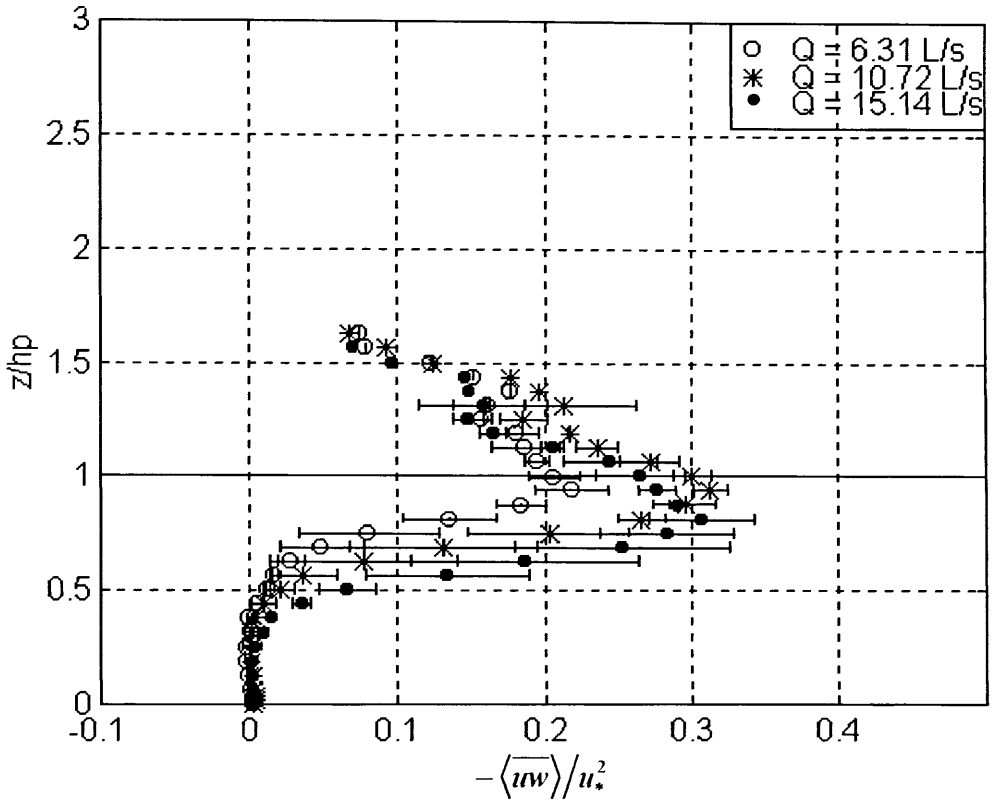

Figure 3.14. Reynolds stress profiles for the *Case B* experimental runs. Increases in the flow discharge lead to larger penetration depths and a larger stress. The effective canopy height, determined from the plant motion experiments, coincides with the peak in the Reynolds stress profiles.

axis is nondimensionalized by the deflected canopy height, h_b, as measured from the plant motion experiments and shown in **Table 3.2**, the peak Reynolds stress for the *Case B* profiles lies at $z/h_b = 1.00$. This collapse demonstrates that an accurate means of measuring the effective canopy height is by locating the peak in the Reynolds stress profile. The correlation between the peak in the Reynolds stress profiles and the deflected canopy height was also observed by Dunn *et al.* (1996), Murota *et al.* (1984) and Tsujimoto *et al.* (1996) for water flow through flexible vegetation.

The Reynolds stress profiles for *Case A* exhibit difference that are attributed to the increase in depth of the surface layer. It has been shown that as h_o increases from the emergent to submerged conditions, the shear at the canopy interface decreases asymptotically to a value of $L_s = 0.68h_p$ after $H/h_p = 1.50$. The Reynolds stress profiles for *Case A* now clarify how the horizontal shear stress between the two layers is distributed over depth. For emergent vegetation, the uniform velocity profile shown in **Figure 3.6** leads to negligible shear stresses, while the velocity gradients for submerged vegetation creates significant shear stresses reflected in the peak at the canopy height. As H/h_p increases, relatively more stress is present at the canopy top and more is transported farther into the lower canopy region. The penetration depth, defined as the distance from the canopy top to the point of zero Reynolds stress, is

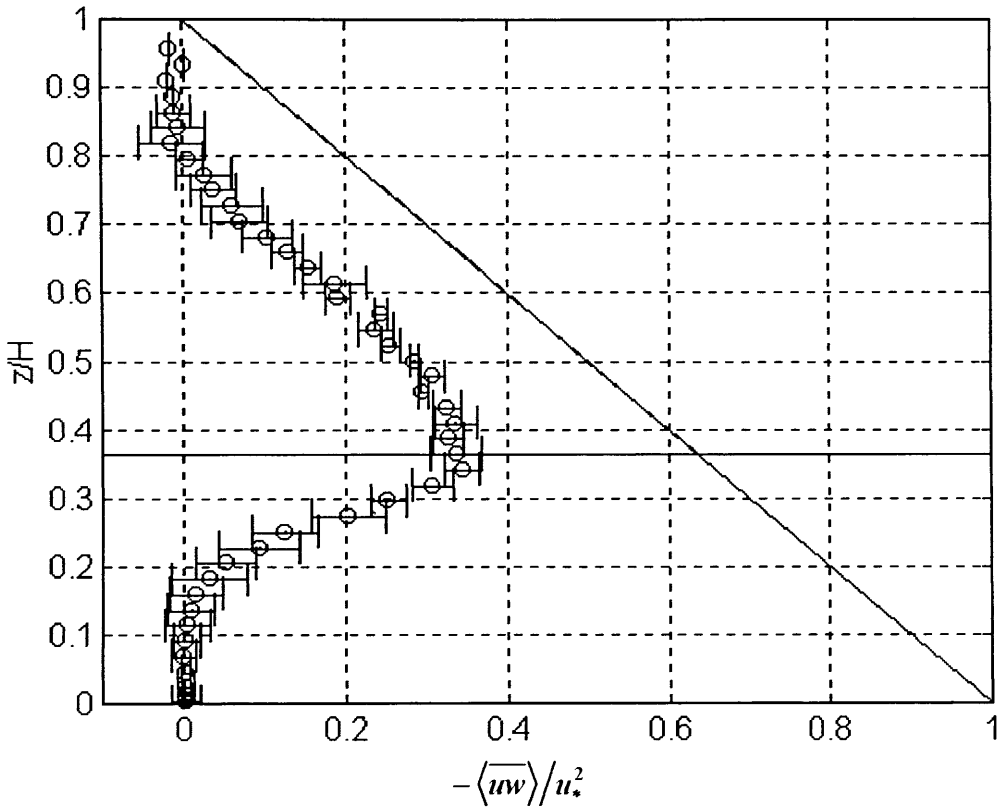

Figure 3.15. Comparison of theoretical total shear stress, represented by the solid line, with the measurements of the Reynolds stress (uw) for the experimental run number 7 (H/h_p = 2.75 and Q = 15.14 L/s). The vertical axis has been nondimensionalized by the total water depth, H, as suggested by the theoretical profile in **Eq. 3.49**. The horizontal solid line represents the canopy height.

found to increase as the characteristic depth increases. A detailed quantification of the penetration of momentum into the canopy from various estimates will be presented in Chapter 4.

The peak value of the nondimensional Reynolds stress varies with the characteristic depth (H/h) for all the experimental cases. In fact, a plot of uw/u_*^2 versus the characteristic depth reveals that an asymptotic variation is observed as the depth of the surface layer is increased. From a value of $uw/u_*^2 = 0.11$ for $H/h = 1.25$ to a value of $uw/u_*^2 = 0.34$ for $H/h = 2.75$, the profile of uw/u_*^2 versus H/h increases sharply as the surface layer initially increases and then levels off for the larger characteristic depths. Although the ratio of the Reynolds stress to the friction velocity could not be formed for the lowest characteristic depth, the expected value for uw at $H/h = 1.00$ is small compared to the friction velocity, so that it should follow the trend exhibited by the other runs. This type of asymptotic behavior has been observed for other turbulence parameters and it reinforces the notion that a critical surface layer depth exists above which there is little change in the value of the parameter.

Other salient features of the Reynolds stress profiles in *Cases A* and *B* are the rapid attenuation of the stress into the canopy and the region of negligible Reynolds stress below approximately $0.5h_p$. The Reynolds stress attenuates faster than the turbulent velocities into the canopy, as will be quantified by calculating the correlation coefficient of the Reynolds stress in Section 3.3.7. The rapid attenuation implies that the top region of the plants are absorbing a great deal of the flow kinetic energy, storing it as strain potential energy and releasing it during plant motion. Alternatively, the mean kinetic energy can be transformed to wake turbulence and dissipated to heat via the effect of viscosity. The canopy acts as an efficient momentum sink with about two thirds of the momentum carried into the canopy being absorbed in the top one quarter of the canopy, an observation seen in other atmospheric plant canopies (Brunet *et al.*, 1994). As mentioned previously, the Reynolds stress does not penetrate into the lower canopy regions. Here, the lack of a Reynolds stress gradient has important implications for the balance of forces in the longitudinal direction, as mentioned in Section 3.1.1 and discussed in detail in regards to the secondary maxima observed in the mean streamwise velocity. The secondary maximum in the velocity profile even leads to small positive stress values, an indication that momentum is transferred upwards in a countergradient direction.

Above the canopy, the Reynolds stress profiles exhibit quite different behavior in an open channel flow confined by a water surface as compared to the unconfined conditions of atmospheric plant canopies. Theoretically, the shear stress in a open channel reaches zero at the free surface if there is no applied shear stress (*i.e.* wind), contrary to the atmospheric boundary layer that has an expansive region of constant stress. **Figures 3.13** and **3.14** show this pattern quite clearly. Linearly extrapolating the stress profile in the surface layer leads to zero-intercepts that are at or near the water surface ($z/h_p = H/h_p$). Only the characteristic depth $H/h_p = 2.75$ shows a significant deviation from this predicted result, probably due to the existence of a near uniform velocity layer near the free surface. The constant stress layer in atmospheric flows makes the Reynolds stress at the canopy height a natural choice for defining the friction velocity, while the choice of a friction velocity for an aquatic system is slightly more complicated, as discussed further in Section 3.4.

3.3.4 Skewness Profiles

The third moment of a random variable nondimensionalized by the root-mean-square is known as the skewness coefficient and can be used to describe the asymmetry of a probability density function. Two types of coefficients of skewness are of interest from the longitudinal and vertical velocity records, the pure skewness and the mixed skewness. The pure skewness coefficients measure the asymmetry of the distribution of u or w, independent of each other, and are defined by:

$$Sk_{uuu} = \frac{\overline{u^3}}{\left(\sqrt{\overline{u^2}}\right)^3} \text{ and } Sk_{www} = \frac{\overline{w^3}}{\left(\sqrt{\overline{w^2}}\right)^3}, \tag{3.50}$$

while the mixed skewness coefficients indicate the asymmetry of the joint probability density of the distribution of the vertical and longitudinal velocities:

$$Sk_{uuw} = \frac{\overline{u^2 w}}{\left(\sqrt{\overline{u^2}}\right)^2 \sqrt{\overline{w^2}}} \text{ and } Sk_{uww} = \frac{\overline{uw^2}}{\sqrt{\overline{u^2}}\left(\sqrt{\overline{w^2}}\right)^2}. \tag{3.51}$$

The value of the skewness coefficient calculated from the velocity records should be compared to that obtained from a Gaussian distribution, $Sk_u = Sk_w = 0$. Positive values for the coefficients of skewness imply that the distribution has a longer tail to the right of the distribution mean, so that larger than average velocities are common, while negative values imply the opposite trend, a longer tail region to the left of the mean (Benjamin and Cornell, 1970). Since the deviations from the mean velocity are associated with turbulence, positive values of the pure skewness coefficients imply $u' > 0$ and $w' > 0$, while negative coefficients imply $u' < 0$ and $w' < 0$. Positive or negative values of the mixed coefficients of skewness indicate which direction is favored in the momentum transport. For example, a negative Sk_{uuw} implies that the vertical transport of streamwise momentum is mostly downwards.

The four skewness profiles for the experimental runs in *Cases A* and *B* are shown in **Figures 3.16** and **3.17**. The skewness of longitudinal and vertical velocities (Sk_{uuu} and Sk_{www}) in both cases demonstrate quite clearly that within the canopy region positive values of u' and negative values of w' are predominant. The skewness profiles all intersect zero at a height of $1.2h_p$, where a reversal in the trend occurs, negative u' and positive w' values are dominant. Above the reversal point, the pair ($u' < 0$ and $w' > 0$) transports longitudinal momentum upwards and vertical momentum in the negative x direction. The mixed skewness profiles suggest that the turbulent velocity pair ($u' > 0$ and $w' < 0$) transports vertical momentum in the positive longitudinal direction ($Sk_{uww} > 0$) and longitudinal momentum downwards ($Sk_{uuw} < 0$) into the canopy. These results are confirmed by the quadrant analysis technique described in Section 3.6, which identify the velocity pairs as downward moving sweeps and upward moving ejections that transfer momentum between the surface layer and the canopy region.

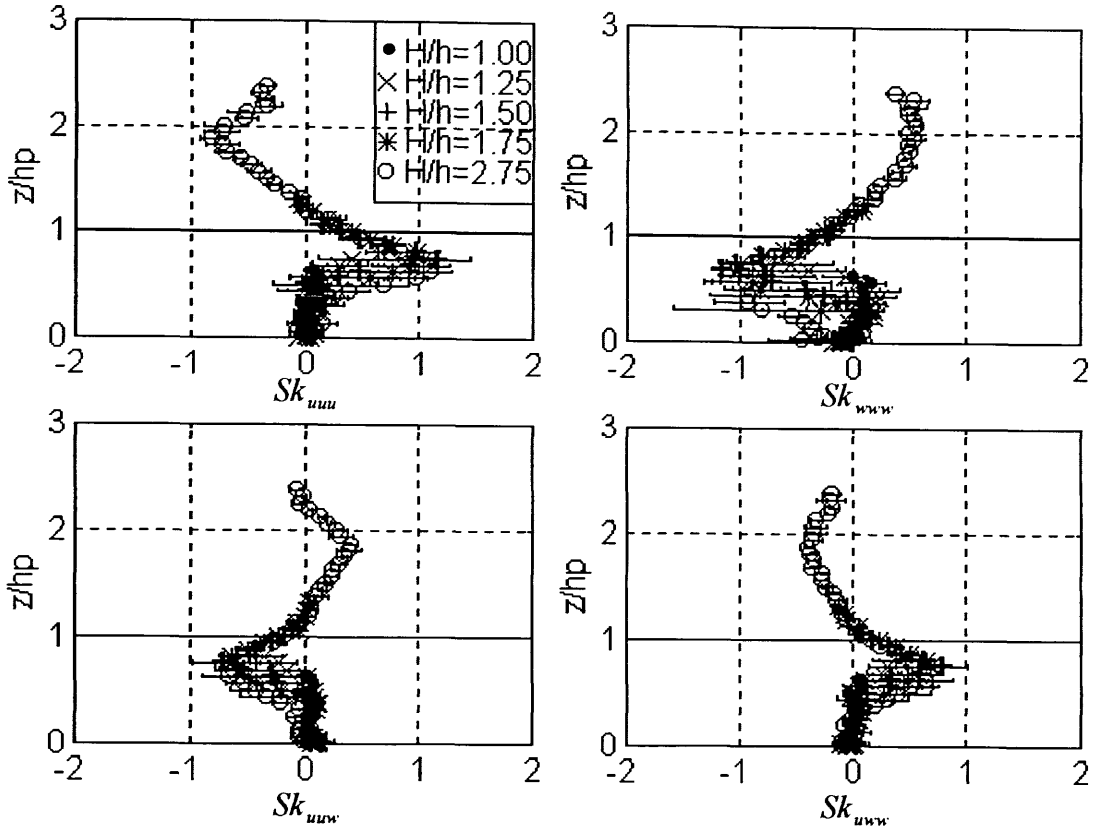

Figure 3.16. Skewness profiles for the *Case A* experimental runs. The pure skewness are shown in the top two plots and the lower two plots show the mixed skewness. The peak values coincide in location for the four skewness profiles and the skewness pairs are mirror images of each other.

The depth variation effect in the *Case A* experimental runs is most evident in the lower part of the peak region extending from z/h_p = 0.5–1.2, where the departure from the Gaussian value becomes more pronounced as the characteristic depth increases. Above the canopy, near the interface and close to the bed, the skewness profiles all collapse onto a single curve demonstrating that the depth of the surface layer has no effect on the skewness coefficients in these regions. The peak in the skewness profiles occurs at a height of $0.75h_p$, with minor variations between the depth cases. The peak value, though, exhibits the asymptotic behavior observed for other parameters, a steady increase from the value at H/h_p = 1.00 (Sk_{uuu} = 0.12; Sk_{www} = –0.14) to 1.50 (Sk_{uuu} = 1.16; Sk_{www} = –1.16) and a constant region thereafter (Sk_{uuu} = 1.11; Sk_{www} = –0.95 for H/h_p = 2.75).

One of the effects of increasing the discharge in the *Case B* experimental runs is to shift the skewness profiles downwards, the peak location decreasing in height from $0.75h_p$ to $0.5h_p$. Using the deflected canopy height, h_b, as the vertical length scale results in a collapse of the profile peaks to a single location suggesting that the behavior is similar amongst the cases despite the decrease in effective canopy height. The other effect is to increase the deviation from the standard value of a Gaussian distribution as the velocity is increased.

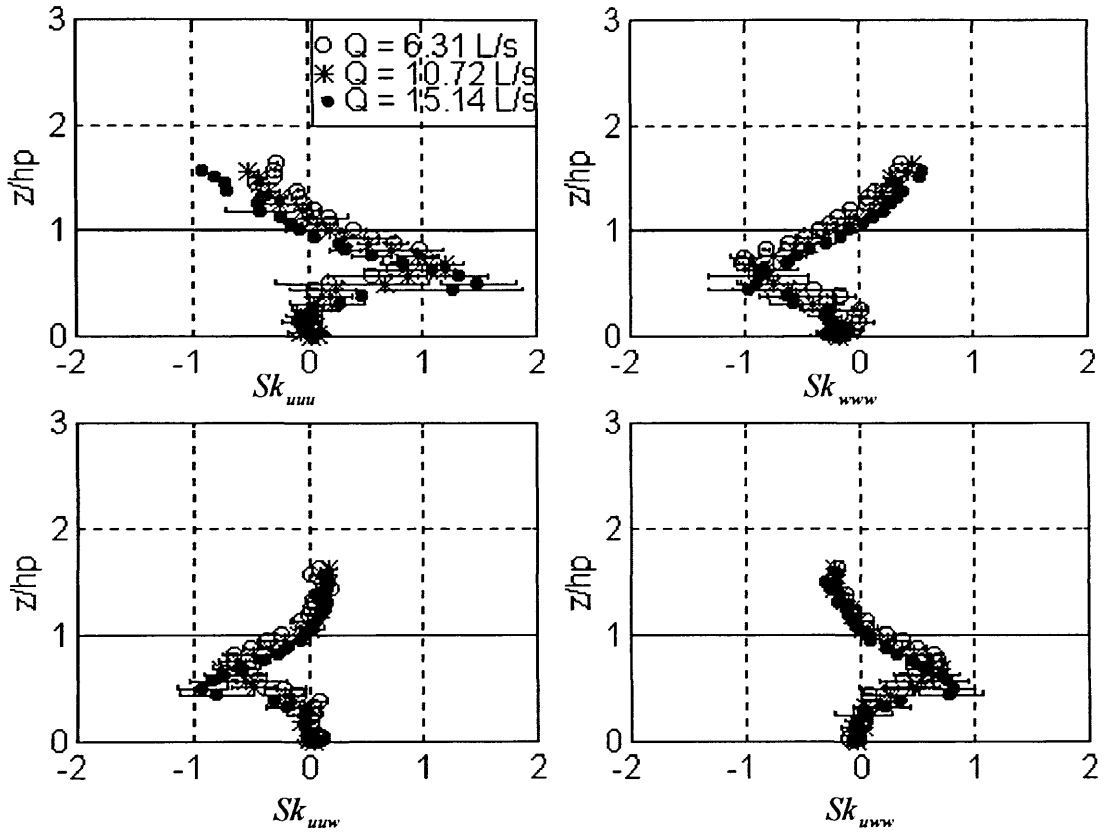

Figure 3.17. Skewness profiles for the *Case B* experimental runs. The increase flow discharge and the resulting decrease in effective canopy height leads to a downwards shift in the skewness profiles. An increase in the peak values are observed with increasing velocity for all the profiles except the pure skewness of w. The horizontal line represents the canopy height, $z/h_p = 1.00$.

Comparison to the published skewness profiles from turbulence studies in atmospheric canopies demonstrate that the peak values obtained in the seagrass meadow are of the same magnitude, if not slightly higher, than typical ranges, $Sk_{uuu} = 0.5$ to 1.0 and $Sk_{www} = -0.5$ to -1.0 (Raupach *et al.*, 1996). Far from the canopy ($z/h_p > 2$), atmospheric skewness profiles approach zero, the value for the atmospheric surface layer. Similarly, in this study, the largest characteristic depth, $H/h_p = 2.75$, approaches zero far from the vegetation layer. The behavior within the seagrass meadow, however, varies substantially from the atmospheric profiles. Some atmospheric profiles have a constant skewness inside the canopy, while others have skewnesses that increase steadily, reaching a maximum value near the bottom boundary (Raupach *et al.*, 1991; Brunet *et al.*, 1994). Both trends indicate that eddies penetrate farther into the canopy for atmospheric flows than for the model seagrass canopy, where the marked peak in the skewness profiles is observed within the meadow at level $0.75h_p$. The peak skewness corresponds to the penetration depths of the momentum-carrying motions, the downward sweeps, and indicates that within the canopy there is a high degree of asymmetry. This is corroborated by the kurtoses profiles at the same height that show that the large values of velocity are intermittent as well.

3.3.5 Kurtoses Profiles

The fourth moment of the distribution of a random variable is used less commonly as a descriptive parameter, yet it gives important insight about the turbulence structure. The kurtoses coefficient or flatness factor is defined as the fourth moment normalized by the fourth power of the root-mean-square or turbulent velocity. For the velocity components of most interest in this system, the streamwise and vertical velocities, the coefficients of kurtoses are:

$$K_u = \frac{\overline{u^4}}{\left(\sqrt{\overline{u^2}}\right)^4} \text{ and } K_w = \frac{\overline{w^4}}{\left(\sqrt{\overline{w^2}}\right)^4}. \qquad (3.52)$$

The usefulness of the kurtoses coefficient lies in a comparison of the measured value to that obtained for a Gaussian distribution, $K_u = K_w = 3$. Values for the kurtoses larger than three imply that the distribution is flatter than the Gaussian distribution at the mean, thus the term flatness factor (Benjamin and Cornell, 1970). Coefficients less than three imply that the distribution is more peaked near the mean.

The kurtoses coefficient is an indication of the level of intermittency of the longitudinal and vertical velocities (Brunet *et al.*, 1994). Larger kurtoses coefficients and flatter distributions indicate that there is a larger contribution from extreme velocity values. Intermittency refers to large temporal separations between events in a velocity record; a highly intermittent record (large kurtoses) consists of extreme events that occur infrequently, while a record with small kurtoses has smaller events that occur frequently and thus are not intermittent. Since the kurtoses coefficient is very sensitive to extreme values, the velocity records from each experimental run were inspected for spurious errors and corrected when deemed necessary due to unreasonably high kurtoses coefficients ($K_{u,w} > 20$).

The profiles of the kurtoses coefficient for the longitudinal and vertical velocities are shown in **Figures 3.18** and **3.19**. With the exception of the region near the bed and the interface of the vegetation and surface layers, rarely is the Gaussian value approached over the flow depth for the experimental runs in *Cases A* and *B*. The prominent peak in the kurtoses profile in the region within the canopy ($0.5 < z/h_p < 0.8$) indicates that infrequent, large values of the velocities are present at this level. The average peak value for the longitudinal and vertical kurtoses are $K_u = 5.58$ and $K_w = 5.43$ for all the experimental runs. The variation of the peak kurtoses value with the depth of the surface layer (*Case A*) exhibits the asymptotic behavior that has characterized other turbulence structure variables, the peak value increasing from $H/h_p = 1.00$ to 1.50 and leveling off for higher characteristic depths. The peak value also exhibits an increasing trend with higher flow discharges (*Case B*) since higher in-canopy velocities and larger degrees of plant motion lead to greater intermittency in the velocity record, *i.e.* the increased possibility of having extreme values that do not occur frequently.

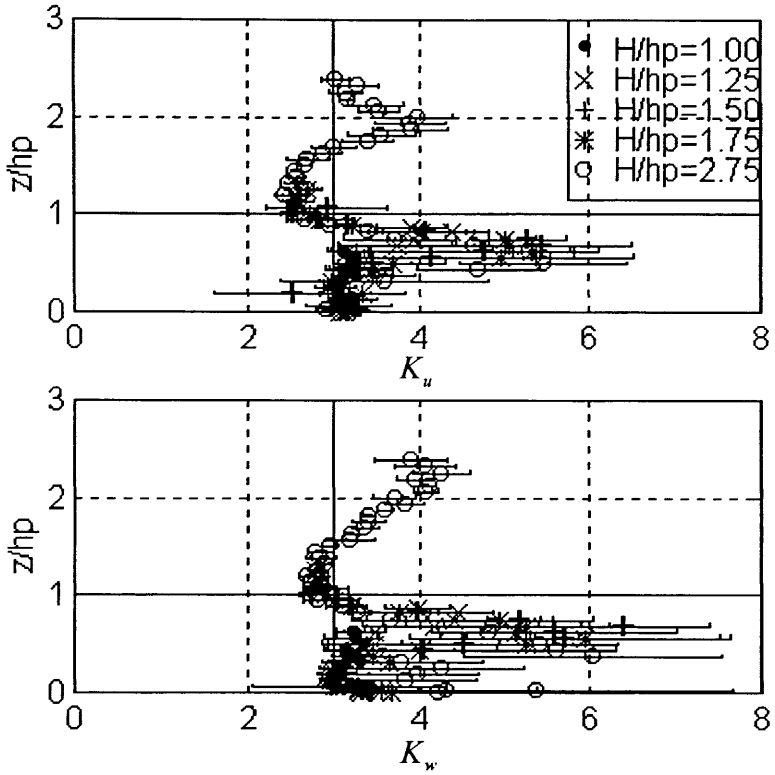

Figure 3.18. Kurtoses profiles for the *Case A* experimental runs. The precise peak value location varies between the experimental runs within the region near $0.75h_p$. The large horizontal variations in the K in the peak region, have been observed in other experiments (Brunet *et al.*, 1994). The solid vertical line represents the Gaussian value for the kurtoses, $K = 3$.

Few studies on the turbulence structure of atmospheric canopies present the kurtoses coefficient profiles. In a model wheat meadow, Brunet *et al.* (1994) showed kurtoses profiles that increased with depth into the canopy, reaching peak values of $K_u = 6$ and $K_w = 9$ at the closest measurement point to the bottom boundary. Similarly, Amiro (1990) presents the kurtoses profiles for three boreal forests, of which the pine forest had profiles that increased into the canopy. The higher kurtoses near the bottom were attributed to a sparse canopy that allowed large eddies to penetrate into the canopy further than smaller eddies. The spruce forest profile, on the other hand, peaked at a level $z/h_p = 0.7$, comparable to the results obtained in this study. Amiro (1990) suggests that the dense canopy structure of the spruce forest was responsible for trapping larger eddies at a specific depth and only allowing certain velocity components to penetrate into the canopy. A similar argument can be applied to the present cases. The level of the peak kurtoses profile is a region that should play an active role in momentum transfer between the vegetation and surface layers by trapping the eddies that penetrate into the canopy. The level of the peak kurtoses marks the bottom of the vegetation layer that has active exchange with the surface layer. Below the level of the kurtoses peak, less turbulence exchange should be expected. These results are supported by evidence of the momentum transport obtained through the quadrant analysis presented in Section 3.6.

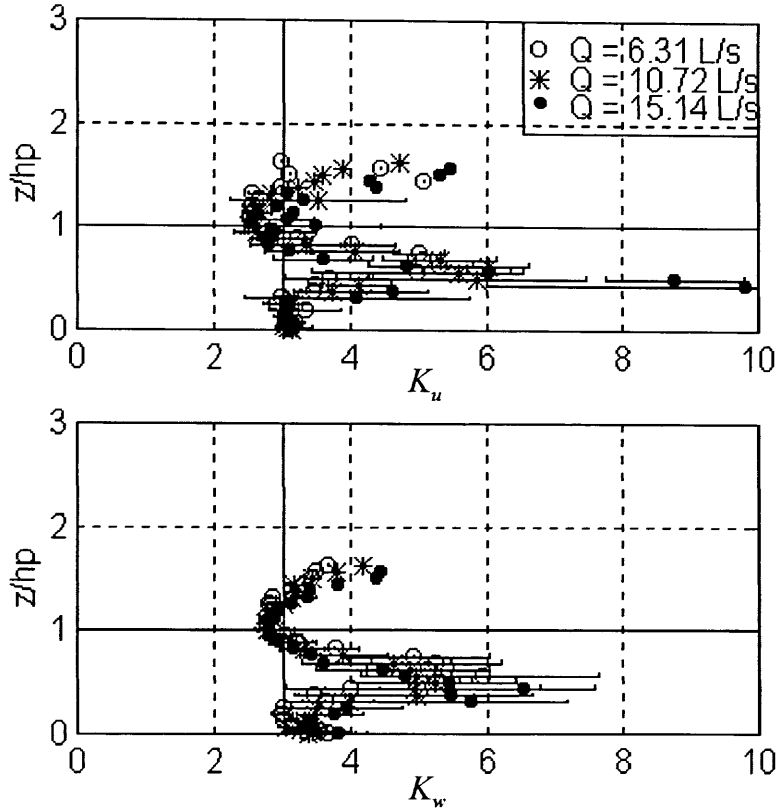

Figure 3.19. Kurtoses profiles for the *Case B* experimental runs. Increases in the flow discharge lead to higher kurtoses values at the peak location and in the region close to the free surface. The large horizontal bars are indicative of the horizontal heterogeneity for this parameter. The solid vertical line represents the Gaussian value for the kurtoses, $K = 3$.

As compared to atmospheric canopy flows, the kurtoses coefficient profile also exhibits different behavior far from the canopy. Near the free surface, the kurtoses of u and w for the experimental runs in *Cases A* and *B* increases beyond the standard value, while the profiles observed by Brunet *et al.* (1994) tend asymptotically to the Gaussian value. Thus, the free surface exerts control over the intermittency that is not present in unbounded canopy flows due to the restrictions in eddy scale imposed by the boundary.

The intermittency described via the kurtoses profile can be compared to other measures of the intermittency, specifically the use of a variable threshold parameter in the analysis of the conditional average Reynolds stress, as presented in Section 3.6. As the threshold parameter is increased, the degree of intermittency of the shear stress can be quantified. The peak in the kurtoses shown in **Figures 3.18** and **3.19** at the level $z/h_p = 0.75$ corresponds well to the level of greatest intermittency obtained from the conditional sampling analysis. In summary, the kurtoses coefficient near the free surface and in the upper canopy region has demonstrated that the vertical and longitudinal velocity distributions depart from the Gaussian behavior and consists of extreme events that occur infrequently that are strongly associated with the penetration height of momentum-carrying downward motions.

3.3.6 Turbulent Kinetic Energy Profiles

The total level of turbulence can be quantified by computing the turbulent kinetic energy of the flow at all scales, which is simply the sum of the contributions to turbulence from the three turbulent velocities described in Section 3.3.2. The turbulent kinetic energy is defined as:

$$TKE = \left\langle \frac{\overline{q^2}}{2} \right\rangle = \frac{1}{2}\left(\overline{u^2} + \overline{v^2} + \overline{w^2}\right). \tag{3.53}$$

Profiles of the turbulent kinetic energy for the experimental runs in *Cases A* and *B* are shown in **Figures 3.20** and **3.21**, respectively. Obtaining the turbulent kinetic energy from the data gathered using the two-dimensional laser Doppler velocimeter required the employment of an empirical relationship to estimate the turbulent velocity of the lateral component. Legg *et al.* (1984) proposed that the lateral *rms* velocity could be estimated from the standard deviations of the two other orthogonal components as:

$$\sqrt{\overline{v^2}} = \sqrt{\left(\sqrt{\overline{u^2}}\right)\left(\sqrt{\overline{w^2}}\right)}. \tag{3.54}$$

This relationship was obtained from turbulence measurements in and above a rigid cylinder canopy with a hot-wire anemometer. Application to this flow condition was tested by comparing the estimated value from **Eq. 3.54** to the measurements from the acoustic Doppler velocimeter. It was found that the empirical relationship adequately represented the lateral turbulent velocity over most of the velocity profile, especially in the shear layer near the canopy interface. Near the bed, however, the error between the two values increased due to the restricted vertical fluctuations. A similar behavior is expected for the estimation of the lateral turbulent velocity from the measurements of u and w using the laser Doppler velocimeter. Since these measurements were restricted to the surface layer, the discrepancy near the bottom can be neglected and the turbulent kinetic energy can be obtained for these points.

The turbulent kinetic energy in **Figures 3.20a** and **3.21a** has been nondimensionalized by the friction velocity, u_*^2, as defined in **Eq. 3.37**, the square root of the product gHS_w. This normalization is successful in collapsing the data in the stem region ($z/h_p < 0.25$), where the turbulence production is mostly from the plant wakes. In the shear zone, however, the friction velocities obtained from the water depth and the surface slope are not the correct velocity scale to collapse the turbulent kinetic energy profiles onto a single curve, as seen by the increase in the peak *TKE* with the characteristic depth. Only the pairs of experimental runs 3, 4 and 5, 6 are successfully collapsed over the entire profiles. For this reason, an alternative velocity scale that is capable of accounting for the increased shear at the canopy top should be sought. One possibility is to utilize the friction velocity defined in **Eq. 3.46**, the square root of the magnitude of the shear stress at the canopy interface. Since the most important source of turbulence in this flow is the shear at the interface of the surface and vegetation layers, then the degree of shear at the canopy height should be an appropriate normalization parameter.

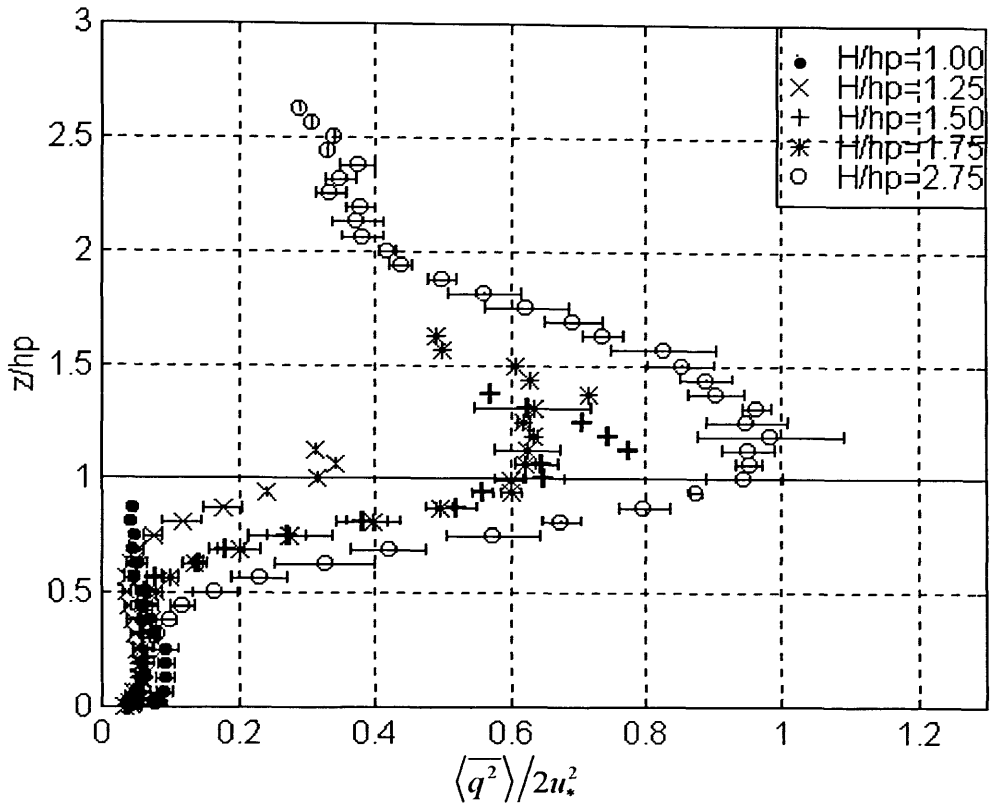

Figure 3.20a. Turbulent kinetic energy profiles for the *Case A* experimental runs, nondimensionalized by the square of the friction velocity (u_*^2) based on the water depth and the water surface slope. The peak in the turbulent kinetic energy profile occurs slightly above the location of the canopy height (z/h_p = 1.00) represented by the horizontal line.

The Reynolds stress at the canopy height $<uw>$ ($z = h_p$) collapses the data well for the experimental runs 2–7, as shown in **Figures 3.20b** and **3.21b**, over most of the profile, but more importantly at the location of maximum turbulent kinetic energy, the canopy height. Using u_* based on the interfacial shear stress, however, has the disadvantage of not being applicable to the emergent case (H/h_p = 1.00) due to the lack of the measurement at the canopy height. Within the stem region, the noticeable difference in the shape of the *TKE* profile for the case H/h_p = 1.25, suggests that the friction velocity derived from the shear stress may not be the appropriate normalization parameter for this region.

The use of two friction velocity estimates for the stem and shear region suggest that two different scales exist in this flow situation. One scale is the set by the shear stress in the surface layer and is felt at the canopy height, while the other scale is set by the forcing in the system and is felt at the bottom boundary. The first scale can be described by the friction velocity at the interface of the surface and vegetation layers, while the second scale is parameterized by the total forcing, gHS_w. Thus, two different friction velocities coexist in the flow at two different levels. The friction velocity estimates and their implications will be discussed in detail in Section 3.4.3.

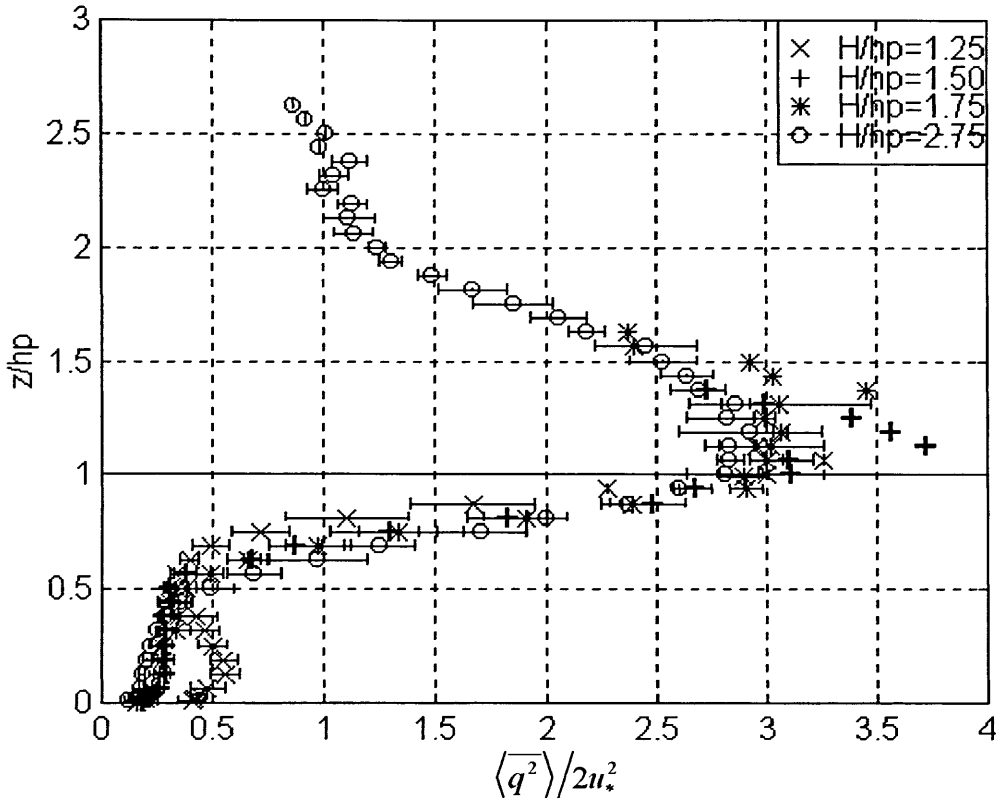

Figure 3.20b. Turbulent kinetic energy profiles for the *Case A* experimental runs, nondimensionalized by the square of the friction velocity (u_*^2) based on the shear at the canopy height. The peak in the turbulent kinetic energy profile occurs slightly above the location of the canopy height (z/h_p = 1.00) represented by the horizontal line.

Using the two normalization schemes, the effect of depth-variation and velocity-variation on the turbulent kinetic energy can be analyzed. For *Case A*, the normalization by the total forcing shows a clear progression in the level of turbulence as the H/h_p increases from the emergent to the fully submerged conditions. The increase in the degree of shear as H/h_p increases leads to larger turbulence levels throughout the canopy and higher turbulence penetration into the lower regions of the vegetation layer. The pronounced peak in the turbulent kinetic energy profile is observed just above the canopy at an average height of $1.14h_p$ for the experimental runs of *Case A*. Normalizing the *TKE* by the shear stress at the canopy height confirms that the variation in *TKE* amongst the depth cases is explained entirely by the increase in shear. The mean value of the nondimensional *TKE* at the location of the peak is 2.96 ± 0.13 for the experimental runs in *Case A*, showing the turbulent kinetic energy is almost three times stronger than the shear stress. Except for H/h_p = 1.25, the profiles in **Figure 3.20b** have similar values within the upper canopy, all within the horizontal uncertainties. This suggests that for $H/h_p \geq 1.50$, the turbulent kinetic energy distributions are similar and that the length scale $h_o \geq 0.5h_p$ is of critical importance in determining the turbulence structure in a submerged plant canopy.

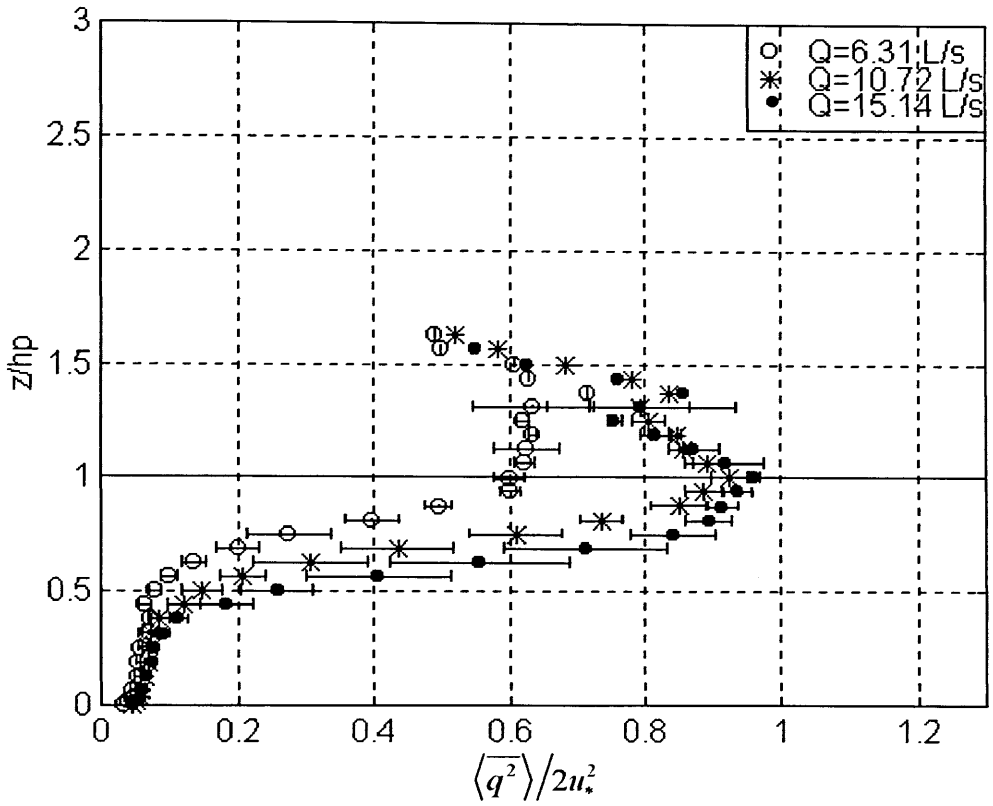

Figure 3.21a. Turbulent kinetic energy profiles for the *Case B* experimental runs. Nondimensionalization by the friction velocity collapses the data for Q = 10.72 and 15.14 L/s.

In absolute terms, the turbulent kinetic energy profiles for the velocity variation cases (*Case B*) increase dramatically with higher flow discharges. The peak location remains approximately equal (z/h_p = 1.00) for the three profiles, but it varies two fold in magnitude between each experimental run. In addition, the turbulent kinetic energy penetrates further into the canopy with increases in velocity. These results are expected based on the higher shear at the interface and the increased plant motion observed in the experimental runs. The normalization based on the shear stress at the canopy height collapses the peak *TKE* values, as shown in **Figure 3.21b**. The average value of the peak turbulent kinetic energy at z/h_p = 1.00 is 2.88 ± 0.05 and decreases rapidly into the canopy. The normalized *TKE* within the upper canopy ($0.5 \leq z/h_p \leq 1.0$) is significantly different as the flow discharge increases. This has been observed by Murota *et al.* (1984), who classified two waving conditions in their experimental study based on the inverse of the normalized *TKE*, a parameter referred to as the structure coefficient S_c. The variation of S_c among the cases was related to the slowly swaying and rapidly swaying plant motion regimes. The results from *Case B* render support to the identification of the plant motion regime with the variation of the ratio between the turbulent kinetic energy and the Reynolds stress. Large values indicate that larger degrees of plant motion and coherent waving are present, while smaller values in the upper canopy region are characteristic of slower plant swaying.

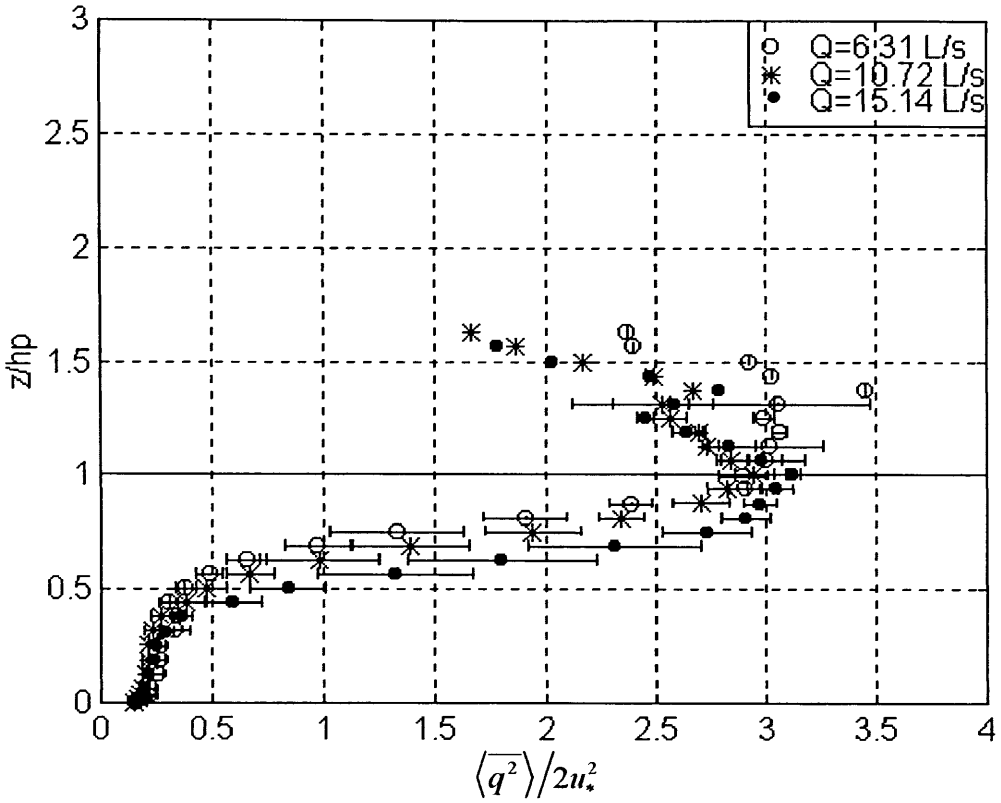

Figure 3.21b Turbulent kinetic energy profiles for the *Case B* experimental runs. Nondimensionalization by the friction velocity based on the Reynold stress at the canopy height collapses the data within the stem region and at the canopy height for the cases with different flow discharges.

The turbulent kinetic energy created in the shear layer between the vegetation and surface layers is attenuated in the canopy, an indication that the turbulent eddies are being absorbed by the plant elements. In addition, the non-zero value for the *TKE* within the lower canopy regions supports the idea that turbulence is present in the lower regions as result of the interaction of the mean flow with the plant elements, despite the fact that the shear generated turbulence does not reach these elevations. The turbulent kinetic energy profiles show the important transition between a wake generated and a shear generated turbulence as the water depth is increased. In **Figure 3.20a**, the uniform *TKE* profile for $H/h_p = 1.00$ is characteristic of turbulence that is generated exclusively from the interaction of the in-canopy velocity with the roughness, *i.e.* wake-generated turbulence. As the depth is increased and the shear layer is formed, the turbulence at the top of the canopy increases while identical conditions are maintained in the lower canopy regions, an indication that the scaling in this region is not related to the shear layer but rather to the total forcing in the system represented by friction velocity based on gHS_w. For the largest characteristic depth, the shear generated turbulence dominates the turbulent kinetic energy profile structure and it penetrates far into the canopy without reaching the zone of wake dominated turbulence.

3.37 Correlation Coefficient

A useful measure of the efficiency of turbulence at transporting momentum is obtained by calculating the correlation coefficient for the Reynolds stress or the covariance of the longitudinal and vertical velocities. The correlation coefficient of a pair of random variables (u,w) is a normalized version of the covariance, the ratio of the Reynolds stress to the standard deviation of the velocities represented by the root-mean-square values (Benjamin and Cornell, 1970):

$$r_{uw} = \frac{\langle \overline{uw} \rangle}{\sqrt{\overline{u^2}}\sqrt{\overline{w^2}}}. \qquad (3.55)$$

The value of the correlation coefficient is related to the shape of the joint probability distribution of the two random variables and can vary from −1 to 1. If the streamwise and vertical velocities are uncorrelated, the correlation coefficient is zero. Highly correlated velocities, either negatively or positively, have correlation coefficients near $r_{uw} = -1$ or 1, respectively.

The correlation coefficient indicates the efficiency of the turbulence in transferring momentum. For atmospheric vegetation canopies, the correlation coefficient peaks at the effective canopy height h_p at a level $r_{uw} = -0.45$ in a model wheat meadow (Brunet *et al.*, 1994) and $r_{uw} \approx -0.5$ over a range of field and laboratory canopies reviewed by Raupach *et al.* (1996). The correlation coefficient decreases rapidly within the upper portions of the canopy and reaches values close to zero at elevations $z/h_p = 0.25$. The shape of the r_{uw} profile indicates that the efficiency of turbulence in transporting momentum downwards decreases away from the interface. Inside the canopy, the turbulence loses its ability for net vertical exchange.

The correlation coefficient was calculated for the experimental runs of *Cases A* and *B*, as shown in **Figures 3.22** and **3.23**. Except for the lowest characteristic depth ($H/h_p = 1.00$), the *Case A* correlation coefficient profiles peak near the same level within the canopy, slightly below the undeflected canopy height ($z/h_p = 0.92$). The average peak value of r_{uw} for the depth variation cases is slightly higher in magnitude for the seagrass meadow, as compared to atmospheric plant canopies, $r_{uw} = -0.56$. Within the horizontal uncertainties, the correlation coefficient peak value is similar for the higher characteristic depths but distinctly lower for $H/h_p = 1.00$ and 1.25. This suggest that the surface layer depth is important in determining how efficient the turbulence in the shear zone is at transporting momentum downwards into the canopy. With increases in the flow discharge, the height of the peak correlation coefficient decreases from $z/h_p = 0.90$ to 0.81. Yet if the vertical axis is nondimensionalized by the deflected canopy height h_b, the peaks in the profiles collapse at the same level, $z/h_b \approx 0.9$. The value of the maximum correlation coefficient does not vary despite the changes in the flow discharge, $r_{uw} = -0.57$ for the three cases. Within the canopy, however, the increase in velocity leads to r_{uw} of higher magnitude (*i.e.* closer to −1), such that the efficiency in downward transport is increased.

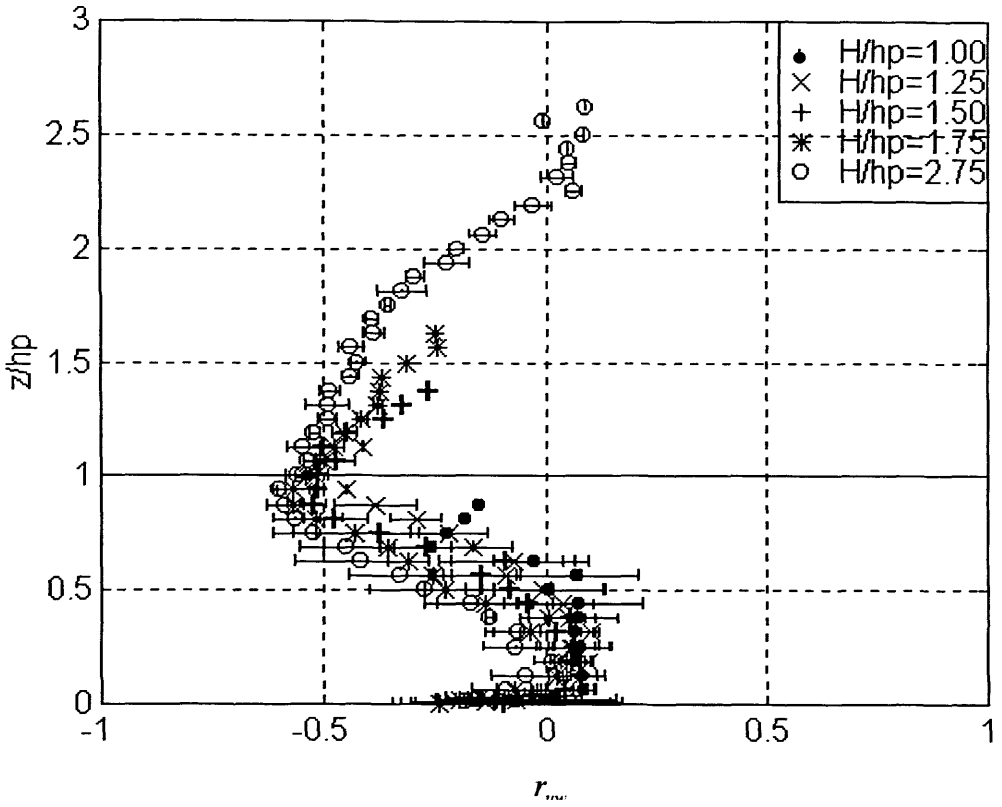

Figure 3.22. Correlation coefficient profiles for the *Case A* experimental runs. The peak correlation coefficient occurs below the undeflected canopy height and varies with the characteristic depth (H/h_p). Values of r_{uw} near zero for $z/h_p \approx 0.25$ are indicative that the turbulence in this region does not transfer momentum in the vertical direction.

The large, negative correlation coefficient indicate that the longitudinal and vertical velocity components are negatively correlated within and above the meadow. A positive u' velocity is more often associated with a negative w' velocity, and viceversa. This reinforces the view that the ($u' > 0$, $w' < 0$) and the ($u' < 0$, $w' > 0$) pairs are common within the system, especially at the level of the canopy height, as established from the skewness coefficient profiles in Section 3.3.4. Above the canopy, the magnitude of the correlation coefficient decreases towards zero for all the experimental cases, so that the dominance of the negatively-correlated velocity pairs decreases. This behavior is different from that observed in atmospheric canopy flows where the correlation coefficient asymptotically decreases to a constant value of $r_{uw} = -0.32$ in the region known as the inertial sublayer of the atmospheric surface layer (ASL), well above the canopy ($z/h_p > 2$) (Raupach *et al.*, 1996). The limitations on the boundary layer growth imposed by the reduced depth above the canopy for aquatic systems lead to this difference.

The shape of the correlation coefficient profiles is indicative of the depth of penetration of momentum from the overlying surface layer into the canopy. Values of r_{uw} that are higher in magnitude farther into the canopy imply that momentum is more efficiently transported to that elevation by turbulence. **Figures 3.22** and **3.23** show that as the characteristic depth (H/h_p) and the flow discharge (Q)

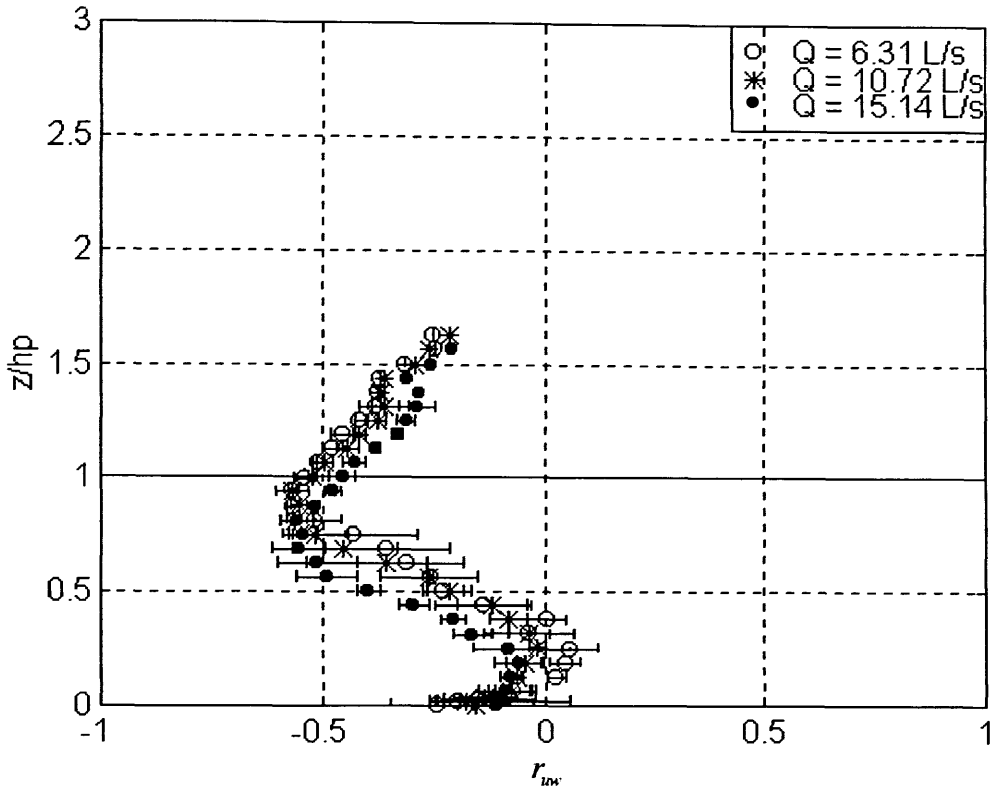

Figure 3.23. Correlation coefficient profiles for the *Case B* experimental runs. The elevation has been nondimensionalized by the undeflected canopy height h_p, highlighting the decrease in depth of the peak correlation coefficient with increasing velocity. Using the deflected canopy height, h_b, collapses the profiles onto a single curve.

are increased in the *Case A* and *B* experimental runs, the vertical exchange of momentum reaches lower portions of the canopy. This result will be corroborated by the estimation of the penetration depths from three different estimates in Chapter 4.

Two final notes on the correlation coefficient should be pointed out. Firstly, the horizontal variation of the correlation coefficient is larger in the in-canopy region ($0.25 < z/h_p < 0.75$) than in the flow above the canopy, in the shear region or near the bed. As an example, the horizontal deviation in this region is three times larger than in the rest of the profile for $H/h_p = 2.75$. The small deviations at the canopy height imply that the turbulence transport is horizontally homogeneous across this interface. Secondly, the near-bed region is characterized by an increase in the magnitude of the correlation coefficient, indicating that the momentum is being transported efficiently to the bottom by the turbulence generated at this shear layer.

3.4 Hydraulic Characterization

This section presents the results from the hydraulic characterization of the flow through the model seagrass canopy. Among the various hydraulic parameters of interest are the relevant velocity scales including the friction velocity, the surface slope, the nondimensional flow parameters such as the Reynolds and Froude number and the resistance coefficients exemplified by Manning's n. In addition, the logarithmic layer law applicable to the flow above the canopy is presented and used to estimate the roughness height and the friction velocity at the canopy height. An extensive discussion is made of the different methods available to estimate the friction velocity. The surface slope measurements are also compared to three different estimates made from the Reynolds stress profile and from a backwater curve model developed by Dunn *et al.* (1996). The estimation the hydraulic parameters are useful for comparing the hydrodynamic system to other rough turbulent boundary layers.

From a hydraulics perspective, vegetation is often considered to be a form of bottom roughness that can be treated as if it were any other type of rough surface, despite the complex three dimensional flow in the canopy space. This simple approach is very useful when attempting to design engineering structures such as earthened canals that must account for the increased resistance provided by the underlying vegetation that can grow within the channel. The interest is to know how the vegetation affects the flow in the surface layer above it, and not necessarily the detailed flow through the canopy. As such, the application of the logarithmic layer law to the surface layer flow is a primary tool for the hydraulic characterization of the flow. The roughness height, displacement height and friction velocity obtained from the logarithmic law describe the flow as if the bottom were elevated to a level near the canopy height, neglecting the flow within the canopy itself. Resistance formulas such as the Manning equation also assume that the vegetation can be treated as a rougher surface by increasing the value of a single parameter in order to balance the forcing in the system provided by a combination of the bed slope and the water surface slope. Knowledge of the forcing in the system is critical to characterizing the hydraulic behavior of a vegetated waterway and for this reason an emphasis has been placed in this experimental study for obtaining an independent measure of the water surface slope.

There is a wealth of empirical and semi-empirical information on the hydraulic behavior of vegetated open channels from studies performed over the past three decades by researchers in the fields of irrigation, hydraulics and wetland engineering. Reference to the results from other studies will be made on occasion to show that the hydraulic parameters obtained in this laboratory experiment of a model seagrass meadow are within the range of natural values. Considerable use will be made of the work by Kouwen and coworkers who have studied the flow through flexible laboratory vegetation canopies.

3.4.1 Logarithmic Layer Profiles

Different theoretical models have been used to describe the velocity profile through plant canopies. The exponential velocity profile, introduced in Section 3.3.1, is capable of reproducing the velocity profile in the upper canopy region ($0.6 < z/h_p < 1$) despite the numerous assumptions made to derive it. Another common theoretical model in wall bounded shear flows is the logarithmic law, which is valid in the region of flow known as the overlap or inertial layer (Kundu, 1990). The velocity profile in the logarithmic region is a result of matching the profiles in the inviscid outer region and the viscous sublayer. The logarithmic layer law has extensive theoretical and experimental support from many types of smooth and rough surface shear flows. The adaptation of the logarithmic layer law to the flow above a rough surface whose elements have a substantial vertical scales is:

$$\langle \overline{U} \rangle (z) = \frac{u_*}{\kappa} \ln\left(\frac{z-d}{z_o}\right), \tag{3.56}$$

where z_o is the roughness height, d is the displacement height, κ is the von Karman constant and u_* is the friction or shear velocity. The logarithmic law in **Eq. 3.56** states that the mean streamwise velocity should have a logarithmic distribution starting at a level $z = d$. On a semilog plot, the logarithmic distribution is a straight line with a slope given by u_*/κ and a zero intercept at the roughness height z_o. Experiments over a wide range of conditions have shown that the von Karman parameter is a universal constant with a value close to $\kappa = 0.4$.

With knowledge of κ and d, the friction velocity and the roughness height can be estimated from the mean streamwise velocity profiles. The friction velocity obtained from the logarithmic layer fit to the velocity profile is an important velocity scale, representing the shear stress on the virtual wall (τ_o), at a level $z = d$, in a nondimensional form:

$$u_* = \sqrt{\frac{\tau_o}{\rho}}, \tag{3.57}$$

where ρ is the density of the fluid medium. In the context of flow above plant canopies, the wall shear stress refers to the stress near the canopy interface since the displacement height places the level of the virtual wall near h_p. This shear stress estimate does not quantify the shear stress on the bottom, which must incorporate both the Reynolds stress and the viscous stress. The roughness height in this context is the elevation above $z = d$ at which the mean streamwise velocity reaches zero. Contrary to wall shear flows with smaller roughness (*i.e.* sand), the roughness height in this context cannot be used to determine the actual roughness scale. Before discussing the friction velocity and the roughness height results obtained from using the logarithmic law, the displacement height for the experimental runs had to be determined from the shear stress profiles.

Table 3.4. Logarithmic layer parameters for the *Case A* and *B* experimental runs.							
Parameter / Run	**1A**	**2A**	**3A**	**4A,B**	**5B**	**6B**	**7A**
Displacement height d (cm)	16.00	14.16	12.70	12.01	11.11	9.26	11.22
Roughness height z_o (cm)	–	0.48	0.57	0.85	0.40	0.50	1.31
Friction velocity u_* (cm/s)	–	1.33	1.46	1.55	2.03	2.95	2.24

The simplest definition for the displacement height is the height to which the vertical axis must be raised such that the logarithmic law is applicable to flow over a rough surface. Thus, it is sometimes called a geometric height or the zero-plane displacement. By definition, a smooth surface has a displacement height equal to zero. For vegetation, Thom (1971) observed that the displacement height coincided with the mean level of momentum absorption, calculated from the moment of the forces acting on the roughness elements. Jackson (1981) lent theoretical support to this concept from a dimensional analysis and showed how the displacement height was the elevation at which mean drag appears to act. The displacement height d can be obtained from the first central moment of the shear stress gradient distribution as (Brunet *et al.*, 1994):

$$d = \frac{\int_0^h z\left(d\langle \overline{uw} \rangle / dz\right) dz}{\int_0^h \left(d\langle \overline{uw} \rangle / dz\right) dz}, \tag{3.58}$$

which can be simplified to the following expression if the Reynolds stress at the bed is much smaller than the Reynolds stress at the canopy height, *i.e.* $uw\ (z = 0) << uw\ (z = h_p)$ (Brunet *et al.*, 1994):

$$d = h - \frac{1}{\langle \overline{uw} \rangle (h)} \int_0^h \langle \overline{uw} \rangle dz\,. \tag{3.59}$$

It was shown in the Reynolds stress profiles in Section 3.3.3 that the assumption made to derive **Eq. 3.59** from **Eq. 3.58** is valid for all the experimental runs. The displacement height for *Cases A* and *B* was calculated using **Eq. 3.59** and the Reynolds stress profiles, the results of which are shown in **Table 3.4**. Over a large range of types of roughness, the displacement height has typical values equal to $d/h_p = 0.7$ (Jackson, 1981). The average value of d for the experimental runs is $0.77h_p$ which places the estimate within the range of other types of surface roughness of comparable roughness density λ.

Table 3.4 shows the variation of the displacement height with the characteristic depth (H/h_p) and the flow discharge (Q). The displacement height decreases with increasing H/h_p which indicates that as the surface layer depth increases the mean level of the drag acts at points further into the canopy. Thus, the depth of the surface layer controls the effective location of momentum absorption by the submerged meadow. If the drag is felt in lower canopy layers, then the momentum is being transported further into the canopy as the overlying depth increases, which is corroborated by the analysis of the momentum

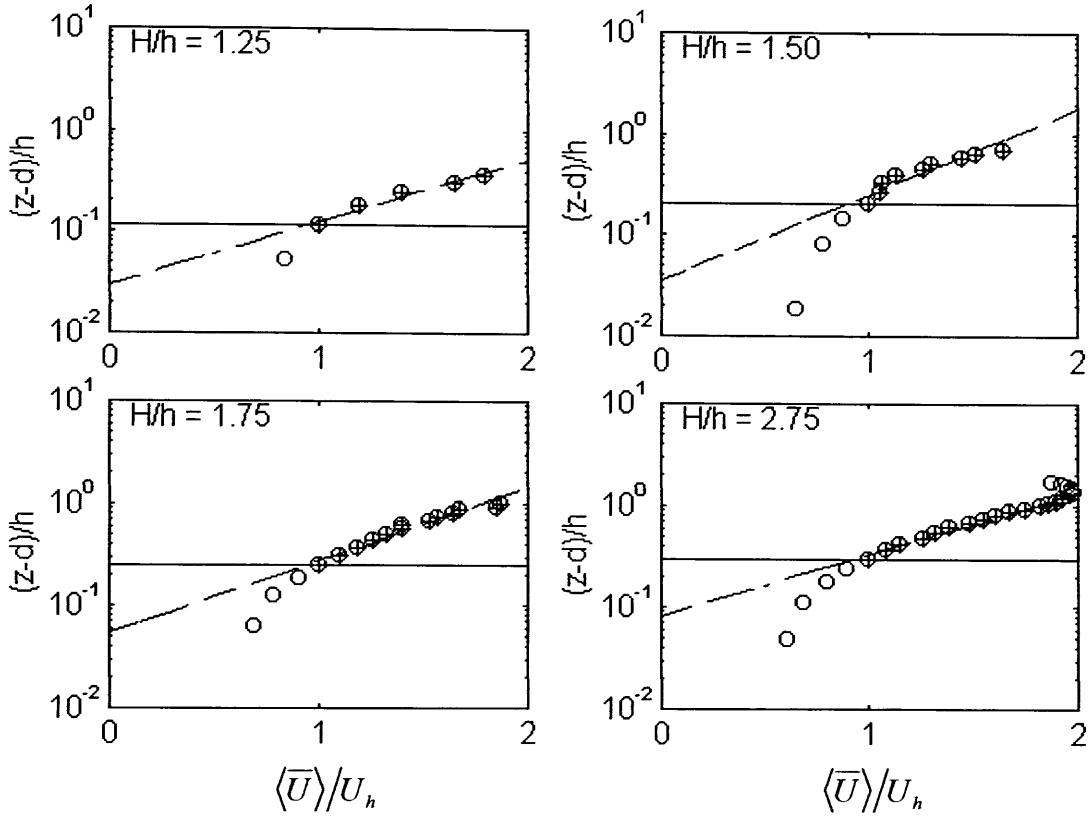

Figure 3.24. Logarithmic layer velocity profile for the *Case A* experimental runs with the characteristic depths (H/h_p) = 1.25, 1.50, 1.75, 2.75. The mean streamwise velocity has been nondimensionalized by the velocity at the canopy height, U_h. The vertical axis has been scaled by the displacement height, d, and nondimensionalized by the undeflected canopy height, h_p. The open circles (o) are the points over which the logarithmic transformation is valid, while the crosses (+) denote the points used to obtain the slope of the log layer, represented by the dashed line (--). The solid horizontal line (–) is the height of the canopy.

exchange presented in Section 3.6. For the lowest characteristic depth H/h_p = 1.00, the lack of a surface layer suggests that the displacement height be located at the canopy height h_p, an assumed value that has been included in **Table 3.4**. The variation in the displacement height with the characteristic depth shows the asymptotic behavior that has been described for other parameters, the displacement height decreases initially as h_o increases and subsequently attains near constant values for the larger characteristic depths.

The variation of the displacement height with the flow discharge in the *Case B* experimental runs follows a similar trend as that described for the peak in the turbulence intensity and the Reynolds stress. As the velocity increases, the displacement height decreases so that the mean level of momentum absorption is farther into the canopy. Nondimensionalizing the displacement height with the deflected canopy height, h_b, removes this trend so that the decrease in d is proportional to the decrease in h_b.

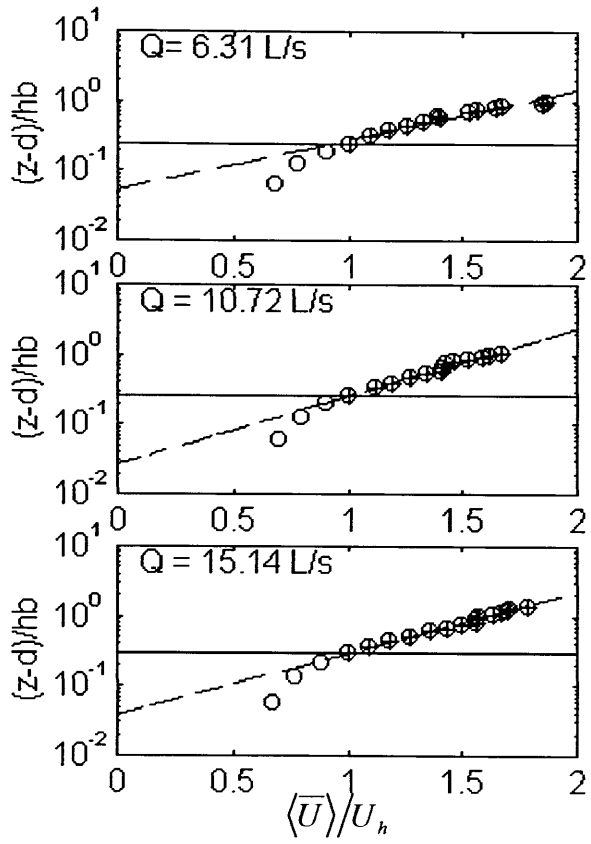

Figure 3.25. Logarithmic layer velocity profile for the *Case B* experimental runs with the flow discharges (Q) = 6.31, 10.72, 15.14 L/s. The mean streamwise velocity has been nondimensionalized by the velocity at the canopy height, U_h. The vertical axis has been scaled by the displacement height, d, and nondimensionalized by the deflected canopy height, h_b. The open circles (o) are the points over which the logarithmic transformation is valid, while the crosses (+) denote the points used to obtain the slope of the log layer, represented by the dashed line (--). The solid horizontal line (–) is the height of the canopy.

Using the displacement height estimates, the mean streamwise velocity profiles presented in Section 3.3.1 were plotted versus the natural log of z-d to find the location of the roughness height and the friction velocity, as shown in **Figures 3.24** and **3.25** for the experimental runs in *Cases A* and *B*. The vertical axis has been nondimensionalized by the effective canopy height for each experimental run, while the mean streamwise velocity has been nondimensionalized by the velocity at the canopy height, U_h. A regression line was fit to the points above the canopy denoted by the crosses (+). In order to reduce the potential errors in the estimation of u_* and z_o, the regression of $U(z)$ on $\ln(z)$ was performed as suggested by Bergeron and Abrahams (1992). The regression lines resulted in an average R^2 value of 0.97 for all the experimental runs. The results from the logarithmic law determination of the friction velocity and the roughness height are shown in **Table 3.4** for all the cases except H/h_p = 1.00, where the lack of a surface layer prevents the formation of a logarithmic layer and the application of **Eq. 3.56**.

The friction velocity obtained from applying the logarithmic law to the velocity profiles is in general agreement with the estimates obtained from **Eq. 3.37**. The results from the *Case A* and *B* experimental runs show that the friction velocity varies linearly with the characteristic depth (H/h_p) and the flow discharge (Q). As a velocity scale representing the interface shear stress, the friction velocity should also be linearly related to the velocity at the canopy height, U_h, for all the experimental runs. The linear relationship between the two parameters is:

$$u_* = 0.147U_h + 0.647, \qquad \textbf{(3.60)}$$

which has an R^2 value of 0.82 for the six data points. A relationship of the form of **Eq. 3.60** substantiated with data from other laboratory and field experiments of flow above submerged vegetation could be a useful means of estimating this important velocity scale from an easy to measure quantity, the velocity at the canopy top. It should be noted, however, that as it presently stands, **Eq. 3.60** indicates that a friction velocity would exist when $U_h = 0$, an erroneous statement. Thus, we limit ourselves to cautiously suggesting that a linear relationship should exist between u_* and U_h, as shown in these flow conditions.

The roughness height obtained from using the logarithmic law and the mean velocity profiles for the *Case A* and *B* experimental runs are within the typical ranges found for flows over rough surfaces and vegetation of comparable roughness density as reviewed by Raupach *et al.* (1991). The average roughness height nondimensionalized by the effective canopy height was $z_o/h_p = 0.04$. The increase in the roughness height with the characteristic depth would seem to contradict the expected trend since the vegetation layer becomes a smaller percentage of the total depth with increasing H/h_p. The explanation lies in that by displacing the logarithmic profile upwards by d, the roughness height is no longer a measure of the roughness vertical scale. The distance $z_o + d$, a more appropriate measure of the roughness scale, follows the expected trend, decreasing with the relative roughness r.

In summary, the mean velocity profile above the seagrass meadow follows the typical logarithmic layer law with the appropriate use of the displacement height. Contrary to the statements made by Fonseca *et al.* (1982) about the applicability of the logarithmic law to flow within a *Zostera marina* canopy, the velocity profile within the canopy deviates significantly from the log law, as recognized by Gambi *et al.* (1990). The log layer extends throughout the entire surface layer depth for the characteristic depths H/h_p = 1.25, 1.50 and 1.75. For H/h_p = 2.75, the log layer extends to a vertical distance $z/h_p = 1.88$, beyond which the velocity profile is nearly uniform, an expression of outer layer behavior.

In addition, there are distinct differences in the region of validity of the logarithmic law in this aquatic system as compared to flow above atmospheric plant canopies. Typically, the flow region immediately above the vegetation does not follow the logarithmic law due to the strong interaction with the roughness elements. This region has been named the roughness sublayer and it may extend to vertical heights, $z = 2h_p$ to $5h_p$ (Raupach *et al.*, 1991). Only above the roughness sublayer, in the inertial sublayer, is the logarithmic profile valid. The velocity profiles obtained in this experimental study do not suggest the existence of a roughness sublayer and the logarithmic law is valid through the entire surface layer.

3.4.2 Water Surface Slope Estimates

The measurement of the water surface slope S_w from the surface displacement gauges was discussed in Section 2.3.4. An independent measure of the surface slope is necessary to evaluate the pressure gradient term in the local force balance, **Eq. 3.22**, and determine the drag coefficient profiles for the flow through the flexible plant canopy. With the proper averaging procedure, the drag coefficient profile can be used to calculate the bulk drag exerted by the canopy on the current, as discussed in detail in Section 3.5. In addition to the measurement of the surface slope, two theoretical models can be employed to estimate the surface slope from the total stress value at the canopy height ($z = h_p$) and the bottom ($z = 0$). A good correlation between the estimated slope and the measurements ensures that the experimental procedure using the surface displacement gauges is suitable.

The surface slope obtained from the measurements for the *Case A* experiments was relatively constant, as expected by matching the characteristic velocity u_s within the plant canopy. The mean surface slope for the five experimental cases was calculated using **Eq. 2.21** from the voltage data and the conversion factors. **Table 3.5** lists the results from the surface slope experiments. The mean slope for all the depth variation cases was $2.34\times10^{-4} \pm 0.29\times10^{-4}$, so that the water depth decreased an average of 1.7 mm over the entire canopy length, $L = 7.32$ m. The uncertainties on the surface slope measurements, obtained by employing the 95% confidence intervals for the voltage readings and the calibration parameters and **Eq. 2.22,** were small, averaging 2.08×10^{-6} for the *Case A* experimental runs.

As expected, the surface slope for the *Case B* experimental runs increased linearly with the flow discharge. The mean surface slope, calculated from **Eq. 2.21**, are shown in **Table 3.5**. The change in the water depth over the canopy length varied from 1.8 mm to 6.0 mm for experimental runs 4 through 6. The uncertainty in the surface slope measurement was also small, although it increased slightly as the mean slope increased, from 2.63×10^{-6} for $Q = 6.31$ L/s to 7.86×10^{-6} for $Q = 15.14$ L/s. The increase in uncertainty is attributed to the larger variations in the water surface elevation at the position of the surface displacement gauge due to the higher surface velocities.

The measurements of the surface slope presented in **Table 3.5** were used in Section 3.3.1 to form the friction velocity. Since the forcing in the system is due exclusively to the surface slope (*i.e.* no bed slope), the parameter gHS_w was used to nondimensionalize the Reynolds stress and describe the distribution of the stress that must balance the forcing in the system. The force balance over the entire water depth involves the pressure gradient due to the surface slope, the Reynolds stress and the plant drag. In the overlying surface layer where there are no plants, the balance of forces involves the surface slope forcing and the Reynolds stress distribution, as discussed in Section 3.3.3. In the vegetation layer, the Reynolds stress decreases sharply and the force balance near the bottom is between the surface slope and the plant drag, as discussed in Section 3.1.1.

The Reynolds stress measurements provide two alternative methods of estimating the water surface slope which can be used to compare the values obtained from the surface slope measurements. First, the Reynolds stress at the effective canopy height, h, can be used to define a friction velocity that is applicable to the surface layer, as described in Section 3.4.3. Without the presence of the canopy elements in the surface layer, the forcing above the canopy gh_oS_w must be balanced by the shear stress at the canopy height. Thus, if the surface layer depth is known and the Reynolds stress is measured at h, an estimate for the water surface slope can be obtained from (Tsujimoto *et al.*, 1992):

$$S_{ho} = \frac{-\langle\overline{uw}\rangle(h)}{gh_o}. \tag{3.61}$$

Second, the Reynolds stress profile in the surface layer can be extrapolated to the bed ($z = 0$) to obtain an estimate of the friction velocity of the entire flow depth, as described in Section 3.3.3 and 3.4.3. Theoretically, the value of the total shear stress at the bed is equal to the product gHS_w, but the small discrepancies in the Reynolds stress profile lead to underestimates of this quantity. Nevertheless, a second estimate of the surface slope can be computed from this relationship as:

$$S_H = \frac{-\langle\overline{uw}\rangle(0)}{gH}. \tag{3.62}$$

The surface slope estimates calculated from **Eq. 3.61** and **3.62** are shown in **Table 3.5** along with the measured surface slopes. The two estimates give comparable results that are on average within 15% of each other. Both estimates from the Reynolds stress are considerably smaller than the measured values, averaging 38% and 28% less than the measured surface slope, for **Eq 3.61** and **3.62**, respectively. Considering that both methods were known *a priori* to underestimate the surface slope, the agreement between the measured value and the estimates is reasonable and follows the expected trend. This renders further support to method used for estimating the surface slope in the laboratory flume.

Recently, Dunn *et al.* (1996) and García (1996) developed a method for estimating the surface slope in an open channel lined with vegetation from a similarity analysis on the spatially and temporally averaged governing equations presented in **Eq. 3.17** and **3.18**. The resulting backwater curve for a gradually varying flow was expressed as:

$$\frac{dH}{dx} = \frac{S - S_f - \frac{1}{2}\overline{aC_D}HFr^2\beta_m}{(1 - Fr^2\beta_m)}, \tag{3.63}$$

where S is the bed slope, Fr is the Froude number, β_m is the Boussinesq coefficient and S_f is the friction slope given by bed shear stress (τ_b) and the water depth:

$$S_f = \frac{\tau_b}{\rho gH}. \tag{3.64}$$

Table 3.5. Water surface slope estimates for the *Case A* and *B* experimental runs.							
Parameter / Run	**1A**	**2A**	**3A**	**4A,B**	**5B**	**6B**	**7A**
Measured Surface Slope, $S_w \times 10^{-4}$	1.95	2.74	2.44	2.52	4.97	8.26	2.05
Estimated Surface Slope **Eq. 3.63**, $S_{ho} \times 10^{-4}$	–	1.44	1.53	1.21	3.34	4.73	1.08
Estimated Surface Slope **Eq. 3.64**, $S_H \times 10^{-4}$	–	1.74	1.95	2.04	3.37	4.82	1.42
Estimated Surface Slope **Eq. 3.66**, $S_B \times 10^{-4}$	1.90	3.48	4.58	6.54	13.82	30.66	16.82

The application of **Eq. 3.63** to the present study may lead to useful estimates of the water surface slope with the proper corrections made to account for the particularities of this study. Without an appreciable bed shear stress, $\tau_b = 0$, as discussed in Section 3.3.3, and without a bed slope, the first two terms in the numerator of **Eq. 3.63** can be neglected. The overbars on a and C_D indicate that these parameters are a result of vertically integrating the density and drag coefficient profiles. The bulk drag coefficient based on the derivations made by Dunn *et al.* (1996) is introduced later in Section 3.5. At this point, it is suffice to say that the bulk drag coefficients are obtained from the drag profiles by calculating a weighted vertical average. The authors, however, did not consider a vertically varying canopy density as has been done here. For this reason, an appropriate way to obtain an averaged canopy density must be introduced in order to use **Eq. 3.63**. The leaf area index (*LAI*) or the roughness density (λ) might seem appropriate, but they are not dimensionally equivalent to the canopy density. A better approach is to define a weighted average density, in the same way as the bulk drag coefficients are computed from the drag profile (**Eq. 3.88**). The bulk canopy density for use in **Eq. 3.63** is defined as:

$$\overline{a} = \int_0^h a\langle\overline{U}\rangle^2 dz \Big/ \int_o^h \langle\overline{U}\rangle^2 dz . \qquad \textbf{(3.65)}$$

Using the definition of the average density from **Eq. 3.65**, the values for Fr and β_m presented in **Table 3.7** and the bulk drag coefficients presented in Section 3.5, an estimate of the surface slope can be obtained from the modified backwater curve:

$$S_B = \frac{0.5\overline{aC_{DC}}HFr^2\beta_m}{(1 - Fr^2\beta_m)} \qquad \textbf{(3.66)}$$

The surface slope calculated from applying **Eq. 3.66**, as shown in **Table 3.5**, overestimates the measured surface slope considerably, except for the lowest characteristic depth. This result is not totally unexpected, however, since the applicability of **Eq. 3.63** is stated to be limited to emergent vegetation (Dunn *et al.*, 1996), despite the experimental study being geared to obtaining values of the bulk drag coefficients for submerged canopies. The authors never verify the validity of **Eq. 3.63** with the data obtained from the laboratory studies and leave it open for interpretation. Here, we have shown that for the gradually varying flow in this study, the backwater curve is only applicable to emergent conditions. Large H/h_p values lead to discrepancies between the estimated and the independently measured surface slope.

3.4.3 Velocity Estimates

The mean streamwise velocity profiles presented in Section 3.3.1 can be used to determine various velocity scales for the flow through the model seagrass meadow. The velocity scales of interest in the system are the in-canopy average velocity, U_c, the depth average velocity, U_m, the interface velocity, U_h, and the friction velocity, u_*. Other relevant velocity parameters, including the vegetation and surface layer velocities, U_1 and U_2, have been discussed in Section 3.3.1.

An important velocity scale is the in-canopy average velocity since it describes the flow conditions which the roughness elements experience. The in-canopy average velocity is determined by integrating the velocity profile from the lowest measurement point to the elevation of the effective canopy height, h, obtained from the plant motion experiments and corroborated by the peak in the Reynolds stress profiles. The in-canopy velocity is defined as:

$$U_c = \frac{1}{h}\int_0^h \langle \overline{U} \rangle dz \,. \tag{3.67}$$

To calculate U_c from the velocity profiles, a weighted averaging procedure was employed to assure that the vertical spacing between the points was taken into account when computing the average velocity. **Table 3.6** shows the variation of U_c for the experimental runs in *Cases A* and *B*. The in-canopy velocity for the depth variation cases averages 3.31 ± 0.43 cm/s, indicating that the flow conditions inside the meadow were comparable across the experimental runs, within 10%, as intended in the experimental design. Similarly, the marked increase in U_c for the velocity variation cases confirms that the canopy experienced progressively higher velocities as the flow discharge is increased.

A vertically-integrated velocity scale similar to the in-canopy velocity can be defined to characterize the flow over the entire water depth. The depth-averaged velocity, U_m, was computed from the velocity profiles obtained from the acoustic and laser Doppler velocimeters as:

$$U_m = \frac{1}{H}\int_0^H \langle \overline{U} \rangle dz \,. \tag{3.68}$$

Comparison of the depth-averaged velocities shown in **Table 3.6** with the channel velocities, $U_{ch} = Q/A$, of **Table 2.5** reveals that U_m and U_{ch} are on average within 5% of each other for the experimental runs in *Cases A* and *B*. The agreement between the two velocities is good, considering that there are some uncertainties in the measurement of the water depth and the flow rate. In addition, the depth-averaged velocity is on average within 15% of the velocity at the effective canopy height, U_h, for the all the experimental cases. The linear variation of U_m with the characteristic depth (H/h_p) and the constant in-canopy velocity throughout the experimental cases confirms that the velocity in the surface layer increases with H/h_p, as observed in **Table 3.3** for the surface region velocity, U_1.

Table 3.6. Velocity scales for the *Case A* and *B* experimental runs.							
Parameter / Run	**1A**	**2A**	**3A**	**4A,B**	**5B**	**6B**	**7A**
In-canopy average velocity U_c (cm/s)	2.66	2.96	3.80	3.41	6.16	7.92	3.73
Depth average velocity U_m (cm/s)	2.69	3.34	5.11	5.58	10.50	15.36	9.92
Interface velocity U_h (cm/s)	2.70	4.73	7.12	6.38	11.36	14.99	7.81
Friction velocity of **Eq. 3.37** (cm/s)	1.75	2.32	2.40	2.63	3.69	4.76	2.97
Friction velocity of **Eq. 3.46** (cm/s)	–	0.75	1.10	1.20	2.06	2.64	1.72
Friction velocity of **Eq. 3.56** (cm/s)	–	1.33	1.46	1.55	2.03	2.95	2.24
Friction velocity of **Eq. 3.69** (cm/s)	1.29	1.62	1.59	1.67	2.35	3.03	1.63
Friction velocity of **Eq. 3.70** (cm/s)	–	1.85	2.14	2.57	3.04	3.64	2.48
Friction velocity of **Eq. 3.71** (cm/s)	–	1.04	1.38	1.72	2.52	3.49	2.37

The friction velocity is an important hydraulic velocity scale in the system. Several methods can be employed to estimate the shear velocity for the flow through the seagrass canopy. At various points in this work, different estimates have been introduced and computed. In Section 3.3.1, an estimate based on the water depth and the water surface slope was used to nondimensionalize the mean streamwise velocity, as shown in **Eq. 3.37**. In Section 3.3.2 and **Eq. 3.46**, the estimate of the friction velocity from the Reynolds stress at the effective canopy height was used to compare the turbulent velocities in the seagrass meadow to the typical values in atmospheric canopies, where the constant stress region makes this friction velocity a natural choice. Finally, the friction velocity estimated from the logarithmic layer law, **Eq. 3.56**, was discussed in Section 3.4.1. In addition to these estimates, three additional possibilities exist for estimating the friction velocity: (1) a friction velocity based on the hydraulic radius and the surface slope:

$$u_* = \sqrt{gR_h S_w}\,, \tag{3.69}$$

(2) a friction velocity determined from the Reynolds stress profile in the surface layer following the theoretical total stress distribution, analogous to **Eq. 3.62**, as described in Section 3.3.3:

$$\tau(z) = u_*^2\left(1 - \frac{z}{H}\right), \tag{3.70}$$

and (3) a friction velocity based on the depth of the surface layer and S_w, analogous to **Eq. 3.37**:

$$u_* = \sqrt{gh_o S_w}\,. \tag{3.71}$$

The friction velocity was computed from each of the six methods outlined above. **Figure 3.26** shows the various u_* estimates for the *Case A* and *B* experimental runs as a function of the characteristic depth (H/h_p) and the flow discharge (Q). The open circles (o) correspond to the estimate based on total forcing in the system, $\sqrt{gHS_w}$, as shown in **Eq. 3.37**. It is quite evident that this method produces the largest estimate of the friction velocity, the reason being that this estimate represents the stress necessary to balance the forcing over the entire flow depth. Similarly, the estimate based on the theoretical stress, as

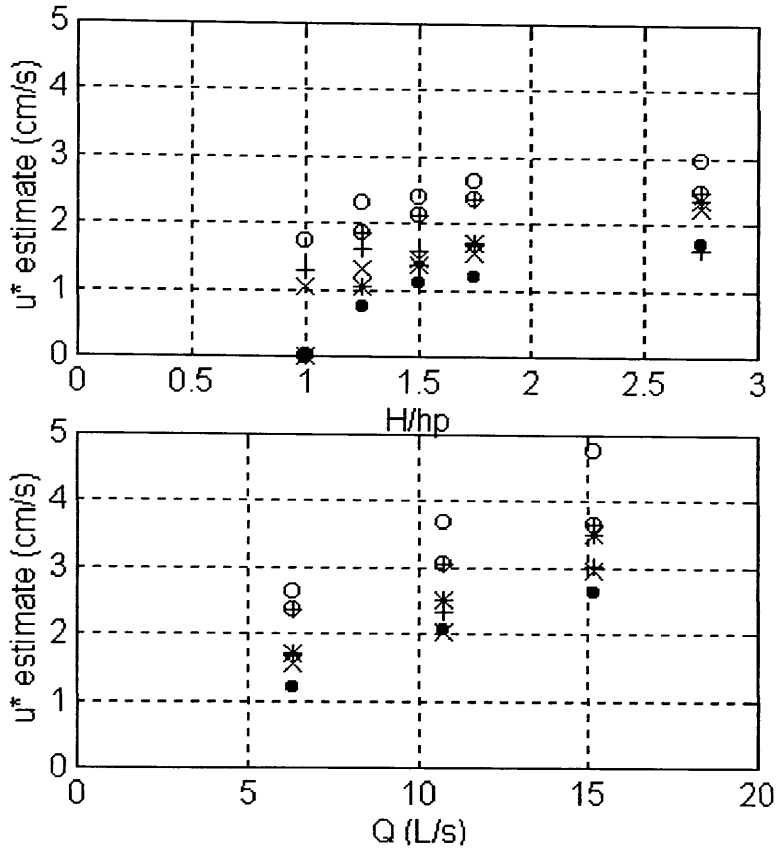

Figure 3.26. Friction velocity estimates from six different methods as a function of the characteristic depth (H/h_p) in the top figure for *Case A*, and as a function of the flow discharge (Q) in the bottom figure for *Case B*. The symbols represent the following equations for u_*: (o) **Eq. 3.37**; (⊕) **Eq. 3.70**; (*) **Eq. 3.71**; (+) **Eq. 3.69**; (×) **Eq. 3.56**; (•) **Eq. 3.46**. The estimates at $H/h_p = 1.00$ that could not be obtained are represented by the value of $u_* = 0$ in the figures.

shown in **Figure 3.15** quantifies the shear stress over the entire depth and expressed at the bottom boundary. By extrapolating the Reynolds stress profile in the surface layer to the bottom boundary, the estimate of the u_* described in **Eq. 3.70** should be reasonably close to the value obtained from $\sqrt{gHS_w}$. This is corroborated by the similar values for the open circle (o) and the circles with the cross (⊕). In contrast to these two estimates, the shear velocities from **Eq. 3.46** (•), **3.56** (×), and **3.71** (*) quantify the stress present exclusively in the surface layer and expressed at the effective canopy height. For this reason, these shear velocities are smaller in magnitude than the previous estimates, as shown in **Figure 3.26**, and therefore not appropriate for the emergent case ($H/h_p = 1.00$). For example, the friction velocity obtained from the logarithmic layer law (×) is 0.6 times smaller the estimate from the square root of gHS_w (o). These friction velocity estimates are appropriate if the interest is in the flow exclusively above the canopy such that u_* expresses the resistance imparted by the vegetation layer on the overlying flow as if it were a rough surface with a virtual bottom at the level of the canopy height. Otherwise, if the interest is on knowing how the vegetation layer affects the total flow, the friction velocity estimates based on the

Reynolds stress distribution or the product gHS_w are more appropriate. Tsujimoto *et al.* (1992) also noted the differences among the two friction velocities defined over H and h_o, with u_* at h_p being 0.72 times smaller than the value of the total friction velocity.

The estimate obtained from the hydraulic radius and the surface slope, **Eq. 3.69** (+), gives results that are comparable to the estimate from the logarithmic law (×) and the surface layer depth (*), which would seem to imply that it should be related to the stress in the surface layer. The similarity in the values, however, should not be inferred as a link among the estimates since the hydraulic radius length scale describes the stress on the entire flow. The casual link and the relatively constant estimate of u_* obtained from **Eq. 3.69** for all the characteristic depths can both be explained by the definition of the R_h, which includes the large, constant value for the channel width, B, as seen in **Eq. 3.79**.

Choosing the appropriate friction velocity estimate for nondimensionalizing the velocity statistics was not an easy task. After an analysis of the alternatives, of the values obtained from the different estimates and of the uncertainties involved in the determination of the velocity scale, the friction velocity estimate from the water depth and the surface slope was chosen as an appropriate nondimensionalizing parameter for the mean velocity profiles, the Reynolds stress profiles and the turbulent kinetic energy profiles, as shown in Section 3.3. This estimate quantifies that the total forcing in the system and creates ratios that imply how the total stress or turbulent kinetic energy available in the system are partitioned. It is also a parameter that can be obtained easily in field conditions from measurements of H and S_w.

The best estimate of the shear at the canopy height between the two different flow regions is believed to be the friction velocity obtained from the logarithmic law for the flow above the canopy. This estimate is based solely on the velocity profile which is considered more accurate than the surface slope measurements, as discussed in Section 3.4.2. For the total resistance within the water depth, however, the best estimate of the shear velocity is obtained from the water depth and surface slope estimate of the friction velocity, gHS_w.

3.4.4 Nondimensional Flow Parameters

The velocity scales defined in Section 3.4.3 allow the calculation of various nondimensional parameters for the flow conditions explored in *Cases A* and *B*. Among the flow parameters of interest are the Reynolds numbers, the Froude number and the Boussinesq coefficient. As described in Section 2.2, the scaling analysis showed that the dynamic conditions between the model and the prototype were matched by assuring that the Reynolds number based on the water depth and a mean velocity in the two systems were comparable. The Froude similarity was considered to be less significant due to the subcritical conditions in both systems. The Froude number and the Boussinesq coefficient are both important parameters for estimating the water surface slope using the backwater curve proposed by Dunn *et al.*, (1996) and described by **Eq. 3.63**.

Several different types of Reynolds number can be formed from the various velocity and length scales in the system, each giving different insight about the flow conditions. The depth Reynolds number, for example, is commonly used to determine the turbulence regime in the system and is defined using the depth averaged velocity (U_m) and the water depth (H) as:

$$Re_H = \frac{U_m H}{\nu}. \tag{3.72}$$

Typically, pipe flows with depth Reynolds numbers greater than 2300 are considered to be turbulent (White, 1986). Open channel flows are generally turbulent due to the large depth scales and the high velocities. The critical depth Reynolds number can be obtained from the criteria for pipe flow since the pipe diameter is four times the hydraulic radius $D = 4R_h$. The flow in all the experimental runs was found to be above the critical Re_H by showing that $U_m R_h/\nu > 600$. **Table 3.7** lists the depth Reynolds numbers for the turbulent flow in the experimental runs of *Cases A* and *B*.

The drag Reynolds number can be used to describe the characteristics of the wake generated behind a roughness element immersed in a flow. The appropriate velocity and length scales for the formation of the drag Reynolds number are the in-canopy average velocity U_c and the element width, taken here to be the width of the blades, $d_b = 0.28$ cm. With the approach velocity represented by U_c and the element represented by a flat plate of width d_b, the drag Reynolds number is simply:

$$Re_D = \frac{U_c d_b}{\nu}. \tag{3.73}$$

The relationship between the drag Reynolds number and the wake characteristics for a flat plate perpendicular to the flow are not readily available in the literature. Nevertheless, for a circular cylinder it is well known that values of Re_D greater than 60, the wake behind the element separates periodically and forms vortices that travel downstream, the initiation of what is to become a turbulent flow regime behind the element. For a flat blade, this transition to vortex shedding and turbulence is expected to occur at lower values of Re_D due to the larger flow separation at the sharp corners. In addition, the movement of the blades relative to the approach flow should induce the formation of turbulent wakes at lower drag Reynolds numbers. **Table 3.7** shows the values of Re_D for the experimental runs in *Cases A* and *B*. All the experimental cases have drag Reynolds numbers such that the wakes behind the plant elements should separate from the blades and their effects extend for considerable distances, as discussed in Section 2.4.2.

The canopy Reynolds number was introduced in Section 3.1.1 to show that the flow in the canopy could be considered as fully rough turbulent conditions. This type of Reynolds number is based on the friction velocity and the height of the roughness elements. For the flow above the canopy, the appropriate estimate for the friction velocity is obtained from the logarithmic layer law, **Eq. 3.56**, while the roughness vertical scale is described by the height of the canopy (h_p). The usefulness of this nondimensional parameter is in the comparison to other rough surfaces and in the description of the flow as dynamically smooth or rough. Raupach *et al.* (1991) present the value of the canopy Reynolds number for a variety of

Table 3.7. Nondimensional flow parameters for the *Case A* and *B* experimental runs.							
Parameter / Run	**1A**	**2A**	**3A**	**4A,B**	**5B**	**6B**	**7A**
Depth Reynolds No. Re_H	4.3×10^3	6.7×10^3	1.2×10^4	1.6×10^4	2.9×10^4	4.3×10^4	4.4×10^4
Drag Reynolds No. Re_D	75	83	106	96	173	222	104
Canopy Reynolds No. Re_C	1664	2128	2336	2480	3045	3835	3584
Rough Reynolds No. Re_*	–	64	83	132	81	148	293
Froude Number Fr	0.02	0.02	0.03	0.03	0.06	0.09	0.05
Boussinesq Coefficient β_m	1.00	1.45	1.46	1.44	1.19	1.19	1.15

field and laboratory conditions with a range varying from $Re_C = 1$ to 10^6. The canopy Reynolds number is expressed as:

$$Re_C = \frac{u_* h_p}{\nu}. \tag{3.74}$$

The values obtained from the experimental runs in *Cases A* and *B*, shown in **Table 3.7**, indicate that the flow is dynamically rough and comparable to the values obtained in other laboratory studies of plant canopy flows (Brunet *et al.*, 1994). The description of the roughness conditions given by the canopy Reynolds number is often supplemented by using another type of nondimensional parameter called the roughness Reynolds number:

$$Re_* = \frac{u_* z_o}{\nu}, \tag{3.75}$$

where u_* is the friction velocity and the z_o is the roughness height both obtained from the logarithmic layer law applied to the flow above the canopy. It is also used to characterize the degree of roughness in a turbulent boundary layer with the minimum value of Re_* for a smooth boundary equal to 0.14 (Raupach *et al.*, 1991). The values of Re_* for the experimental runs are shown in **Table 3.7**.

The Froude number is critical parameter in flows that involve a free surface, describing the relative importance of the mean flow to the speed of a propagating shallow water wave. In open channel flows, the Froude number, calculated as:

$$Fr = \frac{U_m}{\sqrt{gH}}, \tag{3.76}$$

plays an important role for classifying the flow into three regimes, subcritical, critical and supercritical (White, 1986). The Froude numbers in this open channel flow, calculated using **Eq. 3.76** and shown in **Table 3.7**, indicate that the flow is subcritical ($Fr < 1$). For this subcritical condition, the role played by the Froude number is negligible, as discussed in Section 2.2.

Finally, the momentum or Boussinesq coefficient introduced in **Eq. 3.63** arises in the formulation of the backwater curve derived by Dunn *et al.* (1996) when a similarity solution is performed for the

governing momentum equations. This shape factor has a limiting value of 1.00 for a uniform velocity profile and increases with the deviation from uniformity. The Boussinesq coefficient is calculated as:

$$\beta_m = \int_0^1 \left(\frac{\langle \overline{U} \rangle}{U_m} \right)^2 d\left(\frac{z}{H} \right). \tag{3.77}$$

The values obtained from this calculation are shown in **Table 3.7**, where it is evident that for all the experimental cases, except H/h_p = 1.00, large departures from a uniform velocity profile are observed. The large degree of shear in the mean velocity profile is responsible for the high values of β_m. Nevertheless, these results are comparable to those obtained by Dunn *et al.* (1996) for the flow through flexible cylinders which ranged from 1.02 to 1.27. The variation of the Boussinesq coefficient with the depth and the velocity is unclear from the experimental runs in *Cases A* and *B*.

3.4.5 Resistance Coefficients

The resistance offered by the rough surfaces of an open channel flow is often quantified through the calculation of a resistance coefficient. Several types of resistance coefficients are widely-used for the engineering design of canals and waterways. They are also used in hydrodynamic modeling of water bodies to account for the friction imparted on the flow by the underlying surface. For vegetated regions, many attempts have been made to model flow resistance based on empirical equations derived for open channel flow. One such equation, the Manning formula, has been applied by many researchers to the flow through vegetation (*e.g.* Hosokawa and Horie, 1992; Petryk and Bosmajian, 1975; Kouwen *et al.*, 1969). The Manning equation, as it applies to an open channel with vegetation over the entire perimeter, relates the channel uniform velocity to the hydraulic radius and the water surface slope as follows in SI units:

$$U_{ch} = \frac{1}{n} R_h^{2/3} S_w^{1/2}, \tag{3.78}$$

where n is the Manning coefficient, S_w is the water surface slope, U_{ch} is the channel velocity (Q/A) and R_h is the hydraulic radius defined as the area (A) divided by the wetted perimeter (P_w):

$$R_h = \frac{A}{P_w} = \frac{HB}{2H + B}, \tag{3.79}$$

where H is the water depth and B is the flume width (38 cm). The Manning equation is not dimensionally consistent and because the Manning n is often taken to be a dimensionless parameter, the coefficient 1.00 must have dimensions of [$L^{1/3}/T$] (White, 1986). The channel velocity and hydraulic radius in **Eq. 3.78** are expressed in units of meter per second and meters, respectively. For this laboratory flume study, the Manning equation should be modified slightly to account for the fact that the side walls do not play a major role in producing flow resistance since they are smooth glass boundaries. As such, the hydraulic radius should be replaced with the water depth H as a more appropriate length scale:

Table 3.8. Resistance coefficients for the *Case A* and *B* experimental runs.							
Parameter / Run	**1A**	**2A**	**3A**	**4A,B**	**5B**	**6B**	**7A**
Channel velocity U_{ch} (m/s)	0.0207	0.0332	0.0519	0.0593	0.1008	0.1423	0.0906
Hydraulic Radius R_h (m)	0.0869	0.0974	0.1060	0.1132	0.1132	0.1132	0.1327
Water depth H (m)	0.16	0.20	0.24	0.28	0.28	0.28	0.44
Manning coefficient n **Eq. 3.78**	0.13	0.11	0.07	0.06	0.05	0.05	0.04
Manning coefficient n **Eq. 3.80**	0.20	0.17	0.12	0.11	0.09	0.09	0.09
Friction factor f **Eq. 3.81**	3.09	1.90	0.75	0.64	0.43	0.36	0.75
Friction factor f **Eq. 3.82**	5.69	3.90	1.71	1.57	1.07	0.90	0.86

$$U_{ch} = \frac{1}{n} H^{2/3} S_w^{1/2} \qquad \textbf{(3.80)}$$

The result is that the form of the Manning equation in **Eq. 3.80** assumes that all the resistance is exerted by the bottom and that the wall effects are negligible, *i.e.* assuming that the flume of limited width acts like a wide open channel. This form is also more reasonable since the forcing in the system is represented by the product gHS_w, which was used to estimate the total friction velocity in Sections 3.3.1 and 3.4.3.

Values for the Manning n within a vegetated region can be up to an order of magnitude greater that in an unvegetated channel due to the increased resistance imparted by the plants (Petryk and Bosmajian, 1975). Standard texts cite values for the Manning coefficient in vegetated waterways as ranging from 0.03 to 0.15 (White, 1986). Numerous studies have related the value of the Manning n to the product of the hydraulic radius and the flow velocity in plots that have been named n-$U_{ch}R_h$ curves (Kouwen and Unny, 1973; Kao and Barfield, 1978; Temple, 1982, among others). Others have found that n varies with plant morphology, flexibility, canopy density and the depth of submergence (Kouwen and Unny, 1973; Fathi-Maghadam and Kouwen, 1997; Dunn *et al.*, 1996, among others).

The measurements of the water surface slope and the channel velocity and water depth provides an opportunity to calculate the Manning coefficient for the seagrass meadow and investigate the effect of depth and velocity variations on the value of n. **Equations 3.78** and **3.80** were used to solve for the Manning coefficient for the experimental runs in *Cases A* and *B*, as shown in **Table 3.8**. The Manning n ranges from range from 0.04 to 0.13 for the hydraulic radius formulation and from 0.09 to 0.20 for the water depth formulation, well within the values reported for other vegetated waterways (Kouwen and Unny, 1973; White, 1986).

A clear decrease in the value of the Manning coefficient is observed as the characteristic depth (H/h) increases for all the experimental cases. This trend is expected since the vegetation layer becomes a smaller portion of the entire water column (*i.e.* smaller relative roughness) and therefore imparts less

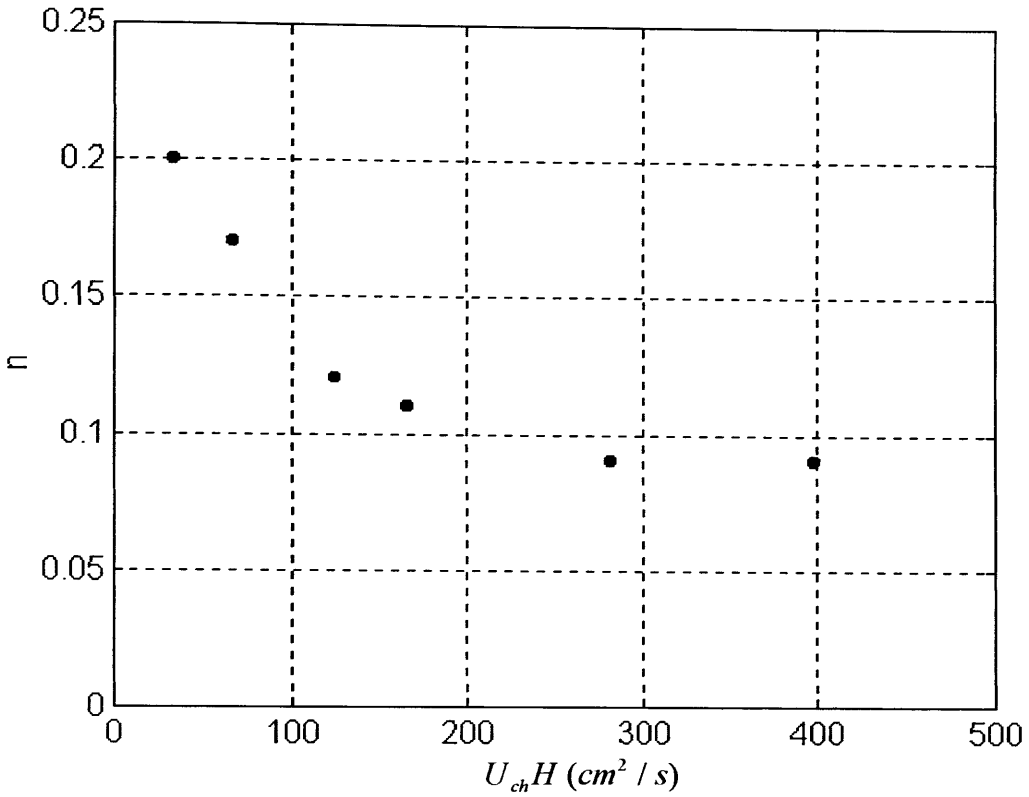

Figure 3.27. Variation of the Manning coefficient n as a function of the product $U_{ch}R_h$.

resistance to the channel flow. These result support previous findings that showed that the Manning n varied with the depth of submergence, decreasing for smaller relative roughness ($r = h/H$) (Kouwen and Unny, 1973; Dunn *et al.*, 1996). For the *Case B* experimental runs conducted at identical water depths, the value of n decreased with increasing flow discharge. Although both the channel velocity and the surface slope increase linearly with the flowrate, the Manning formulation depends on the square root of S_w which ultimately leads to a larger increase in velocity and a smaller n as the flow discharge increases. This results also makes intuitive sense if we consider that as the flow discharge increases the effective canopy height decreases due to plant bending and the plants offer less resistance to the channel flow.

The effect of the flow discharge and the characteristic depth can be summarized by computing the relationship between the Manning n and the product of the channel velocity and the hydraulic radius, as proposed initially by Ree and Palmer (1949) for vegetated waterways. Alternatively, the water depth can be used to form curves of n versus $U_{ch}H$. **Figure 3.27** shows the n-$U_{ch}H$ curve for the experimental runs in *Cases A* and *B*. There is a noticeable asymptotically decreasing trend for the Manning coefficient with the product of the water depth and the channel velocity. The variation of n with the $U_{ch}H$ parameter in **Figure 3.27** gave a better collapse for the data from both experimental cases as compared to the variation of n with $U_{ch}R_h$, giving further support to the use of H as the appropriate length scale.

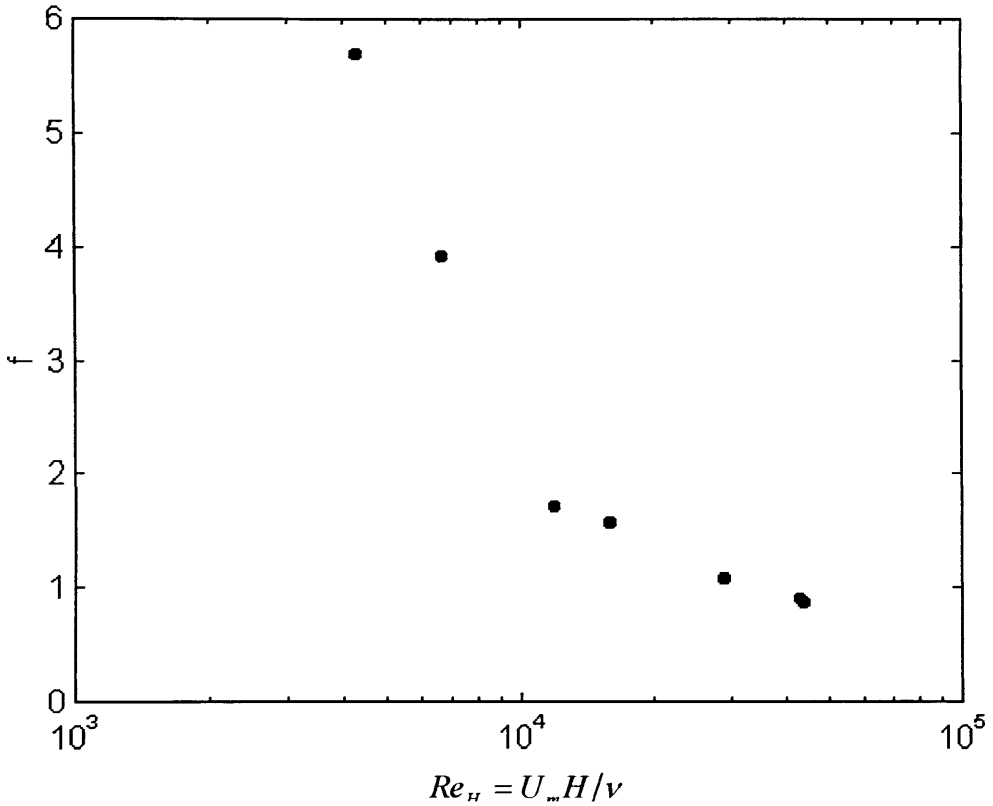

Figure 3.28. Variation of friction factor (**Eq. 3.82**) with the depth Reynolds number, Re_H.

Another way of quantifying the flow resistance in an open channel is through the Darcy-Weisbach friction factor, f, which has a more solid theoretical background than the Manning equation derived from studies of flow through pipes. The use of f is preferred in computing the resistance in vegetated open channels for design and analysis applications (Mastermann and Thorne, 1994). The nondimensional friction factor for an open channel flow is computed from the energy slope, the hydraulic radius and the channel velocity. For the case of having no bed slope, the energy slope is approximated by the slope of the free surface and the friction factor can be obtained as:

$$f = \frac{8gR_h S_w}{U_{ch}^2}. \tag{3.81}$$

The friction factor is simply a coefficient that relates the frictional loss of kinetic energy to the forcing in the system. For the same reasons given for the Manning equation, the hydraulic radius in **Eq. 3.83** should be replaced with the flow depth, H, for this laboratory experiment:

$$f = \frac{8gHS_w}{U_{ch}^2}. \tag{3.82}$$

The results from computing the friction factor using the formulas with the hydraulic radius and the water depth are both shown in **Table 3.8**. As with the Manning coefficient, the agreement between the computed values and the results obtained in other studies of the resistance created by vegetation in open channels is good (Chen, 1976; Kouwen and Unny, 1973). The variation in the water depth and the velocity among the experimental cases results in the same trends observed for n, a decrease in the Manning coefficient with increasing degrees of submergence and a decrease with an increasing flow discharge. The agreement in the trends for the two resistance coefficients is not unexpected since n and f can be linearly related to each other (Kouwen and Unny, 1973). Typically, the friction factor is plotted versus the depth Reynolds number presented in Section 3.4.4. **Figure 3.28** shows that the friction factor obtained from **Eq. 3.82** varies smoothly with Re_H for the experimental runs in *Cases A* and *B*.

Although appealing for their simplicity, the use of the Manning equation or the Darcy-Weisbach friction factor reveal very little about the flow structure within the plant canopy or how the resistance offered by the plants varies with depth. In addition, the use of the two friction formulas assumes vertically uniform channel flow. As has been shown in the velocity profiles, the vegetation layer creates shear conditions that make the flow far from uniform over the depth. A better understanding of the resistance created by the canopy will be explored in the Section 3.5 on the drag characterization of the model meadow.

3.5 Drag Characterization

This section presents the results from the characterization of the drag exerted by the seagrass meadow on the unidirectional current in the laboratory flume. The discussion begins with an introduction to the formulation of the drag for an array of roughness elements and then proceeds to present the drag coefficients profiles obtained from the measurements of the water surface slope, the Reynolds stress gradient, the canopy density and the mean velocity profiles. The vertically-varying drag coefficients can be integrated to obtain a single bulk drag coefficient that describes the overall effect of the seagrass meadow on the flow. The bulk drag coefficients are an improved way of describing the resistance exerted by the plant canopy as compared to the resistance coefficients, the friction factor and the Manning n, introduced in Section 3.4.5. Finally, the partitioning of the total drag between the vegetation and the underlying surface is discussed.

The topic of the drag characterization of the seagrass canopy could potentially be the subject of an entire study due to the great deal of work that has been done on individual roughness elements of simple geometries and the lack of information in the literature on the effects of having a roughness element within an element array. The effect of the canopy density on the drag coefficient has recently been explored for a rigid emergent canopy (Nepf and Vivoni, 1998), but the approach has yet to be extended to a flexible submerged vegetation. In fact, the effect of proximity to other elements on the drag

coefficient, referred to in the atmospheric literature as the shelter effect, is still considered an open research question (Brunet *et al.*, 1994).

In addition to the shelter effect, very little is still known about how the instantaneous drag for the elements varies for a waving plant and how the coherent waving motions affect the drag exerted by the canopy on the flow. Finnigan and Mulhearn (1978) showed through an order of magnitude estimate that the contribution from plant waving to the total drag is comparable to the mean and turbulent form drag. Despite this, most studies in waving plant canopies ignore the time dependency of the drag force and treat the canopy as if it were rigid. This approach has been justified based on the lack of dependence of the time and volume-averaged governing momentum equation, **Eq. 3.13**, on the velocity of the roughness element, as discussed in Section 3.1.1.

The attempt in this section is not to address all the questions that remain to be answered concerning the drag of a flexible, submerged and waving plant canopy. Instead, we seek to apply the momentum equation, **Eq. 3.22**, to the data obtained from the laboratory study and describe the variation of the vertically-varying drag coefficient and the bulk drag coefficients with the level of submergence and the flow discharge. The intent is thus to provide additional experimental data that can be used to support or refute the theoretical developments on this topic.

3.5.1 Vegetative Drag

The total longitudinal drag force (f_x) on an element in a fluid flow is composed of two types of drag, the form or pressure drag (f_{Fi}) and the viscous or skin drag (f_{Vi}). The difference between the high pressure in the front stagnation region and the low pressure in the rear separated region causes a large drag contribution known as form drag (White, 1986). The viscous drag is a result of the integrated shear stress acting directly on the surface of the element. For a blunt body exposed to a high drag Reynolds number flow regime, the form drag is larger than the skin drag due to the occurrence of separation in the wake behind the object (Kundu, 1990). The drag force is then commonly assumed to be composed solely of the form drag term and is parameterized by using a drag coefficient C_D. This nondimensional parameter is simply a ratio of the longitudinal drag force to the mean flow kinetic energy times an element frontal area. The drag coefficients for single elements of various shapes and configurations are routinely tabulated in standard fluid mechanics texts (Granger, 1985; White, 1986). For an array of roughness elements, however, the description of the drag on a particular element in the array is a much more complicated task due to the effect of wake interaction.

In the model seagrass canopy, the precise quantification of the drag on a single plant blade is further complicated by plant flexibility, the random orientation of the plant blades, the movement of the plants in response to the flow and the effect of plant density. In addition, free surface flow through a vegetation stand has other non-idealities that make the description of the drag more complicated,

including free surface effects, turbulence and non-uniform velocity profiles. The standard approach to these difficulties is to incorporate each of the non-idealities into the value of a bulk drag coefficient that characterized the overall effect of the canopy on the flow. In this study, the mean streamwise drag force per unit mass (F_D) is parameterized by using a bulk drag coefficient (C_D), a bulk canopy density (a) and a an averaged velocity (U), where the overbars are implicitly placed on these variables:

$$F_D = \frac{1}{2}\overline{C_D a U}^2 . \tag{3.83}$$

The bulk canopy density, presented in **Eq. 3.65** of Section 3.2.2, is a vertically integrated parameter that accounts for the frontal area of the plant per unit volume and the number of plants in a unit area. For a plant canopy with a vertically homogeneous morphology, the bulk drag coefficient can be shown to reduce to a simple expression involving an element lateral dimension and the spacing between the roughness elements. In the same fashion, the bulk drag coefficient characterizes the average drag force imposed by the canopy and is constant everywhere inside the element array, as discussed later in Section 3.5.3. Since each of the parameters in **Eq. 3.83** is a result of the integration of a vertically-varying quantity, their values depend upon the limits placed on the integration.

Following Dunn *et al.* (1996), two different formulations can be defined to characterize the drag exerted by an emergent or a submerged plant canopy of the flow. To avoid the confusion created by their terminology, the nomenclature for the two drag estimates has been changed. The depth averaged drag, F_{DH}, can be obtained by integrating each term up to the free surface, H, while the canopy averaged drag, F_{DC}, corresponds to an integration up to the effective canopy height, h. For an emergent canopy ($H = h$), the depth and canopy averaged bulk drag coefficients, bulk densities and averaged velocities are equal to each other. As the level of submergence increases, the value of the two estimates should depart since the canopy progressively becomes a smaller part of the total flow and induces less drag. Calculating the canopy-averaged drag for submerged conditions is equivalent to considering the drag exerted by the canopy on its surrounding fluid as if the surface layer were not present. The canopy-averaged drag is a useful estimate of the bulk drag created in an array of roughness elements and has been used to explore the effect of the roughness density on the bulk drag coefficient (Nepf and Vivoni, 1998).

The drag force exerted by the canopy on the entire flow, including the surface layer, can be estimated by modifying **Eq. 3.83** to include the terms integrated up to the water depth, H:

$$F_{DH} = \frac{1}{2}\overline{C_{DH} a_H} U_m^2, \tag{3.84}$$

where U_m is the depth-average velocity defined in **Eq. 3.68**, a_H is the depth-averaged bulk density calculated from **Eq. 3.65** and C_{DH} is the depth-averaged bulk drag coefficient. Similarly, the canopy-averaged drag force within the vegetation layer can be computed as:

Table 3.9. Bulk canopy density parameters for the *Case A* and *B* experimental runs.							
Parameter / Run	**1A**	**2A**	**3A**	**4A,B**	**5B**	**6B**	**7A**
Depth-averaged Bulk Density a_H (cm^{-1})	0.047	0.023	0.015	0.009	0.010	0.007	0.003
Canopy-averaged Bulk Density a_C (cm^{-1})	0.047	0.048	0.050	0.050	0.051	0.050	0.052

$$F_{DC} = \frac{1}{2}\overline{C_{DC} a_C U_c^2}, \tag{3.85}$$

where U_c is the in-canopy velocity defined in **Eq. 3.67**, a_C is the canopy-averaged bulk density defined in **Eq. 3.65** and C_{DC} is the canopy-averaged bulk drag coefficient. The values for U_c and U_m have been presented in **Table 3.6**, while the values for the bulk drag coefficient will be presented in **Table 3.10**.

The depth and canopy-averaged bulk canopy densities for the experimental runs in *Cases A* and *B* are shown in **Table 3.9**. The smaller values of a_H as compared to a_C are expected since the canopy occupies a smaller portion of the integration region for the total depth computation. This is true for all the experimental cases except for the emergent canopy ($H = h$), where the two bulk canopy density definitions match. For the depth-averaged bulk canopy density a_H, the variation in the characteristic depth leads to progressively smaller values since the vegetation layer becomes smaller in relation to the depth of the overlying surface layer. The small variation among the depth and velocity cases for the submerged bulk canopy density a_C is due to the weighting by the mean streamwise velocity profile inside the canopy, which varies slightly across the cases.

3.5.2 Drag Coefficient Profiles

As discussed in the theoretical analysis of the flow through the seagrass canopy, the longitudinal momentum equation reduces to a simple balance between the forcing in the system, the drag exerted by the plant canopy and the turbulent stress, as shown in **Eq. 3.22** and repeated here for reference:

$$C_D(z) = \frac{gS_w - d\left(\langle \overline{uw} \rangle(z)\right)/dz}{1/2\, a(z) \langle \overline{U} \rangle(z)^2}. \tag{3.86}$$

The measurements of the mean streamwise velocity, the Reynolds stress and the canopy density profiles presented in Sections 3.2 and 3.3 allow the computation of the drag coefficient (C_D) profiles for the depth-varied and velocity-varied cases. The mean velocity and the canopy density both vary with elevation so that the drag coefficient is a vertically-varying quantity. The drag coefficient is also a temporal and horizontally-averaged quantity since the mean velocity and the Reynolds stress used to compute C_D have been averaged in time and across the horizontal plane. The gradient in the Reynolds stress (uw) was computed from a finite differencing scheme similar to that employed for the mean velocity gradient and described in Section 3.3.1.

Since the vertically-varying drag coefficient in **Eq 3.86** is a result of the difference between the surface slope and the gradient of the turbulent stress, the value of C_D is very sensitive to the experimental and computational errors made in computing these two quantities. The error analysis presented in Section 2.3.2.3 for the acoustic Doppler velocimeter addressed the uncertainties in the measurement of the mean velocity and the Reynolds stress. For the ten minute sampling interval, it was shown that the average statistics were stationary in the mean and variance, giving confidence in the results. Close to the bed, however, the signal reflection introduces errors in the measurements that affect the value of C_D directly. Considering this deficiency, Dunn *et al.* (1996) calculated C_D at ADV measurement locations that were greater than 2.5 cm from the bed. In this study, the value of C_D is presented at all the measurement elevations with the recognition that the lowest most points may be prone to larger uncertainties.

The drag coefficient profiles computed from **Eq. 3.86** for the experimental runs of *Cases A* and *B* are shown in **Figures 3.29** and **3.30**. The general shape of the drag coefficient profiles for all the experimental cases is similar to the results obtained by Dunn *et al.* (1996) for the flow through a flexible vegetation canopy, a monotonically decreasing function of depth. Specifically, the resemblance is for the cases which the authors described as prone plant conditions, having deflection angles greater than 50 degrees. When the deflection angle was smaller, the drag coefficient profile for the flexible cylinders exhibited a peak at $0.75h_p$, which did not differ substantially from the measurements made in a rigid cylinder canopy, . In this study, the increase in the deflection angle for the *Case B* experimental runs did not have a significant impact on the profile shape, nor does any profile resemble the results obtained by Dunn *et al.* (1996) for the rigid canopy. This suggests that in terms of drag the seagrass meadow can be considered to be flexible, even comparable to prone conditions, despite not having explored this plant flow regime in this experimental study.

Three distinct regions can be identified from the profiles, a near bed region ($z/h_p < 0.2$) characterized by a high value of the drag coefficient, a constant drag coefficient region over most of the plant height ($0.2 < z/h_p < 0.7$) and a region of decreasing or negligible drag coefficient near the canopy height ($z/h_p > 0.7$). Near the bed, the drag coefficient in the cylinder-like stem region is high, reaching values on the order of 3 to 5 for the lowest most measurement point. Typical values for the drag coefficient of a cylinder at the drag Reynolds number within the lower canopy region ($Re_D = 180$) are on the order of $C_D = 2$ (Granger, 1995). Therefore, the drag coefficients for the near bed region in this experimental study are not unreasonably high. It is unclear why the drag coefficients for the points closest to the bed ($z/h_p = 0.006$) are larger than expected. A possible explanation may lie in the fact that these velocity measurements are so close to the bed that significant signal reflections cause errors in the measurement of the velocity statistics, but this point could not been confirmed from the error analysis presented in Section 2.3.2.3. If the lowest points are ignored, the drag coefficient has an average maximum value of $C_D = 1.84$ across the experimental runs in *Cases A* and *B*, reasonably close to the value of the drag coefficient for a single cylinder at the same Reynolds number flow regime.

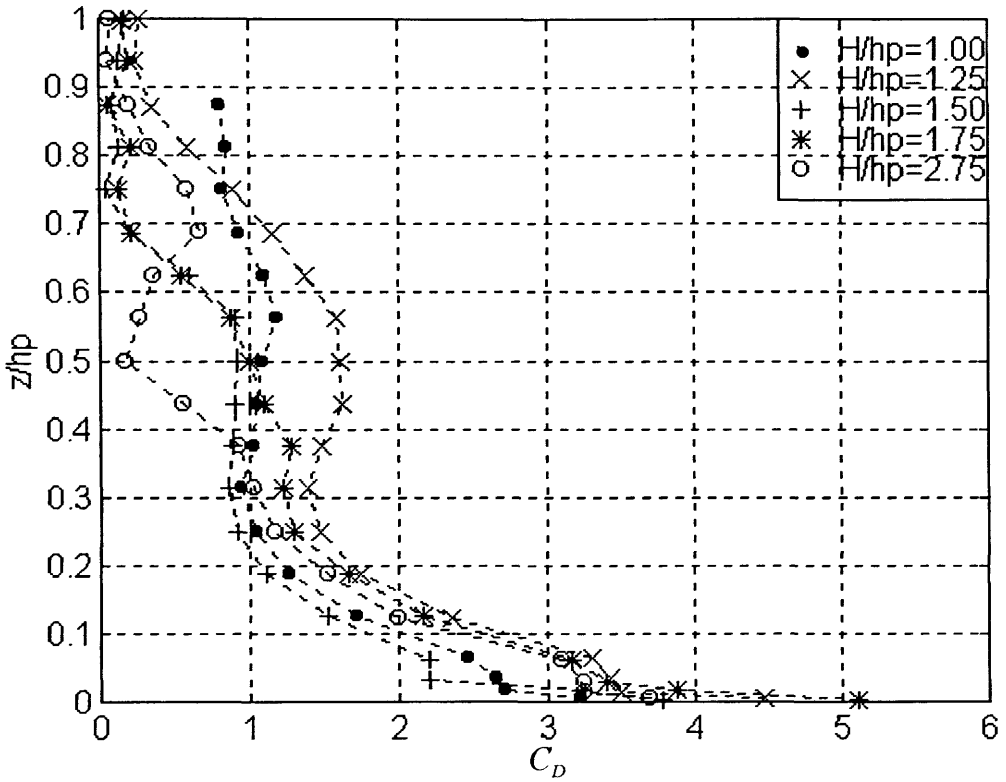

Figure 3.29 Drag coefficient profiles for the *Case A* experimental runs. The vertical axis is normalized by the undeflected canopy height, h_p. The drag coefficient is computed for the region inside the canopy, $z/h_p \leq 1.00$. Note that as H/h_p increases, the region of constant drag coefficient becomes less discernable and the drag coefficient approaches zero at a lower elevation. Since the drag coefficient is computed from the horizontally averaged velocity and shear stress, there is no need to include horizontal bars representing the deviation from the horizontal average.

The interior region in the drag coefficient profiles occurs at the level of the plant sheath and the lower blade region where the blades are fanning out from the underlying stems. A relatively constant drag coefficient is observed over a substantial vertical distance for the experimental runs in *Case A*. The constancy in the drag coefficient is related to the vertically uniform plant morphology in this region for those flows that do not exhibit considerable plant deflection or waving. As the plant vibrational frequency and the plant deflection angle increase, the drag coefficient in the interior region becomes progressively less constant, as seen by the decrease in the extent of the constant C_D region with the increase in the characteristic depth and the flow discharge, as shown in **Figures 3.29** and **3.30**. For the *Case B* runs, it is evident that the drag coefficient decreases steadily from the maximum value near the bed to zero at the canopy height without having any appreciable region of constant C_D. Within the interior region, the values of drag coefficient for the experimental runs in *Case A* averages $C_D = 1.17$, a value that is within those obtained by Dunn *et al.* (1996) over a broader range of canopy densities and drag Reynolds numbers ($a = 0.273 - 2.46$ m^{-1}; $Re_H = 0.57 \times 10^5 - 2.58 \times 10^5$).

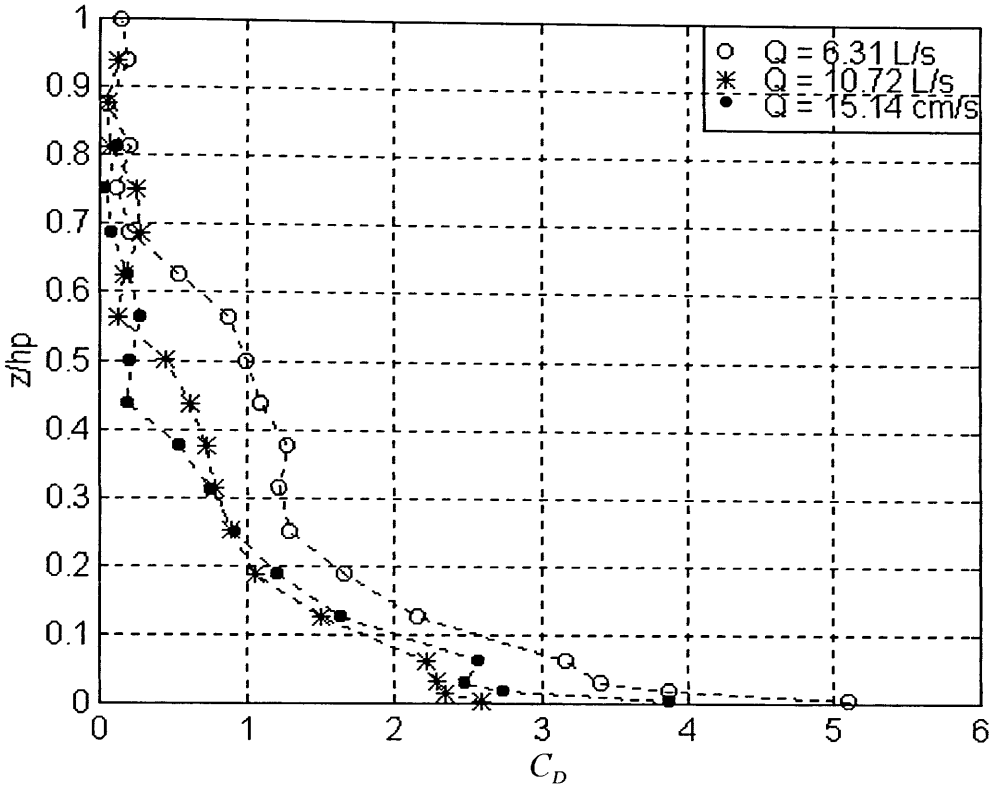

Figure 3.30. Drag coefficient profiles for the *Case B* experimental runs. The vertical axis is normalized by the undeflected canopy height, h_p. The drag coefficient is computed for the region inside the canopy, $z/h_p \leq 1.00$. Note that as the flow discharge (Q) increases, the drag coefficient decreases over most of the profile and reaches zero at a lower elevation.

Near the canopy height, the drag coefficient attains values that are close to zero. The decrease in C_D at the canopy height is expected since the flow around an immersed body of finite length exhibits decreased form drag at the top since the fluid is able to bleed around the end of the object and disrupt the pressure gradient across the body (Brunet *et al.*, 1994). Having a low value for the drag coefficient at the canopy height is not indicative of having low drag since the drag force term (F_D) also contains the mean velocity squared. In fact, the highest levels of drag occur in the upper canopy where the plants absorb a great deal of momentum, as evidenced by plant motion response and the sharp decrease in the mean flow into the canopy.

The effect of the level of submergence and the velocity of the flow in the canopy can be explored by comparing the different profiles for the *Case A* and *B* experimental runs in **Figures 3.29** and **3.30**. Although there does not seem to be a clear progression of the behavior of C_D with the characteristic depth, the profiles become less uniform as H/h_p increases. For the smallest characteristic depth, the C_D profile is practically constant, averaging 1.00 in the region from $z/h_p = 0.2$ to 0.9. In contrast, for $H/h_p = 2.75$, the value of C_D varies from 1.17 at $z/h_p = 0.2$ to 0.2 at $z/h_p = 0.9$, almost a six fold decrease.

The shape of the drag coefficient profile changes from being a uniform to a monotonically decreasing function as the depth of the surface layer increases. This suggest that the drag exerted by the meadow on the unidirectional flow varies according to the relative contribution from a wake versus a shear flow regime, as explained in Section 3.3.1. When the plant canopy is nearly emergent, the flow encounters roughness elements over the entire water depth. The plants extract mean kinetic energy from the flow through drag and convert it to wake turbulence. The resulting turbulence intensity profile for $H/h_p = 1.00$ is uniform over the entire depth, as shown in **Figure 3.10**. Since the generation of turbulence in an emergent canopy is phenomenologically related to the drag exerted by the vegetation (Nepf and Vivoni, 1997), the uniform mean velocity and turbulence intensity profile is an indication that the drag coefficient profile should also be uniform with depth, as confirmed in this experimental study by the $H/h_p = 1.00$ profile. The link between the extraction of mean kinetic energy through drag and its conversion to turbulent kinetic energy in the plant wakes is a strong suggestion that the drag coefficient and the turbulence intensity profiles should be similar.

As the level of submergence increases, the differential drag causes the water to flow through the region of less resistance, the surface layer. The shear generated at the interface of the two flow zones as a result of the differential drag creates the eddy motions that are responsible for the vertical exchange of momentum. As downward moving fluid enters the canopy, the plants move in response to the forcing and extract energy from the mean flow, converting it to turbulence. In the upper canopy region, the plants extract a great deal of kinetic energy, as evidenced by the sharp decrease in the mean velocity profile, and create high levels of turbulence intensity, as shown in the peak values in **Figure 3.10**. Referring once again to the direct link that should exist between the drag coefficient and the turbulence intensity profiles, it is not a surprise that the submerged cases demonstrating a non-uniform turbulence intensity profile also demonstrate a vertically varying C_D profile.

The effect of flow rate on the drag coefficient profiles can be observed in **Figure 3.30**. Increases in Q lead to reductions in the effective canopy height that are translated into a drag coefficient profile that diminishes to zero at lower elevations. For the highest flow discharge (Q = 15.14 L/s), the drag coefficient reaches values close to zero at an elevation $z/h_p = 0.44$, while the lowest flow discharge case (Q = 6.31 L/s) does so at $z/h_p = 0.69$. As the plant blades bend in response to the higher flow rates, the region over which the drag coefficient is defined also diminishes, as shown by the missing data points in the upper canopy region for the higher flow discharge cases. In addition to the decrease in the effective canopy height, the increase in the flow discharge leads to smaller values of C_D within the canopy, due to the streamlining induced by the higher in-canopy velocities.

At this point, it is instructive to use the C_D profiles to estimate the errors in the drag coefficient formula and calculate the characteristic velocity presented in Section 3.1.1. The errors associated with the drag coefficient formulation in **Eq. 3.86** can be evaluated by computing C_D for the region above the canopy. To do so, the value of $a(z)$ has to be assumed to be equal to the density within the upper canopy.

Using the vertical profiles of the mean streamwise velocity and the Reynolds stress for experimental run 7 (H/h_p = 2.75, Q = 15.14 L/s), the average value of the drag coefficient for the points above the canopy was small, C_D = 0.02, relative to the in-canopy values. This confirms that the drag coefficient formula is satisfied throughout the profile. A similar procedure was carried out by Dunn *et al.* (1996), also showing that C_D was negligible above the canopy.

Using the drag coefficient profiles, the characteristic velocity u_s introduced in Section 3.1.1 can be evaluated at the level of negligible Reynolds stress gradient $z = z_b$. Applying **Eq. 3.25** to a vertical location within the stem region (z_b/h_p = 0.25), the characteristic velocity was computed from the values for $C_D(z_b)$, $a(z_b)$ and S_w, as shown in **Table 3.10**. As expected, the results are comparable to the measured velocity values at this location for all the experimental runs, the value of u_s obtained from **Eq. 3.25** being within 5% of the measured velocity. The discrepancy is a result of having assumed a Reynolds stress gradient of zero to obtain **Eq. 3.25** and the measurement of a small value for this parameter at this depth. The values for u_s confirm that this parameter was matched across the depth-variation cases, averaging 2.92 ± 0.12 cm/s, and increases moderately for the flow discharge cases.

3.5.3 Bulk Drag Coefficients

The drag coefficient profiles shown in **Figures 3.29** and **3.30** can be used to determine the bulk properties of the drag coefficient for the different velocity-varied and depth-varied cases. Dunn *et al.* (1996) introduced two bulk drag coefficients, one for an emergent condition and the other for a submerged plant canopy, to characterize the mean effect of the plant canopy on the flow. In this experimental study, these two parameters have been redefined as a depth-averaged and a canopy-averaged bulk drag coefficients due to the possible misinterpretations arising from calculating an emergent drag coefficient for a submerged canopy. The bulk drag coefficients are simply a weighted-average C_D value that can be used for modeling the effect of the vegetation on the flow through a single parameter. The depth-averaged bulk drag coefficient, C_{DH} , appropriate for emergent conditions, is computed from the drag coefficient and the velocity profiles as:

$$\overline{C_{DH}} = \int_0^H C_D(z)\langle\overline{U}\rangle^2 dz \Big/ \int_0^H \langle\overline{U}\rangle^2 dz , \qquad \textbf{(3.87)}$$

where both integrations are carried out from the bottom to the free surface, $z = H$. Calculating the value of C_{DH} for submerged vegetation is equivalent to considering the drag exerted by the canopy on the entire flow. Alternatively, the canopy-averaged bulk drag coefficient can be computed by carrying out the integrations up to the effective canopy height, h:

$$\overline{C_{DC}} = \int_0^h C_D(z)\langle\overline{U}\rangle^2 dz \Big/ \int_0^h \langle\overline{U}\rangle^2 dz . \qquad \textbf{(3.88)}$$

Table 3.10. Bulk drag coefficients and characteristic velocity for *Cases A* and *B* experimental runs.							
Parameter / Run	**1A**	**2A**	**3A**	**4A,B**	**5B**	**6B**	**7A**
Characteristic velocity u_s (cm/s)	2.95	3.08	3.02	2.80	5.07	6.04	2.76
Depth-averaged Drag Coefficient C_{DH}	1.26	0.57	0.16	0.12	0.08	0.05	0.01
Canopy-averaged Drag Coefficient C_{DC}	1.26	1.25	0.58	0.72	0.47	0.47	0.51

The integrals in **Eq. 3.87** and **3.88** were calculated by using a trapezoidal integration scheme for the mean velocity and drag coefficient values at the points in the range of integration. The bulk drag coefficients for the experimental runs in *Cases A* and *B* are shown in **Table 3.10**. As expected, the two bulk drag coefficients for the lowest characteristic depth match ($H = h$). For the other experimental cases the depth-averaged bulk drag coefficient is consistently smaller than the canopy-averaged coefficient since C_{DH} treats the canopy as a small portion of the entire flow while C_{DC} treats the canopy as if there were no surface layer. The depth-averaged bulk drag coefficient is a more appropriate measure of the drag exerted by the meadow on the entire flow and is useful when making a comparison to an alternative drag coefficient estimate made for a similar experimental setup (Morales *et al.*, 1997, unpublished data).

The variation of the bulk drag coefficients with the characteristic depth and the flow discharge are shown in **Figures 3.31** and **3.32**, for C_{DH} and C_{DC}, respectively. The top graph in each figure corresponds to the variation of the bulk drag coefficient with H/h_p, while the bottom graph is the flow discharge variation. The figures show that the bulk drag coefficient varies significantly with the characteristic depth and moderately with the flow discharge, each case leading to smaller values as the parameter is increased. The asymptotic behavior that has been described for other parameters in this experimental study is again seen for the variation of C_{DH} with H/h_p. A sharp decrease in C_{DH} as the surface layer depth is initially increased is followed by a leveling off to a constant value near $C_{DH} = 0.127$ after $H/h_p = 1.50$. After the surface layer is half the plant canopy height, the total drag exerted by the meadow on the flow remains constant for the conditions explored in *Case A*, mainly the constant in-canopy velocity across water depth variation runs. This suggests that the normalized water depth $H/h_p = 1.50$ plays a key role in determining the transition between the two types of drag regimes described in Section 3.5.2. For the canopy-averaged drag coefficient, C_{DC}, a decrease with increasing water depth is also observed. Although not as pronounced as for the depth-averaged coefficient, an asymptotic behavior of C_{DC} is noticeable, reaching an average value of 0.60 for H/h_p greater than 1.50.

The results obtained from the model seagrass canopy are comparable to the bulk drag coefficient estimates made by Dunn *et al.* (1996) for an open channel flow through a flexible cylinder array. The range of values in that study was 0.09–0.27 for C_{DH} and 0.55–1.45 for C_{DC}. The canopy-averaged bulk drag coefficient was found to be a function of the angle of deflection (ϕ_p) and a drop in the value of C_{DC} was attributed to transition from a waving flow regime to prone plant conditions. In this study, the canopy-averaged bulk drag coefficient drops off rapidly after $H/h_p = 1.25$, but the behavior cannot be

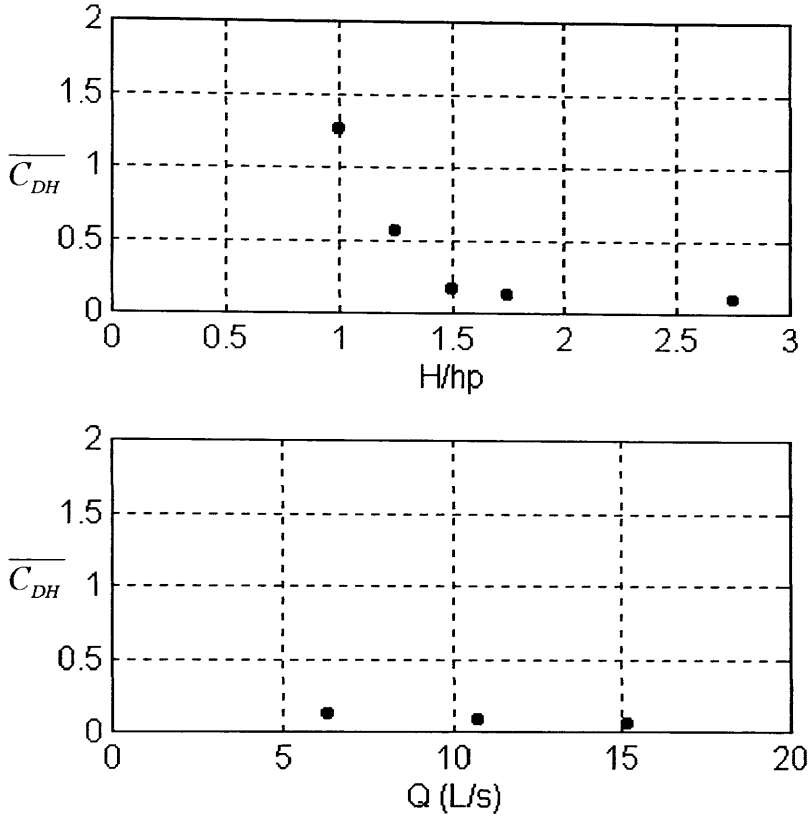

Figure 3.31. Depth-averaged bulk drag coefficient for the *Case A* and *B* experimental runs. The top figure shows the variation with the characteristic depth (H/h_p), while the bottom figure shows the variation with the flow discharge (Q). Note the asymptotic behavior of C_{DH} with H/h_p.

attributed to the deflection angle since the value is relatively small (ϕ_p = 7.45°) and similar to the values at H/h_p = 1.50 and 1.75, as described in Section 3.2.2. The drop off is likely to be an effect of the slightly higher velocities inside the canopy with the increase in the surface layer depth.

Figure 3.33 shows a comparison among the depth-averaged bulk drag coefficients C_{DH} for this study and the values obtained by Dunn *et al.* (1996) for the flexible cylinder array as a function of the characteristic depth, H/h, where using the effective canopy height (h) is more appropriate due to the deflection of the roughness elements. In addition, a third data set is included for comparison of the depth-averaged bulk drag coefficient obtained from a different experimental approach. As part of an undergraduate laboratory project, Morales *et al.* (1997, unpublished data) estimated the drag coefficient of the identical seagrass meadow used in this experimental study under different flow discharge and characteristic depth conditions. The drag coefficient estimate was based on a control volume approach that treated the seagrass canopy as a single unit exerting drag on the gravity forced flow. The bulk drag coefficient was determined from the channel velocity $U_{ch} = Q/A$ and the surface slope measurement, S_w. In addition, by measuring the deflected canopy height, Morales *et al.* (1997) provided information that serves as a useful comparison to the approach taken in this laboratory study.

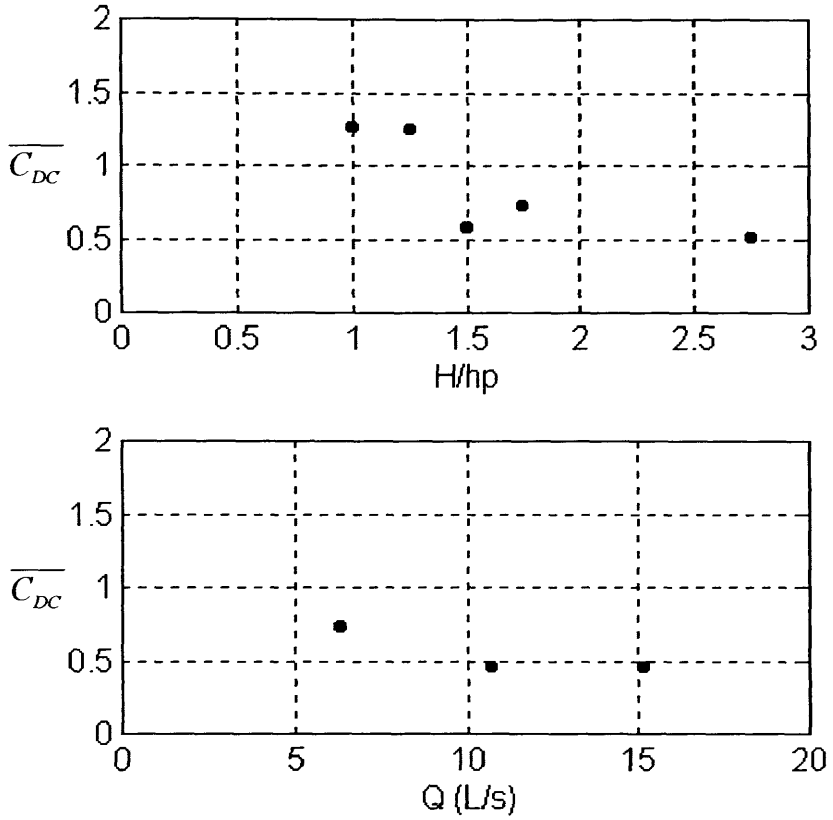

Figure 3.32. Canopy-averaged bulk drag coefficient for the *Case A* and *B* experimental runs. The top figure shows the variation with the characteristic depth (H/h_p), while the bottom figure shows the variation with the flow discharge (Q).

The results shown in **Figure 3.33** indicate that the variation of the emergent bulk drag coefficient for a flexible plant canopy with the characteristic depth collapses onto a common curve for the different flow conditions, plant stiffness and morphologies, and computational approaches used in the three data sets. Thus, the level of submergence is a controlling parameter in the estimation of the drag exerted by flexible vegetation on the entire flow. This result follows the expected trend since the vegetation layer becomes a smaller portion of the total depth as H/h increases and exerts less resistance to the total flow. The data collapse suggests that with additional data on the flow through flexible canopies, a relationship can be obtained between the bulk drag and the relative roughness (h/H). This functional relationship would provide a way of estimating the bulk drag from the knowledge of H and the effective canopy height.

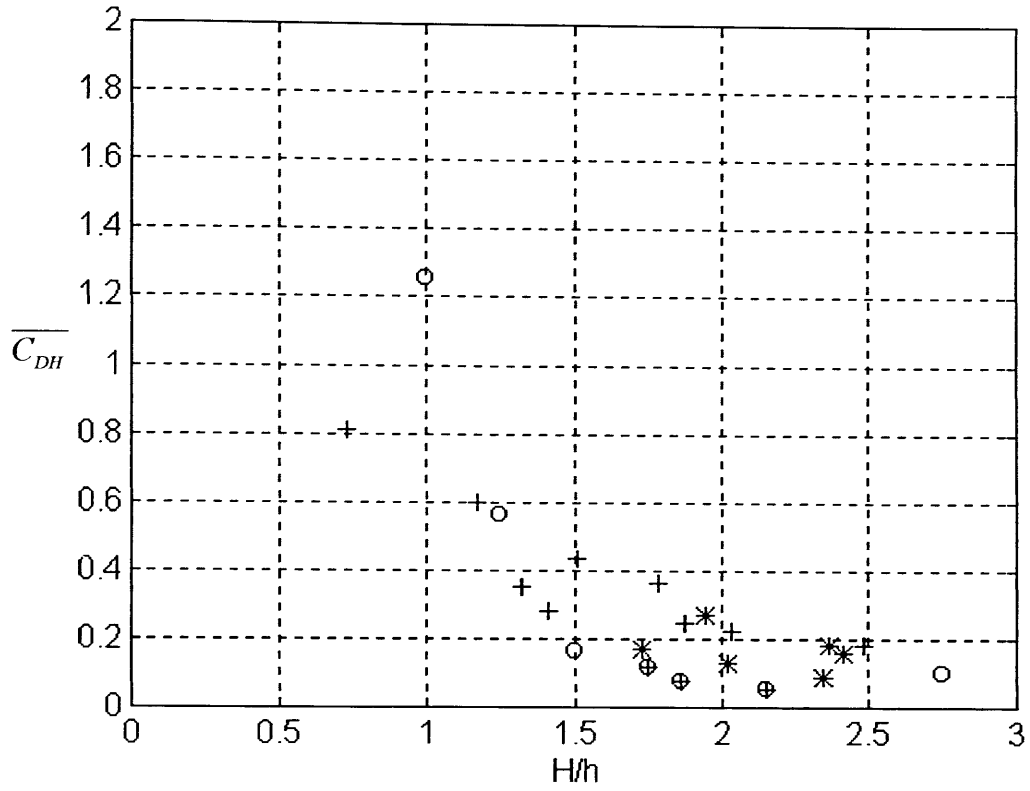

Figure 3.33. Composite plot of the variation of the emergent vegetation bulk drag coefficient with the characteristic depth (H/h) for three data sets: (o) *Case A* experimental runs; (⊕) *Case B* experimental runs; (*) Dunn *et al.* (1996); (+) Unpublished laboratory experiment.

3.5.4 Drag Partitioning

With the information on the bulk drag coefficients, the bulk canopy density and the depth-averaged velocities, the drag force exerted by the seagrass meadow under the emergent and submerged conditions can be computed. The drag force estimates for the model plants can be compared to the drag offered by the underlying bottom in order to determine the relative importance of the seagrass meadow in the total drag in the system. The total drag (D_T) is composed of the contribution from the form drag on the canopy elements (D_P) and the skin friction drag on the bottom substrate (D_S):

$$D_T = D_P + D_S . \tag{3.89}$$

Each drag term can be expressed as a drag force per unit bed area ($\Delta x \Delta y$) and nondimensionalized by the kinetic energy per unit volume $\frac{1}{2}\rho U^2$, where ρ is the density of water and U is the appropriate velocity scale, U_m for the depth-averaged drag formulation and U_c for the canopy-averaged drag. The resulting expression for the plant form drag is similar to the streamwise drag force per unit fluid mass shown in **Eq. 3.83**. For the emergent and submerged plant canopy conditions, the nondimensional drag force per unit bed area due to the plants is:

Table 3.11. Drag partitioning for the *Case A* and *B* experimental runs.							
Parameter / Run	**1A**	**2A**	**3A**	**4A,B**	**5B**	**6B**	**7A**
D_{PH}	0.99	0.26	0.06	0.03	0.02	0.01	0.01
D_{PC}	0.99	0.97	0.46	0.58	0.34	0.29	0.42
D_{SH}	1.95×10^{-3}	1.98×10^{-3}	1.98×10^{-3}	1.99×10^{-3}	1.99×10^{-3}	1.99×10^{-3}	2.00×10^{-3}
D_{SC}	1.95×10^{-3}	1.95×10^{-3}	1.95×10^{-3}	1.95×10^{-3}	1.95×10^{-3}	1.95×10^{-3}	1.95×10^{-3}

$$D_{PH} = \frac{F_{DH}}{\frac{1}{2}\rho U_m^2} = \overline{a_H C_{DH}} H, \tag{3.90}$$

$$D_{PC} = \frac{F_{DC}}{\frac{1}{2}\rho U_c^2} = \overline{a_C C_{DC}} h, \tag{3.91}$$

where the subscripts H and C refer to the emergent and submerged conditions, respectively. The drag due to the bottom is a function of the bed area not occupied by the plants and a skin friction factor, C_b. A typical value of C_b for flow over a smooth flat plate is 0.002 (Schlichting, 1968). After the appropriate manipulations, the nondimensional drag offered by the underlying surface for the flow in a vegetated region under the emergent and submerged plant conditions can be expressed as:

$$D_{SH} = \left(1 - \frac{\pi}{4} d_s \overline{a_H}\right) C_b, \tag{3.92}$$

$$D_{SC} = \left(1 - \frac{\pi}{4} d_s \overline{a_C}\right) C_b, \tag{3.93}$$

where d_s is the stem diameter, 0.64 cm in this study. The values for D_{PH}, D_{PC}, D_{SH} and D_{SC}, shown in **Table 3.11**, reveal that the drag due to the plants is overwhelmingly more important than the drag created by the bottom surface for all the experimental cases. In fact, the plant drag averages 99% of the total drag for the submerged conditions and 93% for the emergent conditions at the plant density of this seagrass meadow. The lack of drag partitioning between the vegetation and the bottom is not surprising considering that the bulk drag coefficients are two to three orders of magnitude larger than the skin friction drag coefficient. Raupach (1992) showed through a theoretical derivation and experimental data that the bottom surface did not contribute significantly to the total drag when the roughness density exceeded a value in the range of 0.03 to 0.1. The roughness density in this seagrass meadow, $\lambda = 0.79$, greatly exceeds this threshold range and it confirms that the effects of the drag imparted by the bottom surface can be safely neglected for all the experimental conditions.

3.6 Structure of Momentum Transport

This section presents the results from the analysis of the structure of the momentum transfer based on the conditional sampling of the Reynolds stress records. It includes the analysis of the stress and time contributions from the different stress events, an analysis of the intermittency of the Reynolds stress, an analysis of the relative contributions made by the stress events and a quantitative description of the frequency of stress events. The last section presents an overall picture of the momentum transfer mechanism for a flexible, submerged plant canopy and a discussion of the effects of the level of submergence and the velocity on the flow sweep-ejection character and the plant motion.

In general, the momentum transfer is observed to be in the downwards directions, as expected since the canopy acts as a sink for the high momentum flow in the surface layer. It is also highly intermittent process, with the major contributions being made during a small portion of the entire time. Large bursts of high momentum fluid impact the canopy elements infrequently, causing the deflection of the flexible plants, the generation of turbulence as the sweep interacts with the plants and the transfer of momentum to the low velocity fluid inside the canopy.

The information provided by the conditional analysis of the Reynolds stress provides a physical explanation for many of the observed velocity statistics presented in Section 3.3 and the plant motion characteristics described in Section 3.2. It also identifies coherent structures within the turbulent flow such that the random process is organized into a periodically describable phenomenon. Conditional analysis has allowed the interpretation of the turbulence in a new light, with an emphasis being placed on describing how coherent eddies formed in the shear region interact with the canopy. A dramatic visualization of the interaction of the turbulent structures with the canopy is the monami, a phenomenon that occurs when the downward moving sweeps force the system at a frequency that approaches the natural frequency response of the flexible plants. As a sweep advances, the downward motion successively bends groups of plants that oscillate out of phase from one another creating the impression of a travelling wave.

As far as it can be concluded from the relevant literature, the determination of the effect of the level of submergence, *i.e.* changing the free surface boundary condition, on the characteristics of the turbulent structures is an original contribution made by this work to the canopy turbulence field. The next sections describe how changing the depth of the surface layer affects the exchange of momentum and thus the water renewal between the surface and vegetation layers.

3.6.1 Quadrant Analysis

The technique of quadrant analysis, introduced in the study of smooth wall laboratory boundary layers (Wallace *et al.*, 1972; Lu and Willmarth, 1973) and extended to rough wall flows (Nagakawa and Nezu, 1977) including vegetation (Raupach, 1981), has become a conventional way to describe the turbulence structure of a wall-bounded flow, with applications made to field investigations as well (*e.g.*, Sukhodolov *et al.*, 1998; Finnigan, 1979b; Anwar, 1981). Quadrant analysis is performed by decomposing the time-averaged turbulent Reynolds stress component, represented in this section by $\overline{u'w'}$, into four categories based upon the sign of the streamwise and vertical turbulent velocities, u' and w'. Each of the four quadrants is associated with a different type of event and a specific form of momentum transport. Quadrant analysis yields information on the contribution of each event to the overall momentum flux and elucidates the dominant turbulent structures present in the flow, although it says nothing about the spatial properties or the flow patterns in turbulent flow (Raupach *et al.*, 1996).

Dividing the $\overline{u'w'}$ plane into four quadrants creates the following events, which are shown in the schematic representation of **Figure 3.34**:

Quadrant 1: $(u'>0)$ and $(w'>0)$	Outward Interaction	S_1
Quadrant 2: $(u'<0)$ and $(w'>0)$	Ejection or Burst	S_2
Quadrant 3: $(u'<0)$ and $(w'<0)$	Inward Interaction	S_3
Quadrant 4: $(u'>0)$ and $(w'<0)$	Sweep or Gust	S_4

The stress transported by the different events is in the opposite direction as that suggested by the quadrant sign. Therefore, the ejection and the sweep events (Quadrants 2 and 4) contribute towards the downwards diffusion of momentum while the interaction events (Quadrants 1 and 3) represent upwards transfer. The dominance of one type of event over another is a telling sign of the turbulent structure in the flow. For example, laboratory studies in smooth walls have shown that the ejection is the most important event throughout most of the boundary layer, but that in the viscous sublayer, the sweep makes the dominant contribution (*e.g.*, Antonia, 1981).

A fifth type of event known as the hole event is usually defined in the quadrant analysis of the Reynolds stress. As indicated in **Figure 3.34** with the shaded area, the hole region is an excluded zone in the (u', w') plane. The shaded region is bounded by the hyperbola $|\overline{u'w'}| = H_o|\overline{u'w'}|$. The hole parameter, H_o, serves as a threshold value and enables the use of quadrant analysis for determining the relative importance of intermittent events. As H_o is increased, a larger portion of the $\overline{u'w'}$ plane is excluded from the analysis and the conditional averaging of the Reynolds stress is focused on larger and less frequent values.

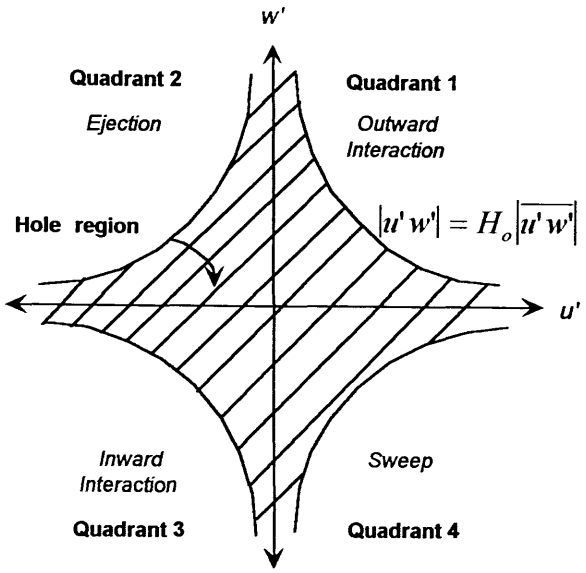

Figure 3.34. Schematic drawing of the five regions utilized in the quadrant analysis of the Reynolds stress ($u'w'$ space). The cross hatched hyperbolic region, defined by **Eq. 3.96,** expands outward as the hole size (H_o) increases.

In order to perform the quadrant analysis, the instantaneous Reynolds stress $u'w'(t)$ is divided into the four categories based on the sign of the turbulent velocities and an average is taken for each quadrant. This conditional-average represents the contribution from an event to the total stress and is defined as:

$$\|u'w'\|_{i,H_o} = \lim_{T_s\to\infty} \frac{1}{T_s}\int_0^{T_s} u'(t)w'(t)I_{i,H_o}(t)dt\,, \qquad \textbf{(3.94)}$$

where the time averaging is performed over a sampling period T_s and the symbol (|| ||) is used to represent the conditional average since the angle brackets have been used to denote the horizontal-average. The indicator function, $I_{i,Ho}$ obeys the following criteria:

$$I_{i,H_o} = \begin{cases} 1, \text{ if the point } (u'w') \text{ lies in the } i\text{th quadrant} \\ \quad \text{and } |u'w'| \geq H_o|\overline{u'w'}| \\ 0, \text{ otherwise.} \end{cases}, \qquad \textbf{(3.95)}$$

The second criteria in defining an indicator value of 1 is based on the definition of the threshold hole size parameter, which is simply a ratio of the magnitude of the instantaneous Reynolds stress to the magnitude of the time-averaged Reynolds stress (Raupach, 1981):

$$H_o = \frac{|u'w'|}{|\overline{u'w'}|}. \qquad \textbf{(3.96)}$$

A hole size parameter of H_o = 4, for example, implies that the value of the Reynolds stress at that time interval is four times larger than the mean for the entire stress time series.

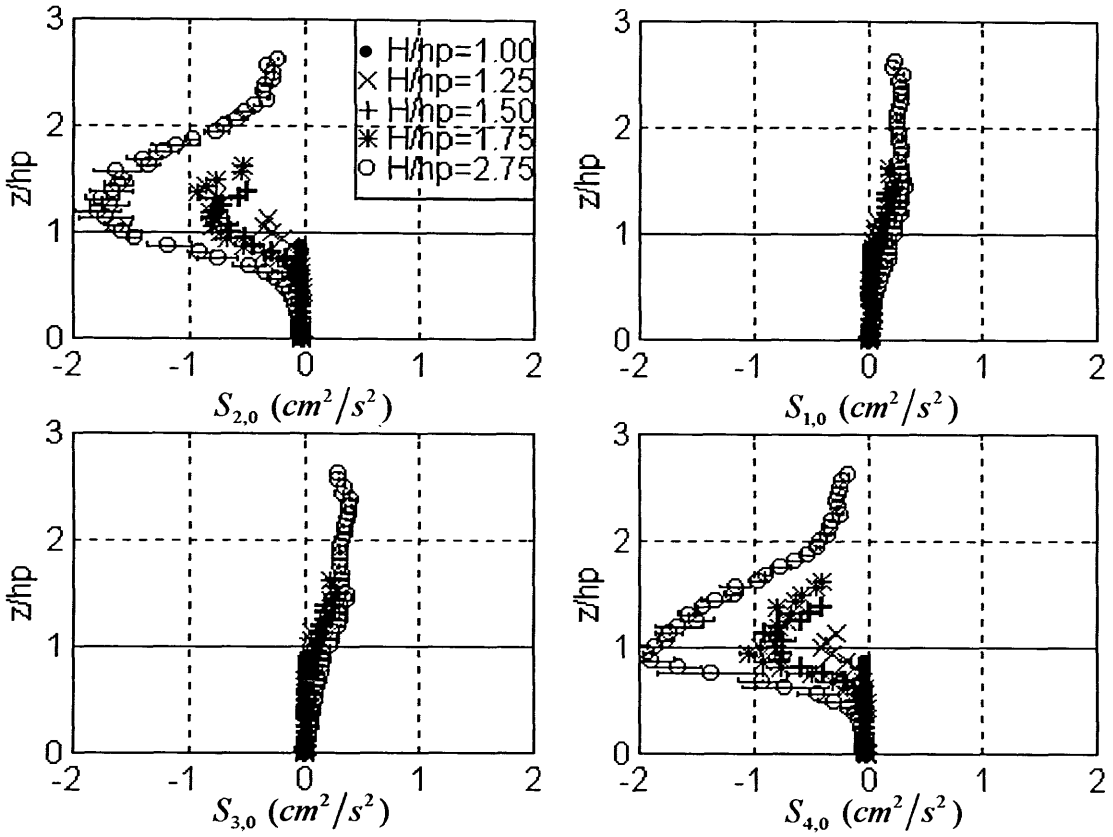

Figure 3.35. Dimensional conditional-averaged stress contribution from each quadrant for the *Case A* experimental runs. The figures are arranged in the pattern of the $u'w'$ plane and the hole size is equal to zero, $S_{i,0}$. The vertical axis is normalized by the canopy height, represented by the horizontal solid line. Downward transport of momentum is negative ($S_{2,0} < 0$, $S_{4,0} < 0$) while upwards transfer by the interaction events is positive ($S_{1,0} > 0$, $S_{3,0} > 0$). The bars represent the variation in the stress contribution from the three vertical profiles (*i.e.* horizontal deviation).

The conditional-averaged contribution from each quadrant to the total shear stress is usually expressed as a stress fraction for easier comparison among each event. The normalization of the conditional stress is performed either by the time-average Reynolds stress (*e.g.*, Raupach, 1981; Shaw, *et al.*, 1983) or by the longitudinal and vertical turbulent velocities (Raupach *et al.*, 1986):

$$\widetilde{S}_{i,H_o} = \left\{ \frac{\left\| u'w' \right\|_{i,H_o}}{\overline{u'w'}}, \quad \frac{\left\| u'w' \right\|_{i,H_o}}{\sigma_u \sigma_w} \right\}. \tag{3.97}$$

In the first normalization scheme, the stress fraction indicates the relative contribution of each event in comparison to the total stress, while in the second scheme, the stress fraction represents the contribution from each quadrant relative to the total level of turbulence at that point. These two definitions imply that the sum of the stress fractions for $H_o = 0$ are equal to one and to the correlation coefficient, respectively:

$$\sum_{i=1}^{4} \widetilde{S}_{i,0} = \left\{ 1, \quad r_{uw} \right\}. \tag{3.98}$$

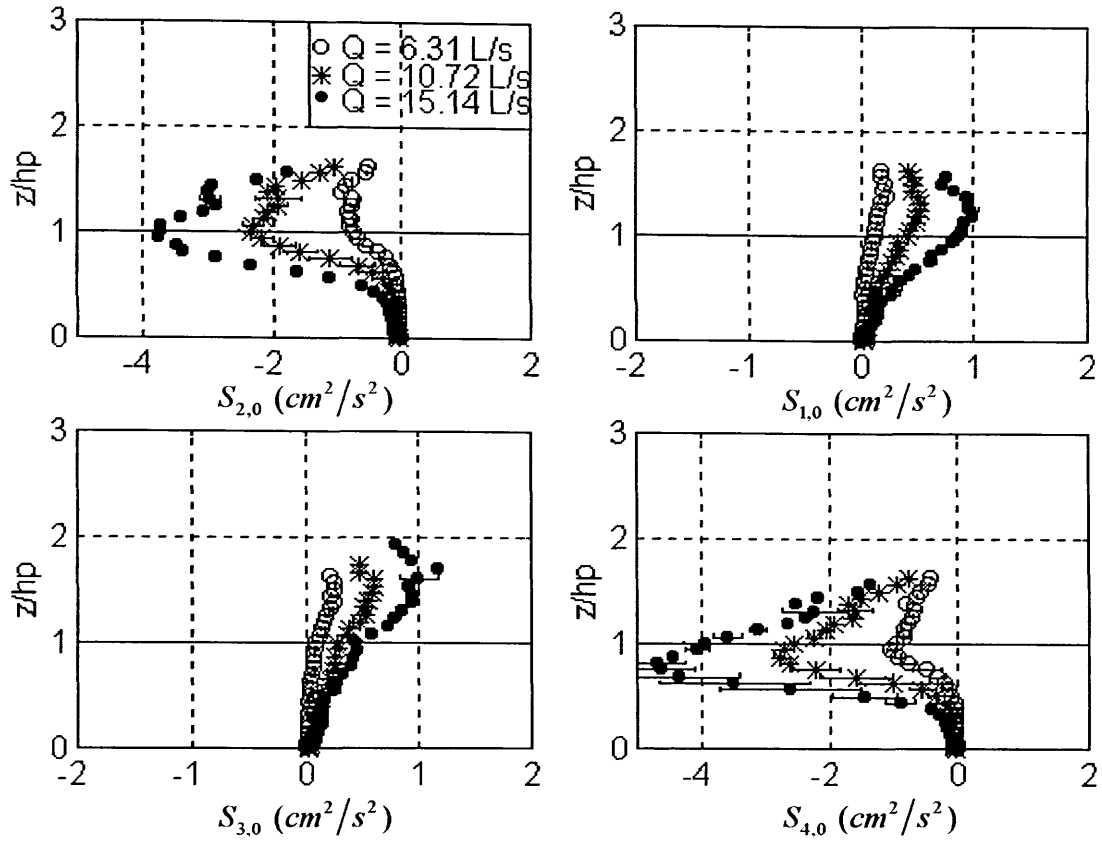

Figure 3.36. Dimensional conditional-averaged stress contribution for the *Case B* experimental runs. Notice that the horizontal axis for the sweep and the ejection events has been extended ($-5 \leq S_{i,0} \leq 2$) relative to the interactions to accommodate the large values for the discharge cases.

Both normalization schemes were considered here. Unfortunately, neither option seemed to be an appropriate choice. Normalizing by the total stress was problematic in the region close to the bed ($z/h_p < 0.25$) where the time-averaged Reynolds stress was either close to zero or positive. As a result, the values of S_{iHo} were either exceedingly high or the sign of each event was reversed because the sign of the shear stress was positive. On the other hand, normalizing by the turbulent velocities resulted in stress fraction profiles that collapsed onto a single curve resembling the correlation coefficient profiles in **Figures 3.22** and **3.23,** which indicates similarity among the r_{uw} profiles. This data collapse obscured the interpretation of the depth and velocity variation. In addition, the normalization hid the absolute differences between the downwards and upwards transport terms. For these reasons, the dimensional stress (cm^2/s^2) is used in the present study with the recognition that the sum of the different components is equal to the total time-averaged Reynolds stress at that the point:

$$S_{i,H_o} = \|u'w'\|_{i,H_o} \text{ and } \sum_{i=1}^{4} S_{i,0} = \overline{u'w'}. \qquad \textbf{(3.99)}$$

For selected comparisons, however, the normalization by the Reynolds stress will be used, as defined in **Eq. 3.97**, so that a fractional contribution at a specific elevation can be computed (*e.g.* **Table 3.12**).

Table 3.12. Stress fractions at the effective canopy height for the *Case A* and *B* experimental runs.							
Parameter / Run	**1A**	**2A**	**3A**	**4A,B**	**5B**	**6B**	**7A**
$S_{1,0}(z = h)/\overline{u'w'}(z = h)$	–	–0.11	–0.11	–0.09	–0.08	–0.09	–0.08
$S_{2,0}(z = h)/\overline{u'w'}(z = h)$	–	0.49	0.53	0.50	0.51	0.48	0.53
$S_{3,0}(z = h)/\overline{u'w'}(z = h)$	–	–0.10	–0.09	–0.07	–0.06	–0.06	–0.07
$S_{4,0}(z = h)/\overline{u'w'}(z = h)$	–	0.72	0.67	0.66	0.64	0.67	0.63

The dimensional stress contributions from each quadrant for $H_o = 0$ are shown in **Figures 3.35** and **3.36** for the experimental runs in *Cases A* and *B*. The first feature to note is that the total Reynolds stress is a result of the sum of two large negative components ($S_{2,0}$ and $S_{4,0}$) and two small positive components ($S_{1,0}$ and $S_{3,0}$). In the region directly above the canopy ($1 \leq z/h_p \leq 1.5$), the ejection or burst contribution is the dominant event, while directly below the canopy height ($0.5 \leq z/h_p \leq 1$), the sweeps or gusts contribute more to the time-averaged Reynolds stress. The larger contributions from $S_{4,0}$ in the upper canopy region indicate that the turbulent velocity pair ($u' > 0$, $w' < 0$) is responsible for the downward movement of surface layer fluid with higher than average longitudinal velocity into the canopy, *i.e.* sweep. The dominance of $S_{2,0}$ in the region above the canopy suggests that the lower velocity fluid within the canopy moves upwards into the surface layer ($u' < 0$, $w' > 0$), *i.e.* ejection. Throughout the profiles, the interaction events make a very small contribution to the shear stress, so that low momentum fluid is rarely transported downwards and high momentum fluid rarely moves upwards. The relationships among the stress components for the $H_o = 0$ case will be explored in Section 3.6.3 with the stress ratios.

At the level of the effective canopy height, h, the fraction of the total stress associated with each event can indicate the direction of the momentum transfer and the variation of the stress distribution among the experimental runs in *Case A* and *B*. **Table 3.12** shows the stress defined in **Eq. 3.99** normalized by the total Reynolds stress $\overline{u'w'}$, which is equivalent to the first element in **Eq. 3.97** at the depth $z = h$. By normalizing with the Reynolds stress, a negative quantity at the canopy height, the sign of each of the events is reversed. The sum of the positive sweep and ejection and the negative interaction components is equal to unity, as mentioned in **Eq. 3.98**. Averaging over all cases, the sweep stress accounts for 49.5% and the ejections for 37.8% of the total Reynolds stress at $z = h$. Across the interface of the vegetation and surface layers, more momentum is being transported downwards by the ejection and sweeps than upwards by the interaction events, which supports the idea that the canopy serves as an efficient sink for momentum originating in the surface layer. The greater degree of sweeps over ejections also suggests that not all the high momentum fluid that moves downward into the canopy causes low-speed fluid to move upwards, so that a portion of the momentum is absorbed by the plant motion. A discussion of a conceptual model for momentum transport based on similar arguments will be given in Section 3.6.5.

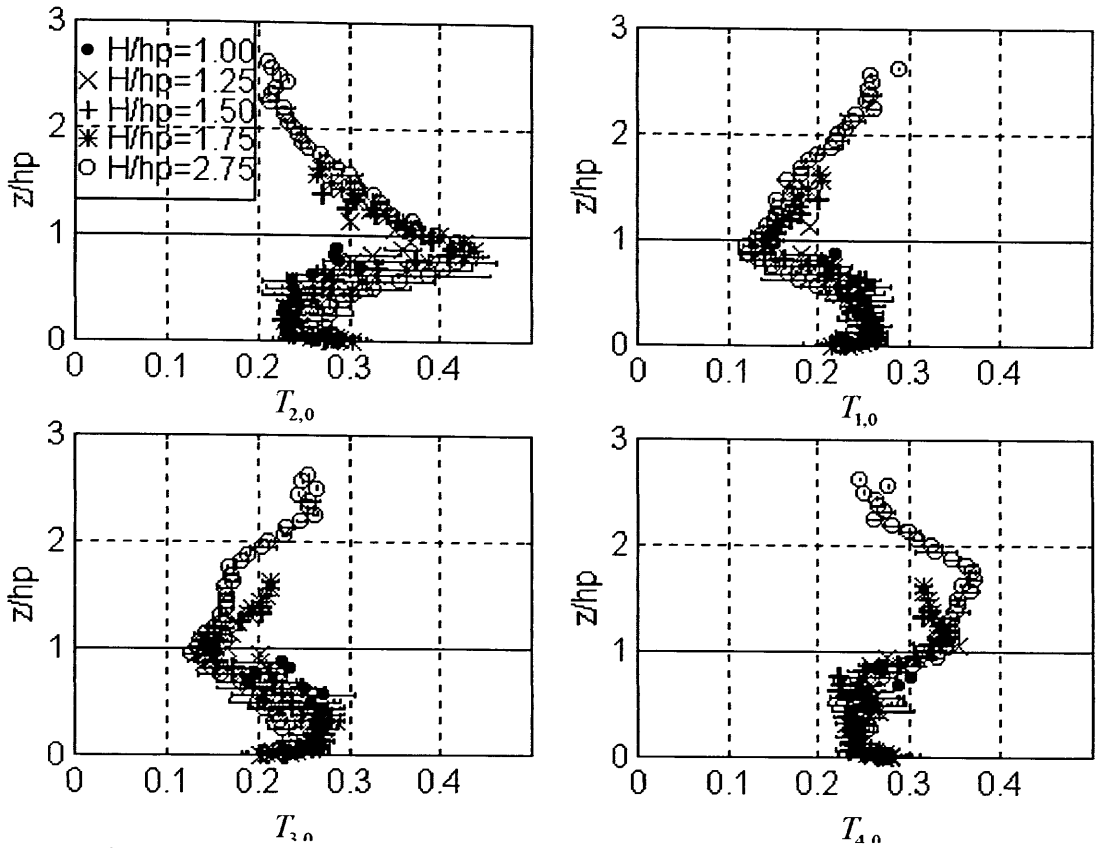

Figure 3.37. Fractional time contribution from each quadrant for the *Case A* experimental runs. Notice the equipartition of time among the quadrants ($T_{i,0} = 0.25$) in the lower canopy region and the dominant role played by the sweep and ejection events ($T_{2,0}$ and $T_{4,0}$) near the canopy height.

In addition to being able to describe the contribution to the total Reynolds stress from different turbulent velocity pairs, the quadrant analysis can also be used to determine the fraction of time in the Reynolds stress record that is occupied by a particular type of event. The time fraction during which the stress contribution is being made is easily determined from the time average of the indicator function described in **Eq. 3.95** and can be expressed formally as:

$$T_{i,H_o} = \lim_{T_s \to \infty} \frac{1}{T_s} \int_o^{T_s} I_{i,H_o}(t)dt \,. \qquad \textbf{(3.100)}$$

When $H_o = 0$, as in **Figures 3.37** and **3.38** for the experimental runs in *Cases A* and *B*, the sum of the fractional time contribution from each event is unity. These two figures indicate that the time occupied by the different events changes over depth. In the lower canopy region ($z/h_p < 0.25$), all the events occupy approximately the same amount of time, so that $T_{i,0}$ is close to 0.25 for all the quadrants. As the canopy height is approached from the bottom, the time fraction of the Reynolds stress corresponding to the sweep and the ejection events increases, with the corresponding decrease for the interaction events. After the peak at $z = h$, the interaction event proportion increases relative to the ejections and sweeps and the $H/h_p = 2.75$ case is suggestive that equipartitioning occurs at large distances from the submerged meadow.

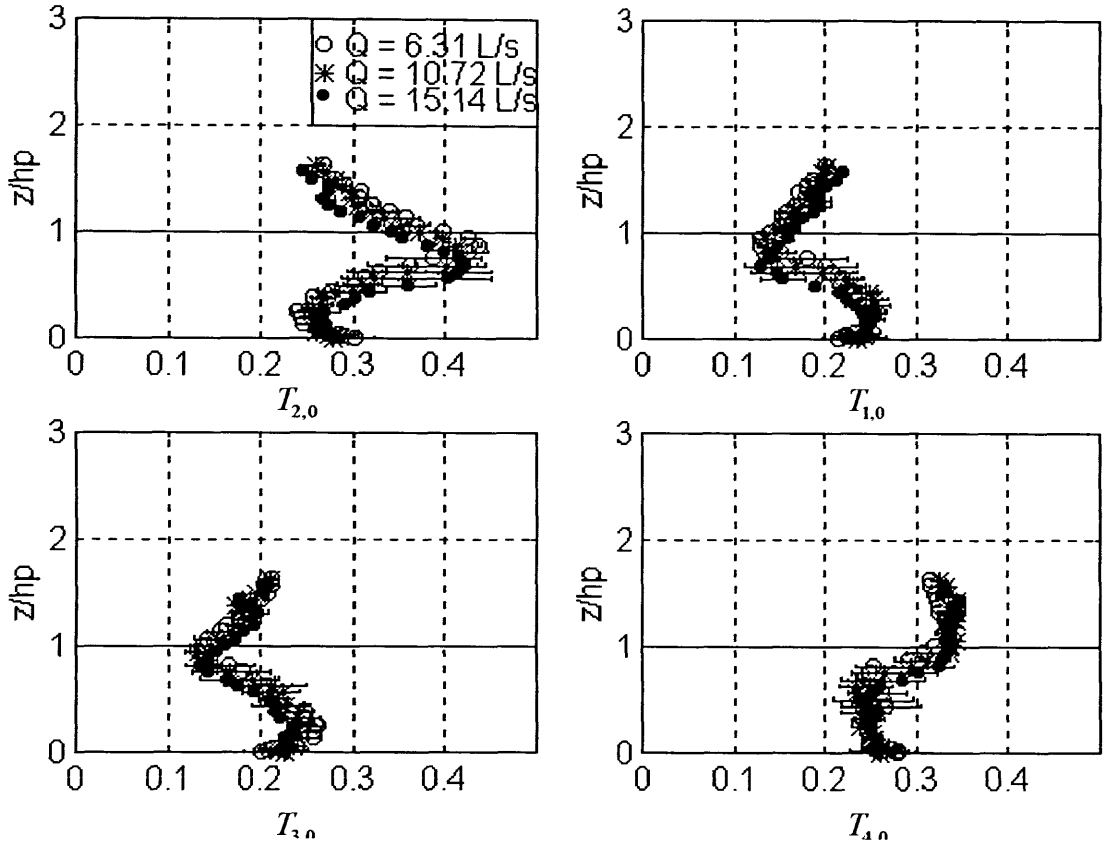

Figure 3.38. Fractional time contribution from each quadrant for the *Case B* experimental runs. As with the stress contribution plot (**Figure 3.36**), the vertical axis is normalized by the undeflected canopy height, h_p. Using the effective canopy height improved the profile collapse.

A closer inspection of the time fraction at the effective canopy height, h, reveals information as to the relative time occupied by each event at the location of vertical exchange between the surface and vegetation layers. **Table 3.13** lists the time fractions at $z = h$ for the experimental runs with available Reynolds stresses (runs 2–7). The events that are responsible for the downward flux of momentum, the ejections and the sweeps, occupy an average of 38.7% and 32.6%, respectively, and together account for 71.3% of the total time. The fact that the sweeps have a larger contribution to the total stress, but occupy a smaller percentage of the total time relative to the ejections is an important observation. It implies that the downward movement of high-speed fluid into the canopy is stronger in an absolute sense than the upward movement of a low-speed fluid volume. Over a slightly shorter time interval, the sweep is able to contribute more to the overall stress than an ejection. In the same sense, because the upward movement of fluid from the interaction events occupies a larger percentage of the total time (28.6%) relative to the contribution made to the total stress (12.7%), the strength of an individual interaction event is exceedingly small compared to the sweep and ejection events. A similar analysis can be made when considering the time fraction at different threshold levels, as presented in Section 3.6.2. In that case, the disparity among the stress and time proportions indicates the degree of intermittency in the Reynolds stress event.

Table 3.13. Time fractions at the effective canopy height for the *Case A* and *B* experimental runs.							
Parameter / Run	**1A**	**2A**	**3A**	**4A,B**	**5B**	**6B**	**7A**
$T_{1,0}$	–	0.15	0.14	0.14	0.14	0.14	0.13
$T_{2,0}$	–	0.37	0.38	0.40	0.40	0.40	0.40
$T_{3,0}$	–	0.17	0.15	0.14	0.13	0.13	0.14
$T_{4,0}$	–	0.31	0.33	0.32	0.34	0.33	0.34

Having described the changes for the stress and time contributions to the total Reynolds stress over the depth profile, it is now appropriate to analyze the specific effects that the characteristic depth and the flow discharge variation have on the $S_{i,0}$ and $T_{i,0}$ profiles in **Figures 3.35** through **3.38**. The increase in the magnitude of the stress contribution (in cm^2/s^2) in each quadrant as the depth and velocity increase is in agreement with the observations made for the velocity statistics in Section 3.3. The larger surface layer depth and the higher flow rate lead to increases in the shear stress at the canopy height and to more turbulent kinetic energy throughout the profile. The progressive increase in $S_{i,H}$ with H/h_p and Q is another expression of this behavior, which can be corroborated by normalizing $S_{i,H}$ with the turbulent velocities, a procedure that collapses the profiles onto a single curve. Similarly, the time fraction profiles in **Figures 3.37** and **3.38** do not demonstrate substantial variability among the depth and velocity cases, so that we conclude that these effects have little impact on the temporal distribution of the stress events.

What the dimensional stresses in **Figures 3.35** and **3.36** do show is the progressive increase and decrease in the peak ejection and sweep location, respectively, as the characteristic depth and flow discharge increase. For $H/h_p = 1.25$, the peak ejection location is at $1.06h_p$ while for $H/h_p = 2.75$ it moves upwards to $1.18h_p$. The sweep location at these characteristic depths decreases modestly from $1.00h_p$ to $0.94h_p$. The implications of these variations are straightforward. As the surface layer depth increases and with it the scale of the turbulent eddies, sweep motions penetrate further into the canopy, thus the sweep peak moves lower. Because the magnitude of the sweep motions are stronger as the characteristic depth increases, the downward inrush of streamwise momentum forces low velocity fluid in the canopy to be ejected farther up away from the canopy height, thus the higher ejection peak.

The effect of flow discharge is a bit more complicated but it ties into this picture quite well. As the flow discharge is increased at the same water depth, the vertical eddy scale is approximately equal, except for the small variations due to the bending of the plants. This implies that an increase in the flow discharge should not affect the location of the sweep peak relative to the deflected height. In effect, if the stress contributions were plotted versus z/h, the sweep peaks all collapse at $z = h$. In the normalization of **Figure 3.37** a slight decrease in the peak sweep is observed. On the other hand, the flow discharge should impact the location of the ejection peak since the turbulent eddies have more momentum to impart to the low velocity fluid inside the canopy. This is corroborated by the normalization z/h that shows that the ejection peak increases from $1.06h$ to $1.18h$, similar to the characteristic depth variation.

The stress contributions from the quadrant regions are intimately related to the joint probability distributions of the longitudinal and turbulent velocities (u' and w') which are described by an infinite set of moments. Nagakawa and Nezu (1977) showed that a cumulant-discard analysis of the third-order Gram-Charlier joint probability distribution of u' and w' described the relationship between the quadrant decomposition of $u'w'$ and the third moments of the longitudinal and vertical velocities. Later, Raupach (1981) demonstrated that the difference between the sweep and ejection stress contribution could be explained sufficiently by the skewness coefficients. The fractional ejection-sweep difference is simply:

$$\Delta S_{H_o} = \widetilde{S}_{4,H_o} - \widetilde{S}_{2,H_o}. \qquad \textbf{(3.101)}$$

The descriptive capability of the ejection-sweep character of the turbulent boundary layer flow by the third moments was mentioned previously in Section 3.3.4 on the skewness coefficients. The peak skewness coefficients at the elevation $z/h_p = 0.75$ ($Sk_{uuu} > 0$ and $Sk_{www} < 0$) showed that within the upper canopy region the strongest turbulent events were associated with the velocity pair ($u' > 0$ and $w' < 0$), which corresponds to the Quadrant 4 sweep events. The peak sweep events at $z/h_p = 0.75$ in **Figures 3.35** and **3.36** and the comparison of the stress fractions in **Table 3.13** corroborate this observation. With the information provided through the quadrant analysis of the Reynolds stress, the peak in the skewness profiles shown in **Figures 3.16** and **3.17** can now be attributed to the dominant role played by the downward moving, high speed fluid in the surface layer. The turbulent events, specifically the sweeps, are responsible for the peculiar shape of the skewness coefficients, which can be divided into two regions: an upper canopy region directly affected by the sweep penetration into the canopy and a lower canopy region where the sweep events do not penetrate. As a consequence, the turbulence in the upper canopy is shear-generated at the elevation $z = h$, while the lower canopy region is characterized by turbulence arising from the interaction of the mean flow with the model plants. The depth of penetration of the sweep events is indicative of the level at which the transition from shear to wake-generated turbulence occurs. The relationship between the sweep penetration and the skewness profiles suggests that the depth of penetration of momentum can be estimated from either statistic. Several estimates for the penetration depth will be described and discussed in Chapter 4.

The fractional difference of the sweep and ejection events was computed from the conditional averages and related to the pure and the mixed skewness coefficients in an attempt to show that a linear relationship among the parameters was valid for the flow through a flexible vegetation canopy in an open channel. To obtain accurate representations of the relationship between ΔS_o and the Sk coefficients, only a limited number of point in the profile could be used. A good correlation was found between the data points that fit the linear relationship and the elevation of the data point. The linear relationship is only valid for those points within the shear zone ($0.5 \leq z/h_p \leq 1.4$), points in the lower canopy region or points close to the free surface did not produce good results and were excluded from the analysis, which makes sense since the sweep-ejection cycle is not a dominant feature of the turbulence in these regions.

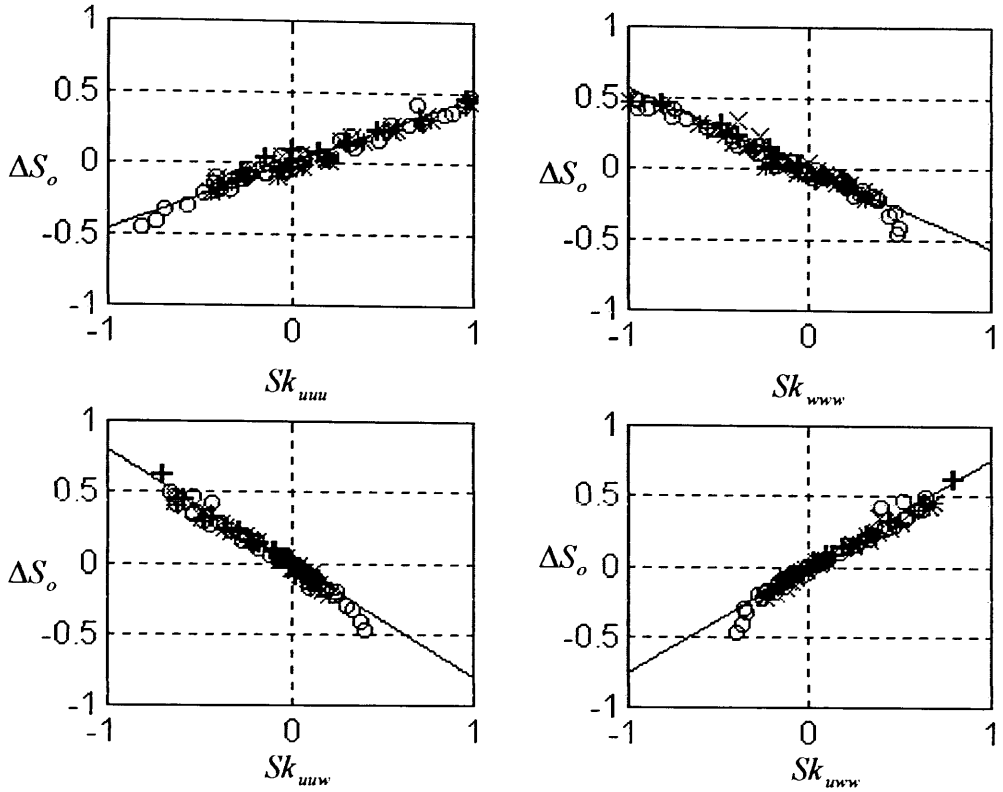

Figure 3.39 Relationship between the skewness coefficients and ΔS_o, the difference between $S_{4,0}$ and $S_{2,0}$ for $H_o = 0$, for *Cases A* and *B*. Experimental run 1 was omitted from the analysis and only the vertical points within the sheared region of each profile ($0.5 \leq z/h_p \leq 1.4$) were used. The lines are the linear regression for the 71 data points and all have R^2 values greater than 0.95.

The skewness profiles in **Figures 3.16** and **3.17** give an indication of this effect since the data collapse is exceptionally good in this same region for the four skewness coefficients. The relationship between the skewness coefficients and the sweep-ejection fractional difference for the experimental runs in *Cases A* and *B* (runs 2–7) are shown in **Figure 3.39**. The regression lines fit the 71 data points well ($R^2 > 0.95$) and result in the following relationships:

$$\Delta S_o = 0.46 Sk_{uuu} = -0.56 Sk_{www} = -0.80 Sk_{uuw} = 0.76 Sk_{uww}. \qquad \textbf{(3.102)}$$

These result are comparable with those obtained in other studies of rough-wall boundary layers. Raupach (1981) with wind tunnel data from five cylinder canopies at different densities found that the coefficients in **Eq. 3.102** were 0.37, –0.63, –0.75 and 0.73, respectively. Similarly, Shaw *et al.* (1983) and Finnigan (1979b) demonstrated that the profiles of the fractional stress difference were proportional to the skewness profiles for a corn and wheat canopy. The data collapse for the experimental conditions suggest that **Eq. 3.102** is valid over velocity and depth variations, except for emergent conditions. The lack of applicability for the $H/h_p = 1.00$ is expected considering that the skewness profiles and the sweep-ejection events depend on the existence of a shear layer that is not present in this condition.

3.6.2 Intermittency Analysis

Quadrant analysis is also a useful tool in determining the intermittency of the momentum transport in a wall-bounded shear flow. For the seagrass meadow, the use of the threshold parameter, H_o, in the definition of the conditional average stress can be used to demonstrate the persistence of the dominant turbulent structures. Persistency, in this context, implies the temporal duration of the turbulence structure. A persistent turbulence structure has sufficient strength to withstand the effects of background turbulence and travel long distances intact. The intermittency analysis consists of calculating the time and stress fractions defined in **Eq. 3.94** and **3.100** for various values of H_o. As the threshold parameter is increased, the excluded region increases in size and the conditional average consists of fewer total points. Only the pairs (u', w') with instantaneous Reynolds stress values larger than H_o times the time-average Reynolds stress are considered in the conditional average. A conditional average stress that decreases slowly with H_o is indicative of a highly intermittent record, one consisting of large instantaneous Reynolds stress values that occur infrequently.

The representation of the intermittency of the turbulent structures is usually done by plotting the contribution to the total stress from each quadrant versus the hole size for a number of relevant positions in the turbulent flow, as depicted in **Figure 3.40** for experimental run 4. The magnitude of the dimensional stress contributions at $H_o = 0$ are identical to the results shown in **Figures 3.35** and **3.36**. For larger hole sizes, the magnitude of the conditional stress diminishes at different rates for the various vertical elevations. The contribution from the interaction events, which was small in any case, becomes negligible after $H_o \approx 4.3$. Lu and Willmarth (1973) defined a critical value of H_o as the hole size after which the interaction events disappear. The sweeps and ejections events that occurred after the critical hole size H_{oc} were considered to be large or violent events. The objective choice for the critical hole size H_{oc}, however, is not simple nor obvious and will depend largely on the particular flow conditions.

Figure 3.40 also reveals that the vertical structure of the ejection and sweep events as functions of H_o are quite different. The maximum and most intermittent ejection events occur at high elevations in the surface layer ($z/h_p = 1.50$). There is clearly a progressive decrease in the magnitude and intermittency of the ejection events as the canopy height is approached from above, with ejection events on the order of the interaction events at $z/h_p = 0.75$. The sweep structure, on the other hand, does not seem to follow as clear a pattern. For small hole sizes, the largest sweep values occur at the canopy height and in the surface layer. As the hole size increases beyond $H_o \approx 5$, the most intermittent sweep events occur within the canopy ($z/h_p = 0.75$). This hole size could potentially serve as an estimator of H_{oc} since it indicates the point at which the intermittency is equivalent at two important locations, the canopy height and the location of the peak intermittency, as shown from the kurtoses profiles in Section 3.4.5. Equal intermittency at these two locations implies that all eddies penetrated uniformly down to $0.75h_p$. Beyond the value of this H_{oc} estimator, the higher intermittency values in the upper canopy region are a direct

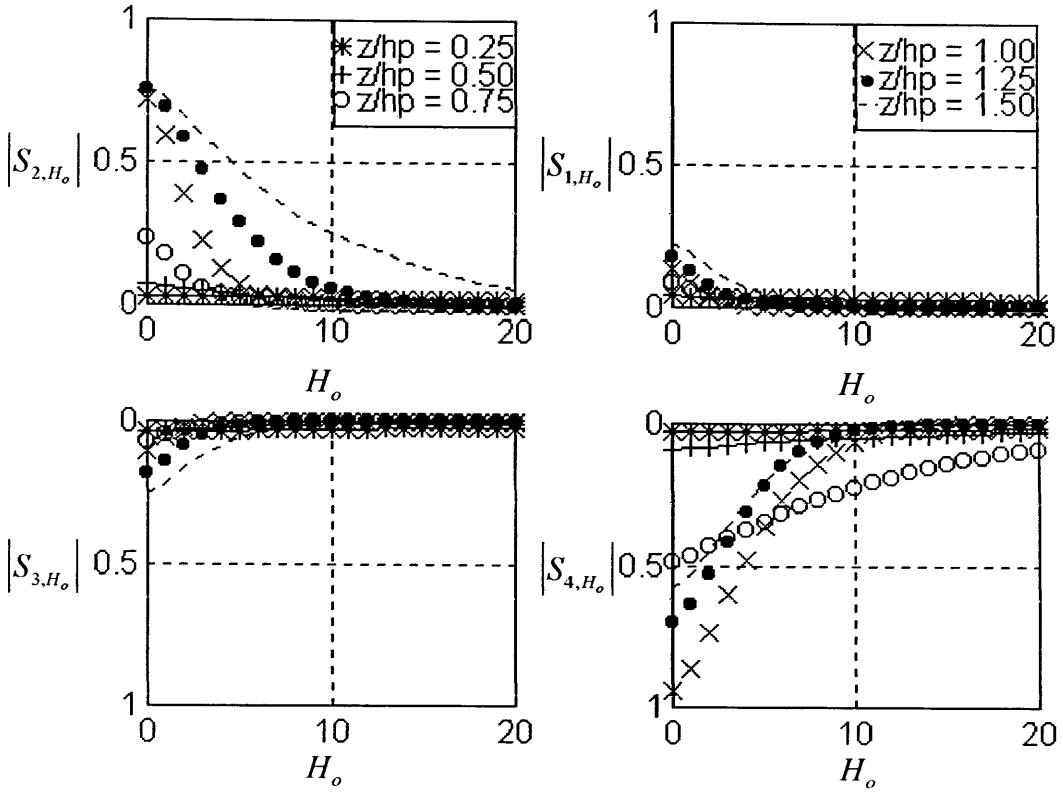

Figure 3.40. Variation of the dimensional stress contribution with the hole size (H_o) for experimental run 4 (H/h_p = 1.75, Q = 6.31 L/s). The absolute value of $S_{i,Ho}$ (cm^2/s^2) is plotted at six different elevations z/h_p = 0.25, 0.50, 0.75, 1.00, 1.25, 1.50. High values of $S_{i,Ho}$ at large H_o is an indication of the intermittency of the event at that specific elevation, *e.g.* (o) in Quadrant 4.

result of the penetration of the largest turbulent structures into the canopy. This critical value is thus an indication of the relative eddy strength required to reach down to the maximum penetration depth. A similar analysis for the other experimental runs in *Cases A* and *B* led to comparable estimators for H_{oc}, the value of which decreases with increasing velocity and depth of the flow.

A more effective way of visualizing the intermittency in the Reynolds stress is to construct contour plots of the conditional averaged stress, as shown in **Figures 3.41** and **3.42** for the ejections and **Figures 3.43** and **3.44** for the sweeps in the *Case A* and *B* experimental runs. The event stress in the (z/h_p, H_o) plane has been normalized by the maximum value at H_o = 0, so that the following nondimensional parameters are formed:

$$\left\{ \Sigma_2 = \frac{S_{2,H}}{S_{2,0}^{max}}, \quad \Sigma_4 = \frac{S_{4,H}}{S_{4,0}^{max}} \right\}. \tag{3.103}$$

for the ejection and sweep contours, respectively. This normalization is successful in highlighting the regions of peak conditional stresses (dark red color) and negligible conditional stress (dark blue color).

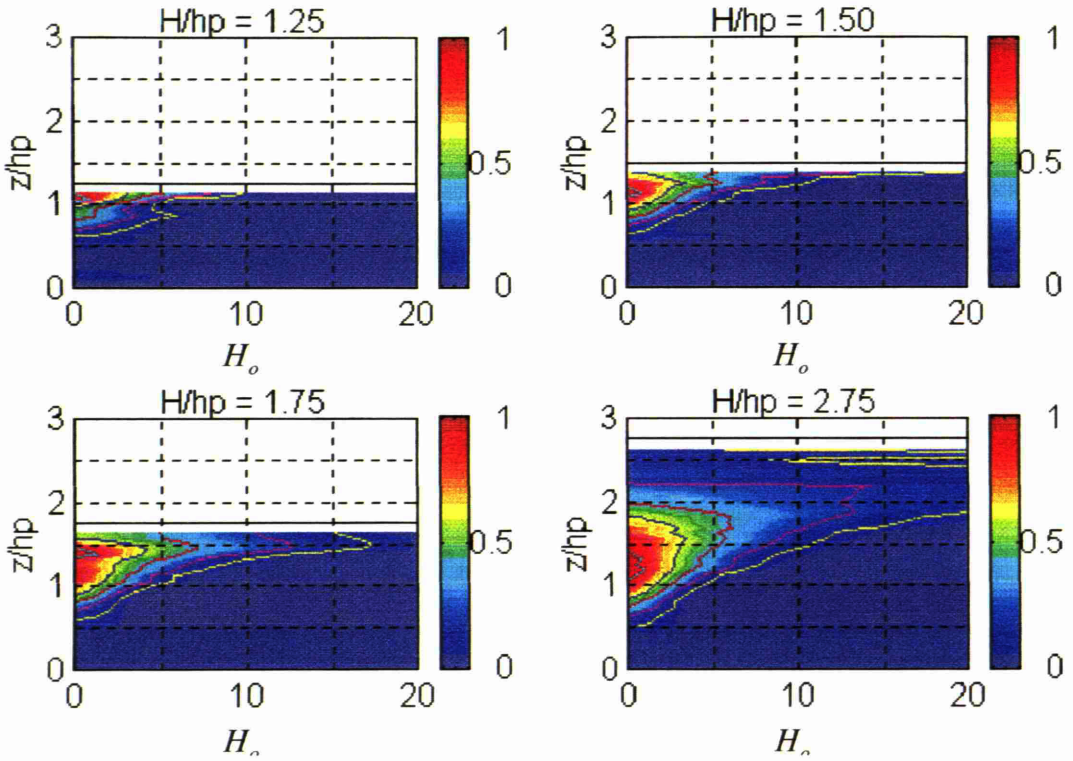

Figure 3.41. Contour plots of Σ_2 (normalized ejection stress) for the *Case A* experimental runs that have characteristic depths (H/h_p) larger than 1.00. The turbulence structure for the emergent case does not have the sweep-ejection character due to the lack of the shear layer. The vertical bars show the color scale associated with the stress relative to the peak value, usually located slightly above $z/h_p = 1.00$. The horizontal solid black line represents the water surface.

The normalization is also an effective way of comparing the contour plots for each of the depth and velocity variation cases since the figures show the distribution of Σ_2 and Σ_4 in the (z/h_p, H_o) plane. The contour plots are a more revealing method of visualizing the variation of the conditional stresses as compared to the more conventional method shown in **Figure 3.40**. The high vertical resolution (~ 1 cm) of the velocity measurements in this laboratory study allows the construction of the contour plots, which to our knowledge have never been published.

Before discussing the features in the contour plots, it should be mentioned that the values in **Figures 3.41** through **3.44** represent the horizontal average of the normalized conditional stress for the different vertical profiles. For contouring purposes, the deviations from the horizontal average have been neglected. In addition, the contour plots extend close to the free surface (represented by the horizontal solid black line) because the data from the two velocity measurement instruments, the ADV and LDV, have been merged. The match between the two data sets is quite acceptable for contouring purposes.

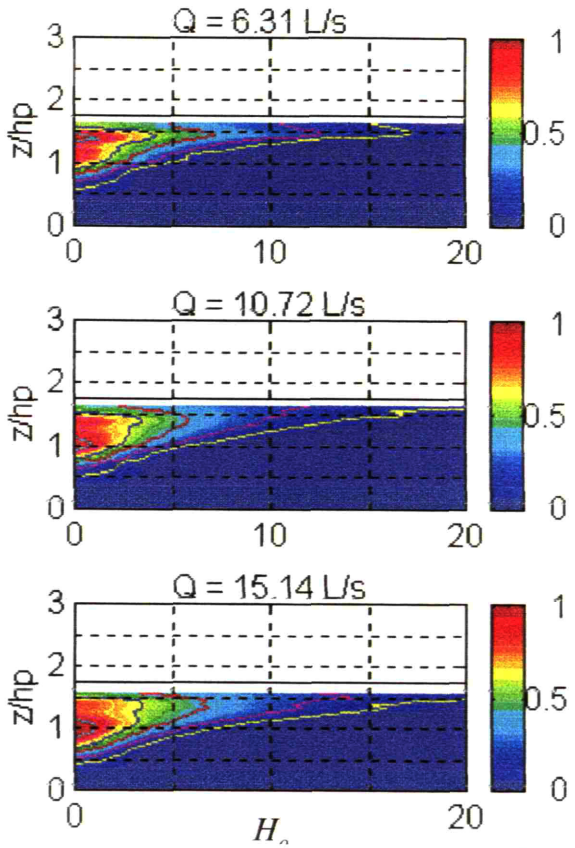

Figure 3.42. Contour plots of Σ_2 (normalized ejection stress) for the *Case B* experimental runs. The vertical bars show the color scale associated with the stress relative to the peak value, located at or slightly above $z/h_p = 1.00$. The horizontal solid black line represents the water surface.

Figures 3.41 and **3.42** demonstrate that the normalized ejection stress peaks at or slightly above the canopy height. The distribution of Σ_2 in the (z/h_p, H_o) plane is identical to the description given in **Figure 3.40**, the ejections are stronger and more intermittent as the free surface is approached. The shift in the location in the normalized ejection stress peak varies with the characteristic depth and the flow discharge according to the discussion made in Section 3.6.1 regarding the peak value at $H_o = 0$. For increasing water depth and flow discharge, the peak moves away from the canopy height. The increase in H/h_p and Q also intensifies the strength of the ejection peak and broadens its size to higher threshold levels and to larger distances away from the canopy height. The contour plots show that less than 50% of the normalized stress is located beyond the suggested critical hole size ($H_{oc} \approx 4$–5) for any of the experimental conditions. This implies that a large portion of the events (those with strengths less than H_{oc}) would classified as weak events if the H_{oc} was set at this level. In Section 3.6.4, the ejection and sweep arrival frequencies will be estimated by varying the critical hole size parameter from $H_{oc} = 1$ to 4, which will be shown to be a more appropriate range for defining an event. If an ejection or sweep persists beyond H_{oc} it is considered violent enough to be counted in the estimation of the time between the arrival of events. Thus, the sweep and ejection frequencies will be highly dependent on the choice of H_{oc}.

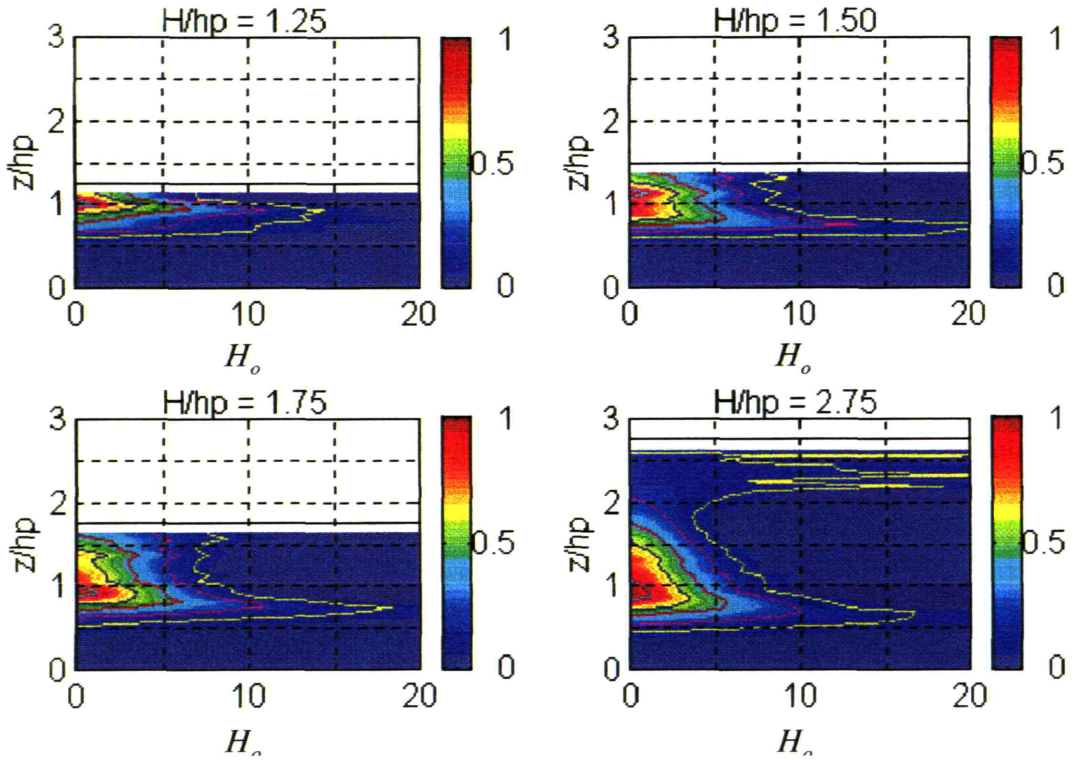

Figure 3.43. Contour plots of Σ_4 (normalized sweep stress) for the *Case A* experimental runs. The vertical bars show the color scale associated with the stress relative to the peak value, located at or slightly below $z/h_p = 1.00$. The horizontal solid black line represents the water surface.

The shape of the ejection event contour plots reflect the idea that these turbulent structures originate within the canopy and move upwards into the surface layer, increasingly becoming more intermittent closer to the free surface. The higher intermittency away from the canopy height is expected since the turbulent structures must travel increasingly larger distances and not all are of sufficient strength to persist within the turbulent flow in the surface layer. The result is that the measurement of the Reynolds stress at positions far away from the canopy height will consist of infrequent ejection events that are surprisingly strong compared to the other quadrant contributions. The higher values of the normalized ejection stress at higher threshold levels in the surface layer are thus an indication of the persistence, strength and intermittency of fluid ejected from the canopy space.

A similar interpretation can be made of the sweep structures from the intermittency analysis shown in **Figures 3.43** and **3.44**. The sweep contour plots indicate that the most intermittent region is within the upper canopy, at approximately $0.75h_p$. Strong sweeps present at this level originate in the surface layer and travel downwards into the canopy where their momentum is ultimately either absorbed by the plants, transformed into fine-scale turbulence or transferred to the low-velocity fluid inside the canopy. If the sweep momentum is imparted onto the lower velocity fluid, this may cause the ejection of

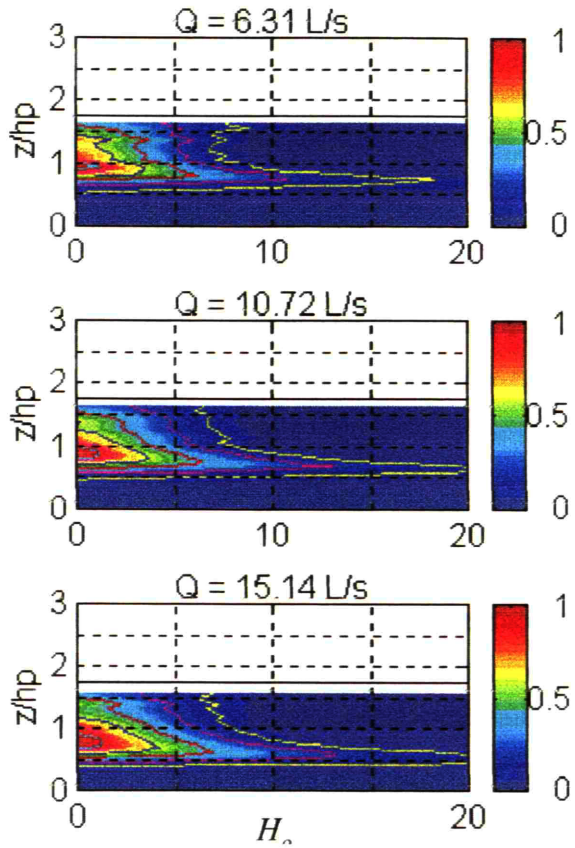

Figure 3.44. Contour plots of Σ_4 (normalized sweep stress) for the *Case B* experimental runs. The vertical bars show the color scale associated with the stress relative to the peak value, located at or slightly below $z/h_p = 1.00$. The horizontal solid black line represents the water surface.

this fluid mass away from the canopy, a sequence of events known as the sweep-ejection cycle. Regardless of the ultimate outcome of the downward moving fluid mass, the higher normalized stress values at the larger threshold sizes in the upper canopy region indicates that only the strongest sweeps able to persist for longer periods of time will penetrate to the mid canopy height. A sharp cutoff is observed in the normalized sweep contour at about half the canopy height, indicating that the sweeps do not penetrate beyond a particular level within the canopy. Thus, the turbulence structure in the lower canopy region does not result from the shear generated at the canopy height, but is exclusively from the plant wakes.

The Σ_4 distribution in **Figures 3.43** and **3.44** also qualitatively indicate the variation of the sweep structure with the changes in the level of submergence and the velocity. The peak sweep stress moves lower into the canopy as the level of submergence increases, presumably because the eddies in the surface layer are of increased size and strength and can penetrate farther into the canopy. The larger values of Σ_4 at larger hole sizes also indicates that the sweep motion become progressively more persistent and intermittent with increasing characteristic depth. A similar trend, although less obvious because of the smaller change in eddy scale as the plant deflection increases the surface layer depth, is observed at higher flow discharges in the experimental runs of *Case B*.

Table 3.14. Sweep and ejection stress and time fractions for various H_o for experimental run 7 at $z = h$.				
Hole Size	**Ejection**		**Sweep**	
	$S_{2,Ho}$	$T_{2,Ho}$	$S_{4,Ho}$	$T_{4,Ho}$
0	0.5154	0.3972	0.6266	0.3350
5	0.0427	0.0072	0.1968	0.0283
10	0.0004	0.0000	0.0283	0.0025
15	0.0000	0.0000	0.0024	0.0002
20	0.0000	0.0000	0.0000	0.0000

The foregoing discussion on the stress fractions has shown that the events dominating the momentum transfer are highly intermittent. A similar hole size analysis of the event time fractions, as defined in **Eq. 3.100**, can be performed to show that the most persistent turbulent structures occupy a small portion of the total time at a particular location. For the time fraction, the use of contour plots is not as revealing as in the stress fraction and have been excluded. To make the intended point, it is sufficient to consider a case at the canopy height for experimental run 7 (H/h_p = 2.75) as an example. **Table 3.14** shows the stress and time fractions for the ejection ($S_{2,Ho}$) and the sweep ($S_{4,Ho}$) events at five different hole sizes, H_o = 0, 5, 10, 15 and 20. Both fractions decrease quickly with the hole size, although the sweeps seem to have a more intermittent nature. For example, sweeps at H_o = 5 account for 20% of the total stress in 2.8% of the total time, an indication that the stress is transported downwards during strong sweeps that make up a small portion of the time. After H_o = 5, the values for the sweep and ejection fractions are negligible, suggesting that strong events are within this H_o value. Similar results are obtained for the other experimental cases supporting the idea that the process of momentum transfer is intermittent and that the degree of intermittency increases farther away from the canopy height, upwards for the ejection events and downwards for the sweeps.

The intermittency analysis confirms the results presented in Section 3.3.5 from the kurtoses profiles regarding the intermittency of the longitudinal and vertical velocities. **Figures 3.18** and **3.19** show distinct peaks in K_u and K_w at the level $0.75h_p$ within the upper canopy region. With the physical interpretation about the turbulent structures provided by the quadrant and intermittency analysis, the results from the kurtoses or flatness factors can be now be interpreted in a new light. In the upper canopy region, the skewness previously demonstrated that the dominant turbulent velocity pair corresponded to sweep events. The kurtoses show that in this region the velocity records have large and infrequent values implying that the sweeps arrive intermittently as a result of having traveled through half the canopy height. Only the strongest and most persistent motions maintain their form and are able to penetrated into the canopy where an observer would witness the strong sweeps arriving infrequently.

3.6.3 Stress Ratios

Important comparisons between the different quadrant contributions to the total Reynolds stress can be made by forming specific ratios between the stress fractions. Three parameters, the exuberance, the efficiency and the exchange ratios, will be used to describe the relative importance of the different turbulent structures and aid in the formulation of a conceptual model for the momentum transport in the seagrass meadow. A comparison will also be made to the results from two field studies, a waving wheat canopy (Finnigan, 1979b) and a stiff corn canopy (Shaw *et al.*, 1983), from which the stress contributions from the different quadrants at H_o = 0 were available. These comparisons will allow us to place the turbulence behavior of the seagrass meadow within the same framework and make conclusions regarding the role of the canopy flexibility.

Shaw *et al.* (1983) introduced the exuberance ratio (*Exu*) as a measure of the direction of the momentum transfer and the relative importance of the interaction events compared to the sweep and ejection events. For this study, the inverse exuberance ratio was found to have more physical meaning and it lent itself to better interpretation. The inverse exuberance (Exu^{-1}) ratio is simply the sum of the quadrants responsible for the downward transport of momentum (2, 4) divided by the sum of the quadrants that induce upwards momentum transfer (1, 3):

$$Exu^{-1} = \left| \frac{(S_{2,H_o} + S_{4,H_o})}{(S_{1,H_o} + S_{3,H_o})} \right|, \qquad \textbf{(3.104)}$$

where the dimensional conditional stresses (**Eq. 3.94**) have been used instead of their nondimensional counterparts (**Eq. 3.100**) since the total Reynolds stress in the denominator will eventually cancel out. Values of Exu^{-1} greater than unity or low exuberance (*Exu*) imply that more sweeps and ejections are present in the Reynolds stress record. Low exuberance is a characteristic of shear-generated turbulence where turbulent structures created in the mixing layer transport momentum to locations away from the interface. A highly exuberant velocity field, as that found by Finnigan (1979b), implies that the interaction events are of relative importance due to the limited ability of the downward momentum flux to remain within the canopy. The author attributed the dominant role played by the outward interaction to the strong waving of the wheat canopy, but as Shaw *et al.* (1983) point out, the peak exuberance did not correspond to the location of the maximum plant motion. This waving seagrass canopy provides an opportunity for comparison with the results obtained by Finnigan and describe the impact that waving has on the interaction event strength.

A more frequently used parameter in the comparison of the event stress contributions is the ratio of the sweep events to the ejection events. The difference between these two stress contributions has already been discussed in Section 3.6.1 and related to the skewness coefficients. Similarly, the ratio of the two events is used to give an indication of the regions within the flow in which each is dominant. An alternative interpretation for the ratio of the sweeps to the ejections is to consider the sweep and ejection

cycle mentioned in Section 3.6.1. As a downward moving parcel of high velocity fluid (sweep) enters the canopy, it imparts momentum to the lower velocity fluid inside the canopy. If this momentum transfer results in the ejection of the low speed fluid out of the canopy, an ejection is created. The ratio of the sweep to the ejection is thus an indication of the efficiency of the sweep-ejection cycle. For this reason, the parameter receives the name of the efficiency ratio in this study and is defined simply as:

$$Eff = \frac{S_{4,H_o}}{S_{2,H_o}} \tag{3.105}$$

A value of unity for the efficiency ratio in the shear region implies that the sweep-ejection cycle is perfectly efficient, each sweep entering the canopy is balanced by an ejection. If *Eff* is less than unity, the downward moving sweeps do not result in the ejection of fluid volumes from the canopy and the momentum carried by the sweep is either absorbed by the model plants and transformed into plant motion or is lost in the canopy by the conversion of mean kinetic energy to turbulence. On the other hand, an efficiency greater than one suggests that ejections are created by other mechanisms that can impart high momentum to the lower velocity fluid inside the canopy.

The high values for the outward interactions observed by Finnigan (1979b) in the waving wheat field prompted the formation of a third parameter describing the relative importance of the sweep and outward interaction events. Conceptually, if the stress contribution from the outward interaction is comparable to the sweep contribution, then the momentum carried by the downward moving sweep in the turbulent eddy does not have the time to be transmitted to the fluid inside the canopy and it escapes the canopy as the turbulent eddy travels away. Thus, the ratio of the sweeps to the outward interactions describes the exchange of high momentum fluid in either the downward or upwards direction and is referred to as the exchange ratio in this experimental study:

$$Exc = \left| \frac{S_{4,H_o}}{S_{1,H_o}} \right|. \tag{3.106}$$

If the sweep momentum does not equilibrate instantaneously with the fluid inside the canopy and the high momentum fluid is merely exchanged from the downward to the upward eddy motions, then the exchange ratio has a value equal to unity. Exchange ratios that are greater than unity imply that the sweep character is the dominant feature in the shear flow and the high velocity fluid transported downwards imparts its momentum either to the fluid inside the canopy or to the canopy elements.

Figures 3.45 and **3.46** show the profiles of the three stress ratios for the experimental runs in *Cases A* and *B* for a threshold level $H_o = 0$. The profiles are a good indication of the relative importance of the different events and can be used to categorize specific flow regions based on the ratios.

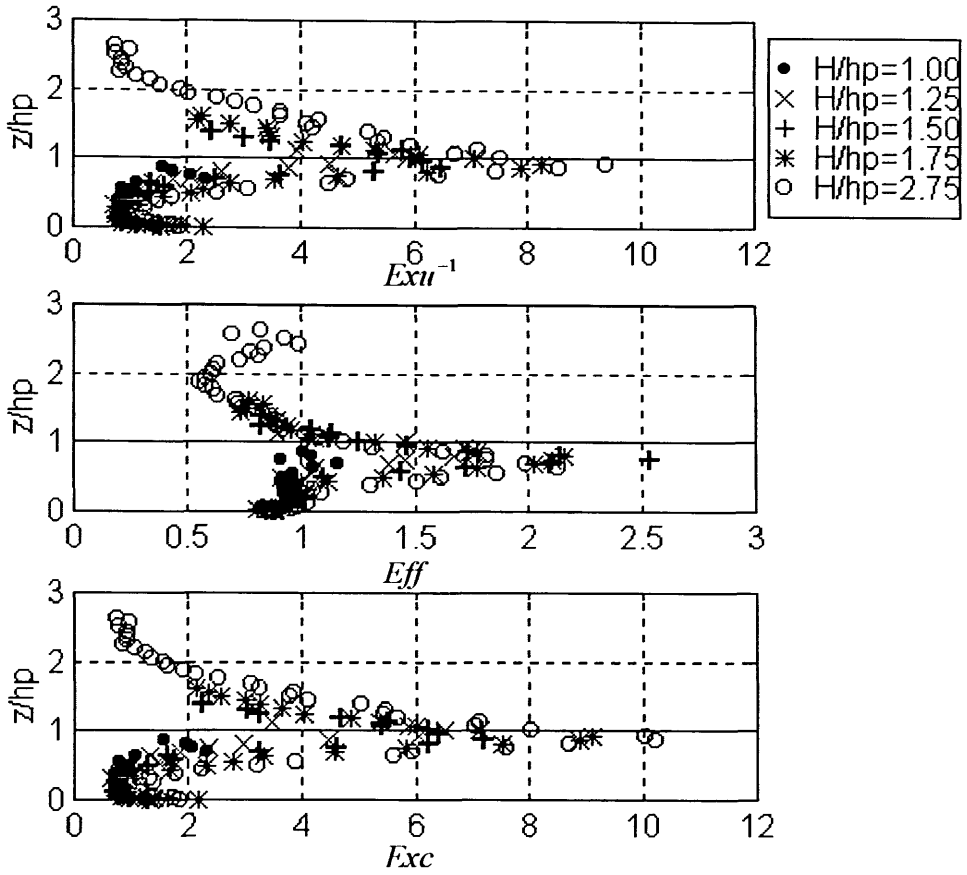

Figure 3.45. Stress ratios for the *Case A* experimental runs. From top to bottom: the inverse exuberance, the efficiency and the exchange ratios. Note the different horizontal scale for the efficiency ratio. The horizontal bars representing the variation among the lateral positions are not shown for clarity.

It should first be noted from **Figures 3.45** and **3.46** that at the level of the canopy height the flow has low exuberance, *i.e.* the events leading to the downward flux of momentum dominate the events leading to the upward flux. This has been shown previously in **Table 3.13** where the stress fractions from Quadrants 2 and 4 were much larger than from the other two quadrants. At the level of the canopy height, the flow has nearly perfect efficiency, implying that the sweeps balance the ejections. Further into the canopy, however, the conditions are far from efficient, as much of the momentum imparted by the sweep is being absorbed by the plants. One possible mechanism for which the downward moving sweep does not cause an ejection is if it does not have the opportunity to equilibrate with the fluid inside the canopy and the high momentum escapes via an outward interaction. If this were true, then the exchange ratio would be close to unity. However, this does not occur for any experimental case. The information provided by the three stress ratios suggests that sweep momentum penetrating far into the canopy is not converted into ejections nor into outward interactions and must, therefore, be absorbed by the plants. Quadrant analysis and the stress ratios have provided a physical understanding of an effect which had been noted in the discussion of the velocity statistics and the drag profiles.

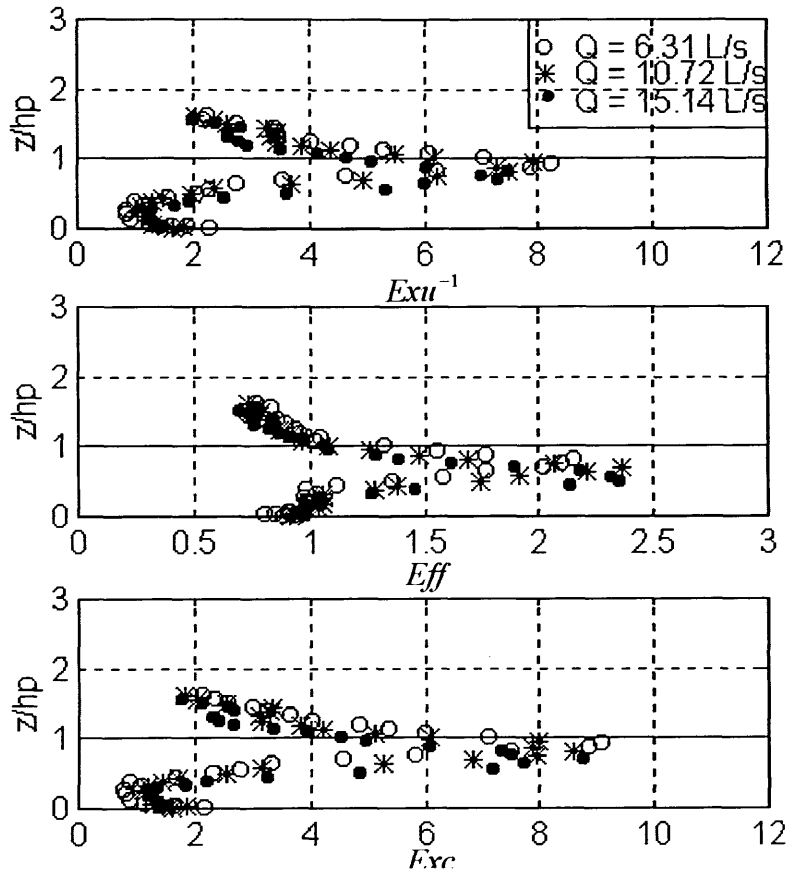

Figure 3.46. Stress ratios for the *Case B* experimental runs. From top to bottom: the inverse exuberance, the efficiency and the exchange ratios. Note the different horizontal scale for the efficiency ratio. The horizontal bars representing the variation among the lateral positions are not shown for clarity. The vertical axis is normalized by the effective canopy height.

The behavior of the stress ratios in the lower canopy region should also be addressed. From **Figures 3.45** and **3.46** it is quite evident that the stress ratios are approximately equal to unity for elevations lower than $z/h_p = 0.25$. The direct implication is that this region is not affected by the sweep-ejection cycle and all the stress components are approximately equal to each other. This has been observed previously in the time and stress fraction profiles and the contour plots of the sweep and ejection intermittency in Sections 3.61 and 3.62. The quadrant analysis has thus identified the lower canopy region as a zone that does not actively participate in the shear turbulence generated at the canopy height. If there is limited exchange between the fluid in the upper and lower canopy regions, then the mean flow below $0.25h_p$ and the secondary maximum in the velocity profile must be due to the blow through effect described in Section 3.3.1. In addition, the turbulence observed in this region is generated exclusively by the interaction of the mean flow with the plants or with the bottom boundary.

The stress ratios vary with the velocity and the characteristic depth. Due to the similarity in definitions, the exuberance and the exchange ratios should follow the same trends. **Figure 3.45** shows an increasing progression for the exchange and exuberance ratios as the characteristic depth (H/h_p) increases, which is most evident at the canopy height. This is the expected result since the increase in the surface layer depth intensifies the shear profile responsible for the formation of the sweep-ejection cycle. As H/h_p increases, the interaction events become less important in relation to the sweeps and ejections. The level of submergence appears to have little effect on the efficiency ratio, as all cases collapse approximately onto the same curve. Knowing that the surface layer depth sets the scale for the maximum eddy size, this result implies the balance between the sweeps and the ejections does not depend on the scale of the turbulent eddy. Regardless of the eddy size producing the sweep event, the proportion of ejections created by the sweep over the profile will remain constant.

Along the same lines, **Figure 3.46** shows that the increased velocity and plant waving experienced as the flow discharge is increased does not significantly impact the stress ratios. In fact, if the vertical axis were normalized by the effective canopy height h, the collapse of the profiles is exceptional. At first glance, these results are surprising because the plant waving is expected to play a role in the formation and/or destruction of the turbulent structures. However, consider the following argument which gives a very simple explanation for this lack of variability. As the flow discharge increases at the same water depth, the eddies of fixed size are advected past the canopy at a faster rate and thus carry more momentum. The total Reynolds stress in the system increases but the distribution among the different stress quadrants remains the same, so that the stress ratios have similar forms. It is the size of the turbulence structure and not its strength that has immediate effects on the turbulence structure. This lack of variability suggests that the plant waving phenomenon (monami) is merely a response to the eddies traveling at the level of the canopy height and does not play a direct role in setting the structure of the momentum transport. If this is so, then the plant flexibility is not as important an issue as has been previously thought (*e.g.*, Shaw *et al.*, 1983)

If the size of the turbulence-carrying motions is what determines the turbulence structure within the canopy, then a comparison to unbounded flow conditions should reveal marked differences to this laboratory study. As described in Section 3.3.1, the free surface in an aquatic plant canopy adds a constraint to the size of the turbulent eddies, the surface layer depth h_o. For atmospheric flows, the shear length scale controls the eddy size which actively influences the vertical exchange of momentum at the canopy interface (Raupach *et al.*, 1996). In a confined aquatic flow, both L_s and h_o play an important role, the domination of one or the other being dependent on the water depth. Conceptually, the relative contributions from the different stress quadrants will be highly dependent on the scale that determines the eddy size. **Figure 3.47** shows the stress ratio profiles for the two field studies mentioned previously and for this laboratory study under the conditions of least confinement, $H/h_p = 2.75$.

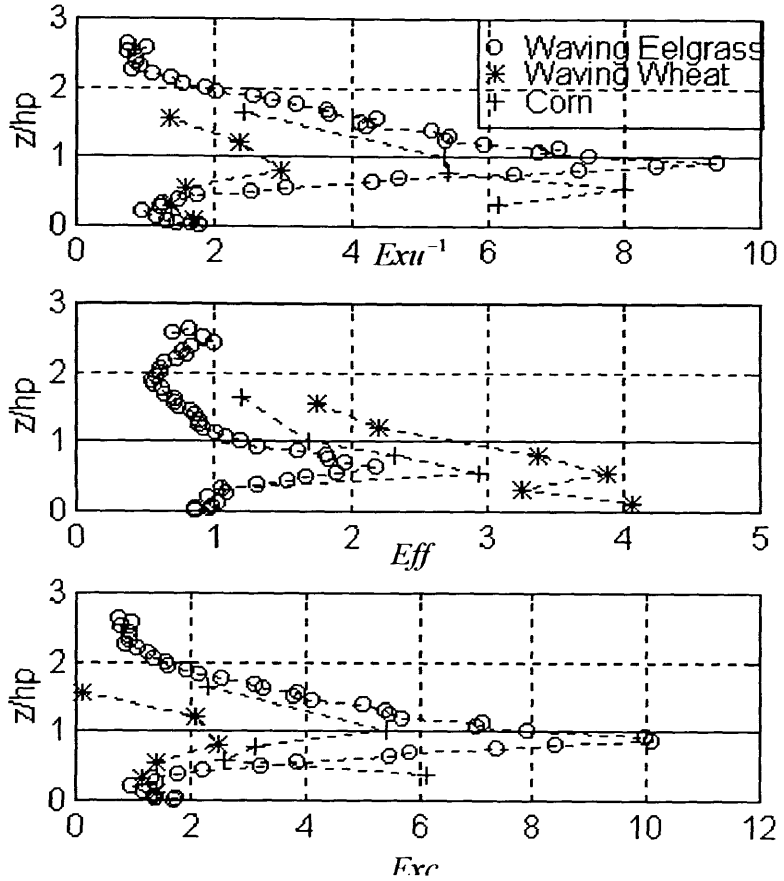

Figure 3.47. Comparison of the stress ratios from the seagrass canopy with a two field studies, a waving wheat field (Finnigan, 1979b) and a corn canopy (Shaw *et al.*, 1983). From top to bottom: the inverse exuberance, the efficiency and the exchange ratios. Experimental run 7 (H/h_p = 2.75, Q = 15.14 L/s) was chosen because it approached the unbounded field conditions.

The confined seagrass meadow exhibits larger inverse exuberance and exchange ratios and a smaller efficiency ratio. Because the comparison is made between the atmospheric canopy flows and the experimental case that approaches an unbounded condition, the differences in the stress ratios can not be attributed to the eddy size. Shaw *et al.* (1983) suggest that the differences between the wheat canopy and the corn canopy can be attributed to the differences in the plant flexibility among the two crops. The authors, however, do not point specifically to how flexibility plays a role in the turbulence structure, other than suggesting that canopy waving may have an effect. In this experimental study, waving conditions were found to have little impact on the stress ratios for an identical level of submergence suggesting that the waving phenomenon does not play a significant role in dynamics of the canopy momentum transport. Without observing a clear pattern in the stress ratios with the flexibility of the three plant canopies, conclusions regarding the role of flexibility cannot be made at this point. The observation made, however, is that the model eelgrass of higher flexibility (J = 10^{-5} Nm^2) has a more prominent domination of downwards momentum flux and a closer balance among the sweeps and ejections as compared to the stiffer crop canopies (J = 7×10^{-2} Nm^2, for wheat) (Finnigan and Mulhearn, 1978).

3.6.4 Event Arrival Frequency

The quadrant and intermittency analysis and the stress ratios have been useful in qualitatively describing the physical picture of the transport of momentum between the surface layer and the vegetation zone. It has been shown that the distinct turbulent structures associated with the downward flux of Reynolds stress characteristically make large contributions during very short time intervals. The intermittency of the sweep and ejection contributions has been related to the persistence of the largest structures as they travel away from the interface. In addition to this qualitative description, a quantitative measure can be obtained by calculating the frequency of arrival of these turbulent structures at a specific point. The frequency of arrival at the height of the canopy should correspond to the measured plant motion frequencies if the sweeps are responsible for the creation and propagation of canopy waves. The sweep arrival frequency should also be related to the frequency of the peak spectral energy if in fact the sweeps generated by the shear turbulence at the canopy height are the dominant source of energy in the system. This comparison will be made in Section 3.8 when the power spectral densities are presented.

The number of sweeps and ejections in a record was counted by setting a threshold hole size, H_o, and identifying the instantaneous Reynolds stress values beyond H_o times the time-averaged Reynolds stress for the entire record. Having identified all the points that met the hole size criteria, a second threshold was used to indicate if the values could properly be considered an event. This was done by counting the number of consecutive points meeting the H_o criteria and determining the minimum number required for the group to be considered a sweep or an ejection. The identification function I_o was assigned a value of one if the number of consecutive points (n_c) exceeded a threshold value (n_{cr}) and a value of zero otherwise:

$$I_o = \begin{cases} 1, \text{ if } n_c \geq n_{cr}. \\ 0, \text{ otherwise.} \end{cases} \tag{3.107}$$

The choice of the critical number of consecutive points, or string length, exceeding the H_o criteria is an arbitrary choice, much in the same way as the hole size is arbitrary. A full analysis of the effect of various string lengths on the number of events identified in the record was not performed because of a particular behavior observed in the records: the points were either in small groups of one or two or they were in larger groups with string lengths of five to twenty. Based on this observation, a critical string length $n_{cr} = 3$ was chosen as an appropriate choice. Because n_{cr} was constant in all the experimental runs, the depth and velocity-variation in the number of events should not be biased by the value of n_{cr}.

The number of stress events in each quadrant in a velocity record, for various hole sizes H_o, is formally defined as:

$$N_{i,H_o} = \lim_{T_s \to \infty} \frac{1}{T_s} \int_0^{T_s} I_{i,H_o}(t) I_o(t) dt . \tag{3.108}$$

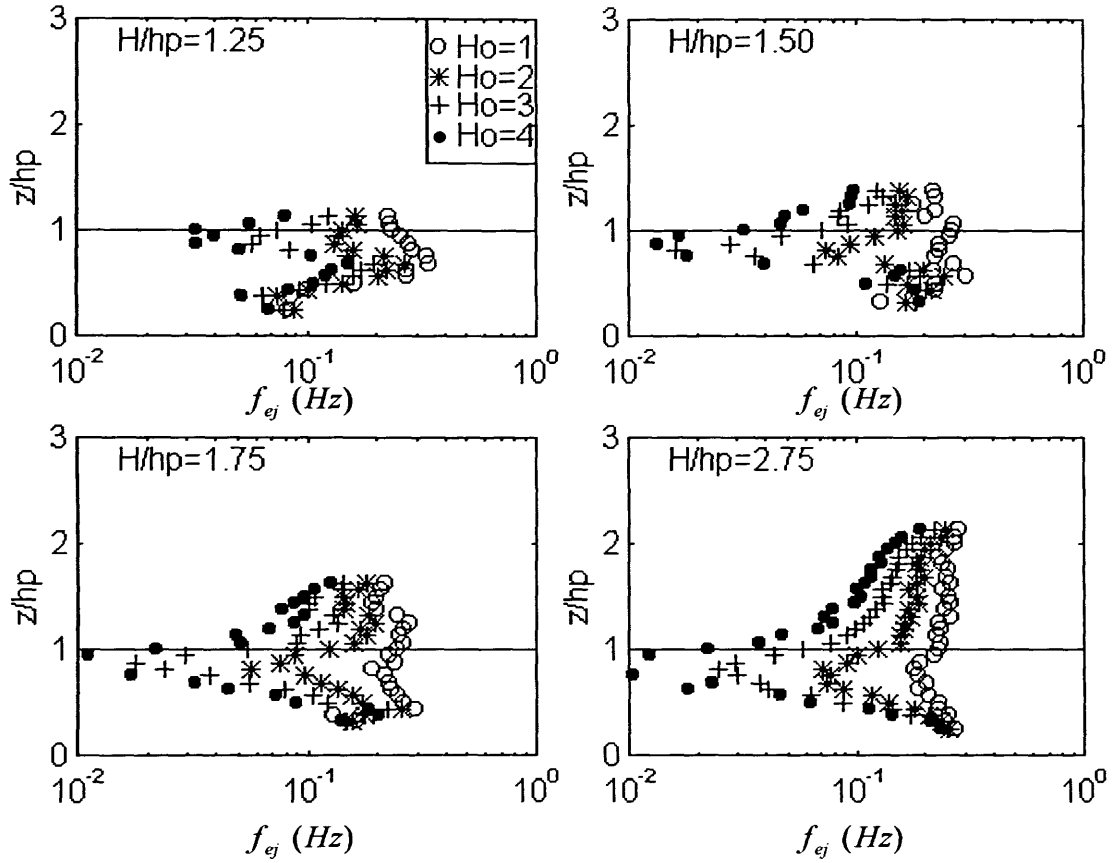

Figure 3.48. Ejection arrival frequency (f_{ej} in Hz) for the experimental runs in *Case A* at various threshold values H_o = 1 to 4. The lowest characteristic depth (H/h_p = 1.00) has been excluded from the analysis. The horizontal axis is presented on a logarithmic scale for easier comparison to the turbulence spectra in Section 3.8. The horizontal bars representing the deviation from the horizontal average have been omitted for clarity.

The mean arrival time or the time between the sweep and ejection events (T_{sw} and T_{ej}) can be computed from the knowledge of $N_{i,Ho}$ and the total record length, T_s, from which the frequency of arrival of the event at a particular location is easily obtained as $f_{sw} = 1/T_{sw}$ and $f_{ej} = 1/T_{ej}$.

The arrival frequencies for the sweep and ejection events (f_{sw} and f_{ej}) in the experimental runs of *Case A* and *B* are shown **Figures 3.48** through **3.51**. Only the experimental runs with characteristic depths greater than unity ($H/h_p > 1.00$) were considered in the present analysis due to the lack of a sweep-ejection character for the emergent case. It is interesting to note the progressively deteriorating form of the arrival frequency profiles as the characteristic depth is decreased, presumably due to the difficulty in identifying the sweeps and ejections when these are weaker and the event durations are shorter and therefore more difficult to define. In addition, only the points in the profiles that have an active sweep-ejection character are included in the analysis, thus the points in the lower canopy region ($z/h_p \leq 0.25$) where the sweeps do not arrive have been excluded.

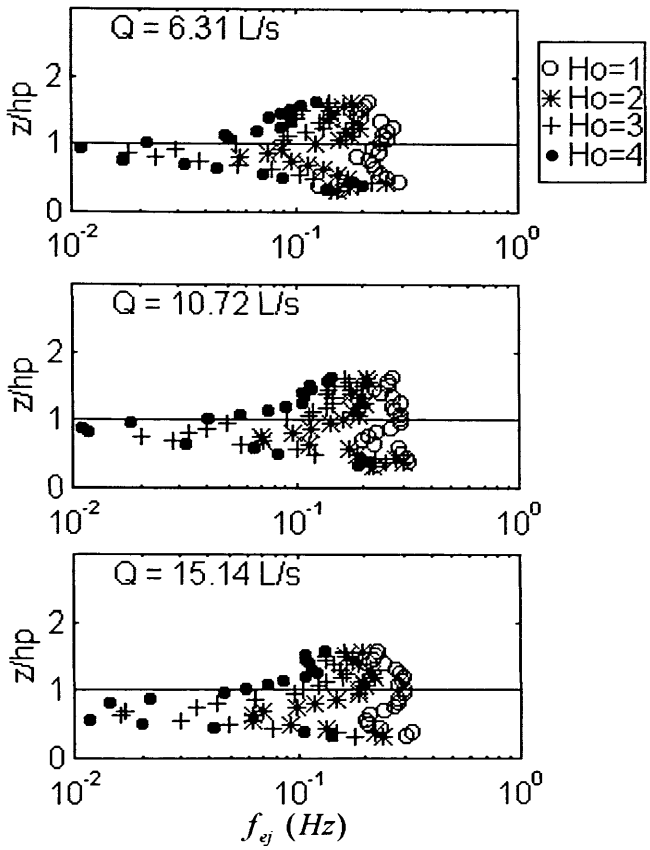

Figure 3.49. Ejection arrival frequency (f_{ej} in Hz) for the experimental runs in *Case B* at various threshold values H_o = 1 to 4. Notice the similarity in the frequency of ejection arrivals across the different flow discharge cases, suggesting that the velocity is not setting the event time scale.

Figures 3.48 through **3.51** show the arrival frequencies estimated at four different threshold levels, H_o = 1–4, at the same critical string length (n_{cr} = 3). The choice of this hole size range was based on the results from the intermittency analysis presented in Section 3.62 that showed that most of the sweep and ejection stress was concentrated at the hole size values smaller than H_o = 5. In addition, the calculation of the arrival frequencies at higher hole sizes did not result in the identification of events over much of the profile, thus leading to negligible frequency values. The arrival frequency analysis can not be performed at a hole size equal to zero because a threshold level is required in order to divide the entire record into identifiable events.

The first feature to note from the ejection and the sweep arrival frequency profiles is the distinctly different profile shapes for the two events. The ejection statistics are relevant in the above canopy region receiving the upward movement of the low momentum fluid. Likewise, the sweep arrival frequencies are only relevant within the canopy, the final destination of the downwards moving gust. As a result, the frequency of the ejection arrival has little variation with hole size (*i.e.* event strength) in the region above the canopy, and similarly, the sweeps are more concentrated inside the canopy. The smaller variation with the hole size indicates that the turbulent structures at these levels are particularly strong and

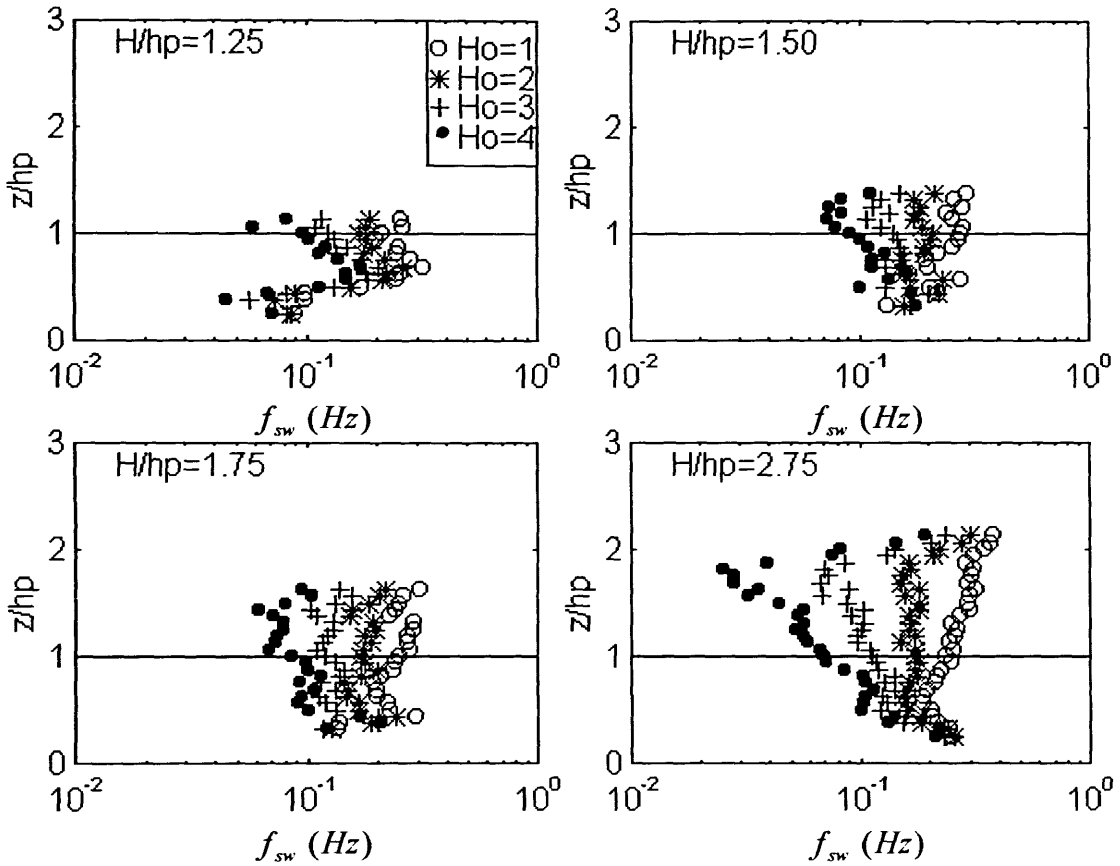

Figure 3.50. Sweep arrival frequency (f_{sw} in Hz) for the experimental runs in *Case A* at various threshold values H_o = 1 to 4. Notice that the same trend is present as that observed for the ejection arrival time, a concentrated frequency band in the region where the event travels to (the upper canopy region in this case) and a broad frequency band where the events are formed (the surface layer in this case). For the ejections, the concentrated frequency band occurs in the surface layer and the broad band inside the canopy.

intermittent. Within the upper canopy, the sweeps arrive at a range of frequencies varying from 0.1 to 0.3 Hz for the experimental runs in *Case A* and *B*. The ejections arising inside the canopy arrive at the surface layer at a similar range of frequency (0.1 to 0.3 Hz) for the experimental runs. In the location where the turbulent structures are created, the range of frequencies is much broader and the variation with the hole size parameter is more significant. This is an indication that the surface layer is composed of many weak sweeps and the canopy region of many weak ejections, which seems reasonable since turbulent structures are being generated in these regions and not all of them are of sufficient strength to travel across the canopy-surface layer interface.

The variation in the shape of the sweep arrival frequency profiles with the hole size is also a revealing feature in **Figures 3.50** and **3.51**. For small hole sizes (H_o = 1), more sweeps are present in the surface layer as compared to the canopy region and the frequency of sweep arrival decreases into the canopy. For larger hole sizes (H_o = 4), the trend is reversed, less sweeps occur above the canopy and the amount increases into the vegetation layer. At intermediate hole size values, the frequency of sweep

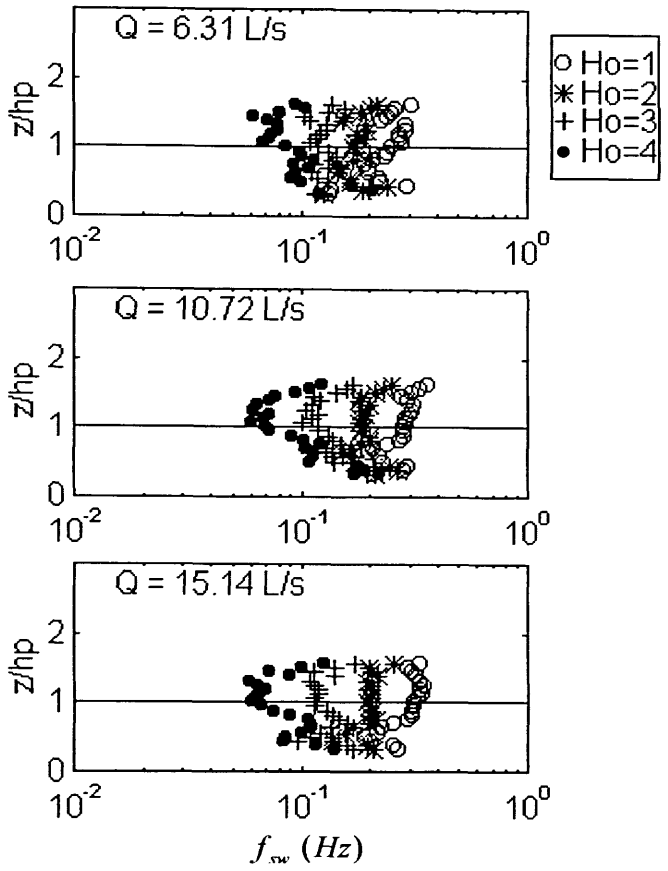

Figure 3.51. Sweep arrival frequency (f_{sw} in Hz) for the experimental runs in *Case B* at various threshold values H_o = 1 to 4. Notice the similarity in the frequency of sweep arrivals across the different flow discharge cases, suggesting that the velocity is not setting the event time scale.

arrival is constant throughout the profile. These behaviors can be explained by considering the implication that the hole size has on event strength. The weaker sweeps (H_o = 1) are more common in the surface layer because they cannot penetrate far into the canopy. Conversely, a strong sweep (H_o = 4) will not remain in the surface layer so it is expected to find more of them within the canopy. The arrival frequency profiles for the larger hole size (H_o = 4) have an increasing trend into the canopy, which might suggest that more sweeps arrive in the canopy than actually pass through the canopy height. This, however, is due to the fact that the hole size represents different absolute values at the two locations, so that more events are counted as sweeps in regions of lower Reynolds stress. The reversal in the sweep arrival frequency profiles is a direct result of the variation of $H_o|u'w'|$ and not indicative of the amount of the strong sweeps which arguably should be constant throughout the upper canopy.

Such a variation is not observed for the ejection arrival frequency in **Figures 3.48** and **3.49**. Instead, a minimum in the ejection frequency is seen slightly below the canopy height at 0.8–0.9h_p. Above and below this minimum, more ejections are identified in the Reynolds stress record. The frequency at the minimum value decreases with the hole size suggesting that the ejections that are present

Table 3.15. Average sweep and ejection arrival frequencies for the *Case A* and *B* experimental runs.							
Parameter / Run	**1A**	**2A**	**3A**	**4A,B**	**5B**	**6B**	**7A**
f_{se} (Hz) $(0.25 \le z/h_p \le 1.00)$	–	0.144	0.145	0.154	0.184	0.177	0.166
f_{ej} (Hz) $(1.00 \le z/h_p \le z/H)$	–	0.144	0.140	0.150	0.176	0.180	0.171

are weak. The link with the 0.5 contour line in the normalized ejection contour plots (as in **Figures 3.41** and **3.42**) at this precise elevation is suggestive that this level is associated with the zone of ejection formation. A plausible interpretation of the minimum in the ejection arrival frequency profiles is that ejections are generated at $0.8–0.9h_p$ from the interaction of the sweep momentum with the lower velocity fluid within the canopy and as such have not made a significant contribution to the total Reynolds stress.

The variation of the ejection and sweep frequencies with the characteristic depth and the flow discharge can also be noted from **Figures 3.48** through **3.51**. As the depth of the surface layer increases, the sweep-ejection character of the flow becomes more pronounced, resulting in smoother arrival frequency profiles and less point to point variation. Asides from this, however, the frequency of sweep and ejection arrival does not seem to be influenced much by the level of submergence. **Table 3.15** shows the variation of the average sweep and ejection arrival frequency in the regions of interest for each event, above the canopy for the ejections and the upper canopy region for the sweeps. The averaging is performed over vertical distances and across hole size values. For the *Case A* experimental runs, the sweep and ejection arrival frequencies increase, but with all the values remaining within 15% of each other. The velocity variation cases also demonstrate that the ejection and the sweep frequencies do not vary appreciably with the flow discharge, implying that the velocity does not set the event time scale. In addition, the average values for the sweep and the ejection arrivals are all within 20% for the experimental runs in *Case B*.

The mean arrival frequencies for the ejection and the sweep events, shown in **Table 3.15**, are quite similar to each other, within a 5% difference. In combination with efficiency ratios on the order of $Eff = 1–2$, this suggest that the arrival of a sweep in the canopy creates an ejection that arrives at a later time at the surface layer. The sweep-ejection cycle is again shown to be an important controlling process in the structure of the momentum transfer. The flexibility of the plant canopy should allow it to respond to the forcing caused by the momentum exchanges in the sweep-ejection cycle. Indeed, a good agreement is seen between the range of the arrival frequencies shown in **Figures 3.48** through **3.51** and the estimated plant vibrational frequencies shown in **Table 3.2**. Except for the higher flow discharges, the mean sweep arrival time is on average within 15% of the measured mean plant vibration frequency (f_p). This suggests that the plant vibrational response for the depth variation cases is tuned to the arrival of the sweep events and that as a sweep enters the canopy it not only induces the ejection of a lower velocity fluid but also the bending of the flexible plant.

3.6.5 Conceptual Model

The information provided by the quadrant analysis, the intermittency analysis, the stress fractions and the sweep-ejection arrival frequencies, allow us to construct a conceptual model for the momentum transport mechanism in the seagrass canopy. As with the previous discussions, this conceptual model draws from the work done by other researchers in the plant canopy turbulence field. In particular, a concise model proposed by Murota *et al.* (1984) gives an indication of how canopy waving fits into the physical picture of the turbulence structure in a submerged plant canopy. The effect of the depth variation on this conceptual model is a contribution obtained for the first time from this laboratory study.

Figure 3.52 shows a schematic of a conceptual model explaining the momentum transfer in a submerged plant canopy subject to velocity and depth variations. The top figure represents the effect of increasing the depth of the surface layer (h_o) while maintaining identical forcing in the system. As the total water depth increases above the canopy, the turbulent eddies created at the canopy height increase in size proportional to h_o. The eddies are responsible for bringing surface layer momentum down into the canopy where the vegetative drag has reduced the mean flow. Larger scale eddies are able to carry fluid further into the canopy, thus increasing the penetration depth of the sweep motions. With a higher penetration comes more vertical momentum exchange and an increase in the ejection of low velocity fluid away from the canopy. Despite the increased vertical scale and penetration depth, the event arrival frequencies remain similar. Since the plant movement in the longitudinal direction occurs as a response to the forcing by the sweep motions, then the frequency of plant vibration is also comparable for the different surface layer depths, as corroborated by the plant motion experiments. Plant vibrations also arises as a result of the interaction of a plant with the eddies shed from upstream plants or because of instabilities over the plant tip. The plant vibration frequency estimated from the visualization experiments, however, matched those predicted for the propagation of eddies at the canopy height.

The two limiting cases for this conceptual model also provides insight into the momentum transfer mechanism. In one extreme, the unbounded flows such as those found in atmospheric canopies are characterized by active eddies whose scale is not set by the boundary layer thickness but by L_s, the degree of shear. It is not uncommon to have turbulent flows over a plant canopy where the turbulent structures extend to the bottom of the canopy. The resulting velocity statistics reflect the vertical exchange of momentum throughout the canopy height. In the constrained flows explored in this laboratory study, the water depth limited the penetration of the sweep-ejection cycle to approximately $z/h_p = 0.25$. The other extreme case, the flow through an emergent canopy, demonstrated how a shift in the nature of the turbulence occurred as the surface layer depth was decreased. The lack of a surface layer and shear zone prevented the formation of the turbulent structures associated with the instabilities in a mixing layer. Without this shear-generated turbulence, the plant canopy is dominated by turbulence resulting from the interaction of the plants with the mean flow.

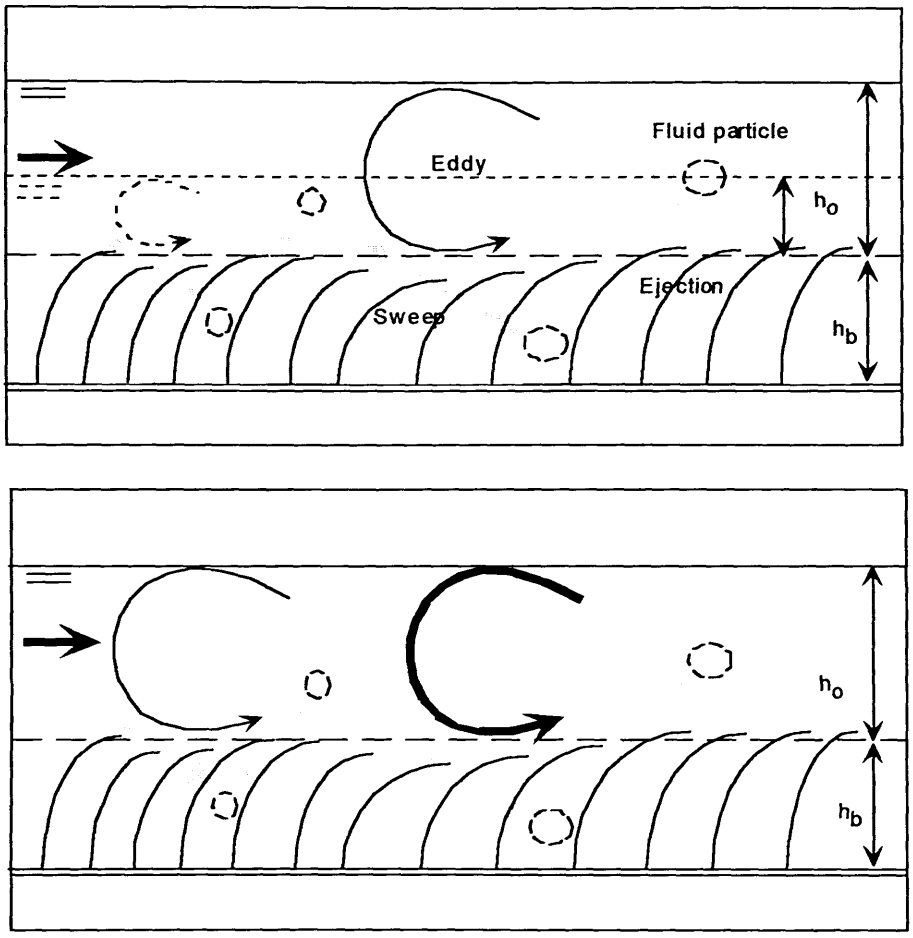

Figure 3.52. Conceptual model of the effect of the surface layer depth (top figure) and the flow discharge (bottom figure) on the momentum transport in a submerged flexible plant canopy. The gray arrows represent the sweep and ejection motions, the dashed circles are the fluid particles transported by the events and the circular arrows represent the largest eddies in the surface layer. The horizontal long dashed line (—) is the effective canopy height (h), while the solid (–) and dashed lines (--) are the two different water depths (H).

The bottom schematic in **Figure 3.52** shows the effect of the variation in velocity at a constant water depth on the momentum transfer mechanism. By varying the flow discharge, the eddy scale does not change, but the intensity of the eddy motions increases. The stronger downward sweeps lead to larger momentum penetration depths and to increased ejection strength from the canopy, as seen in **Figures 3.41** through **3.44**. The increase in the flow rate, however, does not result in a significantly higher mean sweep frequency as expected from the increased plant motion. Despite comparable mean arrival frequencies, the stronger sweeps induce a shift towards events at smaller hole sizes, *i.e.* at higher total Reynolds stress a smaller hole size contains greater instantaneous stress. Thus, the arrival frequency that induces plant motion occurs at smaller H_o and is larger than the mean frequency obtained for all H_o. In this framework, the maximum sweep frequencies match the measured plant vibration frequencies, thus supporting the physical link between the sweep-ejection cycle and the canopy waving. Similar conclusions were made by Murota *et al.* (1984) who associated higher canopy waving with stronger sweep activity.

3.7 Turbulence Scales

The conceptual model of the momentum transfer in the depth limited plant canopy flow presented in Section 3.6 indicated that the eddy scale is important in determining the depth of momentum penetration. One way of obtaining an estimate of the turbulent eddy dimensions from the single-point velocity measurements is by calculating the integral time scale ($\mathfrak{I}_{ui}$) from the autocorrelation function and using Taylor's hypothesis to make the conversion from the temporal to the spatial domain. As described in Section 3.3.2, the applicability of Taylor's hypothesis to the high intensity turbulent flows inside the canopy is suspect. Its use, however, is widespread in the canopy turbulence research field velocity (*e.g.*, Kaimal and Finnigan, 1993; Raupach *et al.*, 1991; Raupach *et al.*, 1996) due to the understanding that eddies travel at faster speeds than the mean local velocity, as evidenced by spatial correlation analyses (Shaw *et al.*, 1995). The higher convection velocities substantiate the use of Taylor's hypothesis by assuring that the actual turbulence intensities calculated with U_{eddy} are smaller than those calculated with the local mean streamwise velocity.

With this precaution in mind, the single point Eulerian integral time scale obtained from the velocity autocorrelation function allows us to estimate the time over which the instantaneous velocity is correlated with itself. The autocorrelation function (ζ) is a normalized form of the autocovariance function (R) and can be expressed in general terms as:

$$\zeta(t_1-t_2) = \frac{\overline{u(t_1)u(t_2)}}{\overline{u^2}} = \frac{R(t_1-t_2)}{\overline{u^2}}, \qquad \textbf{(3.109)}$$

where the difference between the two times, t_1 and t_2, is the time lag, τ. The numerator of **Eq. 3.109** is the covariance of u and the denominator is the variance of u. For a stationary, Gaussian process, the autocorrelation function is a function of the lag time only (Jenkins and Watts, 1968). As discussed in Section 2.4.1, the velocity records are stationary and have a Gaussian distribution described by $N(m,S^2)$.

The autocorrelation function describes the memory of $u_i(t)$, *i.e.* how long in time the instantaneous velocity remembers the previous value. The autocorrelation function for zero lag is by definition equal to unity, since the velocity at a specific point in time is always correlated with itself. As the lag time increases ($\tau \to \infty$), the autocorrelation decreases to zero ($\zeta(\tau) \to 0$) so that the velocity at two specific points in time becomes less correlated. In turbulence research, the autocorrelation is an indication of the eddy time scale since the velocities within a particular eddy moving past a fixed measurement point are correlated with themselves. The autocorrelation function can be used to estimate the integral time scale $\mathfrak{I}_{ui}$ which is simply the maximum time over which the instantaneous velocity is correlated with itself. Formally, the integral time scale is defined as:

$$\mathfrak{I}_{u_i} = \frac{1}{\sigma_{u_i}^2}\int_0^\infty \overline{u_i'(t)u_i'(t+\tau)}\,d\tau = \frac{1}{\sigma_{u_i}^2}\int_0^\infty R(\tau)d\tau\,. \qquad \textbf{(3.110)}$$

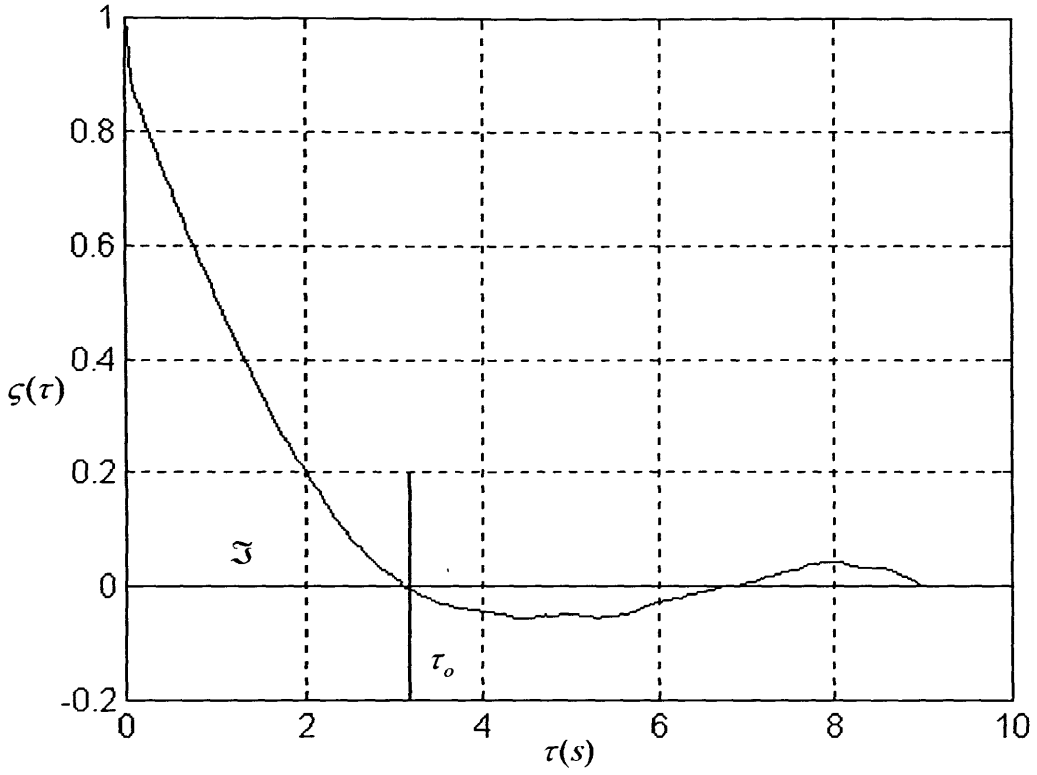

Figure 3.53. Autocorrelation function $\zeta(\tau)$ of the streamwise velocity for experimental run 4 (H/h_p = 1.75, Q = 6.31 L/s) at the canopy height z/h_p = 1.00. The integral time scale ($\mathfrak{I}_{ui}$) is estimated as the area under the autocorrelation function up to a lag time for zero crossing (τ_o).

where the subscript i is an index referring to the three velocity components, σ_{ui}^2 is the variance of the velocity component. In practice, various methods exist for estimating the integral time scale from the autocorrelation function. One way is to assume that the autocorrelation function can be described by a negative exponential function and to calculate $\mathfrak{I}_{ui}$ from the value of τ for which $\zeta(\tau) = 1/e = 0.37$, where e is the natural logarithm base (Kaimal and Finnigan, 1993, p. 35). Alternatively, the integration of the autocorrelation function shown in **Eq. 3.110** is carried out for the lags up to the first zero crossing, τ_o, assuming that the sum of the area underneath the curve for greater lags sum to be negligibly small (*e.g.*, Raupach *et al.*, 1986; Brunet *et al.*, 1994). **Figure 3.53** shows an example of an autocorrelation function calculated at the canopy height (z/h_p = 1.00) for experimental run 4 using the second method. The integral time scale was computed by calculating the integral of $\zeta(\tau)$ up to τ_o, represented in **Figure 3.53** by the vertical line at approximately 3.2 seconds. A trapezoidal integration scheme was used to determine the integral of the autocorrelation function. For a selected number of points, the autocorrelation function did not cross zero and the integration was made up to the first minima in the autocorrelation function.

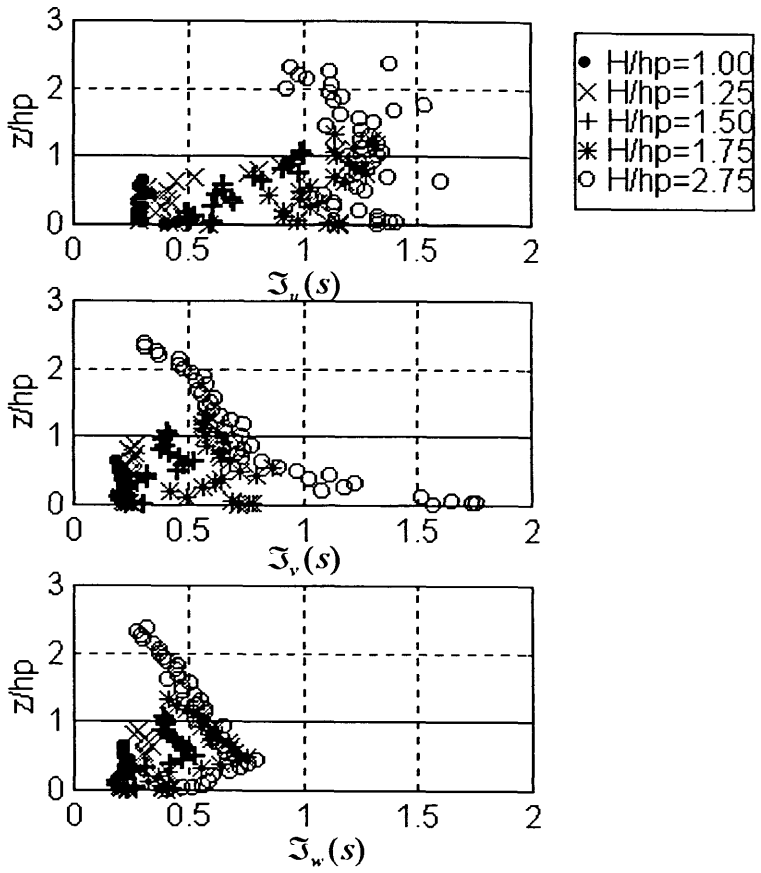

Figure 3.54. Integral time scale for the *Case A* experimental runs. From top to bottom, the figures are the integral time scale in the longitudinal, lateral and vertical directions. The horizontal bars representing the horizontal deviation have been omitted for clarity. The decrease in the integral time scale with the characteristic depth (H/h_p) is associated with the smaller surface layer depth and eddy scale.

The longitudinal scale of the turbulent eddies that dominate the longitudinal, vertical and lateral velocity fluctuations at a fixed point can be quantified by calculating the single point Eulerian integral length scale, L_{ui}. It is obtained from the integral time scale and the local mean streamwise velocity as:

$$L_{u_i} = \langle \overline{U} \rangle \Im_{u_i} . \tag{3.111}$$

The estimates of the integral time scale for the experimental runs in *Cases A* and *B* are shown in **Figures 3.54** and **3.55** for the three velocity components. The correlation time varies for each velocity component, being the largest in the longitudinal direction and the smallest in the vertical direction. The only integral time scale to demonstrate a consistent pattern across the characteristic depth variations is the vertical component, $\Im_w$. The lateral and longitudinal integral time scale profiles show certain disparities across the depth variation cases, in particular the monotonically decreasing profile of $\Im_v$ for $H/h_p = 2.75$ and the monotonically increasing profile of $\Im_u$ for $H/h_p = 1.50$. Fortunately, the time scale of concern for the description of the momentum exchange between the surface and the vegetation layers is the vertical integral scale. In fact, Raupach *et al.* (1996) point out that it is appropriate to use the vertical component

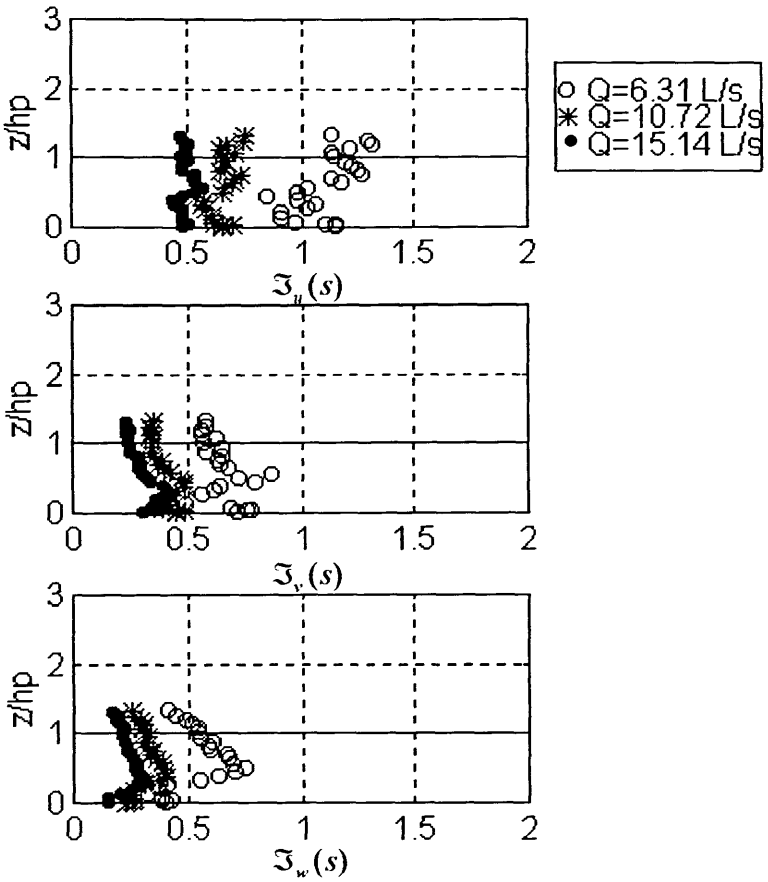

Figure 3.55. Integral time scale for the *Case B* experimental runs. A marked decrease in the integral time scale as the flow discharge (Q) increases is due to the higher eddy convection velocities with the increased velocity at the canopy height.

to determine the turbulence length scale because it reflects the active turbulence near the effective canopy height. The estimates from the other velocity components include contributions from eddies that do not participate in the active vertical exchange. **Figure 3.54** shows that there is a peak in the vertical integral time scale at approximately $0.5h_p$ for the experimental runs in *Case A*. A less noticeable peak is also observed at this level for the lateral component and in the vertical and lateral velocities in the flow discharge variation cases at the same level. These peaks correspond to the location where the velocity is correlated with itself for the longest amount of time, presumably due to the fact that the vertical fluctuations at this level are due exclusively to the turbulence transported from the canopy height. This suggests that the mid canopy height is the depth to which the surface layer eddies penetrate, an indication also provided from the sweep stress contribution to the Reynolds stress presented in Section 3.6.2. Above and below the mid canopy height, the vertical integral time scale decreases due to the presence of multiple smaller eddy scales that diminish the mean value of $\Im_w$ above $0.5h_p$ and the lack of strong vertical fluctuations in the lower canopy regions, respectively. In addition, the lower canopy region has smaller integral time scales due to the transition from shear to wake generated turbulence, which characteristically has smaller temporal correlation scales.

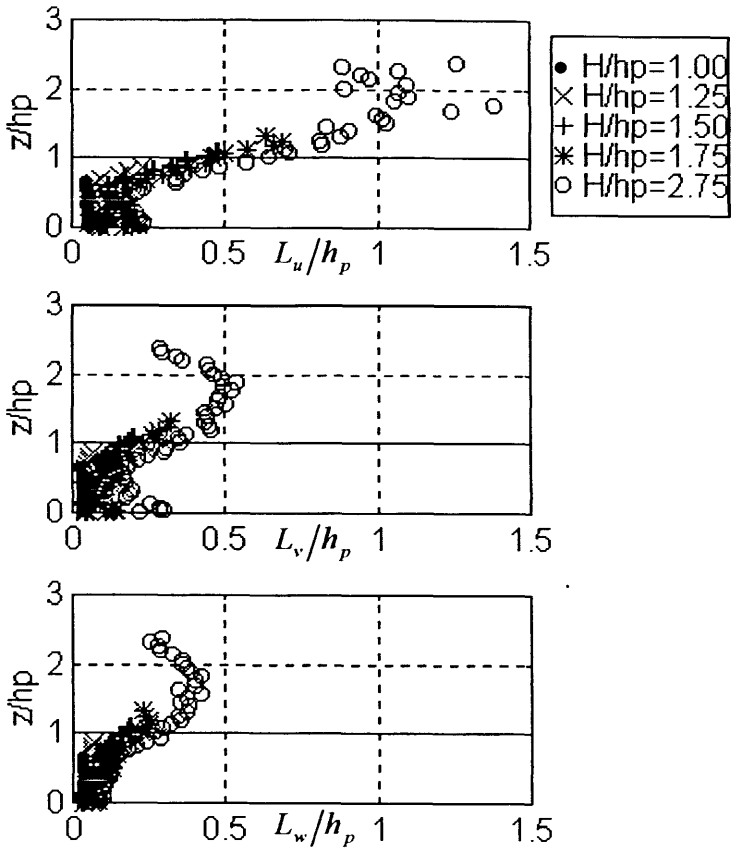

Figure 3.56. Integral length scale variation for the *Case A* experimental runs. The integral length scale has been normalized by the undeflected canopy height, h_p.

In general, **Figures 3.54** and **3.55** show that the integral time scale increases with H/h_p and decreases as Q increases. The former trend is presumably due to the larger eddy scale as the surface layer depth increases, while the latter is due to the larger eddy convection velocities as the flow discharge increases. At $z = h$, for example, the integral time scale increases from 0.36 s to 1.33 s for H/h_p = 1.00 and 2.75, and decreases from 1.15 s to 0.47 s for Q = 6.31 L/s and 15.14 L/s, respectively.

The integral length scales were computed from the time scale and the mean velocity profiles. Due to the relatively uniform distribution of $\mathcal{T}_{ui}$ and the large variation of the mean velocity, the L_{ui} profiles resemble the mean velocity profiles substantially, as shown in **Figures 3.56** and **3.57**. Focusing attention to the vertical integral scale, it is observed that L_w varies from about $0.1h_p$ to $0.25h_p$ from mid canopy height, $z/h_p = 0.5$, to the canopy top, h. For the longitudinal component, the integral length scale increases to $0.5h_p$ at the canopy height. Typically, the values for the streamwise and vertical length scales determined from single points measurements in atmospheric canopy flows are $L_u = h$ and $L_w = 0.3h$ (Raupach *et al.*, 1991) at $z = h$, from which it is inferred that the eddies responsible for the vertical momentum transfer are large turbulent structures. For the depth-limited canopy flows, the turbulent length scales are smaller compared to unbounded terrestrial canopies.

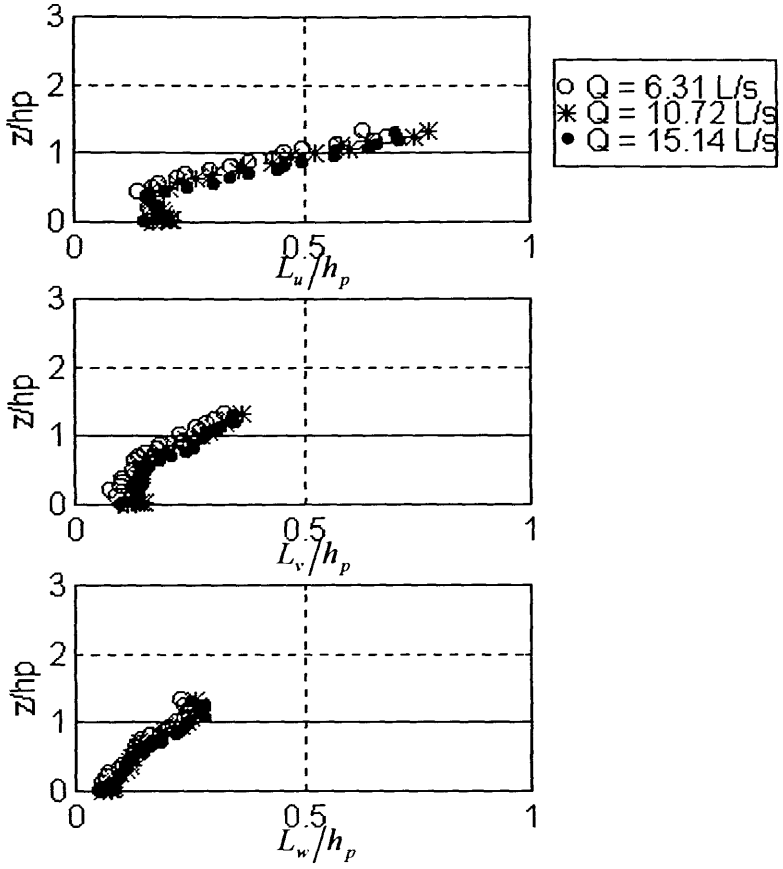

Figure 3.57. Integral length scale variation for the *Case B* experimental runs. The integral length scale has been normalized by the undeflected canopy height, h_p.

The variation of the integral length scale with the characteristic depth (H/h) can be explored by comparing the values obtained at the canopy height for the various experimental runs, as in **Figure 3.58**. The integral length scale has been normalized by the effective canopy height, h, which refers to the undeflected height, h_p, for *Case A* and the deflected height, h_b, for *Case B*. The variation of L_w with depth suggests that the depth limited estimates approach the values for unbounded flows at characteristic depths on the order of 2–3. For the streamwise length scale, the variation of L_u with H/h is observed to asymptote to a slightly smaller value than that quoted in the atmospheric canopy turbulence literature, $0.7h$. This result suggests that the streamwise fluctuations are more sensitive to the limitations of the surface layer depth, which is reasonable since the maximum longitudinal fluctuations at $z = h$ are due to eddies that scale on h_o, while the maximum vertical fluctuations can occur within eddies smaller than h_o. The asymptotic variation of L_w and L_u suggests that that a critical surface layer depth exists beyond which the active eddy scale at the canopy height does not change. This type of asymptotic behavior in regards to the level of submergence has been observed for numerous other parameters derived from the experimental data, giving stronger support to the concept that a critical level of submergence exists. In this case, the eddy scale is governed by the surface layer depth up to about 2 to 3 times the canopy height. Beyond that

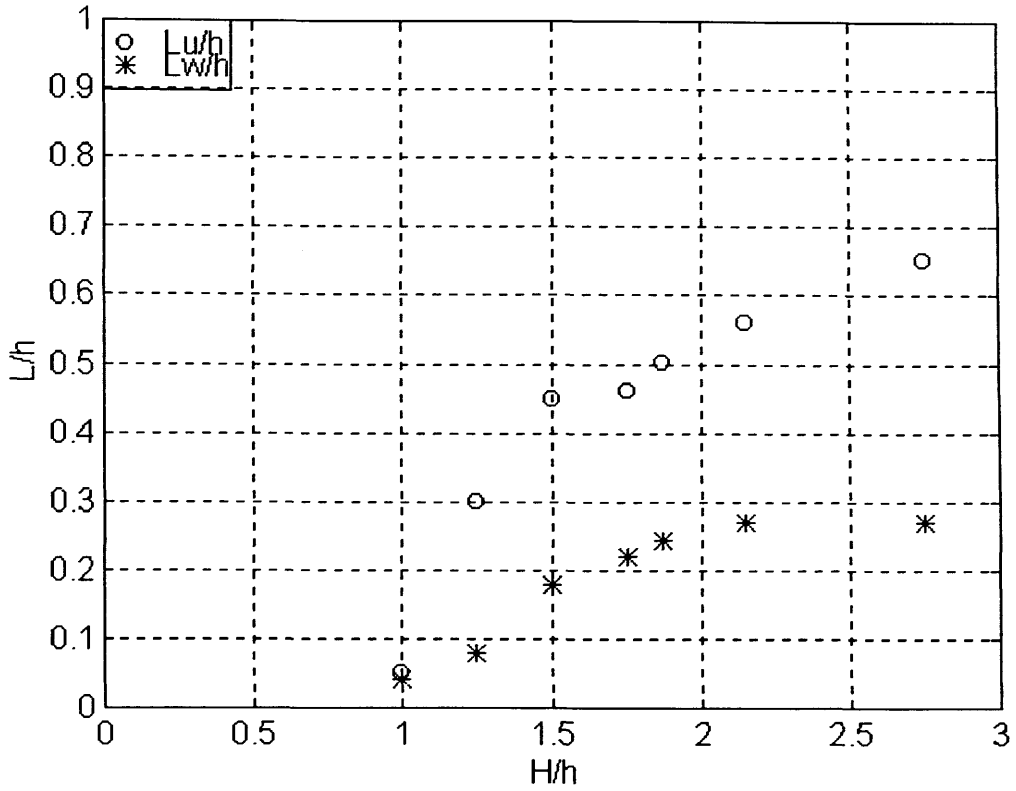

Figure 3.58. Variation of integral length scale L_u and L_w with the characteristic depth (H/h) for the experimental runs in *Cases A* and *B*. The integral length scale has been nondimensionalized by the effective canopy height, h, taken to be the undeflected height for *Case A* and the deflected height for *Case B*. The *Case B* experimental points are located at H/h = 1.87 and 2.15.

point, the active eddy scale is fixed by the shear in the mixing layer created by the momentum sink. The discussion in Section 3.3.1 regarding the shear length scale, the vorticity thickness and the surface layer depth suggested that a changes in the dominant scale occurred as the surface layer increased in size. For small values of h_o, the surface layer depth set the scale for the active eddy size and as h_o was increased, the shear length scale was the appropriate measure of the size of the eddies active in vertical exchange of momentum and mass. Through the quantification of the time of correlation and the use of Taylor's hypothesis, it has been suggested that the eddy size does in fact depend on the surface layer depth for small values of h_o and then becomes independent as h_o is increased beyond a critical value.

In terms of the variation of the integral length scale with the flow discharge, **Figure 3.57** suggests that L_{ui} does not vary significantly with Q despite the noticeable variation in the integral time scale. This behavior is not unexpected, however, considering that the flow discharge increases the eddy convection velocity and decreases the eddy time scale proportionally. Despite this, the increase in the surface layer depth that occurs as a result of the plant deflection at higher flow discharges fits into the description of the variation of L_{ui} with H/h quite well, as seen in **Figure 3.58**. Thus, the turbulent eddy length scale is set exclusively by the variation in the characteristic depth for depth limited flows.

The vertical eddy length scale also provides an opportunity to corroborate the estimates of the streamwise periodicity scale or the distance between successive coherent eddies as measured in the plant motion experiments through the monami wavelength, λ_m. Raupach *et al.* (1996) suggested the following relationship between the streamwise periodicity (Λ_x) and the vertical integral length at the level of the canopy height with the assumption that $U_{eddy}/U_h \approx 1.8$, a ratio obtained from two-point correlation estimates of the eddy length scale (Shaw *et al.*, 1995):

$$\frac{\Lambda_x}{h} = \frac{2\pi L_w(h)}{h}\left(\frac{U_{eddy}}{U_h}\right), \tag{3.112}$$

where the 2π factor relates the streamwise periodicity with the spatial correlation length scale. In Section 3.2.2, the monami wavelength was measured to be λ_m = 40.00 ± 2.15 cm for experimental run 6 (H/h_p = 1.75, Q = 15.14 L/s). This experimental condition exhibited the canopy waving phenomenon most distinctively and allowed the estimation of the half wavelength from the video recordings of the plant motion. Using the assumption made by Raupach et al. (1996) in regards to the ratio between the convection velocity U_{eddy} and the interface velocity U_h and the value for the vertical integral length scale at the canopy height, an estimate of the streamwise periodicity can be made for experimental run 6, resulting in a value of Λ_x = 39.76 ± 1.00 cm, which is comparable to the monami wavelength estimate made from the visualization experiments. This suggests that the streamwise eddy periodicity is reflected in the coherently traveling canopy waves.

Through the use of the integral length scale, the turbulent structures that dominate the momentum transport in and above the flexible plant canopy have been shown to have longitudinal lengths on the order of the canopy height, an indication that the eddies are large compared to the size of the depth limited flow region. In comparison, the eddies formed by the interaction of the mean flow with the plants are of much smaller dimensions, as seen in the integral length scales within the lower canopy region. The values of integral time ($\mathcal{T}_u$, $\mathcal{T}_v$, $\mathcal{T}_w$) and length scales (L_u, L_v, L_w) are typically smaller in the lower canopy regions and are also more comparable to one another since the eddies are generated in the plant wakes, whose size is determined by the plant dimensions. In addition, the eddy scales from the shear generated turbulence at the canopy height are much larger than the scale at which turbulence dissipation occurs, which is set by the Kolmogorov relationship. The relative contribution of the different eddies sizes to the total turbulent energy can be obtained from the spectral analysis of the velocity records for each experimental point in the *Case A* and *B* runs. Through a similar use of the Taylor's frozen turbulence hypothesis, the turbulence spectra in frequency space can be converted to wave number space, as will be performed in Section 3.8. The integral length scales will be shown to be good indicators of the size of the eddies that dominate the turbulence spectrum.

3.8 Turbulence Spectral Characterization

Spectral characterization is an important tool in turbulence research. Turbulence spectra can provide information on how the turbulent kinetic energy (*TKE*) is distributed over a range of frequencies and highlight those processes that contribute to energy production and dissipation. In Section 3.3.6, the *TKE* at all scales was discussed, now the focus is turned to identifying the important scales within the turbulent kinetic energy spectrum and associating them with the turbulence structures and plant motion responses that have been presented so far in this experimental study. This section is dedicated to presenting the results from the characterization of the turbulence spectra. It includes a discussion of the proper spectral scaling for plant canopy flows, an interpretation of the peak in the turbulence spectra at low frequencies as a region of shear production of turbulence, a discussion of the inertial subrange and the evidence of short circuiting of the eddy cascade and the quantification of the turbulent dissipation obtained from the Kolmogorov law.

Before proceeding to discuss the spectral characterization of the turbulent velocity field in the seagrass meadow, some pertinent definitions are useful. The spectral characterization of a stochastic process is simply a description of that process in the frequency domain instead of the time domain representations discussed up to this point. Converting the velocity time series into a spectral representation can be performed by calculating the autocovariance function for the time series and taking its Fourier transform. If the autocovariance function decays to zero for large values of the lag time, then it possesses a Fourier transform (Landahl and Mollo-Christensen, 1992). As shown in Section 3.7, the autocorrelation function $\zeta(\tau)$, which is a normalized autocovariance $R(\tau)$, decays rapidly to zero. The power spectral density $S_{uiui}(f)$ and the autocovariance function $R(\tau)$ form a Fourier transform pair which can be expressed as the following two equations for a one-dimensional, one-sided spectra (Kaimal and Finnigan, 1993, p. 59):

$$S_{u_i u_i}(f_{u_i}) = 2\int_0^\infty R(\tau) e^{-i2\pi f_{u_i}\tau} d\tau, \tag{3.113}$$

$$R(\tau) = \frac{1}{2}\int_0^\infty S_{u_i u_i}(f_{u_i}) e^{-i2\pi f_{u_i}\tau} df_{u_i}. \tag{3.114}$$

where f_{ui} is the cyclic frequency in Hz. Alternatively, the power spectra could be expressed in terms of the radial frequency, $\omega = 2\pi f$, or by applying Taylor's frozen turbulence hypothesis expressed in wave number space instead of frequency space through the conversion:

$$k_{u_i} = \frac{2\pi f_{u_i}}{\langle \overline{U} \rangle} \tag{3.115}$$

where k_{ui} is the wave number (cm^{-1}). In this laboratory study, we will use the frequency representation of the power spectral density and refer to the wave number representation on selected occasions only.

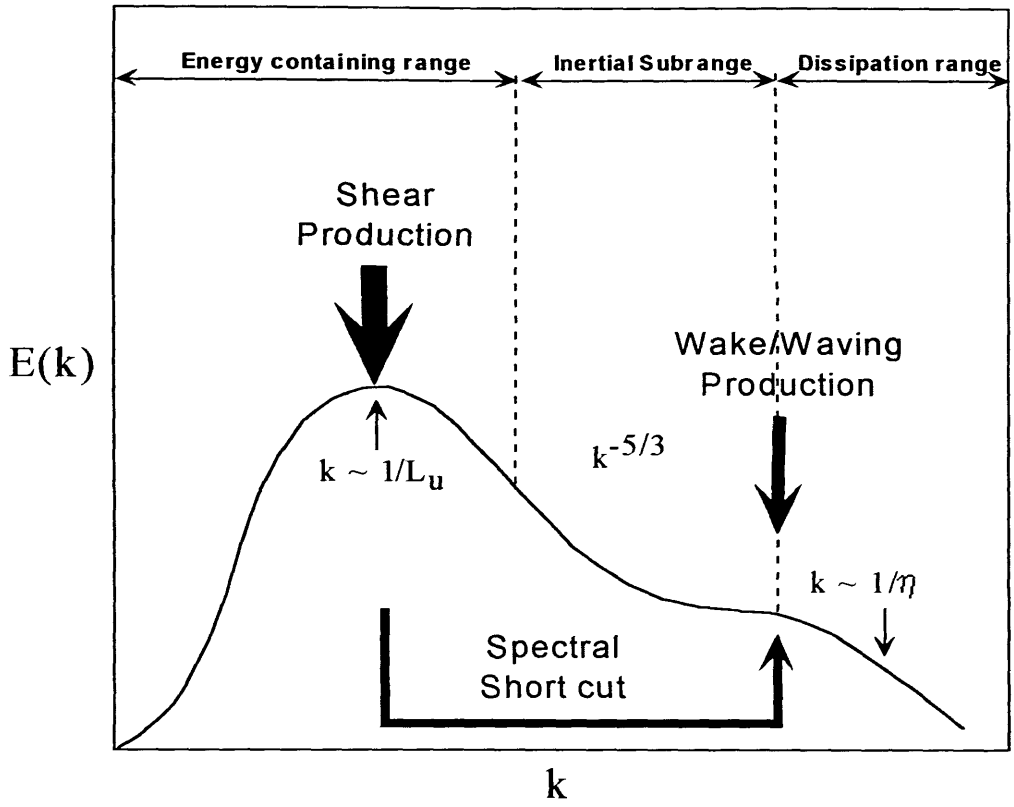

Figure 3.59. Schematic of the turbulent energy spectrum in wave number space $E(k)$ for generic plant canopy turbulence. The wave number space is divided into three different ranges: the energy-containing range, the inertial subrange and the dissipation range. Turbulent energy is introduced at two locations by shear and wake generation and is dissipated at the largest wave numbers by the action of viscosity. From Kaimal and Finnigan (1993) p. 98.

A substantial amount of work has been done in interpreting the spectra obtained from the turbulent velocity fields in and above plant canopies over the last thirty years. For a generic plant canopy, the turbulence is due to both shear and wake production, as depicted in the schematic of **Figure 3.59** which has been borrowed from Kaimal and Finnigan (1993) for illustrative purposes only. It shows the three-dimensional energy spectrum $E(k)$ in wave number space and identifies three broad regions based on the eddy scale and the turbulent behavior: the energy containing range, the inertial subrange and the dissipation range.

Shear production generates low frequency turbulent eddies in the energy containing range, which scale on a wave number related to the integral length scale ($k_{ui} \sim 1/L_{ui}$). These eddies are coherent turbulent structures that transfer momentum to the plant canopy in strong but infrequent gusts, as discussed in Section 3.6. The largest eddies extract kinetic energy directly from the mean flow and transfer it to smaller eddies via the process of vortex stretching (Kundu, 1990). The turbulent kinetic energy is cascaded from larger to smaller eddies scales within the region of the turbulence spectrum known as the inertial subrange. Within the inertial subrange, the turbulence spectrum has a characteristic

slope equal to $k_{ui}^{-5/3}$ or $f_{ui}^{-5/3}$, a scaling law derived theoretically by Kolmogorov and supported by ample experimental evidence (Landau and Mollo-Christensen, 1992). In addition, turbulence within the inertial subrange is neither produced nor dissipated and is locally isotropic. Beyond the inertial subrange, the highest frequency and wave numbers correspond to the smallest eddy structures in the turbulent field, whose size is set by the Kolmogorov microscale ($k_{ui} \sim 1/\eta$). These eddies are directly affected by viscosity which converts the kinetic energy in the eddy to internal energy of the fluid.

The turbulence spectra in a plant canopy has additional contributions from the interaction of the mean flow with the canopy elements. If the plant canopy is flexible and waving, an additional source of turbulence arises from the waving production. These two processes are able to extract energy from the mean flow and the largest eddies and convert it to turbulence at a scale set by the plant dimensions and the waving phenomenon. Thus, the wake and waving production can either introduce turbulent energy directly at frequencies set by the two processes or short-circuit the eddy cascade in the inertial subrange by converting turbulence in the energy-containing range immediately to smaller scales (Kaimal and Finnigan, 1993). The wake and waving production introduce high frequency peaks that may prevent the Kolmogorov law in the inertial subrange from being observed. Evidence of the wake and waving production and the spectral short circuit is abundant in both atmospheric canopy flows and open channel flows with vegetation (*e.g.*, Seginer *et al.*, 1976; Finnigan, 1979a; Lopéz *et al.*, 1995). It has been pointed out by Kaimal and Finnigan (1993), however, that the interpretation of high frequency peaks should be made with caution for flow conditions exhibiting a limited inertial subrange. Under these conditions, the turbulence spectra curves continuously from the energy containing to the dissipation range and does not exhibit the characteristic slope. Aware of this, Brunet *et al.* (1994) showed that the peaks observed in the high frequency region in a study of a model wheat canopy were not due to the introduction of energy by the waving phenomenon but rather by a rapid roll-off caused by an increasing limit frequency, $0.1f_\eta$, where f_η is the Kolmogorov microscale frequency, which limited the length of the inertial subrange.

This section will present the one-dimensional spectra in frequency space obtained from the acoustic Doppler velocimeter (f_S = 25 Hz) for the experimental runs in *Case A* and *B*. Although the data from the laser Doppler velocimeter provided a larger sampling frequency (f_S = 100–200 Hz), the limited use of the instrument prevents the comparison among different locations within the canopy. Within this discussion, the spectral features of interest are the peak behavior in the low frequency region associated with the turbulent structures, the inertial subrange behavior including the slope, the roll-off frequency and the presence of higher frequency peaks associated with the wake production of turbulence. In addition, the spectra provides an opportunity to evaluate the ADV performance and corroborate that the vertical component has inherently less noise, as discussed in Section 2.3.2.3. For the majority of the discussion, attention will be limited to the streamwise and vertical spectra. After discussing several calculation and scaling issues, the turbulence spectra will be presented in two types of figures, spectral profiles and spectral contour maps.

3.8.1 Spectral Calculation and Scaling

Several methods are available to calculate the power spectral density for a stochastic process. The traditional approach is to compute the autocovariance function as an intermediate step to obtaining the sample spectra, as described thoroughly in Jenkins and Watts (1968). The smoothed sample spectrum is calculated by dividing the entire frequency space into bins and summing the product of the autocovariance, the real part of the Fourier term and an appropriate window parameter for each bin. Several degrees of bin averaging and spectral smoothing are achieved by varying the window parameter size in a procedure known as window closing, the selection of the most efficient window size. This procedure is a useful exercise, but results in a long computing time, especially for the large data sets in this experimental study, 15,000 samples per record.

More efficient methods of obtaining the power density spectrum are now available. The fast Fourier Transform (FFT) is an algorithm that calculates the spectrum directly from the time series without the intermediate step of computing the autocovariance. The number of operations required to calculate the spectrum is reduced from $2N_o\log_2 N_o$ to N_o^2, which for N_o = 15,000 samples implies 500 times the amount of operations (Jenkins and Watts, 1968). The power spectral density for this experimental study was computed by using a modified version of a standard MATLAB program called *spectrum.m*. It estimates the power spectral density of a signal using Welch's average periodogram method, a modified FFT algorithm. The signal is divided into non-overlapping sections, each of which is detrended and smoothed by using a Hanning window, then zero padded (MATLAB, 1992). Smoothing of the sample spectrum was achieved by using the window closing technique to determine the appropriate window length. The choice of the window size in the spectral estimate corresponded to a value such that the spectra was smoothed without losing any significant features. The two methods of computing the spectral density were corroborated by applying each to an ADV velocity record. The results from this preliminary test suggested that both methods gave comparable results and either could be chosen for determining the turbulence spectra. For reasons of computing time and simplicity, the latter method employing the fast Fourier transform algorithm has been chosen for this experimental study.

Once the spectra density function was calculated at each point in the velocity profile, the appropriate normalization of the spectra and the frequency was sought. Turbulence spectra in atmospheric canopy flows are traditionally presented in frequency-weighted fashion, *i.e.* the power spectra density (S_{uiui} in cm^2/s) is multiplied by the frequency and normalized by the variance of the velocity component (*e.g.*, Kaimal and Finnigan, 1993; Brunet *et al.*, 1994). The purpose of such a normalization is to highlight the regions of peak turbulent energy by minimizing the effect of the low and high frequency components in the turbulence spectrum. The frequency-weighted spectral densities are normalized by the velocity variance to facilitate the comparison among locations with different turbulence levels for that velocity component. Preliminary observations from the spectra obtained in this laboratory study showed

that this normalization was effective in highlighting the peak frequency associated with the sweep-ejection cycle and minimizing the noise introduced at the extreme frequency values from either the calculation scheme or the instrument performance. The normalized power spectral density (s_{uiui}) is defined as:

$$s_{u_i u_i} = \frac{f_{u_i} S_{u_i u_i}}{\sigma_{u_i}^2}, \tag{3.116}$$

where the subscript u_i refers to the velocity components and the turbulent energy is represented by the variance, σ_{ui}^2. In addition to the normalization, the scaling of the normalized spectra axis must be chosen so as to present the spectral data in the most effective way. Two options exists, a logarithmic and a linear axis. A linear axis accentuates the peak frequency associated with the large turbulent structures considerably. Murota *et al.* (1984) presented the streamwise velocity spectra for a slowly swaying and a rapidly swaying submerged plant canopy in this fashion. The spectra showed successfully that the energy concentration peak at low frequencies extended to the lower canopy region for the rapidly swaying canopy, but was attenuated considerably in the slowly swaying case. Although effective for this purpose, the turbulence spectra plotted on a linear vertical scale, as in **Figure 3.59**, does not demonstrate the inertial subrange linear slope, a feature which is of critical interest in estimating the turbulence dissipation. The logarithmic scale, on the other hand, is effective in showing both the peak in the low frequency range and the $f^{-2/3}$ region and for this reason has been chosen for this experimental study.

The normalization of the frequency has been a more debated issue in the literature on atmospheric plant canopy flows. Some authors prefer not to normalize the frequency because no single length or time scale can describe the several mechanism leading to the turbulence within the plant canopy (*e.g.*, Finnigan, 1979a; Raupach *et al.*, 1986). Others rely on the analogy that can be drawn between the scaling in the atmospheric surface layer and normalize the frequency by two fixed scales, the canopy height and the interface velocity (*e.g.*, Kaimal and Finnigan, 1993; Brunet *et al.*, 1994). For some studies, this normalization achieves a good data collapse over the entire profile, while for others, the collapse is poor due to the introduction of peak frequencies at high frequencies. In this laboratory study, the normalized frequency was applied to the calculation of the spectral density in order compare across the experimental runs with different velocity and length scales. The normalized frequency is simply:

$$n_{u_i} = \frac{f_{u_i} h}{U_h}, \tag{3.117}$$

where h is the effective canopy height and U_h is the mean streamwise velocity at h. Employing the normalized frequency, however, must be done with the recognition that when comparing across different experimental runs, two identical values for n_{ui} do not imply identical values of f_{ui}, due to the variation in U_h and h. To accommodate the potential misinterpretations arising from this normalization scheme, the dimensional frequency and spectral density will be presented when comparisons are made across the depth and velocity variations in the *Case A* and *B* experimental runs.

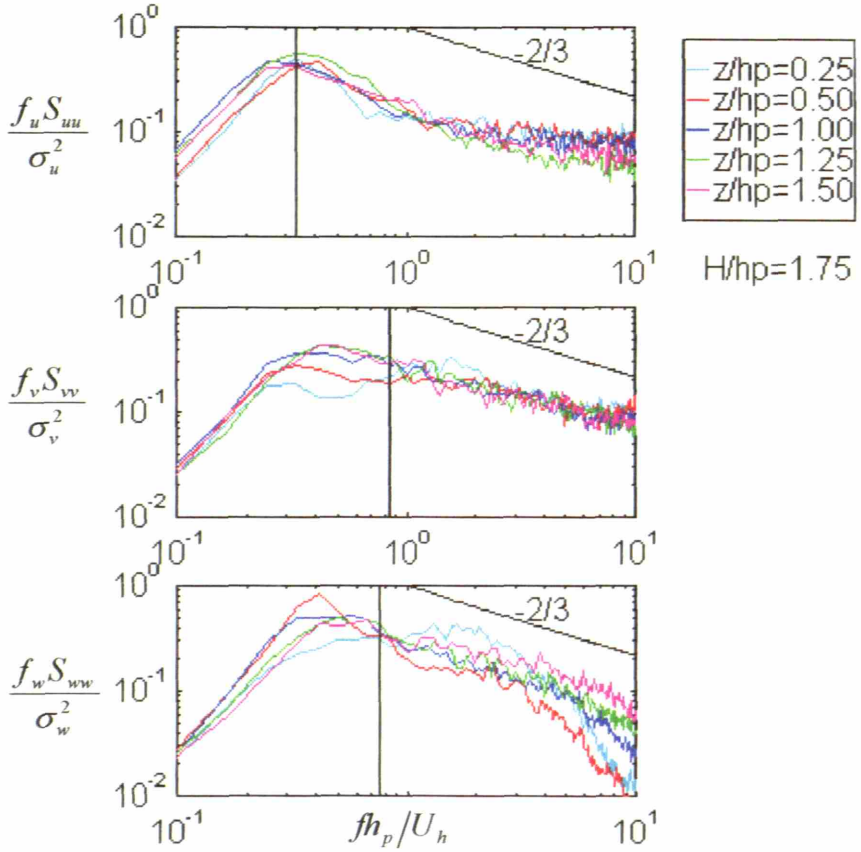

Figure 3.60. Normalized power spectra s_{uiui} versus the normalized frequency n_{ui} for experimental run 4 (H/h_p = 1.75; Q = 6.31 L/s). From top to bottom, the figures represent the streamwise, lateral and vertical one-dimensional spectral at five heights within the profile. The vertical solid line is the frequency (n_{pui}) of the average peak spectra (s_{pui}), while the diagonal solid line represents the –2/3 slope of the inertial subrange. Notice the inertial subrange is best identified in s_{ww}, which also shows a contribution from wake turbulence for z/h_p = 0.25.

An example of the normalized power spectral density at various vertical locations for experimental run 4 is shown in **Figure 3.60**. From top to bottom, the figures represent the streamwise, lateral and vertical one-dimensional spectral at five heights within the vertical profiles (z/h_p = 0.25, 0.5, 1.00, 1.25, 1.50). The characteristic slope in the inertial subrange for the frequency-weighted spectral density, $f^{-2/3}$, is shown as a solid diagonal line in the upper right corner of each figure. Except for the vertical spectra s_{ww} within the canopy at $0.25h_p$ and $0.5h_p$, each of the other points shows a clear fit to the inertial subrange slope in a normalized frequency range that depends on the velocity component. For the longitudinal velocity, an inertial subrange is observed from the peak normalized frequency at n_u = 0.3 to approximately n_u = 3, while for the lateral and vertical components the range is from n_v = 0.9–7 and n_w = 0.8–5, respectively. The existence of the inertial subrange allows us to estimate the turbulent dissipation (ε_T) indirectly from the spectra, without the need to calculate the spatial velocity gradients usually required in the direct computation of the dissipation.

Beyond the inertial subrange, the turbulence spectra either levels off at the value of the noise floor, as seen in the streamwise and lateral components, or rolls off at a rate steeper than $f^{-2/3}$. The cut off normalized frequency in **Figure 3.60** has been chosen as $n_{ui} = 10$ ($f_{ui} = 4$ Hz, for this experimental run) for the turbulence spectra. Considering the ADV sampling frequency ($f_S = 25$ Hz), the maximum frequency obtained from the velocity records is the Nyquist frequency, $f_N = \frac{1}{2}f_S = 12.5$ Hz, a rather limited frequency range as compared to other turbulence studies with instruments having higher sampling capabilities. It is recognized that the cutoff frequency chosen for this experimental run is small compared to the available frequency range, yet it is believed to be an appropriate choice from observations of the turbulence spectra over the entire frequency range. This normalized frequency range captures both the low frequency behavior and the inertial subrange without including the higher frequencies peaks due to the inherent noise in the acoustic Doppler velocimeter. For other experimental runs, the cutoff normalized frequency was chosen using a similar criteria. Despite the variation in U_h and h, the normalized frequency of $n_{ui} = 10$ was observed to consistently be a good estimate of the cutoff frequency.

The solid vertical lines in **Figure 3.60** represents the location of the depth-averaged spectral peak, which includes contributions from the shear and wake generated turbulence. The normalized frequency of the peak varies across velocity components since turbulent energy is introduced at higher frequencies into the lateral and vertical spectra due to the wake or waving production. This causes a shift of the average spectral peak to larger values of the normalized frequency. The streamwise spectra, on the other hand, is not directly affected by either the wake or waving production due to the limited introduction of streamwise fluctuations. As a result, the vertical line coincides with the location of the low frequency streamwise peak, which all cluster around $n_u = 0.3$. The location of the depth-averaged spectral peak is a good indication of the relative importance of shear to wake generated turbulence in an experimental run.

Similar figures were produced for the other experimental cases, but have been omitted due to limitations in space. As a representative plot of the spectral profiles for the experimental runs in both *Case A* and *B*, **Figure 3.60** will be referred to often in the following discussions concerning the low frequency behavior and the inertial subrange. If specific features of the spectral profiles are of interest, such as the inertial subrange fit or the introduction of energy due to wake production, a representative figure will be included in the discussion. In lieu of presenting all the spectral profiles, a more effective means of visualizing the power spectra density in the frequency versus depth (n_{ui}, z/h_p) plane is to construct spectral contour maps, similar to the contour maps presented for the hole size variation of the stress events in Section 3.6.3. The contour maps for all the experimental runs will be presented in an attempt to show the low frequency spectral behavior and associate it to the integral length scale, the event arrival frequencies and plant motion frequency.

3.8.2 Energy Containing Range

In the context of this experimental study, one of the most important features observed from the turbulence spectra is the energy containing region at the lower frequency values. As shown in the schematic of **Figure 3.59**, the energy containing range corresponds to the turbulence produced by the shear in velocity profile. For the submerged seagrass meadow, the shear at the level of the canopy height produces turbulence which is transported downwards into the canopy. As the depth of the surface layer decreases, a transition is observed from shear-generated turbulence to wake-generated turbulence. Using spectral representation, we can identify the frequency range corresponding to the shear produced turbulence and relate it to the sweep arrival frequency and the plant motion response to the sweep forcing. If these frequency ranges are approximately equal, the plausible connection between the sweeps and the plant motion is substantiated by the peak in the turbulent energy. These relations give further evidence of the role played by the shear generated eddies in the turbulence structure of the seagrass meadow.

An extremely useful way of visualizing the data obtained from the spectral profiles is to construct spectral contour maps of s_{uiui} in the normalized frequency and normalized depth plane (n_{ui}, z/h_p). The color scale on the contour map is indicative of the spectral peaks within the particular frequency range and over a particular depth. Because of the large vertical sampling resolution (~1 cm) and frequency resolution, the contouring of the spectral profiles results in smooth and distinguishable peak regions, as shown in **Figures 3.61** to **3.64** for the experimental runs in *Cases A* and *B*.

The spectral contour figures are plotted in area-preserving fashion, which implies that contouring is performed on the normalized and frequency-weighted spectral density on a linear axis. In an area-preserving form, the variance of the velocity is equal to the area under the spectral curve (Finnigan, 1979a), so that a value of unity for s_{uiui} would indicate that all the turbulent energy is concentrated at that frequency. Since the turbulent energy is distributed over a range of frequencies, the peak normalized spectral density observed in **Figures 3.61** through **3.64** corresponds to a value of s_{uiui} from 0.6–0.7, represented by the dark yellow and orange on the color scale. The green and light blue colors are indicative of less turbulent energy at that (n_{ui}, z/h_p) location, while the two shades of dark blue show regions of very little turbulent energy. In addition to the color scale, the contour lines for spectral map have also been included to help in their interpretation. The spectral contour maps of the lateral velocity component have been omitted from the present discussion due to the emphasis placed on u and w for momentum transfer.

Due to the specific interest in the energy-containing range, the spectral contour maps have been limited to a normalized frequency of n_u and n_w = 1, which corresponds to a dimensional frequency in the range of 0.2–1.2 Hz across the experimental runs. Despite this range of dimensional frequencies, the normalized peaks line up in the same rangefor s_{uu} and s_{ww} (0.2–0.6), suggesting that the normalization performed on the frequency collapsed the data from the different experimental runs and is an appropriate

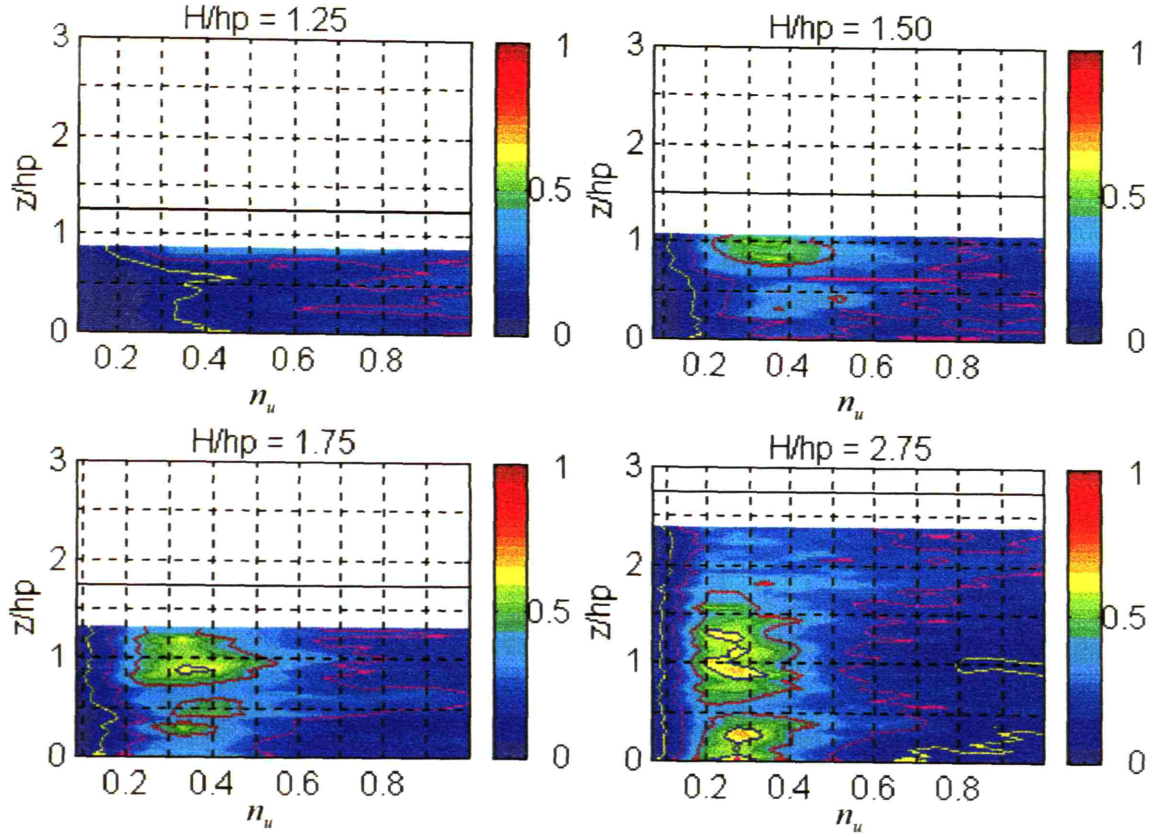

Figure 3.61. Spectral contour plot of the normalized spectral density s_{uu} for the experimental runs in *Case A*. The contouring of s_{uu} is performed for the area-preserving representation, s_{uu} is contoured on a linear axis. The lowest characteristic depth (H/h_p = 1.00) has been omitted due to the lack of a low frequency peak. Notice that the normalized frequency axis extends up to n_u = 1, so that only the low frequency region of the turbulence spectra is plotted. Recall that the cyclic frequency f_u corresponding to n_u varies among the depth cases due to variations in U_h.

choice for spectral scaling. This is most clearly seen in the experimental runs of *Case B* shown in **Figures 3.63** and **3.64**, where the peak spectral regions are at the same normalized frequency range for the three flow discharges despite a factor of three difference in the dimensional frequency between the highest and the lowest discharge. This confirms that the turbulent eddies formed at the canopy top are scaled by the interface velocity U_h and the canopy height, h, and that nondimensionalizing by these two parameters results in similar behavior across the depth and velocity variation cases.

Figures 3.61 and **3.62** show the spectral contour plots for the submerged canopy conditions ($H/h_p > 1.00$), where the presence of a sheared velocity profile leads to the generation of low frequency turbulence. The lack of an appreciable low frequency spectral peak is observed for the characteristic depth, H/h_p = 1.25, where most of the turbulent energy is located at higher normalized frequencies (*e.g.*, n_w = 1–4; f_w = 0.2–0.7 Hz) and distributed uniformly over the depth. Two explanations for this behavior are possible. First, the scaling by U_h and h is not as successful for this lower degree of shear production, such that the normalized frequency corresponding to the low dimensional frequency range is high

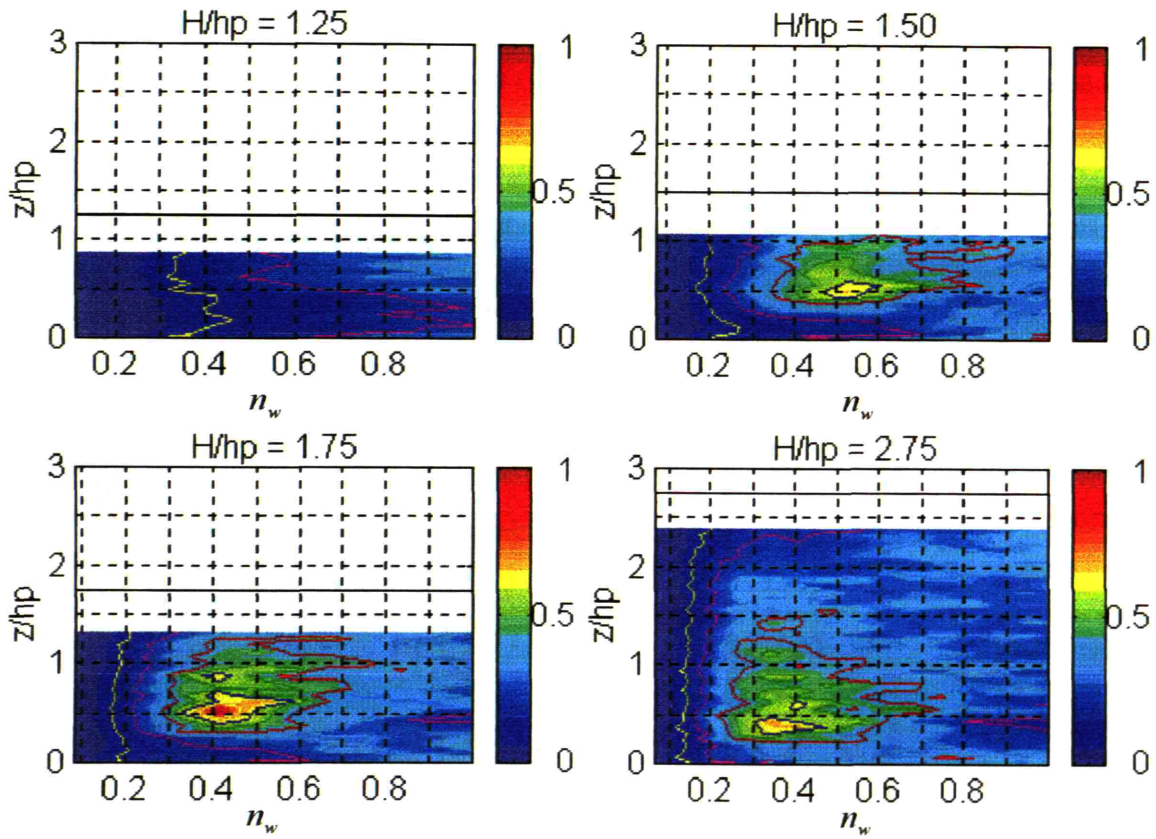

Figure 3.62. Spectral contour plot of the normalized spectral density s_{ww} for the experimental runs in *Case A*. The distinct peak in s_{ww} at n_w = 0.3–0.5 near the mid canopy height (z/h_p = 0.5) is further evidence that the vertical eddies penetrate down to this level, as observed in the vertical integral length scale (L_w). Notice that as compared to the streamwise spectra, large values of the vertical spectra extend to higher normalized frequencies.

compared to the collapse for the other experimental runs. Second, the turbulence is not yet fully differentiated into shear generated and a wake generated regions so that the turbulence spectra shows the combined effect of both shear and wake production at an intermediate frequency. For higher characteristic depths, the shear generated turbulence dominates the turbulence spectra, as seen in the broad peak zone at the normalized frequency range, n_u = 0.2–0.5 and n_w = 0.2–0.8.

As the characteristic depth is increased, the penetration of the peak spectral density into the canopy increases, reaching the bottom for s_{uu} and the level of the lower canopy region (z/h_p = 0.25) for s_{ww}. Constancy in the position of the normalized spectral peak has been observed in most reliable plant canopy flow data sets as reviewed by Kaimal and Finnigan (1993). For the streamwise component in **Figure 3.61**, the turbulence spectra peak extends from z/h_p = 1.50 to the bottom for H/h_p = 2.75. As the surface layer depth decreases, so does the range of the spectral peak, extending from 0.75 to 1.10h_p for H/h_p = 1.50. Despite the lack of stress event penetration to the lower canopy region, the s_{uu} peak reaches the bottom because the perturbations in the streamwise velocity penetrate into the canopy. Thus, the

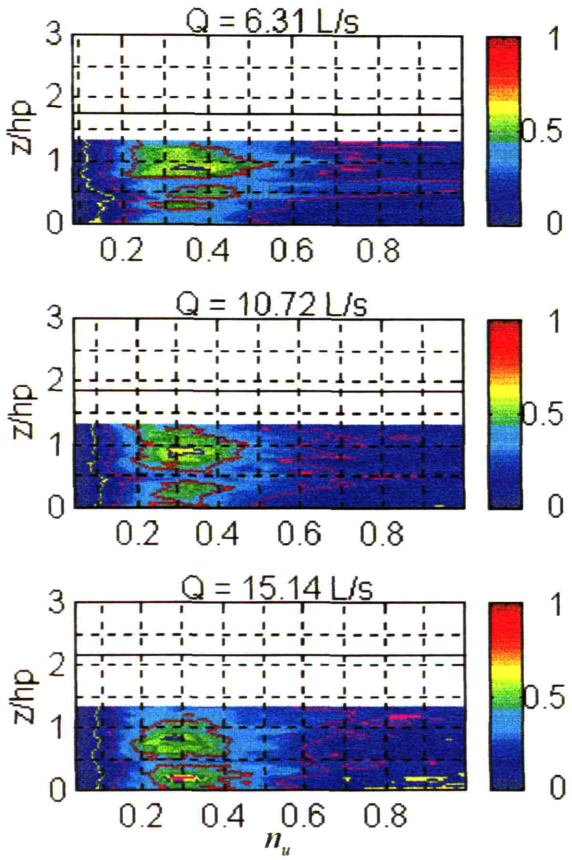

Figure 3.63. Spectral contour plot of the normalized spectral density s_{uu} for the experimental runs in *Case B*. As with the contour plots for *Case A*, notice how the penetration of the peak streamwise spectral density increases as the flow discharge (Q) increases. In addition, despite the differences in U_h and h between the cases, the peak spectral regions occurs at similar n_u values.

perturbations in the longitudinal velocity created at the canopy height are transmitted to the lower canopy region without inducing momentum transport, presumably via another transport mechanism. This behavior for the longitudinal spectral component has been observed in other studies (Brunet *et al.*, 1994; Murota *et al.*, 1984). For s_{ww}, on the other hand, the peak spectra does not reach the lower canopy region since the vertical fluctuations extend into the canopy exclusively due to the downward transport of eddies whose penetration depths are limited by the surface layer length scale. As was observed for the sweep events in **Figure 3.43**, the spectral peak penetration depth increases with higher H/h_p which suggests that sweeps are responsible for carrying the turbulent motions into the canopy. The vertical location of the vertical spectral peak decreases slightly from $0.5h_p$ to $0.3h_p$ as H/h_p increases from 1.50 to 2.75.

A similar variation in the penetration depth of s_{uu} and s_{ww} is observed for the flow discharge runs. As the velocity inside the canopy increases, the perturbations in the streamwise turbulent increase in the lower canopy region and the broad spectral peak for s_{uu} penetrates to the bottom, as seen in **Figure 3.63**. For the vertical turbulence spectra, the increase in the flow discharge broadens the frequency of the s_{ww} peak and increases the penetration depth.

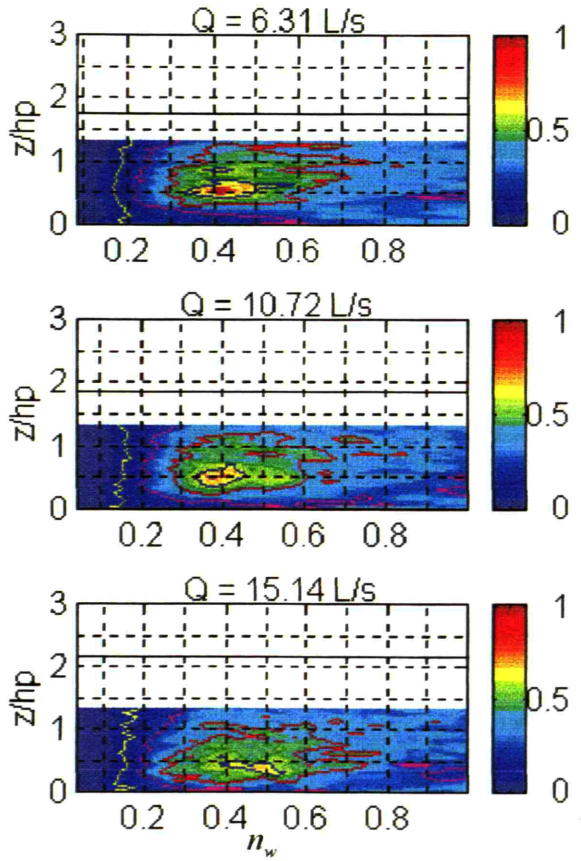

Figure 3.64. Spectral contour plot of the normalized spectral density s_{ww} for the experimental runs in *Case B*. As the flow discharge increases, the spectral density at the low frequency peak is spread over a larger portion of the (n_w, z/h_p) plane, an indication of the effect of the waving phenomenon.

A peculiarity in the s_{uu} contour map is observed at the level of the mid canopy height ($z/h_p = 0.5$) in these experimental runs as well as those from *Case A*. At this level, the streamwise spectral peak is less apparent in the contour map. Inspection of the spectral profiles, as in **Figure 3.60**, shows that at this elevation the low frequency peak contains less of the total turbulent energy and more energy is found at higher frequencies. This is presumably due to an increase in the relative importance of wake generation of s_{uu} at this level which corresponds to the transition zone between the lower stem region and the upper blade region. The turbulence spectra at this elevation show the effect of wake production of turbulence, as will be discussed in more detail in the latter part of Section 3.82.

The variation of the low frequency peak behavior shown in the spectral contour maps with the characteristic depth can be quantified by calculating the average peak location and value over the entire vertical profile. As mentioned in the discussion of **Figure 3.60**, the normalized frequency and spectral density of the vertically-averaged spectra was computed for each experimental run. Observations from the spectral contour maps hint that the behavior of the spectral peak does not vary significantly with the flow discharge and for the larger characteristic depths. In addition, the discussion concerning the alignment of

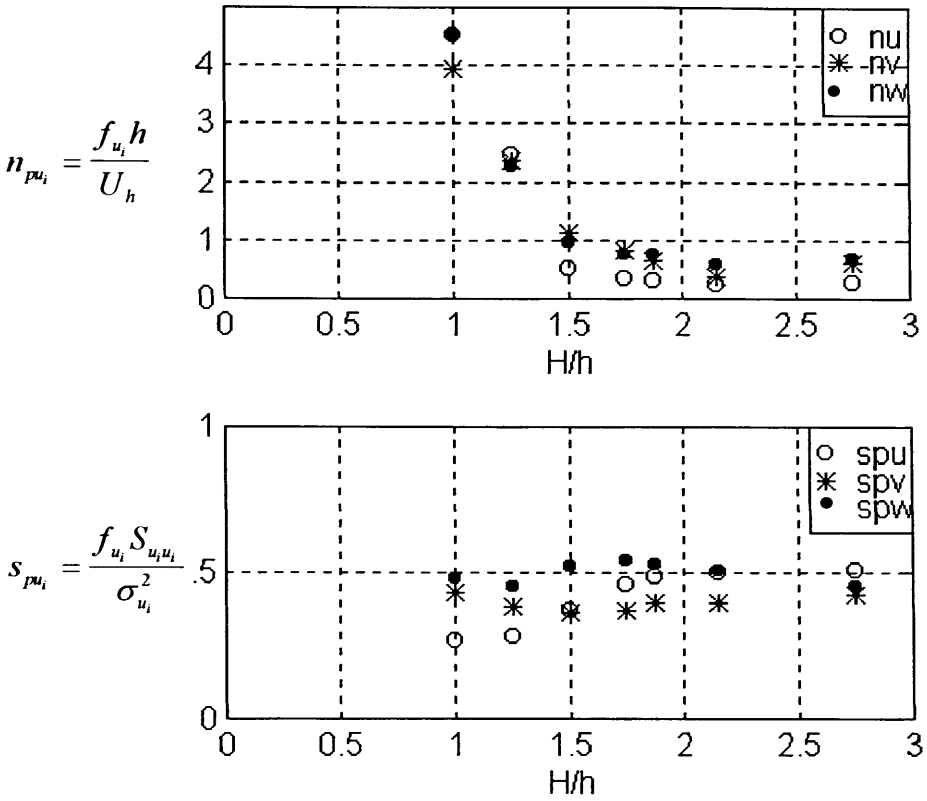

Figure 3.65. Variation of the average location and value of the spectral peak in the energy containing range with the characteristic depth (H/h) for the *Case A* and *B* experimental runs. The location is characterized by the normalized frequency at the peak (n_{pui}) in the top figure, while the value is quantified by the normalized spectral density peak (s_{pui}) in the bottom figure.

the spectral peaks suggested a similar trend. **Figure 3.65** confirms these observations by showing the variation of the averaged peak normalized frequency (n_{pui}) and the averaged peak normalized spectral density (s_{pui}) with the characteristic depth (H/h). The data from all the experimental runs has been included since little variation was observed with Q. The higher flow discharge cases are the points at the characteristic depths H/h = 1.87 and 2.15. The normalized spectral peak value is independent of H/h, which is expected since the normalization by the variance removes the differences among the cases. Averaging over the runs, the spectral peak accounts for 37, 38 and 49% of the total variance for the u, v and w spectra, respectively, and is rather constant across the cases.

The normalized frequency of the spectral peak, however, is observed to be strongly dependent on the characteristic depth. This behavior fits well into the picture that has been described about the effect of the surface layer depth on the turbulence structure in the seagrass meadow. The asymptotic variation in the location of the average peak frequency for the three velocity components is a result of the transition from wake to shear generated turbulence within the flow. When the surface layer depth is negligible or small, the shear layer at the canopy height is either nonexistent or too small to create significant changes

Table 3.16. Peak spectral dimensional frequency (f_{pui}) and wave number (k_{pui}) at the canopy height ($z = h$) for the *Case A* and *B* experimental runs.							
Parameter / Run	**1A**	**2A**	**3A**	**4A,B**	**5B**	**6B**	**7A**
$f_{pu}(z = h)$ (Hz)	–	0.17	0.13	0.13	0.23	0.27	0.01
$f_{pv}(z = h)$ (Hz)	–	0.37	0.40	0.17	0.27	0.27	0.13
$f_{pw}(z = h)$ (Hz)	–	0.77	0.27	0.20	0.23	0.57	0.17
$k_{pu}(z = h)$ (cm^{-1})	–	0.22	0.12	0.13	0.13	0.11	0.08
$k_{pv}(z = h)$ (cm^{-1})	–	0.49	0.35	0.16	0.15	0.11	0.11
$k_{pw}(z = h)$ (cm^{-1})	–	1.02	0.24	0.20	0.13	0.24	0.13

in the turbulence structure. As a result, the only source of turbulent energy is wake production, characteristically introduced at high frequencies set by the dimensions of the plant. After the surface layer is increased beyond a critical depth, the shear generated turbulence becomes the dominant production mechanism over most of the flow. Very little variation is observed for the normalized frequency of the average spectral peak beyond a characteristic depth of H/h = 1.50, which indicates that the shear production is being introduced at equivalent normalized frequencies despite increases in the surface layer depth and flow discharge. In atmospheric plant canopies, the peak location is observed at smaller normalized frequencies than those for these experimental runs. Kaimal and Finnigan (1993) quote values for the normalized peak locations, n_u = 0.15 ± 0.05 and n_w = 0.42 ± 0.05, obtained from data of six different canopy experiments, while Brunet *et al.* (1994) present similar results in a wind-tunnel wheat canopy, n_u = 0.12 and n_w = 0.42. It is not unreasonable to suspect that the asymptotic behavior shown in **Figure 3.65** for H/h up to 2.75 (n_u = 0.27 and n_w = 0.68 at H/h = 2.75)) could lead to values that resembling those for the unbounded canopy flows at higher depths.

Attention is now turned to the comparisons that can be drawn between the low frequency spectral behavior and the momentum transport, plant motion and eddy length scales. If the sweep and ejection cycle is the dominant form of energy transport within the submerged seagrass meadow, then the low frequency spectral behavior should be well correlated with the event arrival frequencies. **Table 3.16** shows the dimensional frequencies (f_{pui}) and wave numbers (k_{pui}) for the peak spectral density in the low frequency region at $z = h$, as an example of the range of values shown in **Figures 3.61** through **3.64**. This vertical location is a good representation of the average sweep behavior within the canopy, as observed in the spectral contour maps. For the most part, the dimensional peak frequencies are comparable to the event arrival frequencies shown in **Figures 3.48** through **3.52** and **Table 3.15**. Although the specific values do not match precisely, each is within the range of frequencies of the other estimate. For example, the sweep arrival frequency for the characteristic depth H/h_p = 2.75 is within the range 0.1–0.3 Hz, while the peak spectral densities for the same case are located at f_{pu} = 0.1–0.2 Hz and f_{pw} = 0.1–0.25 Hz for the streamwise and the vertical spectra. Considering that neither the arrival of sweep events to the canopy

nor the turbulent energy within the canopy is expressed at a single frequency, the match between these ranges is quite good. This comparison is a clear indication that the turbulent energy within the canopy is concentrated at the frequency set by the arrival of the turbulent eddies.

A further step can be taken at this point in the conceptual model described in Section 3.6.4. The turbulent structures are not only responsible for the transport of momentum into the canopy but also for determining the turbulence time scale in the energy containing range. As the turbulent eddies arrive at the canopy, they impart momentum to the plants and to the fluid inside the canopy which results in plant motion and in the ejection of low velocity fluid. Since the plant motion has been related directly to the arrival of the turbulent eddies, then the frequency of the spectral energy peaks should also be comparable to the plant vibrational frequency. Comparing the values quoted in **Table 3.16** and the frequency ranges in **Figures 3.61** through **3.64** with the measured plant vibration frequencies shown in **Table 3.2**, it can be seen that the observed vibrational frequency and the turbulence spectra have similar time scales. For the experimental case with the monami phenomenon (experimental run 6, H/h_p = 1.75, Q = 15.14 L/s), the waving frequency (f_p = 0.42 Hz) coincides with the peak vertical spectral frequency (f_{pw} = 0.43 Hz) remarkably well, as suggested by Kaimal and Finnigan (1993).

The peak spectral frequency of S_{ww} also provides an opportunity to corroborate the estimates of the streamwise periodicity scale, Λ_x, as obtained from the plant motion experiments. Raupach *et al.* (1996) suggested the following relationship between the periodicity and the frequency of the vertical peak spectral density. As in **Eq. 3.112** relating the periodicity to the integral length scale, an assumption is made regarding the ratio of the eddy and the interface velocity $U_{eddy}/U_h \approx 1.8$ (Raupach *et al.*, 1996):

$$\frac{\Lambda_x}{h} = \left(\frac{U_h}{f_{pw}h}\right)\left(\frac{U_{eddy}}{U_h}\right). \qquad \textbf{(3.118)}$$

where the vertical component is chosen since it is more reflective of the active turbulence within the canopy. **Eq. 3.118** is identical to the prediction of the streamwise periodicity made from the integral length scale, **Eq. 3.112**, combined with the relationship $f_{pw} = U_h/(2\pi L_w(h))$. For the experimental run exhibiting the measurable monami phenomenon (H/h_p = 1.75, Q = 15.14 L/s), the nondimensional peak frequency estimated as an average over the entire profile was n_{pw} = 0.58. Using this value and the assumption regarding the velocity ratio, the estimated periodicity is Λ_x = 42.88 cm, comparable to the measured monami wavelength, λ_m = 40.00 ± 2.15 cm. This strongly suggests that the turbulence time scale is set by the arrival of the coherent eddies to the canopy and is reflected in the waving motion.

Finally, the location of the peak spectral density can be related to the eddy length scale obtained in Section 3.7. As mentioned previously and shown in **Figure 3.59**, the energy containing range occurs at wave numbers that scale on the inverse of the integral length scale, $k_{ui} \sim 1/L_{ui}$. By calculating the wave number from the peak frequency using **Eq. 3.115**, the relationship between these two scales can be explored for the points in the *Case A* and *B* experimental runs. **Figure 3.66** shows the results from

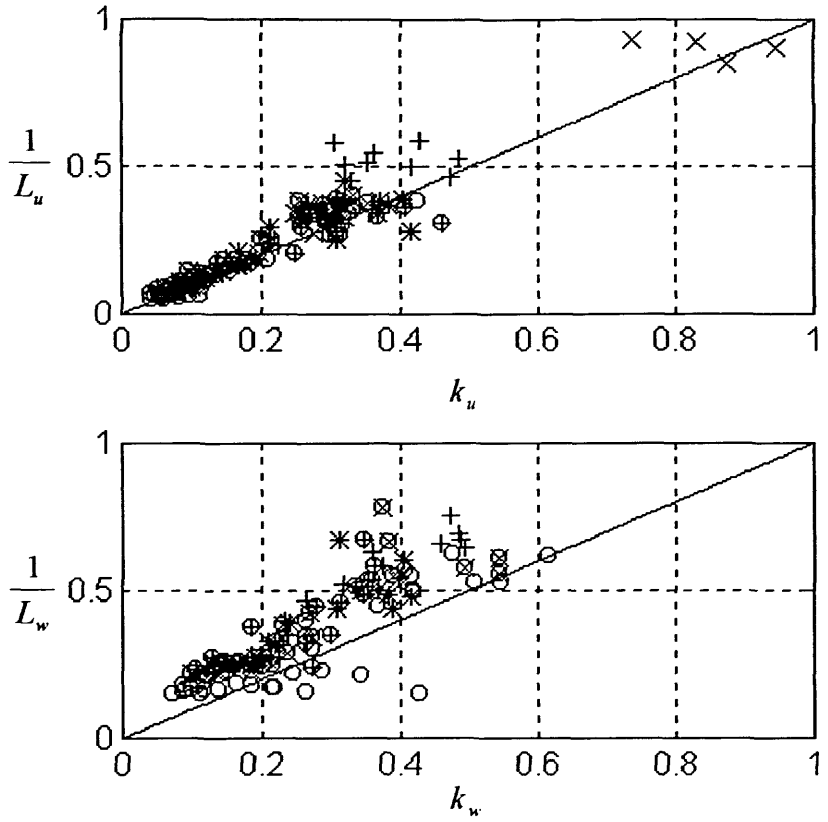

Figure 3.66. Relationship between the peak wave number and the integral length scale for the *Case A* and *B* experimental runs. The top figure is the relationship for the longitudinal velocity component, while the bottom figure is for the vertical velocity component. The symbols represent H/h = 1.00 (•), 1.25 (×), 1.50 (+), 1.75 (*), 1.87 (⊕), 2.15 (⊗), 2.75 (o). The solid lines represent the perfect agreement between ($1/L$) and k.

plotting the inverse integral length scale and the wave number for the streamwise and vertical spectra. For the streamwise component, most of the points lie on the line of perfect agreement between the two variables suggesting that the proportionality factor between two variables approaches unity ($k_u = 1/L_u$). For the vertical component, on the other hand, the proportionality factor is slightly greater than unity, approaching values between 1–2, so that the two variables are only approximately equal ($k_w \sim 1/L_w$).

This relationship corroborates that the frequency of the downward transport of momentum and the turbulence time scale are set directly by the size of the turbulent eddies. Variations in the eddy scale result in changes in the peak spectral frequency, the plant motion response and the event arrival frequency. The behavior of each of these turbulence indicators with variations in H/h_p should be similar, as observed with the asymptotic variation of the eddy length scale, the peak frequency location and various other parameters derived from the experimental data. Thus, the controlling parameter in the turbulence structure of a depth limited plant canopy flow has been confirmed to be the depth of the surface layer or equivalently, the relative roughness or characteristic depth.

3.8.3 Inertial Subrange

In the inertial subrange, the turbulence spectrum becomes independent of the scale set by the largest and smallest eddies in the flow which describe the energy containing and the dissipative regions of the spectrum, respectively. As discussed in Section 3.82, the energy containing region is directly related to the turbulent structures that exchange momentum between the vegetation and surface layer. The dissipative range, on the other hand, is composed of the fine-scale eddies responsible for kinetic energy loss through heat. In the inertial range, the turbulent kinetic energy is cascaded down from larger to smaller eddies through the action of vortex stretching, dissipating very little energy in the process. Kolmogorov postulated that the spectrum should be independent of viscosity in the inertial range and through dimensional arguments derived the variation of the spectrum with the wave number or frequency, finding a $k^{-5/3}$ relationship and a dependence on the dissipation rate of turbulent energy, $\varepsilon_T^{2/3}$ (Kundu, 1990, p. 441). The Kolmogorov relationships applied to the frequency-weighted spectrum $f_{ui}S_{uiui}$ presented earlier can be expressed as the following for the streamwise, lateral and vertical spectra:

$$f_u S_{uu}(f) = \alpha_u \varepsilon_{T_u}^{2/3} \left(\frac{2\pi f_u}{\langle \overline{U} \rangle} \right)^{-2/3}, \tag{3.119}$$

$$f_v S_{vv}(f) = \alpha_v \varepsilon_{T_v}^{2/3} \left(\frac{2\pi f_v}{\langle \overline{U} \rangle} \right)^{-2/3}, \tag{3.120}$$

$$f_w S_{ww}(f) = \alpha_w \varepsilon_{T_w}^{2/3} \left(\frac{2\pi f_w}{\langle \overline{U} \rangle} \right)^{-2/3}, \tag{3.121}$$

where $\alpha_u = (18/55)A_k$ for the one-dimensional spectrum (Lumley and Panofsky, 1964, p. 84). The value for $A_k \cong 1.5$ has been found to be a universal constant for all turbulent flows (Kundu, 1990, p. 442), resulting in a value $\alpha_u = 0.49$. Under the assumption of local isotropy in the inertial subrange, $\alpha_w = \alpha_v = 4/3\alpha_u = 0.65$. This assumption can be tested by computing the rate of dissipation of turbulent energy from the streamwise, vertical and lateral spectra by assuming that the Kolmogorov constants are equal, $\alpha_w = \alpha_v = \alpha_u$, and determining the ratios $\varepsilon_{Tu}/\varepsilon_{Tw}$ and $\varepsilon_{Tu}/\varepsilon_{Tv}$. If local isotropy is observed in the inertial subrange for this experimental study, then the turbulence spectra should be related as:

$$S_{ww}(f) = S_{vv}(f) = \frac{4}{3} S_{uu}(f). \tag{3.122}$$

otherwise the differences in the ratio of the spectra are indicative of the departure from isotropy in the inertial subrange, a feature observed in other studies of plant canopy flows (*e.g.*, Brunet *et al.*, 1994).

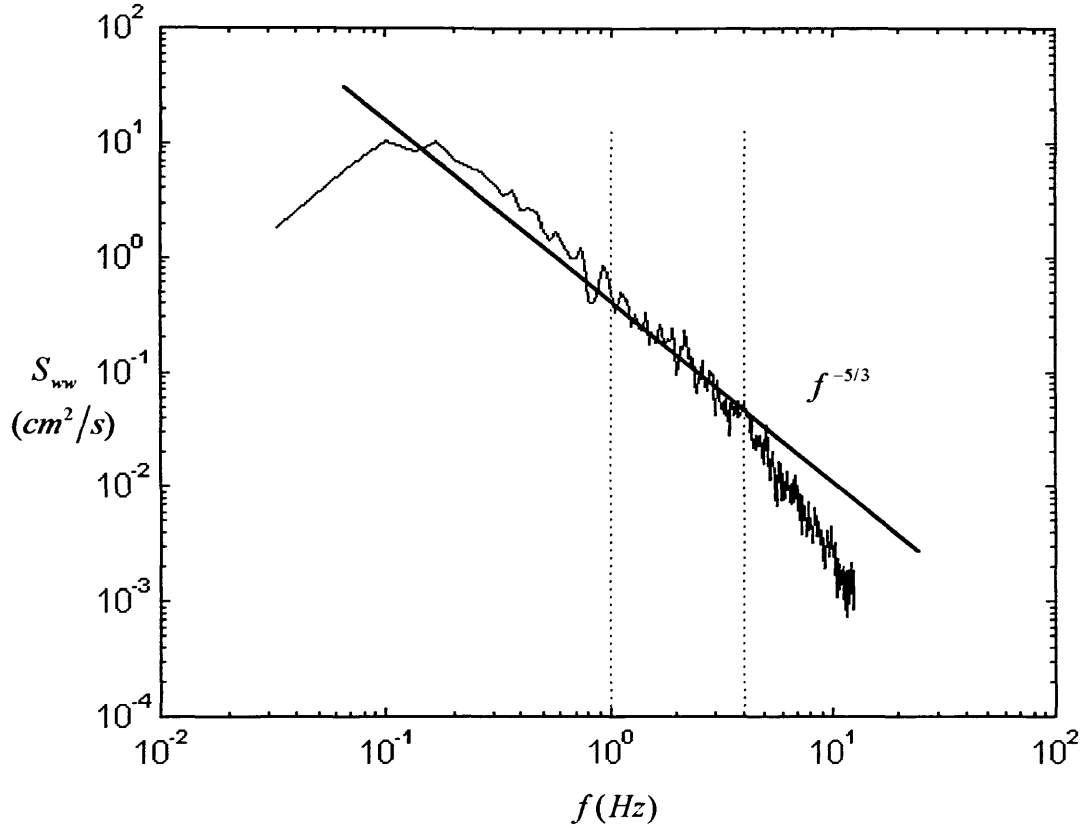

Figure 3.67. Estimation of the turbulent dissipation from the fit of the Kolmogorov law to the inertial subrange of the vertical turbulence spectra S_{ww} for experimental run 7 (H/h_p = 2.75, Q = 15.14 L/s) at an elevation z/h_p = 1.00. The turbulence spectra is plotted in dimensional form with the power spectra density (cm^2/s) versus the cyclic frequency, f (Hz). The solid diagonal line represents the characteristic slope in the inertial subrange ($f^{-5/3}$). The vertical dashed lines are the limits on the frequency range used to obtain the dissipation estimate ($1 < f_w < 4$ Hz).

The Kolmogorov laws in **Eq. 3.119** through **3.121** provide a useful way of estimating the rate of dissipation of turbulent kinetic energy, ε_T (cm^2/s^3). Fitting the Kolmogorov relationship to the inertial subrange is an alternative method of estimating the turbulent dissipation that is much simpler to implement than the strict definition of the dissipation which involves computing spatial velocity gradients. For this experimental study, the turbulence spectra was used to estimate the turbulence dissipation as:

$$\varepsilon_{Tu_i} = \left(\frac{2\pi}{\langle \overline{U} \rangle}\right)\left(\frac{\overline{S_{u_i u_i} f_{u_i}^{5/3}}}{\alpha_{u_i}}\right)^{3/2}, \qquad \textbf{(3.123)}$$

where the overbar on the product of S_{uiui} and $f_{ui}^{5/3}$ implies that an average was taken over a specific frequency range related to the inertial subrange. The frequency range corresponding to the Kolmogorov law was determined to be f_{ui} = 1–4 Hz from an inspection of the turbulence spectra for the majority of the points in the experimental runs. **Figure 3.67** shows the turbulence spectrum S_{ww} for experimental run 7 at the canopy height (z/h_p = 1.00) as an example of the $f^{-5/3}$ fit to the inertial subrange, from which the

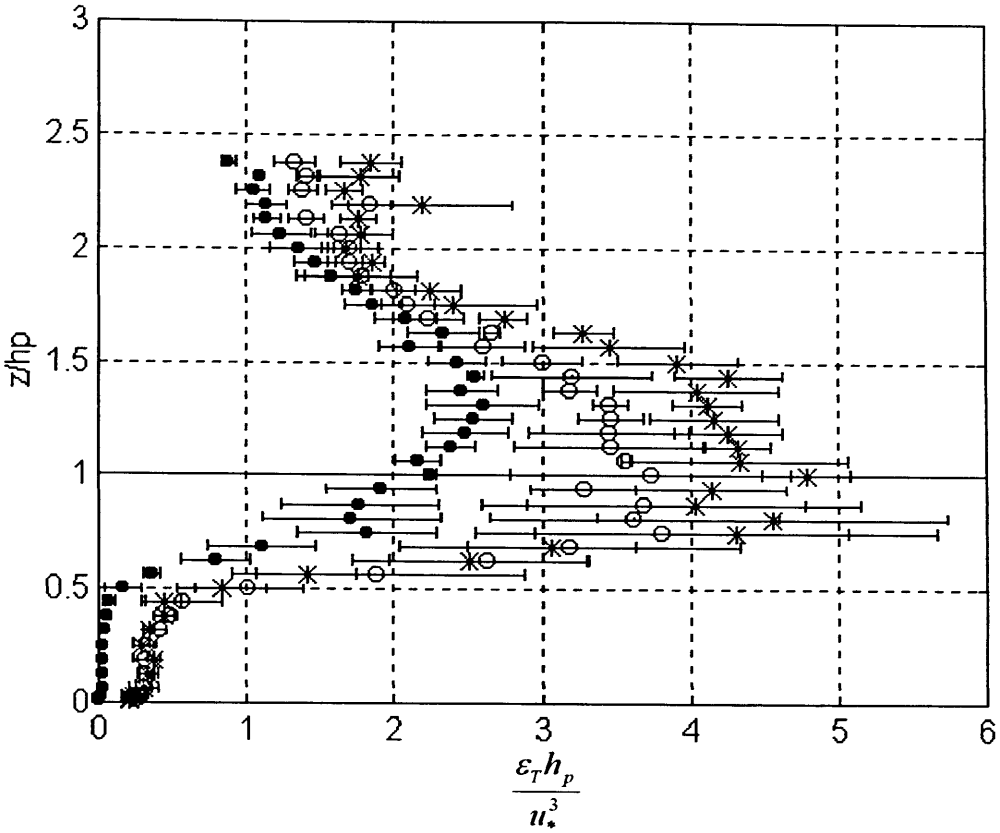

Figure 3.68. Estimate of the dissipation rate of the turbulent kinetic energy, ε_T, normalized by the canopy height, h_p, and the friction velocity, u_*^3 based on the Reynolds stress at $z = h_p$, **Eq. 3.46**, for experimental run 7 (H/h_p = 2.75, Q = 15.14 L/s). The three profiles indicate the estimate from the streamwise (o), lateral (*) and vertical (•) turbulence spectra in the inertial subrange, f_{ui} = 1–4 Hz. **Equations 3.119** through **3.121** have been applied by assuming that $\alpha_u = \alpha_v = \alpha_w = 0.49$ in order to test the isotropy conditions in the inertial subrange of the flow through the seagrass meadow. The horizontal bars represent the horizontal deviation.

turbulence dissipation was estimated. The vertical dashed lines represents the frequency range chosen to estimate the average of $S_{uiui}f_{ui}^{5/3}$ used in **Eq. 3.123**. The fit of the Kolmogorov law to the turbulence spectrum demonstrates that the inertial subrange exists over this limited frequency band.

A similar procedure was followed for each turbulence spectra calculated from the experimental data of *Cases A* and *B* to obtain the variation of the turbulent dissipation with height and across experimental conditions. **Figure 3.68** shows an example of the turbulent dissipation profiles obtained from the spectra of the three velocity components for the largest characteristic depth case, H/h_p = 2.75. The dissipation has been normalized by the canopy height (h_p) and the friction velocity (u_*). The friction velocity estimated from the Reynolds stress at the canopy height, as defined in **Eq. 3.46**, has been used to nondimensionalize the dissipation since this was found to successfully collapse the turbulent kinetic energy profiles in Section 3.3.6. For this particular case, the friction velocity is u_* = 1.72 cm/s, so that the peak normalized dissipation at the canopy height corresponds to 1.19, 1.52 and 0.72 cm^2/s^3 for ε_{Tu}, ε_{Tv} and

Table 3.17. Comparison of depth averaged Kolmogorov and integral length scales for the *Case A and B experimental runs.*							
Parameter / Run	**1A**	**2A**	**3A**	**4A,B**	**5B**	**6B**	**7A**
Kolmogorov scale η (cm)	0.06	0.05	0.05	0.05	0.03	0.03	0.04
Integral length scale L_u (cm)	0.88	1.50	3.12	5.02	5.55	6.02	10.67
$k = 1/\eta$ (cm^{-1})	17.95	18.90	21.46	22.22	30.58	36.90	25.45
$k = 1/L_u$ (cm^{-1})	1.13	0.67	0.32	0.20	0.18	0.17	0.09

ε_{Tw}, respectively. This implies that the dissipation ratios are equal to $\varepsilon_{Tu}/\varepsilon_{Tv} = 0.78$ and $\varepsilon_{Tu}/\varepsilon_{Tw} = 1.65$ at $z = h$ for the inertial subrange. For isotropic conditions, the relationship between the Kolmogorov constants, $\alpha_w = \alpha_v = 4/3\alpha_u$, implies that the dissipation ratios are $\varepsilon_{Tu}/\varepsilon_{Tv} = \varepsilon_{Tu}/\varepsilon_{Tw} = 0.65$. It is immediately apparent that assumption of isotropy within the inertial subrange is not met precisely, although the ratio of the lateral to the streamwise dissipation are quite close to the expected isotropic values. Alternatively, this could also have be shown by comparing the calculated S_{ww}/S_{uu} in the inertial subrange to the expected ratio for isotropic conditions, as defined in **Eq. 3.122**. For this experimental run $S_{ww}/S_{uu} = 0.85$ in the frequency range $f_{ui} = 1$–4 Hz, lower than the isotropic value, $S_{ww}/S_{uu} = 1.33$.

Figure 3.68 demonstrates that the turbulence dissipation estimated from the spectral inertial subrange peaks in the region near the canopy height ($0.75 < z/h_p < 1.5$) and decreases away from $z = h_p$. The dissipation profiles also have distinct differences in the zone of shear turbulence near the canopy height and the zone of wake turbulence in the lower canopy region ($z/h_p \leq 0.25$). Near the bed, the higher rates of dissipation in the streamwise and lateral component correspond to the wake turbulence regime.

The turbulence dissipation estimates from the spectra of the three velocity components can be used to define the Kolmogorov length scale, η, which is indicative of the size of the dissipative eddies within the flow and also of the wavenumber characteristic of the dissipation range, as shown in the schematic of **Figure 3.59**. The Kolmogorov microscale, defined as:

$$\eta = \left(\frac{\nu^3}{\varepsilon_{T_u}} \right)^{1/4}, \qquad \textbf{(3.124)}$$

where ν is the fluid kinematic viscosity, 0.01 cm^2/s for water, was calculated from the streamwise dissipation estimate, ε_{Tu}. The choice of the streamwise dissipation was made due to the lack of applicability of the isotropic assumption for determining α_v and α_w. **Table 3.17** shows the depth average values for η for the experimental runs in *Case A* and *B* along with the average streamwise integral length scale, L_u. The dissipative eddies within the submerged seagrass meadow have small length scales, on the order of 0.5 mm. Typical values for η in atmospheric flows are about twice the value obtained for these experiments, 1 mm (Kaimal and Finnigan, 1993). In addition, the Kolmogorov microscale decreases with increasing characteristic depth and flow discharge. Along with an increase in the streamwise integral

length scale as H/h_p and Q increase, this variation indicates that a broader range of eddy sizes is present in these flow conditions, *i.e.* the inertial subrange broadens in frequency range as expected for higher depth Reynolds number flows (Kundu, 1990).

From the comparison of the integral length scale and the Kolmogorov microscale it can be seen that the requirement for the existence of an inertial subrange ($L_u >> \eta$) is met for all the experimental cases. The extent of the inertial subrange is observed to vary over the flow depth, however. Within the canopy, the dissipation scale increases and the integral length scale decreases, so that the inertial subrange is reduced to a smaller frequency band, as compared to the flow above the canopy. **Table 3.17** also indicates that the wave numbers associated with each length scale are quite separated, which implies that eddies of various scales between the energy containing and the dissipation ranges are present in the flow.

The wave numbers associated with the dissipation range ($k \sim 1/\eta$), suggest that the ADV instrumentation is not capable of resolving the smallest eddy sizes for cases with high depth Reynolds numbers. If we take the value of η for the spectra shown in **Figure 3.67**, $\eta = 0.03$ cm, and the velocity at that elevation, $U_h = 7.81$ cm/s, it is easy to show that the cyclic frequency characterizing the dissipation ($f_\eta = 41$ Hz) is much larger than the Nyquist frequency ($f_N = 12.5$ Hz). Due to the limited sampling frequency, the acoustic Doppler velocimeter can not resolve the dissipation range from the turbulence spectra for the high Re_H cases. For the experimental runs with a lower Re_H, it can be shown that the Nyquist frequency is large enough to resolve the dissipation range. Taking the value at $z/h_p = 0.81$ for $H/h_p = 1.00$, the dissipation frequency, $f_\eta = 6.5$ Hz, is small compared to the Nyquist frequency.

Regardless of the relationship between the dissipation frequency and the Nyquist frequency, the size of the sampling volume also limits the resolution of the smallest eddy size because the horizontal (6 mm) and the vertical (9 mm) length scales of the sampling volume are an order of magnitude larger than the Kolmogorov microscale (0.5 mm). Thus, the smallest eddies can exist within the sampling volume without the acoustic Doppler velocimeter being able to identify them. Fortunately, the sampling volume dimensions are much smaller than the integral length scales so that the eddies in the energy containing range can be resolved and meaningful turbulence measurements made with the ADV.

The estimation of the Kolmogorov microscale provides important information regarding the limit frequency of the inertial subrange. For most cases examined here, the high frequency end of the turbulence spectra does not include the roll-off region containing the dissipative eddies, and is truncated artificially by the Doppler noise or interrupted by the introduction of turbulent energy at high frequencies from wake and waving production. Each of the factors affecting the inertial subrange become more prominent within the canopy which is characterized by lower Reynolds numbers, higher noise levels and the presence of waving and wake production.

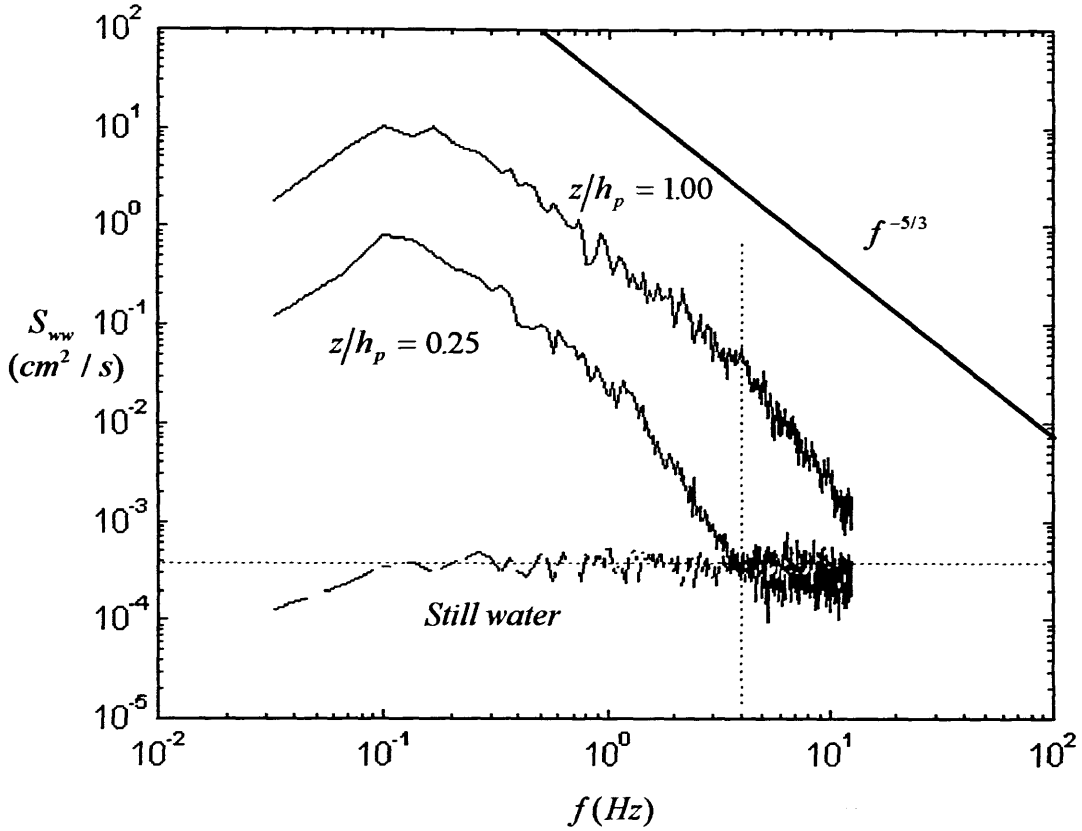

Figure 3.69. Comparison of the vertical spectra S_{ww} from two elevations within the canopy (z/h_p = 0.25 and 1.00) for experimental run 7 and from the still water experiment described in Section 2.3.2.3 and **Table 2.4**. The spectra are shown in dimensional form with the power spectral density plotted versus the dimensional frequency (Hz). The vertical dashed line at the intersection of the Doppler white noise with the spectra for z/h_p= 0.25 represents the characteristic frequency, f_b = 4 Hz, boundary between the turbulence region and the noise region.

Within the canopy, the frequency-weighted u spectra, s_{uu}, is typically truncated by the noise level and exhibits a slope that is less steep than the anticipated $f^{-2/3}$. The normalized vertical spectral density, s_{ww}, on the other hand, rolls off at a higher rate, as can be observed from **Figure 3.60**. Studies on the flow through atmospheric plant canopies reflect different types of roll-off behavior within the canopy. Kaimal and Finnigan (1993), for example, show the spectra from a forest canopy that exhibits the opposite trend to that observed in this experimental study, a steeper roll off for the streamwise component and a less steep roll off for the vertical component. Deep within a waving model wheat canopy, Brunet *et al.* (1994) measured streamwise and vertical turbulence spectra that deviated from the inertial subrange slope in a similar fashion to the deviation observed here for the vertical spectra. The differences among the studies can be attributed to instrument dependent factors that influence the high frequency behavior.

The differences in the high frequency behavior of the turbulence spectra between this study and those of other canopy flows can be attributed to the masking of the turbulence spectra by the Doppler noise. Atmospheric plant canopy experiments usually employ high frequency hot-wire anemometers that

resolve turbulence in the range of 100–500 Hz. The acoustic Doppler velocimeter, on the other hand, suffers from considerable noise, as discussed thoroughly in Section 2.3.2.3. The turbulence spectra are a useful way of analyzing at what frequencies the Doppler noise is introduced into the velocity signals and under what specific flow conditions the noise becomes important. **Figure 3.69** presents the vertical spectra S_{ww} from two elevations ($z/h_p = 0.25$ and 1.00) for experimental run 7 and the spectra from the still water experiment discussed in Section 2.3.2.3. To a first approximation, the spectra for the still water experiment is a Gaussian white noise due to the uniform distribution of the variance across all frequencies (Nikora and Goring, 1998). The horizontal dashed line in **Figure 3.69** represents the average Doppler noise obtained from the still water sample and is located at a spectral density of 0.004 cm^2/s. The intercept of this noise floor with the turbulence spectra is an indication of the boundary frequency, f_b, beyond which the spectra is contaminated by the noise and no useful information can be obtained. If the turbulence level at a particular elevation is low, there stands a chance that the noise becomes an important factor in the turbulence spectra. For example, the spectra at the elevation within the canopy ($z/h_p = 0.25$) is quite low and it intersects the white noise spectra at a boundary frequency equal to 4 Hz. For the spectra at the canopy height, the power spectral density never reaches the noise floor due to the large depth Reynolds number, avoiding the contamination of the turbulence spectra with the Doppler noise.

Figure 3.69 shows the spectra for the vertical velocity component which has inherently less noise than the horizontal velocities. The noise floor for the streamwise and lateral components are higher than for the vertical so that the turbulence spectra should be expected to intersect the noise floor at a lower boundary frequency. The energy content in these directions, however, is larger than in the vertical direction, so that the intersect actually occurs at similar f_b values, as can be observed in **Figure 3.60**. The spectral curves flatten out at frequencies near $f_b = 4$ Hz for those velocity records that are affected by the Doppler noise, an observation that was taken into account when choosing the frequency band over which to average the product of the spectral density and the frequency, as described in **Eq. 3.123**. Thus, the estimate of the turbulent dissipation should not be affected significantly by the introduction of noise at the higher frequencies.

The introduction of Doppler noise to the spectral components is just one reason why the spectra deviate from the inertial subrange slope. Another reason is the introduction of turbulent energy at high frequencies by the wake and waving production. As discussed previously, these two processes are able to extract kinetic energy from the mean flow or from the largest eddies and introduce it at frequencies scaled by the waving motion or the plant dimensions. If the energy is set at a frequency within the expected inertial subrange, the eddy cascade process may be interrupted and the characteristic slope may contain a region of constant spectral density and a roll off at higher frequencies. **Figure 3.70** shows an example of the spectral short circuiting created by the waving or wake production of turbulent kinetic energy. The figure shows the vertical power spectral density S_{ww} at an elevation $z/h_p = 0.25$ within the canopy for the case with the highest in-canopy velocity, experimental run 6 ($H/h_p = 1.75$, $Q = 15.14$ L/s). Several

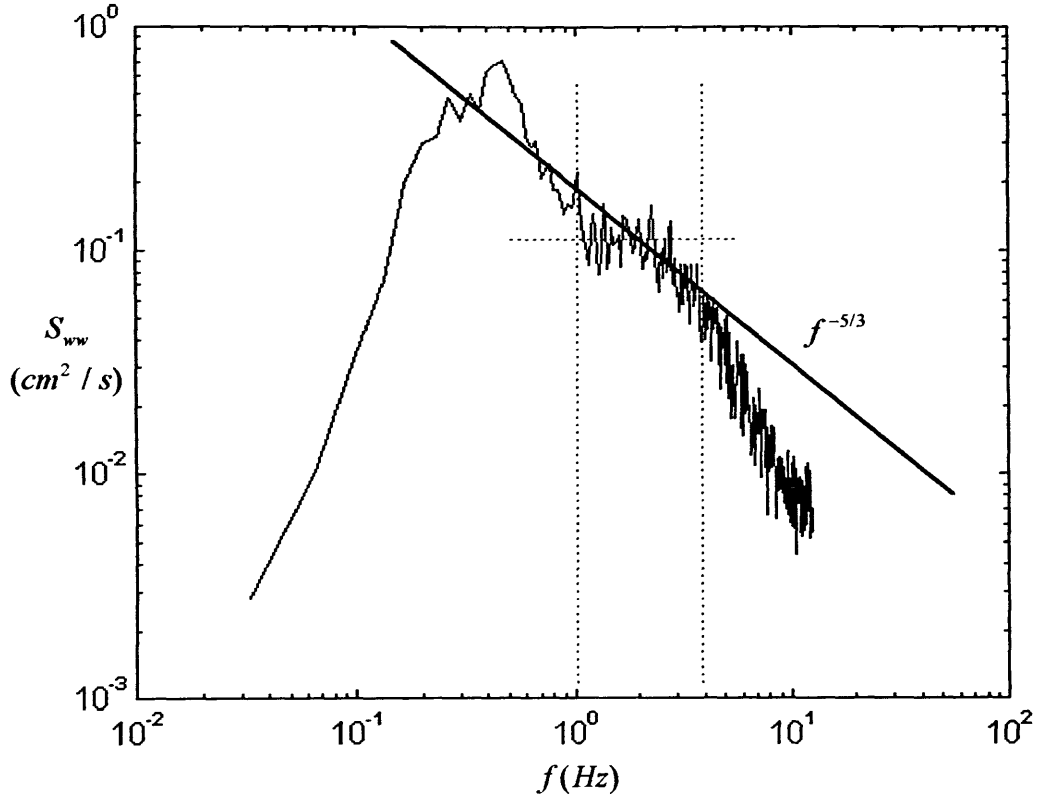

Figure 3.70. Vertical dimensional spectra S_{ww} demonstrating the effect of wake production. Obtained from experimental run 6, with a high in-canopy velocity (U_c) at the elevation $z/h_p = 0.25$. The leveling off of the turbulence spectra in the frequency range 1–2.5 Hz corresponds to turbulent energy input from stem scale generation.

features should be noted from **Figure 3.70**. First, the increased turbulent energy under these flow conditions prevents the spectra from reaching the noise floor. Second, a relatively constant spectral density region is observed within the frequency band 1–4 Hz. This leveling off should be a result of the production of turbulent energy from the plant wakes since the effects from the sweep motions are negligible at this elevation. The introduction of energy at this frequency changes the shape of the turbulence spectrum considerably, interrupting the cascade of energy from the eddies originating in the shear zone to the dissipative eddies within the canopy. Third, the characteristic slope is observed for a limited frequency band (2.5–4 Hz), after which it rolls off at a steeper rate as anticipated for the dissipation range (Tennekes and Lumley, 1972, p. 269)

To summarize, the inertial subrange is an important region within the turbulence spectrum, permitting the estimation and analysis of the turbulence dissipation, an important component of the turbulent kinetic energy budget. Various types of information were extracted from knowledge of the turbulent dissipation, which have improved our overall understanding of the velocity measurements and the details of the fine scale turbulence structure within the seagrass meadow.

3.9 Turbulent Kinetic Energy Budget

The discussions concerning the structure of the momentum transport and the spectral analysis of the turbulence signatures have addressed, in varying degrees of complexity, various issues concerning the production, transport and dissipation of turbulent energy. It has been shown that turbulence is generated at the canopy height by the large shear located there induced by the vegetative drag. Shear generated turbulence is transported into the canopy by downwards moving turbulent structures, where it is dissipated in the canopy space or absorbed through the plant motion. Although extremely useful for interpretative purposes, the information provided by the turbulence spectral analysis and the quadrant analysis of the Reynolds stress does not provide a quantifiable measure of the relative importance of turbulence production, transport and dissipation within and above the canopy. This type of information must be obtained from evaluating the budgets of the second moment equations, in particular the turbulent kinetic energy budget.

Following Raupach *et al.* (1991) and Brunet *et al.* (1994), the *TKE* budget can be expressed in the following form, indicating that the time rate of change of the turbulent kinetic energy $\langle q^2 \rangle$ is composed of the contributions from seven different terms:

$$1/2\,\partial\left\langle \overline{q^2} \right\rangle / \partial t = 0 = P_s + P_W + P_v + T_t + T_d + T_p - \left\langle \varepsilon_T \right\rangle \qquad \textbf{(3.125)}$$

where each of the terms in **Eq. 3.125** will be defined shortly. This equation is obtained by multiplying the momentum equation, as in **Eq. 3.2**, by the three dimensional velocity field and separating it into its mean and turbulence components, as was performed for the governing equations in Section 4.1.1. Then, the appropriate spatial averaging is performed over the canopy space by introducing the volume averaging operator, defined in **Eq. 3.11**, to each of the terms in the turbulent kinetic energy budget. In practice, this averaging procedure results in the conversion of the single point turbulent kinetic energy terms into horizontally-average quantities and in the incorporation of terms that arise from the horizontal heterogeneity of the velocity field. The horizontally-averaged shear production (P_s), turbulence transport (T_t), pressure transport (T_p) and dissipation (ε_T) arise naturally from the turbulent kinetic energy budget at a single point, while the wake production (P_W), waving production (P_v) and dispersive transport (T_d) are due specifically to the heterogeneity at the scale of the roughness elements (Raupach *et al.*, 1991). A detailed description of the averaging procedure for the second moments and the resulting *TKE* budget for a canopy flow can be found in Raupach and Shaw (1992).

Several assumptions were made to simplify the turbulent kinetic energy budget for practical use: a high Reynolds number regime, steady flow, negligible advection and no streamwise development. The rough turbulent conditions in this laboratory study, as shown from the roughness Reynolds number criteria, permit the disregard of the molecular transport terms in the *TKE* budget, so that viscosity only plays a role in the determination of the turbulence dissipation. Steadiness assures that the terms composing the *TKE* budget add up to zero and allows for the closure of the budget through the estimation

of the residual component. The analysis of the behavior of the turbulence statistics performed in Sections 2.3.2.2 and 2.4.1 showed that the time-averaged quantities were long enough to consider the flow as stationary in the mean and the variance, justifying the steadiness assumption made in **Eq. 3.125**. Neglecting the advective terms is justified based on having the flow principally along one velocity axis such that the mean streamwise velocity is much larger than the mean lateral and vertical velocities $U >> V, W$. Choosing a longitudinal location within the canopy where the velocity statistics reached equilibrium, assures that there is no streamwise variation of the turbulent kinetic energy.

The first term in the turbulent kinetic energy budget (P_s) is the shear production term, which also arises in mean kinetic energy equation but with an opposite sign. It represents a loss of mean kinetic energy (*MKE*) and a gain in turbulent kinetic energy caused by the interaction of the Reynolds stress components with the mean shear. In the quasi-two dimensional (x, z) flow through a seagrass meadow, the most important Reynolds stress and velocity components are the covariance uw and the mean streamwise velocity U, so that the production of turbulence via shear can be expressed simply as:

$$P_s = -\langle \overline{uw} \rangle \frac{\partial \langle \overline{U} \rangle}{\partial z}. \qquad \textbf{(3.126)}$$

The shear production can be evaluated from the temporally and horizontally-averaged Reynolds stress profiles presented in Section 3.3.3 and the vertical gradient of the mean streamwise profiles of Section 3.3.1 for each experimental run in *Case A* and *B*. **Figures 3.7.2** and **3.7.3** present the shear production profiles (o, used as symbol) for all the experimental runs, except the emergent case (H/h_p = 1.00), which does not contain a shear contribution to the total turbulent kinetic energy budget.

The wake production term (P_W) accounts for the creation of turbulent kinetic energy at the scale of the plant wakes and arises from horizontally averaging across local wake shear. Like the shear production, P_W converts mean kinetic energy to turbulence but at a very different scale set by the plant dimensions (d_b), rather than at a length scale on the order of the canopy height, h_p. In tensor notation, the wake production term is expressed formally as:

$$P_W = -\left\langle \overline{u_i'' u_j''} \frac{\partial \overline{U}_i''}{\partial x_j} \right\rangle, \qquad \textbf{(3.127)}$$

where the i, j indexes are repeated over the three orthogonal directions and the double primes represent the variation from the horizontal average. As pointed out by Kaimal and Finnigan (1993), the wake production term has the same form as P_s, but it depends on the interaction of the local variations in the shear stress with the local velocity gradients, which occur in the plant wakes. Under the typical assumptions made to derive the turbulent kinetic energy budget, steady flow and horizontal homogeneity on a large scale, **Eq. 3.127** can be reduced to a simpler form involving the mean streamwise velocity and the gradient of the sum of the Reynolds stress and the dispersive stress (Kaimal and Finnigan, 1993):

$$P_W = -\langle \overline{U} \rangle \frac{\partial}{\partial z} \left(\langle \overline{uw} \rangle + \langle \overline{u}'' \overline{w}'' \rangle \right). \quad \textbf{(3.128)}$$

As discussed in Section 4.1.1, the dispersive stress, the second term in **Eq. 3.128**, is expected to be small compared to the Reynolds stress on grounds that the dimensions of the spatial variability are small. Experimental evidence from flow over rough surfaces and laboratory models of plant canopies has confirmed that the dispersive stress term is on the order of a few percent of the total shear stress and is therefore negligible (Raupach *et al.*, 1980; Raupach *et al.*, 1986). Neglecting the dispersive momentum flux leads to an equation that can be used to estimate the wake production from the vertical profiles of the Reynolds stress and velocity, without the need of the detailed spatial velocity variations within the wakes:

$$P_W \approx -\langle \overline{U} \rangle \frac{\partial \langle \overline{uw} \rangle}{\partial z}. \quad \textbf{(3.129)}$$

The wake turbulence production estimated using the simplified expression in **Eq. 3.129** for the experimental runs in *Cases A* and *B* are shown in **Figures 3.72** and **3.73** as well, represented by the (*) symbol. An alternative estimate can be made by considering that wake turbulence is produced by the working of the mean flow against plant drag, which assumes that all the *MKE* is converted to wake turbulence (Raupach and Shaw, 1982; Raupach *et al.*, 1986). The wake production term arising from this assumption is parameterized as the work input, *i.e.* the product of the total streamwise drag force (f_x) and the mean streamwise velocity, which can be expressed in the following forms:

$$P_W = -\langle \overline{U} \rangle f_x = -\langle \overline{U} \rangle \left(f_{Fi} + f_{Vi} \right) = \tfrac{1}{2} C_D a \langle \overline{U} \rangle^3. \quad \textbf{(3.130)}$$

The drag coefficient, C_D, was obtained from the longitudinal force balance, **Eq. 3.22**, and incorporates the effects of the form drag (f_{Fi}) and the viscous drag (f_{Vi}). Using the vertically varying drag coefficient and canopy density, and the mean streamwise velocity, **Eq. 3.130** was compared to **Eq. 3.129** for experimental run 7 (H/h_p = 2.75, Q = 15.14 L/s). **Figure 3.71** shows the comparison of the two wake production estimates and indicates that there are substantial differences in the two methods, especially in the lower canopy region (z/h_p < 0.4). Physical reasoning suggests that the interaction of the mean flow with the plants should generated wake turbulence if the drag Reynolds number is sufficiently high, so that P_W is a non-negligible term, as obtained from the drag estimate, **Eq. 3.130**. However, the low drag Reynolds number conditions inside the canopy (Re_D ~ 100) are not conducive to separation and vortex shedding, so that drag does not produce wake turbulence. For this reason, **Eq. 3.130** is expected to overestimate P_W considerably. Due to the dominance of viscous drag within the lower canopy region, P_W should be negligible as estimated from **Eq. 3.129**, the formulation which will be used to estimate the contribution of wake turbulence to the turbulent kinetic energy budget.

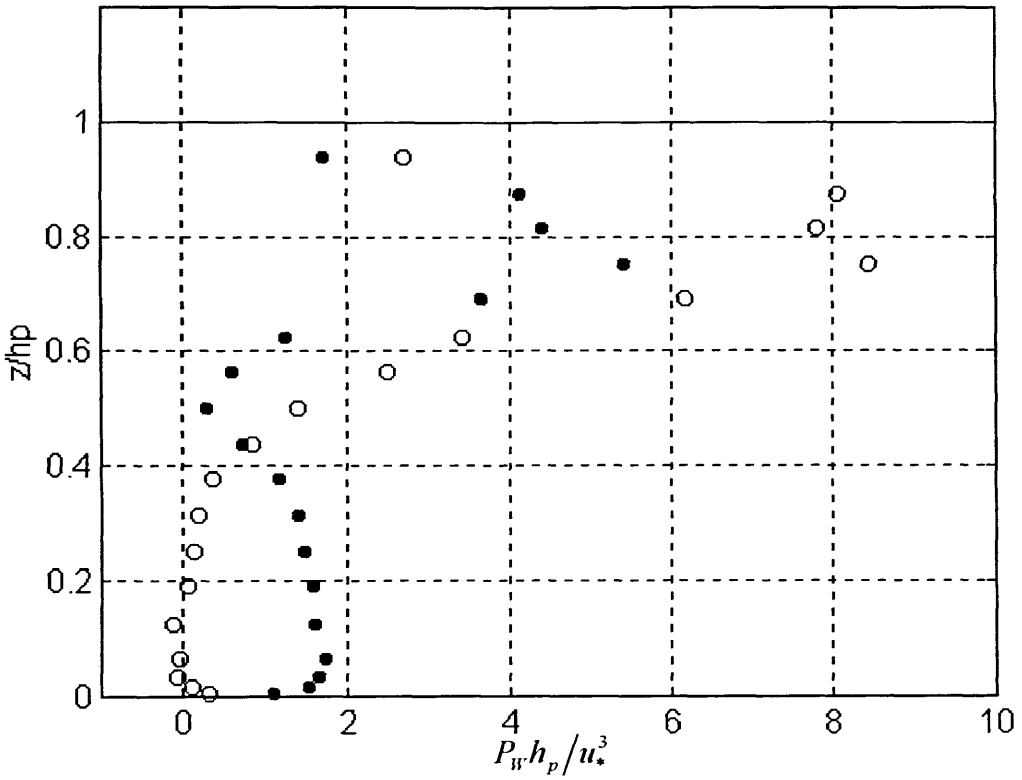

Figure 3.71. Comparison between the two estimates for the wake production (P_W) for experimental run 7 (H/h_p = 2.75, Q = 15.14 L/s) normalized by the canopy height, h_p, and the friction velocity, u_*. The open circles (o) are P_W estimated from **Eq. 3.129**, while the closed circles (•) are the estimate from **Eq. 3.130**. The wake production profiles are shown up to the vicinity of the canopy height (z/h_p = 0.94) and show a substantial deviation from one another.

As discussed in the spectral characterization of the turbulence within and above the seagrass meadow, the contributions from wake and waving production could potentially lead to increased turbulence levels and a short-circuiting of the eddy cascade process. The waving production of turbulence is obtained from the volume averaging operation performed on the *TKE* budget for a canopy whose roughness elements move relative to the fixed coordinate system. The waving production can be expressed in an integral form as (Brunet *et al.*, 1994):

$$P_v = \frac{1}{V}\iint_{S_i} \overline{v_i'\left(p' n_i - \upsilon \frac{\partial u_i'}{\partial n}\right)} dS, \qquad \textbf{(3.131)}$$

where V is the averaging volume, S_i is the plant element surface, v_i is the plant velocity and n_i is the unit normal vector to the plant surface. As expressed in **Eq. 3.131**, the waving production is not an easily measured quantity because the instantaneous plant position, the pressure fluctuations and velocity normal to the plant need to be known over a large averaging volume. Fortunately, the waving production term

has been found to be of little importance to the turbulent kinetic energy budget (Kaimal and Finnigan, 1993) and is often neglected in studies with waving or moving roughness (*e.g*, Brunet *et al.*, 1994).

The reasoning behind the neglect of the waving production term is quite straightforward. At the locations where waving occurs violently ($z/h_p = 1.00$), waving production of turbulent energy is introduced at frequencies that match the arrival of the turbulent structures and the energy containing range, as corroborated by the observations of the plant motion at the same frequencies. The waving production acts to pass turbulent energy from the large scale to the small scale eddies, thereby possibly short circuiting the inertial subrange, and potentially converting the forcing at one frequency to its preferred resonant frequency. Therefore, waving production does not have a net effect on the turbulent kinetic energy budget. By averaging over all frequencies, the *TKE* budget cancels out the effect of waving production so that the P_v term can be safely neglected for a flexible plant canopy that exhibits coherent waving.

The fourth term in the turbulent kinetic energy budget corresponds to the transport of turbulence by the vertical velocity fluctuations. The turbulence transport (T_t) is indicative of the transfer of turbulence generated in one location to other elevations within the flow and as such is directly related to the structure of the momentum transfer discussed in Section 3.6. Arising directly from the horizontal average of the second moment equation, the turbulence transport can be computed from the profiles of the vertical *rms* velocity and the turbulent kinetic energy q^2 presented in Sections 3.3.2 and 3.3.6 as:

$$T_t = -\frac{\partial}{\partial z}\left\langle \frac{\overline{wq^2}}{2} \right\rangle. \qquad \textbf{(3.132)}$$

The turbulence transport profiles for each experimental run in *Case A* and *B* are shown in **Figures 3.72** and **3.73** along with the other terms of the *TKE* budget, represented by the symbol (+). Contrary to the behavior of the two turbulence production terms, P_s and P_W, that peak near the canopy height, the turbulence transport term changes sign at an elevation near $z/h_p = 0.8$. The turbulence produced in the shear layer is transported downwards resulting in a loss of TKE in the region ($T_t < 0$) above the canopy and a gain in turbulent kinetic energy in the upper canopy region ($T_t > 0$). The importance of T_t inside the canopy is related to the dominant role played by the downward moving sweeps and is consistent with the large skewness values observed at the same level in Section 3.3.4. It also implies that the turbulence in this region is not locally generated, one reason why the eddy diffusivity parameterization of the momentum transport, *K*-diffusion theory, fails within plant canopy flows.

Two additional transport terms are presented in **Eq. 3.125**, the transport of turbulence by the dispersive momentum flux (T_d) and the pressure-induced *TKE* flux (T_p). The dispersive transport of turbulent kinetic energy arises from the horizontal averaging of the *TKE* budget and can be expressed as:

$$T_d = -\frac{\partial}{\partial z}\left\langle \frac{\overline{W}^{"}\overline{q^2}^{"}}{2} \right\rangle, \qquad \textbf{(3.133)}$$

where W represents the vertical velocity. As mentioned previously, the dispersive momentum flux has been shown experimentally to be small in relation to the other contributing factors to the total shear stress. From similar arguments, the dispersive transport is usually neglected in the estimation of the *TKE* budget as compared to the magnitude of the turbulence transport T_t (*e.g.*, Raupach *et al.*, 1991). This result is extremely fortunate for experimental studies based on profile measurements taken at a single location that do not properly estimate the spatial variation of the velocity statistics within the canopy.

The pressure transport term, on the other hand, is expected to have a significant contribution to the *TKE* budget, but its calculation within plant canopy flows has eluded researchers for some time. Recent turbulence modeling efforts using large scale eddy simulation (LES) suggest that the pressure transport, which is parameterized as:

$$T_p = -\frac{\partial}{\partial z}\left\langle \overline{wp} \right\rangle, \tag{3.134}$$

is significant within the canopy, becoming the most important turbulence source term below the shear production peak (Shen and Leclerc, 1997; Dwyer *et al.*, 1997). Unfortunately, the results from the LES simulations are difficult to extrapolate to the experimental studies because the wake production term is missing from the LES budgets due to its occurrence at a subgrid level. Experimental evidence confirming the pressure transport behavior in the LES simulations is still lacking due to the difficulty in estimating the pressure fluctuations. In fact, the available data from measurements within atmospheric plant canopies are quite contradictory. The most convincing evidence for the variation of the pressure transport within the canopy has been provided by Brunet *et al.* (1994) who showed through a residual analysis and two closure models that the pressure transport should be equal in magnitude but opposite in sign to the turbulence transport term. This implies a completely different role as that suggested by the LES simulations since the pressure transport becomes a net sink of *TKE* within the canopy and a net source above the canopy. An inspection of the residual term obtained from this experimental study supports the behavior of the pressure transport term suggested by Brunet *et al.* (1994).

The viscous dissipation of turbulent kinetic energy is an important term in the *TKE* budget. Formally, the turbulent dissipation is defined as the mean of the square of the spatial gradients of the velocity components and directly involves the viscosity of the fluid:

$$\varepsilon_T = -\nu\overline{\left(\frac{\partial u_i}{\partial x_j}\right)\left(\frac{\partial u_i}{\partial x_j}\right)}. \tag{3.135}$$

In practice, however, the estimation of the turbulent dissipation is made through the use of the Kolmogorov laws, **Eq. 3.119** through **3.121**, within the inertial subrange of the turbulence spectra. For the data in this experimental study, the dissipation is estimated from the streamwise velocity spectra s_{uu}, as discussed thoroughly in Section 3.8. The results of the dissipation estimates for the *Case A* and *B*

experimental runs are shown in **Figures 3.72** and **3.73** along with the other *TKE* budget components and are represented by the (×) symbols.

Although the pressure transport was not measurable within the seagrass meadow during this experimental study, the residual of the remaining terms may indicate the magnitude and trend of T_p. The residual was estimated from the measured values for the shear and wake production, the turbulence transport and the dissipation. This residual is simply the value that balances the *TKE* budget at each profile depth, *i.e.* the time rate of change of the temporal and horizontal-averaged turbulent kinetic energy is made to equal zero by the residual:

$$R_e = -\left(P_s + P_W + T_t - \left\langle \varepsilon_T \right\rangle\right) = T_d + T_p . \qquad \textbf{(3.136)}$$

Knowing that the dispersive transport (T_d) is a negligible term in the *TKE* budget, the residual is expected to closely follow the pressure transport variation. As shown in **Figures 3.72** and **3.73** for the experimental runs in *Cases A* and *B*, the value for R_e, represented by a dashed line (--), is for the most part opposite in sign to the turbulence transport and has a large peak at the same level as the wake production.

Attention is now turned specifically to the variation of each of the terms in the turbulent kinetic energy budget along the depth profile and across the submerged flow conditions. **Figures 3.72** and **3.73** show the quantifiable *TKE* terms (in cm^2/s^3) and the residual normalized by the canopy height, h_p, and the cube of the friction velocity, u_*. The friction velocity scale chosen to nondimensionalize the turbulent kinetic energy budget is the square root of the Reynolds stress at the canopy height, defined in **Eq. 3.46**. This estimate was chosen based on its exceptionally good collapse of the turbulent kinetic energy profiles presented in Section 3.3.6. As is customary, the horizontal axis is labeled with the normalized time rate of change of the turbulent kinetic energy. This normalization introduced variations in the horizontal axis since the friction velocity varies by a factor of three over the experimental runs. It should be noted, in particular, that the dimensional profiles of the terms in the *TKE* budget have a higher magnitude as the characteristic depth and the flow discharge are increased. The similarities observed in **Figures 3.72** and **3.73** are due to the normalization procedure.

Several general features should be noted from the *TKE* budgets. Both the wake and the shear production profiles peak near the canopy height, as does the turbulence dissipation and the turbulence transport of *TKE*. At this elevation, the estimated terms exactly balance, so that the residual calculated from **Eq. 3.136** is negligible. This implies that the all turbulent energy derived from the mean flow at this level is either transported away from $z = h_p$ by turbulent structures or dissipated quickly. In the upper canopy region, the wake production term, determined from **Eq. 3.129**, peaks slightly below the shear peak and is slightly higher in magnitude. Similar behaviors are observed in the *TKE* budgets of several atmospheric canopies (*e.g.*, Brunet *et al.*, 1994; Raupach *et al.*, 1991). The decrease to zero of the turbulence transport at $0.8h_p$ and the slight decrease in dissipation in the upper canopy region lead to a substantial unbalance in estimated terms, which leads to a large residual minimum near $0.75h_p$. If the

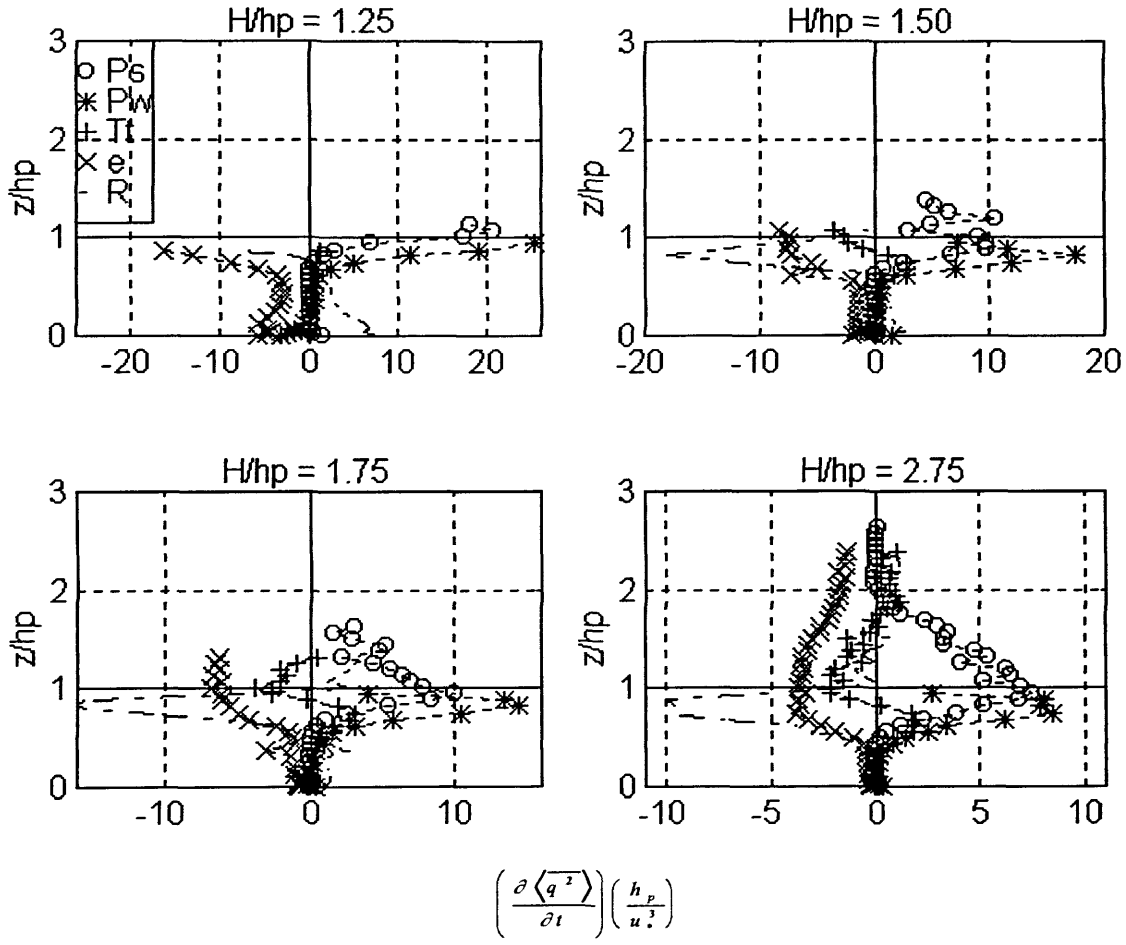

Figure 3.72. Turbulent kinetic energy budget terms evaluated for the experimental runs in *Case A*. The shear production, P_s (o), the wake production, P_w (*) and the turbulence transport terms, T_t (+), are evaluated from the vertical gradients of the velocity statistics. The dissipation, ε_T (×), is estimated from the turbulence spectra for the streamwise velocity, S_{uu}. The residual, R (–), which includes contributions from the waving production and the pressure transport is obtained as the difference between the other estimates. Each term in the *TKE* budget is normalized by the canopy height, h_p, and the friction velocity, u_*.

residual is indicative of the pressure transport of turbulent kinetic energy, the loss of *TKE* in the upper canopy region should be expected to be due to a significant contribution from T_p. Otherwise, the unbalance may be due to the overestimation of the P_W or an underestimation of ε_T or both.

The terms in the *TKE* budget decrease rapidly into the canopy and are small below $0.4h_p$, an indication that the shear generated turbulence is not transported downwards into the lower canopy region and that the mean velocity profile lacks an appreciable degree of shear. Within this region, the wake turbulence and the turbulent dissipation are approximately in balance $P_W \approx \varepsilon_T$, which suggests that the interaction of mean flow with the plants results in wake turbulence that is dissipated locally within the lower canopy. A similar behavior should be observed from the emergent canopy conditions ($H/h_p = 1.00$), although the two P_W estimates and the dissipation for this case do not corroborated the expected result.

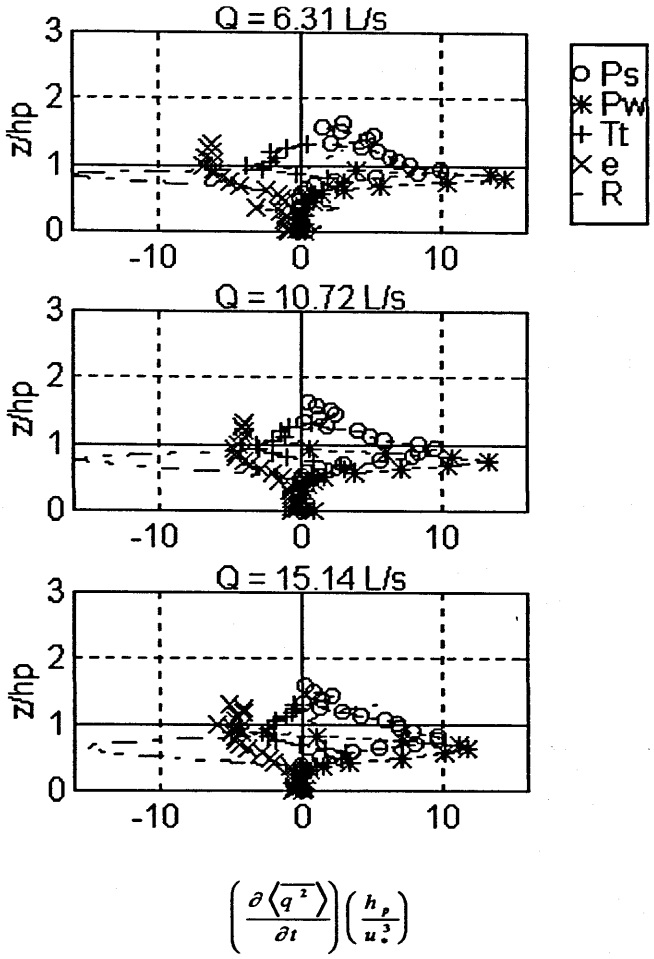

Figure 3.73. Turbulent kinetic energy budget terms evaluated for the experimental runs in *Case B*. The symbols are as indicated in the legend and discussed in **Figure 3.71**. Notice the nearly identical *TKE* budgets for the different cases, despite the large variation in turbulent kinetic energy, an indication of the effectiveness of the normalization by h_p and u_*.

Moving away from the canopy, the wake production term decreases to zero near the canopy height, as expected from the lack of wake generation above $z = h_p$. The shear production term, on the other hand, decreases less rapidly above the canopy and for $H/h_p = 2.75$ is observed to be negligible above $z = 2h_p$. The turbulent dissipation has a similar variation above the canopy as the shear production. In fact, for $H/h_p = 2.75$ these two terms balance each other, $P_s \approx \varepsilon_T$, over a limited range above the canopy, $1.5–2h_p$, an indication of a second region of local equilibrium, *i.e.* shear production balanced by dissipation.

Figures 3.72 and **3.73** also demonstrate the effect of varying the level of submergence and the flow discharge within the seagrass canopy have on the turbulent kinetic energy budget. As with the *TKE* profiles, increasing the characteristic depth or the flow rate results in a net increase in all the components of *TKE* budget. For example, the peak wake production in the upper canopy region increases from 0.67 to 2.68 cm^2/s^3 from $H/h_p = 1.25$ to 2.75. The increase in the value of the peak wake production is even more

substantial as the flow discharge increases, changing from 1.56 to 13.50 cm^2/s^3 from Q = 6.31 to 15.14 L/s. The other TKE budget terms increase proportional to each other as either H/h_p or Q increase. resulting in a similar distribution of the terms over the depth and across the flow conditions. This is further shown by the appropriate normalization made to the budget through the use of the canopy height and the friction velocity. The collapse for the velocity variation runs of *Case B* in **Figure 3.73** improves if the deflected canopy height, h_b, is used as the normalization scale.

The only noticeable difference among the experimental runs is the relative increase in the dissipation estimate in the lower canopy region as the flow depth is decreased. Presumably, the dissipation rate increases since the wake dissipation plays an important part in the overall turbulence structure. Since the eddy scale in wake turbulence, on the order of the plant dimensions. is much smaller than the eddy scale of the shear turbulence, scaled by the canopy height, the dissipation rate of wake turbulence is much higher. The larger in canopy dissipation of turbulent energy in the lower canopy regions is not balanced by a corresponding turbulent production or transport term, suggesting that there is not an account for the mean flow induced by the water surface slope forcing in the wake production term of **Eq. 3.129**. The reason behind the discrepancy for this case and for the emergent case (H/h_p = 1.00) is not clear, except for the noted effects of the low Reynolds number regime which may lead to an overestimation of P_W from the form drag expression.

The turbulent kinetic energy budget presented in this section has demonstrated the relative importance of the various turbulent production, dissipation and transport terms over the flow depth and ties in well with the previous discussions concerning the structure of the momentum transport and the spectral characterization of the turbulence. In the Chapter 4, a synthesis is provided that attempts to place all the evidence obtained from this laboratory study into a single framework, and demonstrate the effect that depth limitation has on the turbulence structure through a submerged canopy. In addition, several key parameters will be used to estimate the variation of the penetration depth of the momentum as the characteristic depth changes.

CHAPTER 4. Synthesis and Conclusions

The aim of this research has been to investigate the effects of the water depth and the flow velocity variations on the turbulence structure of a seagrass meadow. In order to accomplish this, a properly scaled laboratory model in an open channel flume was constructed to mimic the field conditions of a typical *Zostera marina* meadow exposed to a unidirectional current. The model for a low-density seagrass meadow is composed of flexible plants with a complicated morphology that reproduces the dynamic behavior observed in these expansive plant communities populating low-lying coastal areas. The hydrodynamic characterization of these systems through controllable laboratory experiments allows the interpretation of the various biological, geochemical and ecological processes that are influenced to a great extent by the flow environment within the plant canopy. From this perspective, the hydrodynamic results obtained from this study should be useful to other researchers interested in understanding the interaction of flow with the seagrass ecosystem. On the other hand, the results also have applications to the understanding of the hydrodynamics within and above a depth-limited rough boundary layer composed of a roughness array.

The intent of this chapter is not to summarized in great detail the myriad of topics that have been covered in this thesis, but to give some final thoughts concerning the major issues which have been addressed through the diverse set of experimental evidence. Four themes have been at the forefront of the discussion of each parameter derived from the velocity, slope and plant motion measurements: the penetration of streamwise momentum, the asymptotic behavior exhibited with the variation of the level of submergence, the transition from a wake-generated to a shear-generated turbulence regime, and the effect of plant waving on the turbulence structure. Each of these themes will be discussed in an attempt to coherently mesh the various lines of evidence into a plausible explanation of each phenomenon. Each of the interrelated topics will show how the controlling parameter in the depth-limited canopy flow is the level of submergence, which is directly responsible for the transition between the confined canopy conditions with a wake dominated turbulence structure and the unbounded conditions with a shear dominated turbulence structure, and that the phenomenon of canopy waving as investigated in the velocity variation cases is merely a response to the shear generated turbulence regime and not an active modifier of the turbulence structure.

4.1 Momentum and Turbulence Penetration

One of the common themes that has permeated the discussion of the experimental results has been the substantial effect of the characteristic depth on the momentum transport between the surface and vegetation layers. The turbulent eddies generated in the shear region between the canopy and the overlying water induce vertical exchanges of momentum and the renewal of in-canopy water, which should have important implications for the transport of nutrients and other water constituents. Coherent motions that transfer momentum into the canopy also bring with them a considerable amount of turbulence, so that the momentum penetration depth should correspond closely to the depth of penetration of shear-generated turbulence. The inner canopy region is characterized by non-local sources for both properties. The penetration of surface layer momentum and turbulence has been examined by a quadrant analysis of the Reynolds stress and through the turbulence transport term in the turbulent kinetic energy budget. From these profiles, it is possible to quantify the depth of momentum and turbulence penetration and identify the portion of the canopy that actively participates in the vertical exchange of mass, momentum and heat. The penetration depth will also mark the boundary between the two water renewal zones that have been identified from the mean and turbulence velocity fields: the upper canopy region actively exchanging with the surface layer and the inner canopy region near the bed affected exclusively by the blow-through flow entering through the meadow edges.

In order to quantify the penetration depth, profiles of the turbulence transport term (T_t), the sweep event stress (S_4) and the Reynolds stress (uw) were examined to determine a value that defined the minimum for each profile across the experimental runs in *Cases A* and *B*. Once the threshold value was chosen, the elevation (h_m) at which each parameter crossed its threshold level was used to define the penetration depth as:

$$h_{pen} = h - h_m . \tag{3.137}$$

The penetration depth is defined as the distance from the effective canopy height, h, such that a value of $h_{pen} = 0$ implies no penetration into the canopy, while $h_{pen} = h$ results from the penetration down to the bottom boundary. The key figures leading to the estimate of the penetration depth are **Figures 3.13** and **3.14** for the Reynolds stress, **Figures 3.35** and **3.36** for the sweep stress at $H_o = 0$, and **Figures 3.72** and **3.73** for the turbulence transport term.

The choice of these three parameters for determining the penetration depth of the surface layer momentum is not arbitrary. As discussed previously, the sweep events are associated with the downward transport of high momentum fluid ($u' > 0$, $w' < 0$) and represent the major contribution to the momentum transport into the canopy. Similarly, T_t directly indicates the depth of penetration of shear-generated turbulence. Both terms specifically reflect how the turbulent eddies generated at the canopy height bring momentum and turbulence into the lower canopy regions. The total Reynolds stress profile, on the other

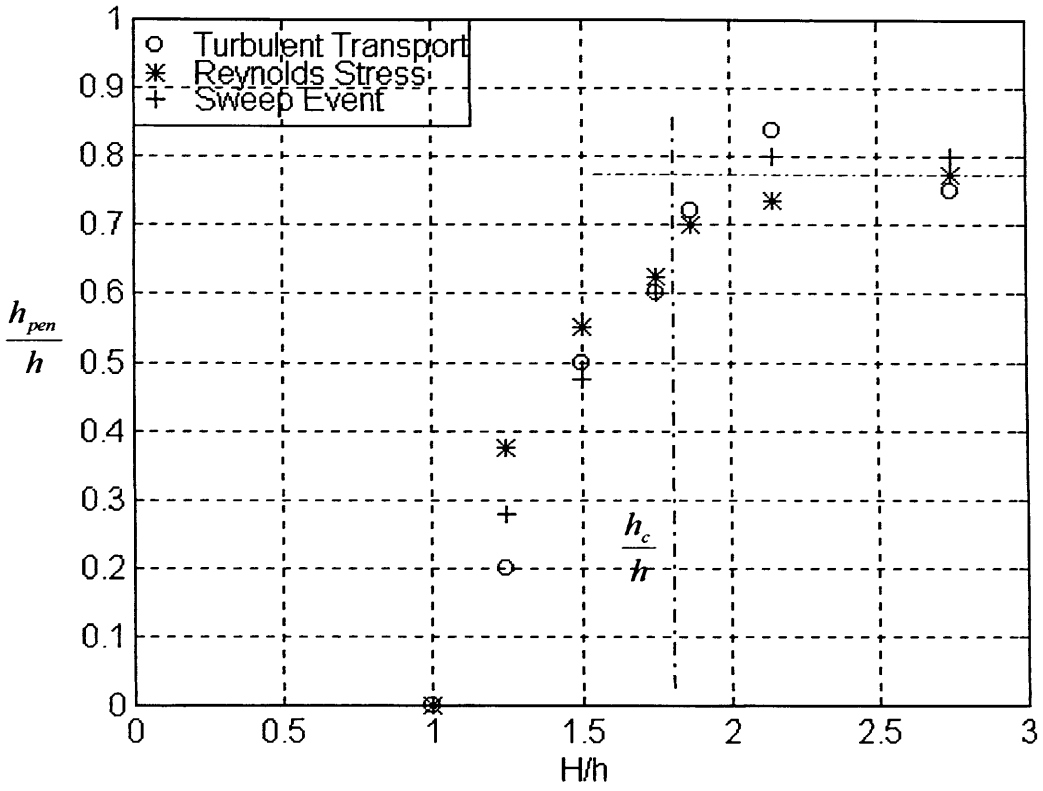

Figure 3.74. Variation of the estimated normalized penetration depth (h_{pen}/h) with the characteristic depth (H/h) for the experimental runs in *Case A* and *B*. The momentum penetration depth was obtained from three separate sources: the turbulence transport of *TKE*, T_t (o), the Reynolds stress profile uw (*), and the normalized sweep stress event contour maps Σ_4 (+). The experimental runs in *Case B* are shown at their respective H/h values, 1.87 and 2.15, for experimental run 5 and 6, respectively. The dashed vertical and horizontal lines indicate the region of constant penetration depth and the value for the critical surface layer depth (h_c/h).

hand, contains contribution from the other conditional averages and is not as indicative of the momentum penetration. Nevertheless, it has been included as a complementary estimate of the penetration depth. The turbulent kinetic energy profile could have also been included as another estimate of the vertical penetration of turbulence, but this estimator is also affected by the wake generated turbulence.

Figure 3.74 presents the value of the penetration depth from the three estimation methods as a function of the characteristic depth H/h for all the experimental cases. The penetration depth has been normalized by the effective canopy height, so that a value of h_{pen}/h = 1.00 is indicative transport of momentum and turbulence through the entire canopy. The striking collapse of the variation of the momentum and turbulence penetration from the three estimation methods reemphasizes the idea that both flow properties are transported simultaneously by the same turbulence mechanism, the coherent eddies travelling along the canopy height. The consistent variation of h_{pen}/h for all the experimental conditions suggest that the depth of the surface layer has a strong degree of control on the turbulence structure of a

depth limited canopy flow. This asymptotic variation also suggests that the transition between unconfined plant canopy flows, such as those that form the bottom boundary of the atmospheric surface layer, and confined canopy flows, such as emergent, coastal plant canopies, is smooth. It also is indicative of the existence of a critical surface layer depth, h_c, beyond which an aquatic canopy behaves as its unconfined atmospheric counterpart.

4.2 Asymptotic Behavior

The evidence presented so far as to the asymptotic tendencies of the flow parameters strongly suggest that the transition from a constrained canopy flow to an unbounded flow is gradual. An asymptotic behavior was observed for numerous parameters asides from the penetration depth mentioned previously. The characterization of the plant motion, the velocity moments, the vegetative drag and resistance, the flow hydraulics, the momentum transport, the turbulence scales, the turbulence spectra and the *TKE* budgets all demonstrated asymptotic variations with the characteristic depth. Every facet of the mean flow, turbulence and drag characterization of a depth-limited canopy flow is directly affected by the surface layer depth, suggesting that knowledge of this single parameter can be crucial for the description of canopy turbulence. Presumably, the turbulence structure of a seagrass meadow, or any hydrodynamic system with comparable boundary conditions, can be described *a priori* by simply knowing the relative roughness, or the percentage of the total depth occupied by the roughness array.

The asymptotic behavior can be explained in a general form in a very straightforward fashion. As the level of submergence increases initially from the emergent case ($H \leq h$), there is a noticeable change in the value of a flow parameter, as observed for the penetration depth of turbulence and momentum in **Figure 3.74**. This initial behavior is followed by a decreasing rate of change as the surface layer depth increases, ultimately leading to a constant value for the parameter at the largest experimental depths, as seen for the highest characteristic depths ($H > 1.50h$). The design of the depth-variation experiments in this laboratory study was robust enough to capture the shift from a depth-dependent to the depth-independent behavior in sufficient detail to make conclusive comments regarding the transition from a confined to an unconfined canopy flow.

At this point, it would be worthwhile to refer back to some of the figures that demonstrate the asymptotic behavior, *e.g.* **Figure 3.31** for the change in the depth-averaged bulk drag coefficient, **Figure 3.58** for the variation of the turbulence length scale, and **Figure 3.65** showing the variation of the peak spectral frequency. These figures suggest that not only do the *Case A* experiments provide evidence for this variation, but under the proper normalization, the *Case B* experiments also fit into this model. For example, increases in the flow discharge are reflected in canopy streamlining and an increase in the surface layer depth which is equivalent to an increase in the characteristic depth. The data from the flow discharge cases (*Case B*) consistently fit into the asymptotic trend described by the water depth cases

(*Case A*), making the case that the characteristic depth controls the turbulence structure in a depth limited canopy flow even stronger.

A critical surface layer depth can be identified from the variation of the flow parameters with the characteristic depth. The dashed horizontal and vertical lines in **Figure 3.74** indicate the region of constant penetration depth and an estimate for the critical surface layer depth, $H/h = 2.25$, in this example. A review of the other asymptotically-varying parameters suggest that a consensus estimate of the critical surface depth is half the effective canopy height, $h_c = 0.5h$ or $H/h = 1.50$. If the surface layer is less than this critical value, the turbulence structure characterizing the flow through the plant canopy is closely related to the emergent canopy conditions. Once this critical value is exceeded, the canopy turbulence structure is no longer depth-limited, approaching the characteristics found in atmospheric plant canopies. Thus, the critical surface layer depth defines the depth limitation threshold for the flow in and above a plant canopy constrained by a free surface.

The existence of a critical surface layer depth allows us to reinterpret many of the results obtained in this laboratory study by looking at how the two smallest characteristic depth cases ($H/h_p = 1.00$ and 1.25) differ from the other three cases ($H/h_p = 1.50$, 1.75 and 2.75). Distinct differences are observed among the two sets. The lower depth cases exhibit behavior that reflects local interaction of the canopy with a mean flow and the creation of turbulence at a scale comparable to the plant dimensions. The vertical profiles of the turbulence intensity and drag coefficient tend to be uniform with depth, because shear production plays a less prominent role. The turbulence integral length scale and the dominant turbulent frequency are both associated with the wake production of turbulence. In addition, the transport of momentum and turbulence is negligible due to the vertical homogeneity over the flow depth.

For the higher depth cases, on the other hand, the shear zone created at the interface of the surface and vegetation layers, leads to a distinctly different mean and turbulence velocity fields as compared to a vertically uniform emergent canopy. The vertical inhomogeneity in resistance induced by the vegetation drag causes distinctive peaks in the profiles of the velocity moments, similar to those observed in a mixing layer. The instabilities created at the level of the mean velocity inflection point ultimately dominate the turbulence structure in the seagrass meadow. The turbulence within the canopy is not locally produced but transported into the region by the eddies generated at the canopy height. These coherent eddies are responsible for the transport of momentum and turbulence into the canopy and for the plant motion in the flexible meadow. For the small characteristic depths in a constrained system, the eddy size is limited by the depth of the surface layer. As the surface layer depth is increased, the asymptotic behavior demonstrates that the turbulence structure is no longer affected by this scale, but rather by the degree of shear in the velocity profile, as has been observed in atmospheric flows. For the highest characteristic depths, the conditions in this depth-limited canopy flow approach the typical characterization of an unbounded system as is evidenced in many descriptive parameters of the turbulence structure of the seagrass meadow.

4.3 Turbulence Generation Regimes

The asymptotic behavior also shows how changing the surface layer depth leads to different turbulence generation regimes. The first indication of this was provided by the variation of the turbulence intensity profiles with the characteristic depth. For the emergent canopy, the streamwise intensity profile exhibited small values and was uniform with depth, an indication that the turbulence was produced locally by the interaction of mean flow with the meadow. The ratio of the lateral and streamwise *rms* velocities also approached a value of unity, further suggesting that the turbulence was wake-generated. As the depth of the surface layer increased, the turbulence intensity profiles demonstrated a distinct peak, characteristic of shear production within the upper canopy. For the largest depth case, the shear-generated turbulence dominated most of the profile, except in the lower most stem region where the existence of a blow-through mean flow and the lack of penetration of the coherent turbulent eddies led to a region devoid of shear turbulence effects. Thus, for larger depths, turbulence is characterized by the coexistence of two generation mechanisms in distinct flow regions.

Further indications of the two turbulence generation mechanisms was provided by the quadrant analysis of the Reynolds stress which showed that the turbulence within the seagrass meadow exhibited an organized pattern called the sweep-ejection cycle. The penetration depth of the sweep events was found to be indicative of the level at which the transition from shear to wake-generated turbulence occurs and defines the boundary between the two flow regions. This observation has not been reported previously in the literature concerning canopy flows in atmospheric and aquatic systems. The presence of the surface slope-induced blow-through in a region of low canopy density coupled with a limited penetration of shear turbulence for these experimental conditions has produced a system where the two turbulence mechanisms can coexist simultaneously. This multiplicity of turbulence scales has important implications for modeling the transport of scalars within a seagrass meadow and the understanding of the exchange between the seagrass meadow environment and the surrounding open water.

Evidence from turbulence spectra and integral length scales lent support to the coexistence of the turbulence regimes in the higher depth cases and for the transition from wake to shear-generated turbulence as the surface layer depth increases. For the lower characteristic depth and in the lower canopy region, the turbulent energy was concentrated at high frequencies and the eddy length scales were found to be small, both an indication that the plant dimensions set the time and length scale for the turbulent eddies through wake production. In the upper canopy region of the higher characteristic depths, the low frequency peak due to the arrival of the turbulent eddies and an eddy length scale on the order of canopy height, both suggest that the shear-generated turbulence regime sets the turbulent time and length scales. The gradual transition between the upper and lower canopy region was observed in the spectral peaks and the eddy length scale variation with the depth inside the canopy and further indicated the existence of the two flow regions.

A final and more conclusive corroboration of the existence of two different turbulence generation regimes was provided by the turbulent kinetic energy budget. For the lowest characteristic depths and in the lower canopy region, wake production is the dominant source term, with the dissipation measured in the lower canopy region balanced exclusively by the production of turbulence in the plant wakes. As the characteristic depth increases, the wake and shear production of turbulence both become important contributors to the budget in the upper canopy region with the shear turbulence balancing the dissipation far away from the canopy in the surface layer. The results from the turbulent kinetic energy budget also emphasize that the wake and shear production of turbulence coexist simultaneously within the upper canopy region, a fact that had not been observed from the other lines of evidence. The apparent lack of wake turbulence in the upper canopy region from the spectral characterization and the other analysis is due to the fact that the larger time and length scales associated with the shear turbulence mask the presence of the wake-generated eddies, but these are still present as observed by the contribution to the *TKE* budget. Thus, the wake generated turbulence is significant throughout the vegetation layer, while the shear generated turbulence is only present when a shear zone is present above the canopy and in the regions in the canopy that are directly affected by the downwards transport of shear turbulence.

4.4 Coherent Waving

At the onset of this experimental investigation the effect of canopy waving on the turbulence structure within the model seagrass meadow was expected to be significant. The monami is such a visually impressive phenomenon, that it was assumed *a priori* to be a controlling factor imparting distinct changes to the transport of momentum, turbulence and mass between the surface layer and the submerged canopy. The limited literature on the coherent, canopy-scale waving of atmospheric crops and seagrass meadows also suggested that this phenomenon was of critical importance. The results from this laboratory study, however, lead to a very different conceptualization of how the monami activity affects the turbulence structure of a submerged plant canopy. In particular, the experimental runs in *Case B* show that the monami causes variations in the turbulence intensity but does not significantly affect the structure of the turbulence. In fact, the monami can be considered as an in-tune response to the system forcing rather than as a dynamically significant interaction between the flow and the flexible plants.

This realization leads to the following understanding about the relationship between the shear generated eddies created at the interface of two coflowing streams and the response observed within a flexible plant canopy. The instabilities generated in the shear region between the vegetation and the surface layers are always present in varying intensities. For a weak degree of shear or a small surface layer depth, the strength and frequency of the shear-generated eddies does not result in plant movement. As the eddy strength and size is increased through changes in the flow discharge or surface layer depth, the downward transport of momentum and turbulence through the sweep events is able to cause a plant

motion response, which is visually observed as the canopy waving. If the canopy were rigid, the coherent eddies would still be present but their impact on the roughness elements would not be visually observed. A flexible seagrass meadow can respond to the periodic forcing of sweep events and exhibit the monami phenomenon in flow conditions that have a forcing frequency that approaches the natural frequency of vibration of the plant elements.

In this system, the arrival frequency of the turbulent structures to the canopy and the natural frequency do not match for any flow condition. In fact, the experimental run demonstrating the monami phenomenon (H/h_p = 1.75, Q = 15.14 L/s) has a forcing frequency that is an order of magnitude smaller than the natural resonant frequency. Nevertheless, the forced response allows us to visually observe the passage of the turbulent eddies at the canopy height and quantify that the plant motion response is highly correlated with the arrival of the sweep events, the eddy length scale, and the turbulent energy frequency peak. It also leads us to conclude that the shear generated monami phenomenon is a passive response to the periodic sweep forcing and does not play an active role in determining the characteristics of the turbulent flow.

4.5 Summary and Recommendations

This laboratory investigation showed that a clear link exists between the shear generated eddies arising at the interface of the canopy and the surface layer and the vertical exchange of momentum, the plant motion characteristics and the turbulence time and length scales. The turbulence field in the seagrass meadow was shown to be composed of a shear-generated turbulence zone near the canopy height and a wake-generated zone near the stems, where a mean flow due to the pressure gradient was found to create a region of secondary maxima in the mean velocity profile. The controlling parameter in describing the seagrass turbulence structure was determined to be the characteristic depth. The range of values considered for H/h showed a clear transition from a confined canopy flow to an unbounded canopy flow with an asymptotic variation observed for numerous turbulence parameters. From this analysis, a critical surface layer depth governing the transition between the two canopy flow conditions is identified as half the effective canopy height, $h_o = 0.5h$ or H/h = 1.50..

Despite the progress made with this laboratory study in regards to the turbulence structure of a depth-limited canopy flow, this is by no means the definitive answer to all the research questions concerning the hydrodynamics of these aquatic systems. From the onset, it has been emphasized that this experimental study was restricted to very specific flow conditions that could be reproduced within a laboratory flume. Ignoring the three dimensional current and wave regimes present in field conditions, the flow through a natural seagrass meadow has been modeled simply as a unidirectional flow forced by a pressure gradient with the intention of describing the effects that tidal variations of the water depth and flow velocity have on the turbulence structure. Due to this simplification, an important future step is the corroboration through field measurements of the behavior described in this laboratory study. Identifying

the separation between the blow-through flow in the lower canopy and the vertical exchange in the upper canopy, for example, would render a great deal of support for these laboratory results.

In addition to field data corroboration, this experimental study has opened up a range of potential research venues. On one part, although the monami phenomenon was shown to have an insignificant effect on the turbulence structure, it deserves more a careful investigation from a hydrodynamics perspective. Other researchers have identified the coherent eddies responsible for the monami from visualization experiments and two-point correlation analysis, but issues concerning the onset and development of the phenomenon have been largely ignored. Studying the monami should provide a great insight into the instabilities generated in a shear layer. On a different note, the interaction of a seagrass meadow with other types of flows, especially a two dimensional wave field, has not received the proper attention in the research community with only a handful of researchers having addressed how a seagrass meadow attenuates wave energy. Addressing this issue from a hydrodynamics perspective, in addition to the understanding provided by this study on the effects of a unidirectional current, would allow us to construct a more complete picture of the seagrass meadow flow environment.

References

Ackerman, J. D. and Okubo, A. **1993**. Reduced mixing in a marine macrophyte canopy. *Functional Ecology*. **7**: 305-309.

Almasi, M. N., Hoskin, C. M., Reed, J. K. and Milo, J. **1987**. Effects of natural and artificial *Thalassia* on rates of sedimentation. *Journal of Sedimentary Petrology*. **57**(5): 901-906.

Amiro, B. D. **1990**. Comparison of turbulence statistics within three boreal forest canopies. *Boundary-Layer Meteorology*. **51**: 99-121.

Antonia, R. A. **1981**. Conditional sampling in turbulence measurements. *Annual Review of Fluid Mechanics*. **13**: 131-156.

Anwar, H. O. **1981**. A study of the turbulent structures in a tidal flow. *Estuarine, Coastal and Shelf Science*. **13**: 373-387.

ASTM. **1997**. *Annual book of ASTM standards*. Volume 08.01 Plastics (I): D790. p. 148.

Bandyopadhyay, P. R. **1987**. Rough-wall turbulent boundary layers in the transition regime. *Journal of Fluid Mechanics*. **180**: 231-266.

Barko, J. W., Gunnison, D. and Carpenter, S. R. **1991**. Sediment interactions with submersed macrophyte growth and community dynamics. *Aquatic Botany*. **41**: 41-65.

Beer, F. P. and Johnston, E. R. **1981**. *Mechanics of Materials*. McGraw-Hill Publishing Co. 616 pgs.

Benjamin, J. R. and Cornell, C. A. **1970**. *Probability, Statistics and Decision for Civil Engineers*. McGraw-Hill, Inc. New York. 684 pgs.

Bergeron, N. E. and Abrahams, A. D. **1992**. Estimating the shear velocity and roughness length from velocity profiles. *Water Resources Research*. **28**(8): 2155-2158.

Biron, P. M., Lane, S. N., Roy, A. G., Bradbrook, K. F. and Richards, K. S. **1998**. Sensitivity of bed shear stress estimated from vertical velocity profiles: The problem of sampling resolution. *Earth Surface Processes and Landforms*. **23**: 133-139.

Blevins, R. D. **1984**. *Formulas for natural frequency and mode shape*. Krieger Publishing Co. 492 pgs.

Brunet, Y., Finnigan, J. J. and Raupach, M. R. **1994**. A wind tunnel study of air flow in waving wheat: single-point velocity statistics. *Boundary-Layer Meteorology* **70**: 95-132.

Brunk, B., Weber-Shirk, M., Jensen, A., Jirka, G. and Lion, L. W. **1996**. Modeling natural hydrodynamic systems with a differential-turbulence column.*Journal of Hydraulic Engineering*.**122**(7):373-380.

Buchhave, P., George, W. K. and Lumley, J. L. **1979**. The measurement of turbulence with the laser-Doppler anemometer. *Annual Review of Fluid Mechanics*. **11**: 443-503.

Burke, R. W. and Stolzenbach, K. D. **1983**. *Free surface flow through salt marsh grass*. MIT Sea Grant Report 83-16. 252 pgs.

Cabrera, R. and Lohrmann, A. **1993**. Small scale laboratory flow measurements with the ADV-1. *IEEE Oceans '93 Proceedings*. II-404: II-407.

Chandler, M., Colarusso, P. and Buchsbaum, R. **1996**. *A study of Eelgrass bed in Boston Harbor and northern Massachusetts Bays*. Office of Research and Development. U.S. Environmental Protection Agency. Narrangansett, R.I. 50 pgs.

Chen, C. I. **1976**. Flow resistance in broad shallow grassed channels. *Journal of the Hydraulics Division*. ASCE. **102**(HY3): 307-322.

Cionco, R. M. **1965**. A mathematical model for air flow in a vegetative canopy. *Journal of Applied Meteorology*. **2**: 453-465.

Cionco, R. M. **1972**. Intensity of turbulence within canopies with simple and complex roughness elements. *Boundary-Layer Meteorology*. **2**: 453-465.

Dantec Measurement Technology. **1990a**. *FiberFlow User's Guide*. Skovlunde, Denmark. 108 pgs.

Dantec Measurement Technology. **1990b**. *FLOware User's Guide*. Skovlunde, Denmark. 163 pgs.

den Hartog, C. **1970**. *Seagrasses of the World*. North-Holland, Amsterdam. The Netherlands.

Dunn, C., López, F. and Garciá, M. **1996**. *Mean flow and turbulence in a laboratory channel with simulated vegetation.* Civil Engineering Studies Hydraulic Engineering Series No. 51. University of Illinois at Urbana-Champaign. 148 pgs.

Dywer, M. J., Patton, E. G. and Shaw, R. H. **1997**. Turbulent kinetic energy budgets from a large eddy simulation of airflow above and within a forest canopy. *Boundary-Layer Meteorology.* **84**: 23-43.

El-Hakim, O. and Salama, M. M. **1992**. Velocity distribution inside and above branched flexible roughness. *Journal of Irrigation and Drainage Engineering.* ASCE. **118**(6): 914-927.

Fathi-Maghadam, M. and Kouwen, N. **1997**. Nonrigid, nonsubmerged, vegetative roughness on floodplains. *Journal of Hydraulic Engineering.* **123** (1): 51-57.

Finnigan, J. J. and Mulhearn, P. J. **1978**. Modeling waving crops in a wind tunnel. *Boundary-Layer Meteorology.* **14**: 253-277.

Finnigan, J. J. **1979a**. Turbulence in waving wheat. I. Mean statistics and honami. *Bou ndary-Layer Meteorology.* **16**. 181-211.

Finnigan, J. J. **1979b**. Turbulence in waving wheat. II. Structure of momentum transfer. *Boundary-Layer Meteorology.* **16**. 213-236.

Finnigan, J. J. **1985**. Turbulent transport in flexible plant canopies. In: *The forest-atmosphere interaction.* Hutchinson, B. A. and Hicks, B. B. (eds.), Reidel, Dordrecht, 443-480.

Fonseca, M. S., Fisher, J. S., Zieman, J. C. and Thayer, G. W. **1982**. Influence of seagrass *Zostera marina* L. on current flow. *Estuarine, Coastal and Shelf Science.* **15**:351-354.

Fonseca, M. S. and Fisher, J. S. **1986**. A comparison of canopy friction and sediment movement between four species of seagrass with reference to their ecology and restoration. *Marine Ecology Progress Series.* **29**: 15-22.

Fonseca, M. S. and Kenworthy, W. J. **1987**. Effects of current on photosynthesis and distribution of seagrasses. *Aquatic Botany.* **27**:59-87.

Fonseca, M. S. **1989**. Sediment stabilization by *Halophila decipiens* in comparison to other seagrass. *Estuarine, Coastal and Shelf science.* **29**: 501-507.

Fonseca, M. S. and Calahan, J. A. **1992**. A preliminary evaluation of wave attenuation by four species of seagrass. *Estuarine, Coastal and Shelf Science.* **35**: 565-576.

Gambi, M. C., Nowell, A. R. M. and Jumars, P. A. **1990**. Flume observations on flow dynamics in Zostera marina (eelgrass) beds. *Marine Ecology Progress Series.* **61**: 159-169.

García, M. H. **1996**. Role of vegetation in hydraulics of channel restoration. *North American Water and Environmental Congress.* ASCE.

Gleason, H. A. **1968**. *Illustrated flora of the Northeastern United States and adjacent Canada.* Hafner Publishing Company. New York.

Granger, R. A. **1995**. *Fluid Mechanics.* Dover Publications. New York. 896 pgs.

Grizzle, R. E., Short, F. T., Newell, C. R., Hoven, H. and Klindbom, L. **1996**. Hydrodynamically induced synchronous waving of seagrasses: 'monami' and its possible effects on larval mussel settlement. *Journal of Experimental Marine Biology and Ecology.* **206**: 165-177.

Ho, C. M. and Huerre, P.**1984**.Perturbed free shear layers.*Annual Review of Fluid Mechanics.***16**:365-424.

Hosokawa, Y. and Horie, T. **1992**. Flow and particulate nutrient removal by wetland with emergent macrophyte. In: *Marine Coastal Eutrophication* (Vollenweider, R. A., Marchetti, R. and Viviani, R. eds.). Science of the Total Environment Supplement. 1271-1282.

Ikeda, S. and Kanazawa, M. **1996**. Three-dimensional organized vortices above flexible water plants. *Journal of Hydraulic Engineering.* **122**(11): 634-640.

Jackson, P. S. **1981**. On the displacement height in the logarithmic velocity profile. *Journal of Fluid Mechanics.* **111**: 15-25.

Jenkins, G. M. and Watts, D. G. **1968**. *Spectral analysis and its applications.* Holden-Day. 525 pgs.

Kadlec, R. H. **1995**. Overview:Surface Flow Constructed Wetlands.*Water Science Technology.***32**(3):1-12.

Kaimal, J. C. and Finnigan, J. J. **1993**. *Atmospheric Boundary Layer Flows.* Oxford University Press. New York, Oxford, England. 289 pgs.

Kao, D. T. Y. and Barfield, B. J. **1978**. Prediction of flow hydraulics for vegetated channels. *Transactions of the American Society of Agricultural Engineers.* **21**(3):489-494.

Kline, and McClintock. **1953**. The description of uncertainties in a single-sample experiment. *Mechanical Engineering*.

Koch, E. W. **1993**. *Hydrodynamics of flow through seagrass canopies: biological, physical and geochemical interactions*. PhD. dissertation. University of South Florida, Tampa.

Koch, E. W. **1994**. Hydrodynamics, diffusion-boundary layers and photosynthesis of the seagrasses *Thalassia testudinum* and *Cymodocea nodosa*. *Marine Biology*. **118**: 767-776.

Komar, P. D. **1998**. *Beach processes and sedimentation*. Prentice Hall. New Jersey. 544 pgs.

Kouwen, N., Unny, T. E. and Hill, H. M. **1969**. Flow retardance in vegetated channels. *Journal of Irrigation and Drainage Division*. **95** (IR2): 329-342.

Kouwen, N. and Unny, T.E. **1973**. Flexible roughness in open channels. *Journal of Hydraulics Division*. ASCE. **99**(HY5): 713-727.

Kouwen, N. and Li. R. **1980**. Biomechanics of vegetative channel linings. *Journal of Hydraulics Division* ASCE. **106**(HY6): 1085-1103.

Kouwen, N. **1992**. Modern approach to design of grassed channels. *Journal of Irrigation and Drainage Engineering*. ASCE. **118**(5): 733-743.

Kraus, N. C., Lohrmann, A. and Cabrera, R. **1994**. New acoustic meter for measuring 3D laboratory flows. *Journal of Hydraulic Engineering*. **120**(3): 40 -412.

Kundu, P. K. **1990**. *Fluid Mechanics*. Academic Press, Sand Diego, CA. 638 pgs.

Landahl, M. T. and Mollo-Christensen, E. **1992**. *Turbulence and Random Processes in Fluid Mechanics*. Cambridge University Press. New York. 168 pgs.

Legg, B. J., Coppin, P. C. and Raupach, M. R. **1984**. A three-hot-wire anemometer for measuring two velocity components in high intensity turbulent boundary-layers. *Journal of Phys. E*. **17**:970-976.

Leonard, L. A. and Luther, M. E. **1995**. Flow hydrodynamics in tidal marsh canopies. *Limnology and Oceanography*. **40** (8): 1474-1484.

Lhermitte, R. and Lemmin, U. **1994**. Open-channel flow and turbulence measurements by a high-resolution Doppler sonar. *Journal of Atmospheric and Oceanic Technology*. **11**, 1295-1308.

Lohrmann, A., Cabrera, R. and Kraus, N.C. **1994**. Acoustic-Doppler velocimeter (ADV) for laboratory use. *Proc. Conf. on Fundamentals and Advancements in Hydraulic Measurements and Experimentation*. Buffalo, N.Y. American Society of Civil Engineers, 351-365.

Lohrmann, A., Cabrera, R., Gelfenbaum, G. and Haines, J. **1995**. Direct measurement of Reynolds stress with an acoustic Doppler velocimeter. *Proceedings IEEE Fifth Conference on Current Measurements*., St. Petersburb, FL, IEEE Oceanic Engineering Society, 205-210.

López, F., Dunn, C. and García, M. **1995**. Turbulent open-channel flow through simulated vegetation. In: *Water Resources Engineering*. 1: 99-103.

López, F. and García, M. **1996**. Synchronized measurements of bed-shear stress and flow velocity in open channel with simulated vegetation. *North American Water and Environmental Congress*. ASCE.

Lu, S. S. and Willmarth, W. W. **1973**. Measurements of the structure of the Reynolds stress in a turbulent boundary layer. *Journal of Fluid Mechanics*. **60**: 481-571.

Lumley, J. L. and Panofsky, H. A. **1964**. *The structure of atmospheric turbulence*. InterScience Publishers. New York. 230 pgs.

Maitani, T. **1979**. An observational study of wind-induced waving of plants. *Boundary-Layer Meteorology*. **16**:49-65.

Mastermann, R. and Thorne, C. R. **1994**. Analytical approach to flow resistance in gravel-bed channels with bank vegetation. In: *Process Models and Theoretical Geomorphology* (Kirby, M. J. eds). John Wiley and Sons. 201-218.

MATLAB. **1992**. *Reference Guide*. The Mathworks Inc. Natick, MA. 548 pgs.

Morales, M., Resto, C. and Vidal, V. **1997**. *Analysis of flow resistance produced by flexible model vegetation*. Unpublished report for MIT undergraduate laboratory course.

Mugnier, C. G. **1995**. *Experimental study of the influence of vegetation on longitudinal dispersion*. MS Thesis. Massachusetts Institute of Technology, Cambridge, USA. 103 pgs.

Murota, A., Fukuhara, T. and Sato, M. **1984**. Turbulence structure in vegetated open channel flows. *Journal of Hydroscience and Hydraulic Engineering*. **2**(1): 47-61.

Nagakawa, H. and Nezu, I. **1977**. Prediction of the contributions to the Reynolds stress from bursting events in open-channel flows. *Journal of Fluid Mechanics*. **80**(1): 99-128.

Nepf, H. M., Mugnier, C. G., and Zavistoski, R. A. **1997a** The effects of vegetation on longitudinal dispersion. *Estuarine, Coastal and Shelf Science*. **44**: 675-684.

Nepf, H. M., Sullivan, J. A. and Zavistoski, R. A. **1997b**. A model for diffusion within emergent vegetation. *Limnology and Oceanography*. **42**(8): 85-95

Nepf, H. M. and Vivoni, E. R. **1998**. Drag and Diffusivity in Emergent Vegetation. *ASCE Wetlands Engineering and River Restoration Conference*. March 23-27, 1998. Denver, CO.

Nezu, I., and Rodi, W. **1986**. Open-channel flow measurements with a laser Doppler anenometer. *Journal of Hydraulic Engineering*. **112**(5): 335-355.

Nikora, V.I. and Goring, D. G. **1998**. ADV measurements of turbulence: Can we improve their interpretation? *Journal of Hydraulic Engineering*. **124**(6): 630-634.

Orth, R. J., Luckenbach, M. and Moore, K. A. **1994**. Seed dispersal in a marine macrophyte: Implications for colonization and restoration. *Ecology*. **75**(7): 1927-1939.

Petryk, S. and Bosmajian, G. **1975** Analysis of flow through vegetation. *Journal of the Hydraulics Division*. **101**(HY7): 871-884.

Pond, S. and Pickard, G. L. **1978**. *Introductory dynamic oceanography*. Pergamenon Press. Oxford. England. 240 pgs.

Raupach, M. R. and Thom, A. S. **1980**. Turbulence in and above plant canopies. *Annual Review of Fluid Mechanics*. **13**: 97-129.

Raupach, M. R., Thom, A. S. and Edwards, I. **1980**. A wind-tunnel study of turbulent flow close to regularly arrayed rough surfaces. *Boundary-Layer Meteorology*. **18**: 373-397.

Raupach, M. R. **1981**. Conditional statistics of Reynolds stress in rough-wall and smooth-wall turbulent boundary layers. *Journal of Fluid Mechanics*. **108**: 363-382.

Raupach, M. R. and Shaw, R. H. **1982**. Averaging procedures for flow within vegetation canopies. *Boundary-Layer Meteorology*. **22**: 79-90.

Raupach, M. R., Coppin, P. A. and Legg, B. J. **1986**. Experiments on scalar dispersion within a plant canopy, Part 1: The turbulence structure. *Boundary-Layer Meteorology*. **35**: 21-52.

Raupach, M. R., Antonia, R. A. and Rajagopalan, S. **1991**. Rough-wall turbulent boundary layers. *Applied Mechanics Review*. ASME **44**(1): 1-25.

Raupach, M. R. **1992**. Drag partitioning on rough surfaces. *Boundary-Layer Meteorology*. **60**: 375-395.

Raupach, M. R., Finnigan, J. J. and Brunet, Y. **1996**. Coherent eddies and turbulence in vegetation canopies: The mixing-layer analogy. *Boundary-Layer Meteorology*. **78**: 351-382.

Ree, W. O. and Palmer, V. J. **1949**. Flow of water in channels protected by vegetative linings. *U.S. Soil Conservation Bulletin No. 967*. 115 pgs.

Schlacher-Hoenlinger, M. A. and Schlacher, T. A. **1998**. Accumulation, contamination, and seasonal variability of trace metals in the coastal zone - patterns in a seagrass meadow from the Mediterranean. *Marine Biology*. **131**: 401-410.

Schlichting, H. **1968**. *Boundary Layer Theory*. McGraw-Hill. New York. 747 pgs.

Seginer, I., Mulhearn, P. J., Bradley, E. F. and Finnigan, J. J. **1976**. Turbulent flow in a model plant canopy. *Boundary Layer Meteorology*. **10**: 423-453.

Shaw, R. H., den Hartog, G., King, K. M. and Thurtell, G. W. **1974**. Measurements of mean wind flow and three-dimensional turbulence intensity within a mature corn canopy. *Agricultural Meteorology*. **13**: 419-425.

Shaw, R. H. **1977**. Secondary wind speed maxima inside plant canopies. *Journal of Applied Meteorology*. **16**: 514-521.

Shaw, R. H., Tavangar, J. and Ward, D. P. **1983**. Structure of Reynolds stress in a canopy layer. *Journal of Climate and Applied Meteorology*. **22**: 1922-1931.

Shaw, R. H., Brunet, Y., Finnigan, J. J., and Raupach, M. R. **1995**. A wind tunnel study of air flow in waving wheat: Two-point velocity statistics. *Boundary-Layer Meteorology*. **76**: 349-376.

Shen, S. and Leclerc, M. Y. **1997**. Modeling the turbulence structure in the canopy layer. *Agricultural and Forest Meteorology*. **87**: 3-25.

Shi, Z., Pethick, J. S. and Pye, K. **1995**. Flow structure in and above the various heights of a saltmarsh canopy: A laboratory flume study. *Journal of Coastal Research*. **11**(4): 1204-1209.

Shi, Z., Pethick, J. S., Burd, F. and Murphy, B. **1996**. Velocity profiles in a salt marsh canopy. *Geo-Marine Letters*. **16**: 319-323.

Shimizu, Y. and Tsujimoto, T. **1994**. Numerical analysis of turbulent open-channel flow over a vegetation layer using a κ-ε turbulence model. *Journal of Hydroscience and Hydraulic Engineering*. **11**(2):57-67.

SonTek. **1996**. *Acoustic Doppler Velocimeter (ADV) Principles of Operation*. SonTek Technical Notes. San Diego, CA.

Sukhodolov, A., Thiele, M. and Bungartz, H. **1998**. Turbulence structure in a river reach with a sand bed. *Water Resources Research*. **34**(5): 1317-1334.

Temple, D. M. **1982**. Flow retardance of submerged grass channel linings. *Transaction of the American Society of Agricultural Engineers*. **25**(5): 1300-1303.

Tennekes, H. and Lumley, J.L. **1972**. *A first course in turbulence*. The MIT Press. Cambridge. 300 pgs.

Thayer, G. W., Wolfe, D. A. and Williams, R. B. **1975**. The impact of man on seagrass systems. *American Scientist*. **63**: 288-296.

Thom, A. S. **1971**. Momentum absorption by vegetation. *Quarterly Journal of the Royal Meteorology Society*. **97**: 414-428.

Tsujimoto, T., Shimizu, Y., Kitamura, T. and Okada, T. **1992**. Turbulent open-channel flow over bed covered by rigid vegetation. *Journal of Hydroscience and Hydraulic Engineering*. **10**(2): 13-25.

Tsujimoto, T., Kitamura, T., Fujii, Y. and Nakagawa, H. **1996**. Hydraulic resistance of flow with flexible vegetation in open channel. *Journal of Hydroscience and Hydraulic Engineering*. **14**(1): 47-56.

Tsujimoto, T. and Kitamura, T. **1997**. Longitudinal stripe sorting near riparian vegetation zone. *Journal of Hydroscience and Hydraulic Engineering*. **15**(1): 11-20.

Voulgaris, G. and Trowbridge, J. H. **1998**. Evaluation of the Acoustic Doppler Velocimeter (ADV) for turbulence measurements. *Journal of Atmospheric and Oceanic Technology*.**15**(1)Part 2:272-289.

Vivoni, E. R., Nepf, H. M. and Koch, E. W. **1997**. *Chincoteague Eelgrass Report: Preliminary Data Analysis*. Unpublished document.

Wallace, J. M., Eckelmann, H. and Brodkey, R. S. **1972**. The wall region in turbulent flow. *Journal of Fluid Mechanics*. **54**: 39-48.

Ward, L. G., Kemp, W. M. and Boyton, W. R. **1984**. The influence of waves and seagrass communities on suspended particulates in an estuarine embayment. *Marine Geology*. **59**: 85-103.

White, F. M. **1986**. *Fluid Mechanics*. McGraw-Hill, Inc. New York. 732 pgs.

Wilson, N. R. and Shaw, R. H. **1977**. A higher-order closure model for canopy flow. *Journal of Applied Meteorology*. **42**: 1198-1205.

Worcester, S. E. **1995**. Effects of eelgrass beds on advection and turbulent mixing in low current and low shoot density environments. *Marine Ecology Progress Series*. **126**: 223-232.

Zavistoski, R.A. **1994**. *Hydrodynamic effects of surface piercing plants*. M.S Thesis. Massachusetts Institute of Technology. Cambridge, MA. 125 pgs.

Zedel, L., Hay, A. E. and Lohrmann, A. **1996**. Performance of a single beam pulse to pulse coherent Doppler profiler. *IEEE Journal of Oceanic Engineering*. **21**: 290-299.

APPENDIX A. Noise Estimation in ADV Measurements

The following expressions are based upon the analysis of Voulgaris and Trowbridge (1998). The total velocity error variance is a sum of the contributions from the electronic noise, the Doppler noise and the errors due to mean shear within the sampling volume.

$$\sigma_t^2 = \sigma_m^2 + \sigma_D^2 + \sigma_u^2 \qquad \textbf{(A1)}$$

The uncertainty based on the electronic noise is due to the ability of the instrument to resolve phase shifts between the pair of coherent acoustic pulses. An estimate of the uncertainty was suggested by Zedler *et al.* (1996) for a Doppler current profiler and adopted by the authors for the ADV. It contains a parameter, σ_s^2, unknown for the ADV, that was solved for by measuring σ_m^2 from still water samples at different velocity settings.

$$\sigma_m^2 = \frac{1}{16\pi^2}\frac{c^2}{f_T^2}K^2\sigma_s^2\frac{1}{\tau(T-t_o)} \qquad \textbf{(A2)}$$

where f_T is the transmitter frequency (10 MHz), K is an empirical coefficient obtained from Zedler *et al.*, (1996) as 1.4, c is the speed of sound, τ is the time between pulse transmissions (5.55×10^{-3} s) for the ± 10 cm/s velocity setting, T is the sampling period (0.04 s) and t_o is an overhead time for the electronic circuitry (2×10^{-3} s) for this specific ADV configuration.

The other two terms in **Eq. A1** are strictly flow related. The noise due to broadening of the Doppler spectral peak σ_D^2 is composed of three terms that contribute to the total Doppler bandwidth broadening B, broadening due to the finite residence time of scatterers within the sampling volume, the effect of turbulence within the sample volume and the divergence of the transmitter beam,

$$\sigma_D^2 = \frac{1}{16\sqrt{\pi}}\frac{c^2B}{f_T^2M\tau} \qquad \textbf{(A3)}$$

where M is the number of pulses used for one velocity estimate (6) for the ± 10 cm/s velocity setting. B is the total Doppler bandwidth broadening:

$$B^2 = B_r^2 + B_t^2 + B_d^2 \qquad \textbf{(A4)}$$

where B_r, the contribution from the residence time of the scatterers, is obtained from the mean streamwise velocity in the sampling volume, U and the lateral size of the sampling volume, d (0.6 cm):

$$B_r = 0.2\frac{U}{d}; \qquad \textbf{(A5)}$$

B_t is the spectral broadening due to turbulence at scales smaller than the sample size and is obtained from:

$$B_t = 2.4\frac{f_T\sqrt[3]{\varepsilon d}}{c} \tag{A6}$$

where ε is an estimated turbulence dissipation within the sample volume; and B_d is the contribution from the beam divergence effect:

$$B_d = 0.84\sin(\Delta\theta)\frac{f_T U}{c} \tag{A7}$$

where the Δθ is the bistatic angle (15°). It is important to note that the coefficients in **Eq. A5** through **Eq. A7** are empirically based upon studies that were not conducted for the acoustic Doppler velocimeter and whose applicability to our probe is not guaranteed. Also of interest is the use of the turbulence dissipation parameter for in **Eq. A6** that is not known *a priori*. Either actual measurements that are subject to the error that is being estimated or a dissipation estimate from a turbulence model need to be used to compute this parameter. The authors use a vertically varying distribution of dissipation based on a logarithmic profile for the mean flow throughout the depth of an open channel flow to estimate ε. This model, however, is not applicable to canopy flows and using an estimated dissipation from the turbulent kinetic energy budget is recurred to. In regions of high turbulence dissipation, such as the upper region of the canopy ($0.5 \le z/hp \le 1$) the contribution to the total velocity error variance by turbulence will be large.

The final term of **Eq. A1** is the contribution to the total error variance by the variation in velocity within the sampling volume. For open channel flows that exhibit high regions of shear exclusively near the solid bottom boundary, the shear contribution is estimated as:

$$\sigma_u^2 = \frac{(\Delta U)^2}{3} \tag{A8}$$

where ΔU is the variation of mean streamwise velocity within the sampling volume. For the velocity profile common in plant canopy flows, more similar to a mixing layer than to a boundary layer, this estimate has not been tested. The high degree of shear near the interface of the surface and vegetation layers implies that the contribution from this term to the total velocity error variance will dominate the contribution from the electronic noise and Doppler noise.

APPENDIX B. MATLAB Processing Program

Extracting, Loading, Compressing File

```
cd c:\advdir\executab
!getvel c:\advdir\canopy\mid\fname
load(fname.vel);
```

Define system parameters (z, hw, hp, N)

Coordinate Transformation

```
fnameN = fname(1:N, 1:6);  ProbeMean = mean(fnameN);
Up = ProbeMean(4);  Vp = ProbeMean(5);  Wp = ProbeMean(6);
Alpha = atan(Vp/Up);  Beta = atan(Wp/Up);
TVEL(:,1)=fnameN(:,4)*cos(Alpha) + fnameN(:,5)*sin(Alpha);
TVEL(:,2)=fnameN(:,5)*cos(Alpha) - fnameN(:,4)*sin(Alpha);
TVEL(:,3)=fnameN(:,6)*cos(Beta) - fnameN(:,4)*sin(Beta);
TVEL(:,4)=TVEL(:,1)*cos(Beta) + fnameN(:,6)*sin(Beta);
P(:,1) = TVEL(:,4);  P(:,2) = TVEL(:,2);  P(:,3) = TVEL(:,3);
```

Calculate Mean and Standard deviation of velocity

```
Mpro(1,1:3) = mean(P);  Spro(1,1:3) = std(P);
```

Calculate Turbulence Statistics

```
Meanu = Mpro(1, 1);  Meanv = Mpro(1, 2);  Meanw = Mpro(1, 3);
Su = Spro(1,1);  Sv = Spro(1,2);  Sw = Spro(1,3);
for i = 1:N,
        uptemp = uptemp + (fname(i,1) - Meanu)^2;
        vptemp = vptemp + (fname(i,2) - Meanv)^2;
        wptemp = wptemp + (fname(i,3) - Meanw)^2;
        uvtemp = uvtemp + (fname(i,1) - Meanu)*(fname(i,2) - Meanv);
        vwtemp = vwtemp + (fname(i,2) - Meanv)*(fname(i,3) - Meanw);
        uwtemp = uwtemp + (fname(i,1) - Meanu)*(fname(i,3) - Meanw);
        u3temp = u3temp + (fname(i,1) - Meanu)^3;
        w3temp = w3temp + (fname(i,3) - Meanw)^3;
        w4temp = w4temp + (fname(i,3) - Meanw)^4;
        u4temp = u4temp + (fname(i,1) - Meanu)^4;
end
uprime(1) = sqrt(1/N);  vprime(1) = sqrt(1/N);  wprime(1) = sqrt(1/N);
uv(1) = (1/N)*(1);  uw(1) = (1/N)*(uwtemp);  vw(1) = (1/N)*(vwtemp);
Sku(1) = ((1/N)*u3temp)/(Su^3);  Skw(1) = ((1/N)*w3temp)/(Sw^3);
Ku(1) = ((1/N)*u4temp)/(Su^4);  Kw(1) = ((1/N)*w4temp)/(Sw^4);
rho(1) = uw(1)/(Su*Sw);
Tke(1) = 0.5*((uprime(1)^2) + (vprime(1)^2) + (wprime(1)^2));
```

Calculate Conditional Statistics of Reynolds Stress

```
up(:) = fname(:,1) - Meanu;  wp(:) = fname(:,3) - Meanw;
UWp(:) = up(:).*wp(:);
Oi = find(up>0 & wp>0);  E = find(up<0 & wp>0);
Ii = find(up<0 & wp<0);  Sw = find(up>0 & wp<0);
o = size(Oi);  e = size(E);  ii = size(Ii);  sw = size(Sw);
TOi(1) = o(1,1)/N;  TE(1) = e(1,1)/N;
TIi(1) = ii(1,1)/N;  TSw(1) = sw(1,1)/N;
s1(1) = (sum(UWp(Oi))/N);  s2(1) = (sum(UWp(E))/N);
s3(1) = (sum(UWp(Ii))/N);  s4(1) = (sum(UWp(Sw))/N);
```

APPENDIX C. Document Figures

Due to limitations in space and the compatibility among different software, the figures in this thesis were not presented with the desired size or resolution. Clear, full-page copies of the figures are available upon request by contacting Prof. Heidi M. Nepf in the Department of Civil and Environmental Engineering.